COMPUTER SIMULATION STUDIES OF SPINEL $LiMn_2O_4$ AND SPINEL $LiNi_XMn_{2-X}O_4$ $(0 \leq x \leq 2)$

By

KEMERIDGE TUMELO MALALTJI

Thesis Submitted in fulfilment of the requirements for the degree of

Doctor of Philosophy

In

Physics

in the

FACULTY OF SCIENCES AND AGRICULTURE

(School of Physical and Mineral Sciences)

at the

UNIVERSITY OF LIMPOPO

SUPERVISOR: Prof. R.R. Maphanga

CO- SUPERVISORS: Prof. P.E. Ngoepe

(Dated: 29 October 2019)

Declaration

I, Kemeridge Tumelo Malatji confirm that the work presented in this thesis is my own. Where information has been derived from other sources, I confirm that this has been indicated in the thesis. I agree that the Library may lend or copy this dissertation on request.

Signature: [redacted] Date: **29/10/2019**

Name**: Mr K.T. Malatji**

Abstract

$LiMn_2O_4$ spinel (LMO) is a promising cathode material for secondary lithium-ion batteries which, despite its high average voltage of lithium intercalation, suffers crystal symmetry lowering due to the Jahn-Teller active six-fold Mn^{3+} cations. Although Ni has been proposed as a suitable substitutional dopant to improve the energy density of $LiMn_2O_4$ and enhance the average lithium intercalation voltage, the thermodynamics of Ni incorporation and its effect on the electrochemical properties of this spinel are not fully understood.

Firstly, structural, electronic and mechanical properties of spinel $LiMn_2O_4$ and $LiNi_xMn_{2-x}O_4$ have been calculated out using density functional theory employing the pseudo-potential plane-wave approach within the generalised gradient approximation, together with Virtual Cluster Approximation. The structural properties included equilibrium lattice parameters; electronic properties cover both total and partial density of states and mechanical properties investigated elastic properties of all systems. Secondly, the pressure variation of several properties was investigated, from 0 GPa to 50 GPa. Nickel concentration was changed and the systems $LiNi_{0.25}Mn_{1.75}O_4$, $LiNi_{0.5}Mn_{1.5}O_4$ $LiNi_{0.75}Mn_{1.25}O_4$ and $LiNi_{0.875}Mn_{1.125}O_4$ were studied. Calculated lattice parameters for $LiMn_2O_4$ and $LiNi_{0.5}Mn_{1.5}O_4$ systems are consistent with the available experimental and literature results. The average Mn(Ni)-O bond length for all systems was found to be 1.9 Å. The bond lengths decreased with an increase in nickel content, except for $LiNi_{0.75}Mn_{1.25}O_4$, which gave the same results as $LiNi_{0.25}Mn_{1.75}O_4$. Generally, analysis of electronic properties predicted the nature of bonding for both pure and doped systems with partial density of states showing the contribution of each metal in our systems. All systems are shown to be metallic as it has been previously observed for pure spinel $LiMn_2O_4$, and mechanical properties, as deduced from elastic properties, depicted their stabilities.

Furthermore, the cluster expansion formalism was used to investigate the nickel doped $LiMn_2O_4$ phase stabilities. The method determines stable multi-component crystal structures and ranks metastable structures by the enthalpy of formation while

maintaining the predictive power and accuracy of first-principles density functional methods. The ground-state phase diagram with occupancy of Mn 0.81 and Ni 0.31 generated various structures with different concentrations and symmetries. The findings predict that all nickel doped LMO structures on the ground state line are most likely stable. Relevant structures ($Li_4Ni_8O_{16}$, $Li_{12}MnNi_{17}O_{48}$, $Li_4Mn_6Ni_2O_{16}$, $Li_4Mn_7NiO_{16}$ and $Li_4Mn_8O_{16}$) were selected on the basis of how well they weighed the cross-validation (CV) score of 1.1 meV, which is a statistical way of describing how good the cluster expansion is at predicting the energy of each stable structure. Although the structures have different symmetries and space groups they were further investigated by calculating the mechanical and vibrational properties, where the elastic constants and phonon vibrations indicated that the structures are stable in accordance with stability conditions of mechanical properties and phonon dispersions.

Lastly, a computer program that identifies different site occupancy configurations for any structure with arbitrary supercell size, space group or composition was employed to investigate voltage profiles for $LiNi_xMn_{2-x}O_4$. The density functional theory calculations, with a Hubbard Hamiltonian (DFT+*U*), was used to study the thermodynamics of mixing for $Li(Mn_{1-x}Ni_x)_2O_4$ solid solution. The results suggested that $LiMn_{1.5}Ni_{0.5}O_4$ is the most stable composition from room temperature up to at least 1000K, which is in excellent agreement with experiments. It was also found that the configurational entropy is much lower than the maximum entropy at 1000K, indicating that higher temperatures are required to reach a fully disordered solid solution. The maximum average lithium intercalation voltage of 4.8 eV was calculated for the $LiMn_{1.5}Ni_{0.5}O_4$ composition which correlates very well with the experimental value. The temperature has a negligible effect on the Li intercalation voltage of the most stable composition. The approach presented here shows that moderate Ni doping of the $LiMn_2O_4$ leads to a substantial change in the average voltage of lithium intercalation, suggesting an attractive route for tuning the cathode properties of this spinel.

ACKNOWLEDGEMENTS

I would like to thank my supervisor Prof. R.R. Maphanga for all the unconditional encouragement, guidance, support, mentoring. Thanks for making the journey in the research field an interesting one. My gratitude also goes to my co-supervisor Prof. P.E. Ngoepe for this opportunity, contribution throughout this study and award of the project. I am forever humbled by what you saw in me and for your mentorship.

Above all, I would like to thank the almighty God for all the strength, patience and perseverance He has installed in me during all the years of my studies, without Him this work wouldn't have been started. I fully acknowledge the financial support from the National Research Foundation. This research wouldn't have been a success if it was not of their financial backing and it encouraged my work ethic. Ample thanks to all the compatriots of the Material Modeling Center whose friendship, guidance and support had made the center more than an area to study at; "It is and will always be a jam to work with you fellas".

Finally, abundant thanks to my parents Mosadi Sophy Malatji and Johannes Anaph Malatji for their warm support, constant believe, encouragement and the love they showed me during this journey and life. They have contributed to me being the man I am today. My brothers (Kholofelo Brian Malatji and Tshegofatjo Anaph Malatji) thanks a lot your brotherhood, which reminded me that my efforts would make a difference in your lives. To my grandmothers (Shibe and Boreadi), aunts and uncle, your contribution will always be of paramount significance in my heart. To my beautiful partner your support from reading my work and pushing me to finish meant a lot. I would also like to give thanks to my many friends and extended family members who were always positively inquisitive about my progress. I wish to thank everybody with whom I have shared experiences in life. Most importantly, ample thanks to my late grandfather Samson Galiade Gozo 'aka Gita' for always making me believe on how important education is. Always full of laughter.

Dedication

This work is dedicated to my lovely parents Johannes Anaph Malatji and Mosadi Sophy Malatji, my brothers (Kholofelo Brian Malatji and Tshegofatjo Anaph Malatji). To my late grandfather wherever you are, this is for you, may your soul rest in peace "Galiade".

"It's better to die for an idea that will live than to live for an idea that will die" –Onkgopotse Abram Tiro

Chapter 1 Contents

List of Figures

List of Tables

Chapter 1

Introduction

1.1 General Introduction

Due to a shortage of the fossil-fuels and serious environmental pollution caused by motor vehicle emissions, alternative sources of energy have been urgently demanded world-wide. Demands on lifetime and energy/power density are increasing significantly over the past decade and increasing to extend the duration in which the battery can be used [1]. The requirements of appropriate energy storage devices differ notably in each area of application. Hence research in the field of rechargeable lithium batteries has intensified, attempting to further improve lithium-ion batteries.

Renewable energy technologies such as rechargeable batteries are clean sources of energy that have a much lower environmental impact than conventional energy technologies. Lithium-ion batteries have been successful in portable electronics market regarded as the most prospective power source for electric vehicles (EVs) and hybrid electric vehicles (HEVs) due to their high energy density [2] [3] [4] [5]. However, increasing interest in lithium-ion batteries for electric vehicle (EV), hybrid electric vehicle (HEV) and plug-in electric vehicle (PHEV) applications requires alternative cathode materials due to the high cost, toxicity, and limited power capability of the layered $LiCoO_2$ cathode. The oldest commercially used electrodes are $LiCoO_2$, it exhibits a relatively stable cyclability and an excellent rate performance. However, cobalt metal is much less abundant in nature and characterized with a medium-cost, and these problems are obstacles to applications of $LiCoO_2$ as cathode material for large-scale lithium batteries for load-levelling systems and electric vehicles [6]. The other commercially used electrodes are spinel $LiMn_2O_4$ due to the low-cost, environmentally friendly, highly abundant material that is used as a cathode material in Li-ion batteries.

Great efforts have been made to improve the electrochemical performance of $LiMn_2O_4$ spinel [2] [7] Presently, four main methods are adopted to overcome the capacity deterioration problem, (i) introducing cation defects or vacancies ($Li_{1-x}Mn_{2-x}O_4$), (ii) doping with excess lithium to form the solid solution, $Li_{1+x}Mn_{2-x}O_4$ and (iii) doping with different metals (for example, Mg, Ni, Cu, Zn, Cr and Al) on the manganese octahedral 16d sites, (iv) among them, surface modification has demonstrated excellent performance, (v) thermo-stability of $LiMn_2O_4$-based batteries at elevated temperatures, [8] [9]. These efforts are made to increase the amount of Mn^{4+} by slightly increasing the Li/Mn atomic ratio, where the Jahn-Teller distortion becomes less severe, therefore, the structural stability increases and the cyclability is improved. Some of the measures have improved the cyclability of the Li-ion batteries to a great extent and they were accompanied by the significant loss capacity.

1.2 Lithium-ion Batteries

A battery is an electrochemical device that stores chemical energy and releases it in the form of electrical energy when needed. Batteries can be categorised as primary and secondary batteries based on the reversibility of the chemical reactions involved. The reaction in a secondary battery is reversible and irreversible in a primary battery [10] [11]**.** The first true battery (primary batteries) was invented by Alessandro Volta in 1800, which is known as a Voltaic Pile [10]. Since then, lithium manganese dioxide battery, alkaline battery, lithium primary battery, and zinc-air battery have been designed and commercialised [11]. Lead-acid batteries were the first rechargeable battery launched by Gaston Planté in 1860, with success in automobile and other applications with advantages of high rate and good low-temperature performances. Therefore the most popular battery technologies are the lithium-ion batteries because they have high energy- and power density as well as their high lifetime compared to other types [12].

The lithium-ion battery is composed of four main components: a negative electrode (anode), a positive electrode (cathode), an electrolyte and a separator. When the

battery is charged, the lithium-ions in the cathode material migrate through the separator to the anode with the flow of charging current through the external circuit. In the opposite way, the lithium-ions in the anode migrate through the separator to the cathode material with the flow of discharging current through the external circuit (see Figure 1-1). The main property of the electrolyte is the transportation of ions from the anode to the cathode or vice-versa while ensuring as little as possible side reactions with the Li-ions. Mostly it consists of water with some dissolved salts, the most used lithium hexafluorophosphate, to ensure good ion conductivity. Layered $LiCoO_2$ is widely used in most commercial lithium-ion batteries due to its good cyclability, reasonable capacity and easy synthesis [13].

However, certain issues associated with safety, cost and the environmental hazard of cobalt have stimulated the development and improvement of alternative cathode materials. Several cathodes with different compositions, metal ions, or crystal structures have been investigated [14]. The electrochemical storage of energy in a lithium-ion battery is attained along intercalation in the positive and negative electrode, presented by equation (1) [15]:

$$Li^+ + e^- + \theta \longleftrightarrow Li - \theta \quad \text{..... (1)}$$

With:

θ the insertion material

$\theta - Li$ Lithium inserted in the material

$\theta\ e$ − an electron Li+ A lithium-ion

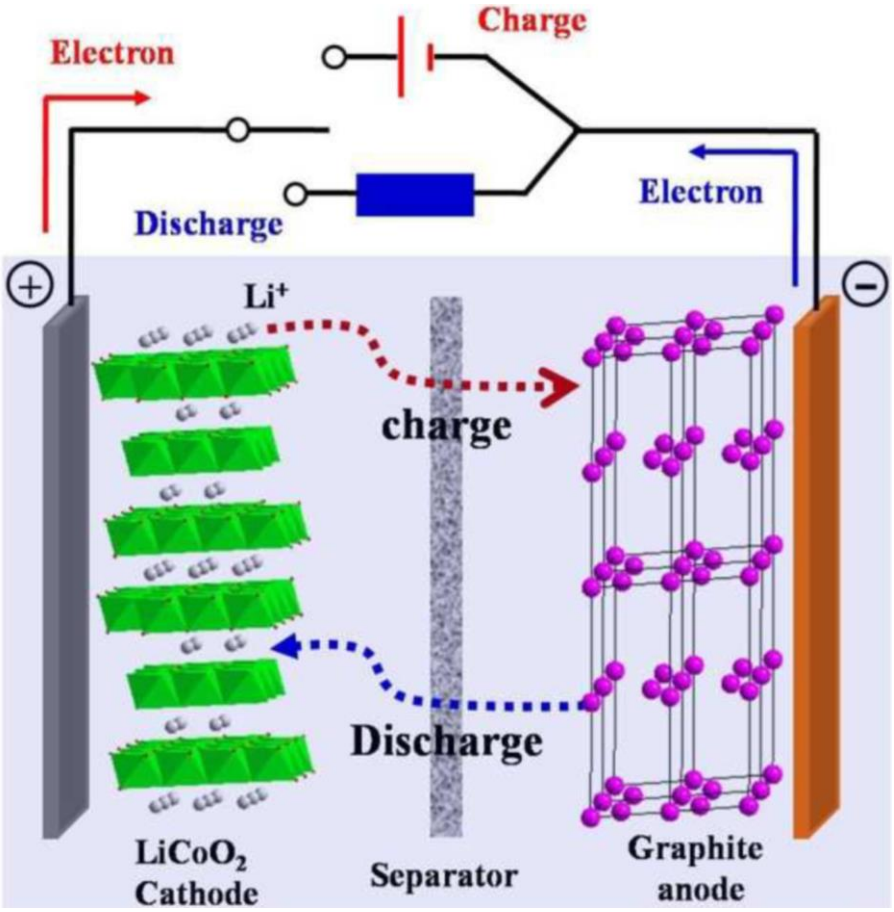

Figure 1-1: Schematic representation of lithium-ion battery during the charge-discharge process [16].

Spinel $LiMn_2O_4$ has been studied extensively in order to replace $LiCoO_2$ as a cathode material for secondary lithium-ion batteries due to its low cost, environmental friendliness and non-toxicity [17] [18]. The major problem of this material is a rapid capacity deterioration, especially at elevated temperatures; due to Mn dissolution, the crystal structure changes due to Jahn-Teller distortion in a deeply discharged state, and the decomposition of organic electrolytes on its surface during charge process [19].

Since lithium metal constituted a safety problem, in1980 a breakthrough in concept was generated. Lazzari and Scrosati [20] proposed the “rocking chair battery” based two insertion compounds, Li_xWO_2 and Li_yTiS_2. Though this system could solve the problem of safety, it was unable to provide the practical energy required to make it an attractive rechargeable system. In 1980 when the $LiCoO_2$ was demonstrated

firstly as a possible cathode material for rechargeable lithium battery, the transition metal intercalation oxides have caught the major research interests as the LIB cathodes [21] [22]. They are categorised by structure, the conventional cathode materials include layered compounds $LiMO_2$ (M = Co, Ni, Mn etc.), spinel compounds LiM_2O_4 (M=Mn etc.), and olivine compounds $LiMPO_4$ (M = Fe, Mn, Ni, Co, etc.). Most of the research is performed on these materials and their derivatives. Lithium-ion is now a worldwide project and widely accepted by the battery community, although there is no lithium metal in the cell. Both electrodes operate by intercalation of lithium ions into the structure of the active materials. AT Battery Co., a joint venture of Toshiba Battery Co. and Asahi Chemical Co. was the second to commercialise the technology using Asahi patent portfolio [23].

There are observations that the minor change in impedance of the electrode on cycling cannot account for the observed capacity fading and Premanand *et al.* [24] concluded that the main cause is the structural change and associated active material dissolution in the electrolyte. The capacity of $LiMn_2O_4$ fades during cycling for several reasons, such as instability of an organic-base electrolyte in a high operation voltage [25], structure-related dissolution of manganese into electrolyte [26] [27] [28], change in a crystal lattice arrangement with cycling [29] and so on. In general, $LiM_xMn_{2-x}O_4$ (M=Co, Ni, Cr, etc.) material was prepared using the conventional solid-state method at low (600~700℃) or high temperatures (750~850℃) [30] [31]. In the process, the oxides or carbonates containing manganese and lithium cations are physically mixed by mechanical methods, and all the solid particles may not completely react, which results in undesirable impurities in the final product. Therefore, a considerable improvement in the preparation of $LiM_xMn_{2-x}O_4$ cathode materials has been accomplished using the wet methods [32] [33] [34] and all components homogeneously distributed in samples using the wet method [35]. To improve the stability of $LiMn_2O_4$ spinel structure, Ni-doped spinel samples synthesised through the improved precipitation method [2], and the effects of Ni content of the structure and electrochemical performance of $LiMn_2O_4$ were investigated in detail Bao *et a*l [36] and Sun *et al* [37] have reported that the introduction of anion substitution in the form of spinel oxy-fluorides can reduce the Mn oxidation state and then increase the specific capacity. Thus, dual

cationic and anionic substitutions can be assumed to be an alternate way of improving the material's electrochemical properties [38]. The charge-discharge capacity and cycle performance of $LiMn_2O_4$ were greatly affected by the synthesis methods and conditions. $LiMn_2O_4$ can be obtained by a solid-state reaction at a high temperature and the soft chemistry method at low temperature [38]. The sol-gel method gives the $LiMn_2O_4$ in fine particle size a narrow size distribution and uniform composition, so it has been widely used to prepare the positive electrode materials of lithium-ion batteries [39]. However, the $LiMn_2O_4$-based cathode for lithium-ion batteries suffers severe capacity deterioration especially at elevated temperature, which might be related to Mn dissolution in acidic electrolytes [2] [40] Jahn-Teller distortion of Mn^{3+} at deeply discharge state [9], and oxygen deficiency [41].

In order to address the issues, using the other transitional metal (e.g. Ni, Fe, Co, Al) to replace Mn have been explored for the cathodes of lithium-ion batteries [42] [43] [44] [45]. Among these materials, $LiNi_xMn_{2-x}O_4$ shows the best cycling stability, it is still crucial and desirable to design and develop new strategies in this field [46]. This improvement probably comes from the strong chemical bond of Mn-O-Ni that stabilises the octahedral spinel sites, prevents the dissolution of Mn^{3+} ions into the electrolyte, and restrains the Jahn-Teller distortion [47]. Since a large amount of Ni doping could render a significant decrease of the capacity at 4 V [48], most studies about $LiNi_xMn_{2-x}O_4$ were confined in the case of $x \leq 0.2$ for stable crystal structure and good cyclic performance [49] [50] [51] [52]. So far, the performance of $LiNi_xMn_{2-x}O_4$ at room temperature has been well documented, but that at elevated temperature is studied to a less extent [53] [54], particularly at a high-rate charge/discharge.

The electrochemical property of $LiMn_2O_4$-based spinel is highly dependent on its synthetic routes, such as the Pechini process [55], sol-gel [56], emulsion method [57], the citric method [58], etc. However, most of these methods involve complicated treatment processes or expensive reagent, which is time-consuming and highly costly for commercial applications. The Mn-substitution in $LiMn_2O_4$ indicates improved charge-discharge cycling stability both at ambient temperature and at 50℃ up to 80 cycles at a 0.5C rate and was ascribed to structural stabilisation

induced by the substitution [59]. To date, spinel $LiNi_{0.5}Mn_{1.5}O_4$ doped with Ru has been reported to have the best electrochemical performance. Wang *et al*. reported the high rate capability of nanostructured Ru doped spinel $LiNi_{0.5}Mn_{1.5}O_4$ [60].

1.3 Doping in $LiMn_2O_4$

The performance of cathode materials can be improved by doping. However, the interpretation of doping effects can be complicated due to interrelations between doping and microstructural morphology [61]. This two problem engage various factors involving the cation ordering related to Mn^{3+} content, particle morphology, surface modification and the surface crystalline planes in contact with the electrolyte, whereas, all factors are profoundly influenced by the different synthesis procedures and circumstances [46]. Various divalent and trivalent ions, which make the structure more stable, have been tried as dopants in several studies, in particular, aluminium, chromium, magnesium and other transitional metals [62] [63] [64]. Chromium-doped spinels have shown to operate successfully in a higher voltage range. Magnesium was found to be successful in suppressing the oxygen non-stoichiometry in $LiMn_2O_4$, which was a necessary condition for the structural transition of $LiMn_2O_4$ near room temperature.

Doping is very useful for keeping structure stability and improving the cyclability of the $LiMn_2O_4$ spinel material since it's widely explored. Due to the capacity deterioration of $LiMn_2O_4$ spinel is greatly associated with Mn dissolution caused by Mn^{3+} disproportion reaction and Jahn-Teller distortion, which can be restrained by doping appropriate concentration into the bulk or surface spinel for cation or anion substitution. The investigated doping ions can be divided into two categories, cations and anions and the doped elements were replaced (manganese) and rise to manganese ions average valence, confining the Mn^{3+} solution and declining the Jahn-teller deformation. To the best of our knowledge, the cationic doping elements mainly include Fe, Co, Ni, Al, Cl, Ti, F, and S as a doped element and studies the influence of the charge/discharge properties of the doped $LiMn_2O_4$ material [2]. The defect aspect of nickel or cobalt doped LMO spinel is more complicated because both Ni and Co can exhibit different oxidation states of +2, +3 and +4 in $LiMn_2O_4$.

Previous studies reported that when doping spinel with nickel or cobalt ions occupy octahedral 16d sites as in the form of Ni^{2+} or Co^{3+} by the substitution for Mn ions [65] [66] [67] [68]. $LiNi_{0.5}Mn_{1.5}O_4$ is the most promising and attractive material because of its acceptable stability, a dominant potential plateau at around 4.7 V, good cyclic property and relatively high capacity [69]. The high cycling performance of $LiNi_{0.5}Mn_{1.5}O_4$ may be due to the shortening of the average chemical bond length of Mn(Ni)–O, which increases/decreases the mean chemical bond energy and enhances the structural stability [70] [71]. The high operating voltage and chemical stability of $LiNi_{0.5}Mn_{1.5}O_4$ make it a strong cathode candidate for next-generation Li-ion cells with high energy and power densities [34]. Recently, the density functional theory methods have been widely employed to investigate spinel $LiMn_2O_4$ system, which provided information on clarifying and explaining some experimental phenomena [72]. The electronic properties of spinel show that the bonding between O and metal (i.e. Mn and Ni) is also strengthened due to the Ni doping, which improves the structural stability of $LiNi_{0.5}Mn_{1.5}O_4$. Furthermore, Ni-doped spinel has a lower formation enthalpy than that of the pristine, indicating that the Ni doping improves the structural stability of spinel [47].

A study on chromium-doped $LiMn_2O_4$ using the local density approximation (LDA) has been carried out by Shi *et al*. [73]. Calculations were performed on un-relaxed systems and a very slight increase in the charge density around manganese atoms even for the maximum doping content of chromium was observed. A major change in the charge density was found for oxygen atoms. It was also observed that the shape of the density of states plot for both manganese and oxygen atoms remains almost unchanged after doping with chromium. Mishra *et al* [74] performed spin polarization (antiferromagnetic) generalized gradient approximation (GGA) calculations $LiMn_2O_4$ and $LiCrMnO_4$. Mishra and Ceder in their study on the structural stability of lithium manganese oxides have stressed the use of GGA. A phase diagram of the $Li_xMn_2O_4$ has been calculated using local density approximation to the density functional theory [75]. The study successfully explains the phase transformation when x varies from 1 to 2 (cubic to tetragonal phase transformation). However, the phase stability, lattice change and voltage are not consistent with the experimental observations when x varies in the range of 0 to1.

This can be attributed to the fact that neither the LDA nor the GGA approach can give the distinguished electronic structures of $Mn^{3+/}Mn^{4+}$ ions in $LiMn_2O_4$ [75] [76]. However, $LiMn_2O_4$ suffers from both the inferior theoretical capacity (148 $mAh.g^{-1}$ compared with 274 $mAh.g^{-1}$ of $LiCoO_2$) and an unacceptable performance fade. To improve its cycling performance, especially at elevated temperature (≥50℃), several approaches such as doping at the Mn site, surface modification, and various preparatory conditions have been shown to be successful [12] [56] [77] [78] [79] [80] [81] [82] [83] [84] [85] [86] [87] [88] [89]. The increased impedance contribution of the $LiMn_2O_4$ electrode with cycling was also correlated with the observed capacity fading in spinel compounds [90] [91].

There are two kinds of doping, the substitutional and interstitial doping. As an example, $Li_{1.1}Mn_2O_4$ is obtained by interstitial doping while $Li[Mn_{1.7}Fe_{0.3}]O_4$ is obtained by substitutional doping. Substitutional doping is therefore taken as the introduction of foreign elements into the host material to take the place of some proportion of the original host chemical or element. Substitutional doping, thus, preserves the crystal structure of the compound while interstitial doping may change or modify the structure. The important point is that, for substitutionally doped compounds, the positions of the atoms are precisely known in the crystal lattice whereas, for an interstitially doped compound, the atoms/ions may sit in interstitials whereby the position is not precisely known. Thus, it is quite problematic to analyse stoichiometry of interstitially doped materials in terms of the position of the foreign elements in the crystal structure of the materials.

When constructing a CE for a specific bulk structure, there are major tasks to consider (i) the type of figures (pairs, three-body,…) and how many are needed for a utilised alloy system, and (ii) how to obtain the magnitude of the selected interactions {J} from a well-posed microscopic theory of electronic structure [92]. Although the first-principles investigations of the thermodynamics of binary alloys using a cluster expansion have so far neglected the presence of vacancies. It is also clear that the doping of Ni may lead to an improvement in cathode performance, both the underlying mechanism and, more fundamentally, the question of nickel solubility in bulk LMO remain open [93]. Several computational approaches have also been made to investigate the behaviour of the cationic disorder. In this work,

we study the conditions under which nickel doping and cluster expansion into LMO bulk may be feasible. The temperature dependence of cationic disorder has also been studied, although only within a few short-range interactions, using statistical mechanics techniques to calculate the finite-temperature properties. Warren *et al*. calculated the degree of inversion using a Monte Carlo simulation with a NN pair and NN triangle interactions parameterized using the energies of 10 ordered structures obtained within local density approximation LDA [94] [95]. Rocha et al. studied the effects of high pressure on the cationic disorder using a mean-field approximation, in addition to the behaviour under normal pressure [96]. The free energy of disordered spinels was evaluated from a modified effective thermodynamic model combining a regular solution with a quadratic form of internal energy. Generally speaking, the prediction of order-disorder transition temperature and phase diagram characteristics needs multi-electron volt accuracy and many-body to obtain the magnitude of the chosen interactions {J}. Effective cluster interactions in the cluster expansion are determined by the minimisation of the cross-validation score using a genetic algorithm.

1.4 Structural Properties of $LiMn_2O_4$

The spinel $LiMn_2O_4$ structure has a general chemical formula ($[Li]_{tet}[Mn_2]_{Oct}O_4$) belonging to the space-group Fd-3m, which each lattice is made up of 2 lithium atoms, 4 manganese atoms and 8 oxygen atoms. $LiMn_2O_4$ adopts the spinel crystal structure with lithium ions occupying tetrahedral 8a sites, an equal amount of Mn^{3+} and Mn^{4+} ions on octahedral 16d sites with an average charge of +3.5 and oxygen ions on 32e sites. The 8a and 16d sites form a three-dimensional pathway for lithium ions diffusion. Empty tetrahedral (8a) and octahedral (16c) sites that share faces create a 3-D tunnel structure that allows lithium ions to move easily through the structure. Oxygen atoms located at 32e sites are arranged in a close-packed cubic array and construct a face-centred cubic. When Li-ions diffuse into the structure, first moves from 8a site to the neighbouring 16d site, and then to the next 8a site in a way that it enables three-dimensional lithium diffusion. The 8a tetrahedral site is situated furthest away from the 16d site of all the interstitial tetrahedral (8a, 8b and 48f) and octahedral (16c). The Mn ions have octahedral coordination to the

oxygen's, and the MnO_6 octahedra share edges in a three-dimensional host for the Li guest ions [97].

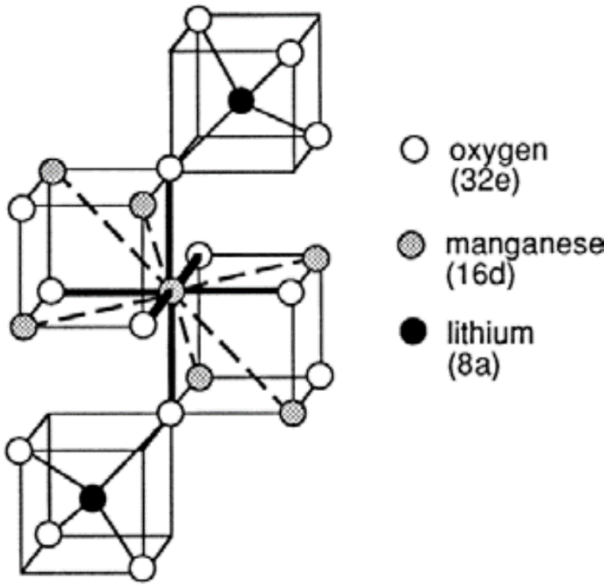

Figure 1-2: Part of the unit cell of $LiMn_2O_4$ showing the local structure around octahedral coordinated Mn in an ideal spinel lattice. Mn-O bonds are represented by heavy solid lines; linear chains of manganese ions in neighbouring edge-sharing octahedral are indicated by dashed lines [98].

Recently, it was found that $LiNi_{0.5}Mn_{1.5}O_4$ has two crystallographic symmetries of Fd-3m and $P4_332$ spinel's as the high voltage cathode materials were investigated by the first-principles theory. A common example of a normal stoichiometric magnesium aluminate spinel is $MgAl_2O_4$, contains equimolar proportions of Al_2O_3 and MgO [99]. Thackeray *et al.* [100] proposed the spinel cathode $LiMn_2O_4$ and the material have been extensively developed by Bellcore labs [101] [102]. The crystal structure of spinel $LiMn_2O_4$ is shown in figure 1-2.

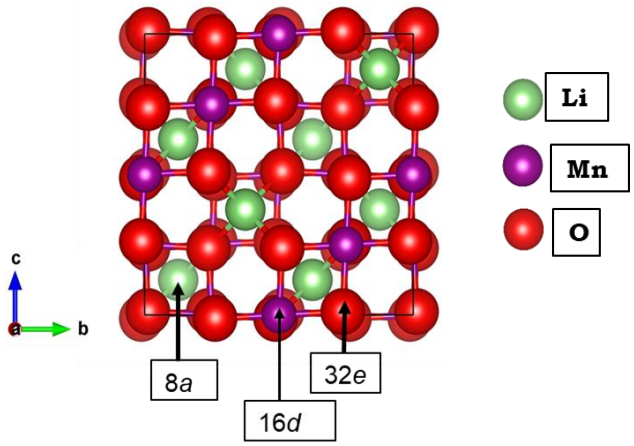

Figure 1-3: Crystal structures of spinel $LiMn_2O_4$, (x=0.25, 0.5, 0.875) where green, purple and red atoms represent Lithium, manganese and oxygen atoms respectively.

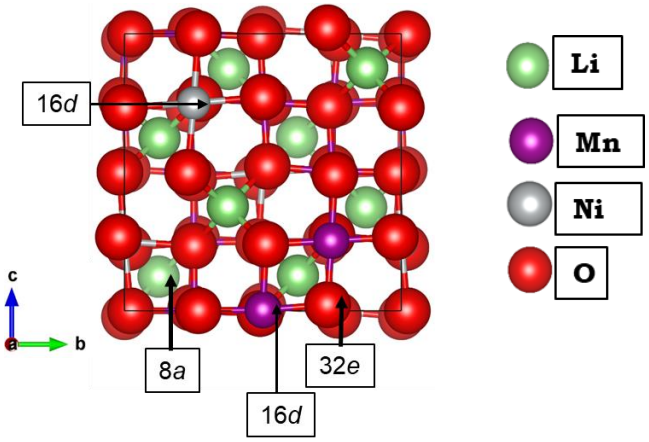

Figure 1-4: Crystal structure of spinel nickel doped $LiNi_xMn_{2-x}O_4$; where green, purple, silver, and red atoms represent Lithium, manganese, nickel and oxygen atoms respectively.

1.5 The rationale of the Study

Lithium-ion batteries (LIBs) together with the development of science and technology are the major power source for portable electronic devices, electric automotive applications and grid support. Thus far layered $LiCoO_2$, spinel $LiMn_2O_4$ and olivine-like polyanion $LiFePO_4$ oxides have been mainly used commercially due to their exceptional cycling ability and reasonably high energy/power density. Among various cathode materials for LIBs the cheap, safe and rich in resources $LiMn_2O_4$ cathode material has become a research hotspot. However, both existing and emerging technology require LIBs with energy and power capabilities that are beyond the existing state of-the-art. The more widely studied high-voltage mixed Mn, Ni, Co oxides (NMCs) are more increasingly being used in LIBs. Various efforts

have been tried to improve the electrochemical performance of spinel $LiMn_2O_4$ cathode materials, including bulk doping, surface coating and morphology control.

On the down side, the scarcity and high cost of cobalt pose impediments in their long term usage. With a high intercalation working voltage of ~ 4.7 V vs. Li, high rate capability, high energy density, low environmental impact and reasonable cost, the mixed manganese based spinel materials such as $LiNi_{0.5}Mn_{1.5}O_4$ (LNMO), are considered the most promising for high-energy-density LIB. However, the cycle life of such materials is insufficient for practical applications, and increasing cycling performance has been the focus of intense recent research. Hence, further studies on the thermodynamics of the Ni incorporation in $LiMn_2O_4$ to improve the structural stability and resulting electrochemical properties, including enhancement of the average lithium intercalation voltage, is necessary.

In the current study different approaches will be used to predict new and improve existing structures resulting from nickel as a substitutional dopant for $LiMn_2O_4$. Consequently, first principles density functional methods embodied in the Castep code, in conjunction with Virtual Crystal Approximation (VCA), will be invoked. The latter is well suited offering technically the simplest approach, allowing calculations for the generation of disordered systems to be carried out at the same cost as calculations for ordered structures. Although the approach neglects effects such as local distortions around atoms, it is also not expected to reproduce the finer details of the disordered structures very accurately and it is important to be aware of its limitations. Furthermore, the Universal Cluster Expansion (UNCLE) package will be employed to set up, construct and automatically converge a cluster expansion for $LiMn_2O_4$ spinel systems in order to generate unique structures within the random mixing of $LiMn_2O_4$-$LiNi_2O_4$ and to carry out related thermodynamic analysis. Lastly, the site occupancy disorder (SOD) code, will produce complete configurational space for each Ni concentration in the spinel $LiMn_2O_4$. This will show how substantial changes in the average voltage of lithium intercalation occur with moderate Ni incorporation in $LiMn_2O_4$.

1.6 Outline of the Study

This dissertation is organised into five chapters as follows with regard to the density functional approach, focusing on the GGA-PBE approximation:

Chapter 1 consists of a general introduction to the study, applications, properties, structural aspects and background on computational modelling of materials and intention of the current study.

Chapter 2 reviews the theoretical methodologies for density functional theory together with virtual crystal approximation, cluster expansion and side occupancy disorder.

Chapter 3 presents the calculations in details, results, discussions on structural properties lattice parameters, pressure, electronic properties and mechanical stabilities of spinel $LiMn_2O_4$ and nickel doped $LiMn_2O_4$ structures, where virtual approximation and ab initio methods have been invoked.

Chapter 4 focuses on electronic properties and mechanical properties, where we observe any various change in pressure impact on the total density of states, the partial density of states and elastic constants.

Chapter 5 focuses on the binary diagram that generates five new stable configurations with low heats of formation. Then calculate the mechanical properties, electronic properties and their phonon spectrum for stability verification.

Chapter 6 indicates that any small change in the tuning of the Ni concentration, achieved via temperature change during the thermodynamics of mixing and controlling of the lithium intercalation will be reflected in the properties of the stable structure.

Chapter 7 gives a summary of the main results presented in this thesis and several recommendations for future research are also listed.

Chapter 2

Methodology

2.1 Introduction

In this chapter, a brief overview of the theoretical background of methodologies used in this study is presented. First-principles modelling refers to the application of quantum mechanics to determine the structure and properties of materials. In this work we have based our approach on quantum mechanical calculations, being the density functional theory. Quantum mechanical methods are widely used to study the structure, chemical, electrical, optical and magnetic properties of a material. The description of the use of first-principles methods to obtain information on the pure and nickel doped spinel, structural, density of states, mechanical and pressure properties in spinel lithium manganese oxide for rechargeable lithium batteries is presented. The technique employed is called a CASTEP module which employs a plane-wave technique to deal with weak pseudo-potentials. Most importantly, it is capable of simulating electronic relaxation to ground states for metals, insulators or semiconductors and hence predicts with accuracy the forces acting on atoms and the stress on the unit cells. We further deployed two approaches; the Universal cluster expansion which determined stable multi-component crystal structures and ranks metastable structures by the enthalpy of formation, while maintaining the accuracy of first-principles density functional methods. In the second approach, we employed density functional theory calculations with a Hubbard Hamiltonian (DFT+*U*) to investigate the thermodynamics of mixing of the $LiMn_{1-x}Ni_xO_4$ solid solution with the site occupancy disorder generated configurations.

2.2 Density Functional Theory

The success of the density functional theory (DFT) as a tool for ab initio calculation of various properties of solids has inspired scientists to apply it and even to study defects (both uncharged and charged) in metals and semiconductors. DFT is a quantum mechanical theory applied in physics and chemistry and is used to

investigate the electronic structure of many-body systems, in particular atoms, molecules and the condensed matter [103]. Within the DFT, the properties of a many-electron system can be determined by using a functional, which in this case is the spatially dependent electron density. Hence the name Density Functional Theory comes from the use of functional of the electron density.

DFT has its conceptual roots in the Thomas-Fermi model from 1920s and it was put on a firm theoretical footing by the two Hohenberg-Kohn (H-K) theorems [104]. The original H-K theorem held only for non-degenerate ground states in the absence of a magnetic field [105], although they have since been generalised. The first H-K theorem demonstrates that the ground state properties of a many-electron system are uniquely determined by an electron density that depends on only three spatial coordinates. It lays the groundwork for reducing the many-body problem of N electrons with 3N spatial coordinates to 3 spatial coordinates, through the use of the functional of the electron density. This theorem can be extended to the time-independent domain to develop time-dependent density functional theory, which can be used to describe excited states.

The second H-K theorem defines energy functional for the system and proves that the correct ground-state electron density minimises this energy functional. Within the framework of Kohn-Sham DFT [106], the intractable many-body problem of interacting electrons in static potentials is reduced to a tractable problem of non-interacting electrons moving in an effective potential.

The total energy of the system is expressed as a function of the electron density for a given position of atom nuclei. The minimum value of the total energy functional is the ground state energy of the system. In DFT, the total energy is given by:

$$E = E[\rho(r), R_\alpha], \tag{1}$$

where the electron density ρ and total energy E depend on the type and arrangement of the atomic nuclei R_α denotes the position of the nuclei α in the

system. Equation (1) is the key to atomic scale understanding of structural, electronic, mechanical and magnetic properties of materials.

The original H-K theorem shows that it is possible to use the ground state density to calculate properties of the materials, but does not provide wayfinding with the ground state. Hence Kohn and Sham [86] introduced a special type of wave-functions into the formalism, to treat kinetic and interaction energy. They derived an effective three terms Schrödinger equation expressing the functional as the sum of three terms, written as:

$$E[\rho] = T_0[\rho] + U[\rho] + E_{XC}[\rho], \tag{2}$$

where T_0 is the kinetic energy of the electrons, U as classical Coulomb repulsion energy of the electrons, E_{XC} is the exchange correlation energy. In the DFT, if each effective electron is described by a single wave functionψ_i, then the kinetic energy of all electrons in the system is given by:

$$T_o = \sum n_i \int \psi_i(r) \left[\frac{\hbar^2 \nabla^2}{2m}\right] \psi_i dr \tag{3}$$

where n_i denotes the number of electrons in state$i$. The Coulomb energy U which is purely classical contains the electrostatic energy arising from the columbic attraction between the electrons and nuclei, the repulsion between the electronics, and the repulsion between the nuclei. It can be written as follows:

$$U[\rho] = U_{en}[\rho] + U_{ee}\rho + U_{ion-ion}. \tag{4}$$

The exchange correlation, energy E_{xc} accounts for all the remaining electronic contributions to the total energy.

In DFT, only the minimum value of the Kohn-Sham energy functional has a physical meaning, therefore it is necessary to determine the ground-state total energy of the system, by determining the set of wave-functions$\psi_i(r)$. The set of wave functions

$\psi_i(r)$ minimises the Kohn-Sham energy functional and is given by the self-consistent solutions of the equation:

$$\left[\frac{-\hbar^2}{2m}\nabla^2 + \nabla_{ion}(\acute{r}) + V_H(\acute{r}) + V_{xc}(\acute{r})\right]\psi_i(\acute{r}) = \varepsilon_i\psi_i(\acute{r}), \quad (5)$$

where, ψ_i is the wave function of electronic state i and ε_i is the Kohn-Sham eigenvalue, V_{ion} is the ionic potential describing the attractive interaction between electrons and nuclei and V_H is the Hartree potential of the electron which is given by

$$V_H(r) = e^2 \int \frac{\rho(r')}{|r-r'|} d^3r', \quad (6)$$

and V_{XC} is the exchange-correlation potential given by the functional derivative,

$$V_{XC}(r) = \frac{\delta E_{XC}[\rho(r)]}{\delta\rho(r)}, \quad (7)$$

the electron density,$\rho(r)$, is given by

$$\rho(r) = 2\sum_i \left|\psi_i(r)\right|^2. \quad (8)$$

Hence, the Kohn-Sham total energy functional for a set of doubly occupied electronic states Ψ can be written as:

$$E = \{\psi_i\} = 2\sum_i \left(\frac{\hbar^2}{2m}\right)\nabla_{ion}\nabla^2\psi_i d^3r + \int v_{ion}(r)\rho(r)\, d^3r + \frac{e^2}{2}\int \frac{\rho(r)(\rho\acute{r})}{|r-r'|} d^3\, r d^3r' + E_{xc}[\rho(r)] + E_{ion(\{R_i\})}, \quad (9)$$

where E_{ion} is the Coulomb energy associated with interactions among the nuclei (or ions) at positions$\{R_i\}$. The exchange-correlation potential cannot be obtained explicitly because the exact exchange-correlation energy is unknown. To solve this problem, approximation methods are employed and will be discussed in the next two sections.

2.2.1 Local Density Approximation

The simplest method of describing the exchange correlation energy of an electronic system is to use the local density approximation (LDA). The LDA is a class of approximations to the exchange-correlation E_{xc} energy the functional in density functional theory and a widely used approximation in physics [107]**.** It locally substitutes the exchange-correlation energy density of an inhomogeneous system by that of an electron gas evaluated at the local density. The exchange-correlation energy gives the smallest contribution to the total energy and the energy depends only on the local electron density around each volume element dr.

The LDA rests on two basic assumptions:

(i) the exchange and correlation effects come predominantly from the immediate vicinity of the point r and

(ii) these exchange and correlation effects do not depend strongly on the variations of the electron density near r.

If the two basic assumptions are well fulfilled, then the contribution from volume element *dr* would be the same as if these volume elements were surrounded by a constant electron density $\rho(r)$ of the same value as within *dr*. In local density approximation, the exchange-correlation energy of an electronic system is constructed by assuming that the exchange-correlation energy per electron at a point r in the electron gas $E_{XC}(r)$ depends only of the local electron density around each volume element *dr* and thus

$$E_{XC}^{LDA}[\rho(r)] \approx \int \varepsilon_{xc}(r)\rho(r)d^3\,r\ , \tag{10}$$

and

$$\frac{\delta E_{XC}^{LDA}[\rho(r)]}{\delta\rho(r)} = \frac{\partial[\rho(r)\varepsilon_{xc}(r)]}{\partial\rho(r)}\ , \tag{11}$$

with

$$\varepsilon(r) = \varepsilon_{xc}^{hom}[\rho(r)], \tag{12}$$

where $\varepsilon_{xc}^{hom} = [\rho(r)]$ is the exchange-correlation energy per particle of the homogeneous electron gas calculated at the local density [108]**.** The quantity can be split into two parts and gives:

$$\varepsilon_{XC}\rho(r) = \varepsilon_X[\rho(r)] + \varepsilon_C[\rho(r)], \tag{13}$$

The exchange part $\varepsilon_X[\rho(r)]$ can be derived analytically with Hartree-Fork expression and be expressed as

$$\varepsilon_X[\rho(r)] = \frac{3}{4}\sqrt[3]{\frac{3\rho(r)}{\pi}}, \tag{14}$$

2.2.2 Generalised Gradient Approximation

The remarkable success of LDA has led to the various generalised gradient approximations (GGA's) with distinct improvement over LDA. The generalised gradient approximations can now provide the accuracy required for density functional theory simulations. The LDA is inaccurate in the strongly correlated system, where the dependent particle breaks down did not perform well in many areas of chemistry [109]. For non-uniform charge densities, the exchange-correlation energy can deviate significantly from the uniform result. This deviation can be expressed in terms of the gradient and higher spatial derivatives of the total charge density. The generalized gradient approximation by Perdew [110], Becke [111], Perdew and Wang [112] and Perdew *et al*. [113] uses the gradient of the charge density, $|\nabla\rho(r)|$, to correct this deviation. Generalised gradient approximation denotes a variety of ways proposed by functions that modify the behaviour at large gradients, such that the desired properties are preserved. The GGA exchange correlation energy is written as

$$E_X^{GGA}[\rho] = \int dr\rho(r) = E_{XC}^{GGA}[\rho(r), \nabla\rho(r)], \tag{15}$$

where E_{xc} is the exchange correlation energy and $\nabla\rho(r)$ is the gradient term.

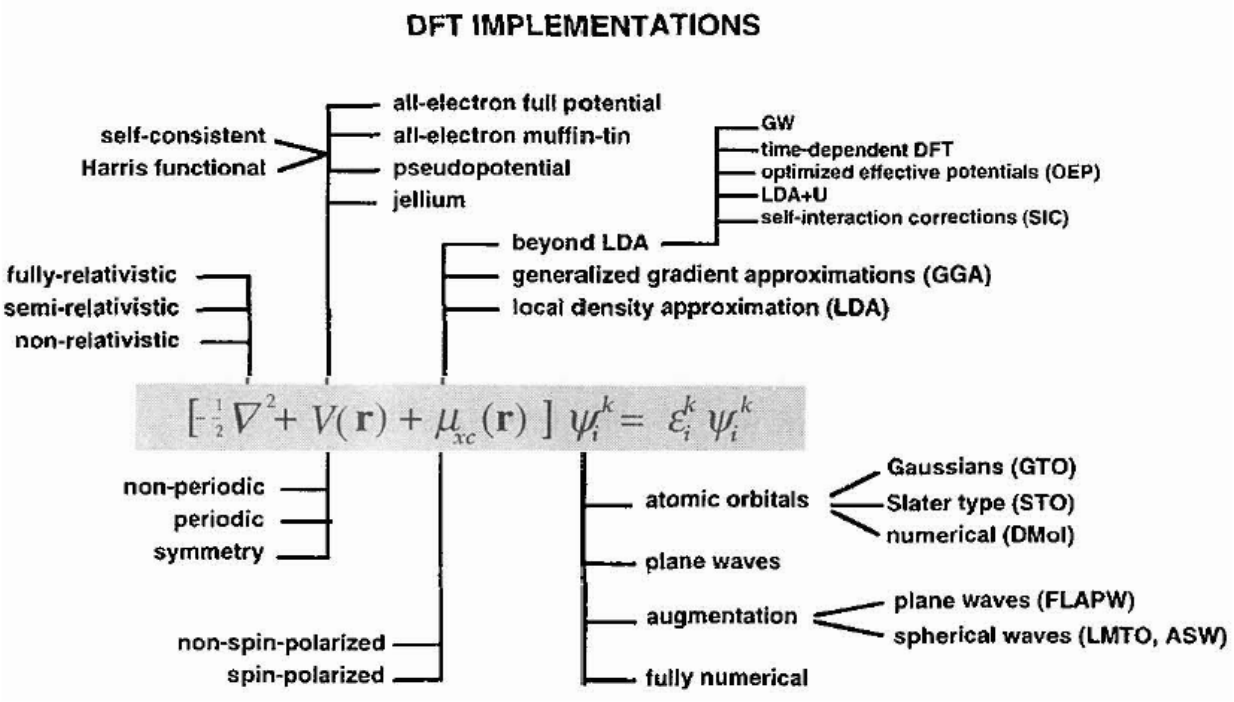

Figure 2-1: Overview of electronic structure methods for solving the Kohn-Sham equation [114].

2.3 Hybrid Functionals

The hybrid functionals are used to improve the description of the exchange term in DFT calculations based on the partial $(0 < a < 1)$incorporation of an exact exchange part from HF in hybrid functionals:

$$E_{xc} = (1 - a)E_x^{DFT} + aE_x^{HF} + aE_c^{HF} \tag{17}$$

The incorporation of the non-local HF exchange part also provides some degree of self-interaction cancellation and the classical Coulomb interaction have opposite signs. The use of only the exact HF exchange, $a = 1$ in equation (above), produces poor hybrid functional results as there is an important error cancellation element taking place between the DFT exchange and correlation functionals [115].

2.4 DFT + *U* Method

The electronic self-interaction is another shortcoming associated with most DFT methods. It arises when the correlation term is not treated exactly and produces artificially delocalized electron densities. In materials with strongly interacting and very localised electrons, such as in many transition metal oxides, the DFT method is unable to reproduce a realistic electronic structure, as it fails to open the bandgap [116] [117] or underestimates it [118] [119]. This DFT limitation is not only exclusive to transition metal oxides, the magnetic moments are too small for the semiconducting transition metal oxides [120] but are also found in rare earth compounds and some non-metal oxides [121].

The different formulations of the DFT+*U* approximation have been devised [122] [123] [124] to treat the strong on-site Coulomb interaction of localized electrons, which is not correctly described by LDA nor GGA, with an additional Hubbard-like term. This be an increment in energy associated with the introduction of an electron in certain d-orbitals, i.e. $U = E(d^{n+1}) + E(d^{n-1}) - 2E(d)$, which opens band gaps close to the experimental ones or those obtained from more demanding computational methods. There are two types of DFT + *U* methods and in this thesis, we implemented the Hamiltonian in the proposed version by Dudarev *et al.* (1998) which takes the form:

$$E_{DFT} = E_{DFT} + \frac{U_{eff}}{2}\sum_{\sigma}[\rho^{\sigma} - \rho^{\sigma}\rho^{\sigma}] \quad (16)$$

where ρ^{σ} is the atomic orbital occupation matrix of the *d*-electrons with spin σ and U_{eff} is equal to the difference between *U*, the spherically averaged Hubbard parameter, and *J*, the screened exchange energy. The *U* and *J* are the effective Coulomb and exchange parameters, respectively, where they can in principle, be computed from first principles. However, the theoretical values of U and J give poor results, and therefore, these parameters are adjusted by fitting to experimental data, such as the oxide band gap or the lattice parameters.

The DFT + *U* method only makes physical sense when U_{eff} and $[\rho^{\sigma} - \rho^{\sigma}\rho^{\sigma}]$are both greater than 0. The latter can be shown easily in the idempotency limit ofρ^{σ}. This means that the eigenvalue of this matrix is either 0 to 1, which are values associated with fully unoccupied or occupied *d*-levels. The net result is a DFT + *U* energy which is always greater than the pure DFT energy.

The DFT + *U* method can be applied to both local and gradient corrected functional. Since better results are typically obtained with GGA while different *U* values are usually required for each type of function to obtain comparable results [125]. Therefore, the method also affects geometrical factors indirectly after the variation of electronic properties [125] [126]. In this thesis, the U_{eff} values used to describe adequately the *d* bands of each transition metal ion were dependant on the functional use.

2.5 Planewave Pseudopotential Method

Pseudo-potential plane-wave methods have become a work-horse for the study of structural and electronic properties based on quantum mechanical treatment. The method allows the electronic wave functions to be expanded in terms of a smaller number of plane-wave basis states. It simplifies the DFT problem by considering only the valence electrons. The core electrons are excluded based on the assumption that their change density is not affected by the changes in the environment.

2.5.1 Planewave Basis

An infinite plane-wave basis set is used to expand the electronic wave functions of the system. The method is described by using Bloch's theorem, which allows the electronic wave function to be expanded in terms of a discrete set of plane waves. The electronic wave functions of a periodic solid can be written as:

$$\Psi_i(r) = e^{[ik.r]} f_i(r), \tag{18}$$

This expression has a wavelike and cell-periodic part. The function $f_i(r)$ defines the periodicity of the solid and can be expressed as:

$$f_i(r) = \sum_G C_{i,G} \exp[iG.r], \tag{19}$$

where G are vectors of the reciprocal lattice of the periodic cell and are required for the resolution of rapid variations in the wave functions and charge density. Hence, each electronic wave function can be written as a sum of plane waves,

$$\Psi_i = \sum_G C_{i,k,G} \exp[i(k+G).r], \tag{20}$$

where $C_{i,k,G}$ are the coefficients for the plane waves and dependent on the specific kinetic energy, $\left[\frac{\hbar^2}{2m}\right] \left|k+G\right|^2$. The convergence of this expansion is controlled by the choice of the kinetic energy cut-off. The plane wave basis set is limited by including all plane waves whose kinetic energies are less than some energy cut-off E_{cut}. Thus, only the plane waves that obeys

$$\left[\frac{\hbar^2}{2m}\right] \left|k+G\right|^2 < E_{cut}, \tag{21}$$

are included in the basis set. Introduction of E_{cut} to the discrete plane wave basis set produces a finite basis set. The plane wave set at finite cut-off energy will lead to an error in the computed total energy. Hence the energy cut-off should be increased until the calculated energy has converged. The plane waves are used as a basis set for the electronic wave functions and substituting equation $\Psi_i = \sum_G C_{i,k,G} \exp[i(k+G).r]$, into Kohn-Sham equation $\left[\frac{-\hbar^2}{2m}\nabla^2 + \nabla_{ion}(\acute{r}) + V_H(\acute{r}) + V_{xc}(\acute{r})\right]\psi_i(\acute{r}) = \varepsilon_i\psi_i(\acute{r})$, gives the equation:

$$\sum[\frac{\hbar^2}{2m} \left|k+G\right|^2 \delta_{GG'} + V_{ion}(G-G') + V_H(G-G') + V_{XC}(G-G')]\, C_{i,k,G'} = \varepsilon_i C_{i,k,G}, \tag{20}$$

The kinetic energy is diagonal and the various potential contributions are given by the Fourier transforms. A solution of equation 33 precedes by diagonalisation of a Hamiltonian matrix whose matrix elements $H_{k+G+k+G'}$. The matrix's size is obtained by the choice of cut-off energy $\left[\frac{\hbar^2}{2m}\right] \left|k + G_C\right|^2$, and will be large for the systems that contain both valence and core electrons.

2.5.2 Pseudopotentials

This method is designed for periodic solids but is also used for problems such as atoms and surfaces employing the super-cell approach. Physical properties of solids are much dependable on the valence electrons than on the tightly bound core electrons [127] [128] [129]. In this method, the weaker pseudo potential replaces the core electrons and the strong attractive Coulomb potential inside the ionic core. The weaker pseudo-potential describes all hence that describes all silent features of a valence electron moving through a crystal, including relativistic effects [127] [128] [129] [130]. Thus, the original solid is now replaced by pseudo-ion cores pseudo valence electron. These pseudo electrons experience the same potential outside the core region as the original electrons but have a much weaker potential inside the core region.

The schematic diagram in Figure 2-2 illustrates the following quantities; an ionic potential (Z/r), valence wave-function (Ψ_v) and the corresponding pseudo-potential (V_{pseudo}) and pseudo wave function (Ψ_{pseudo}).

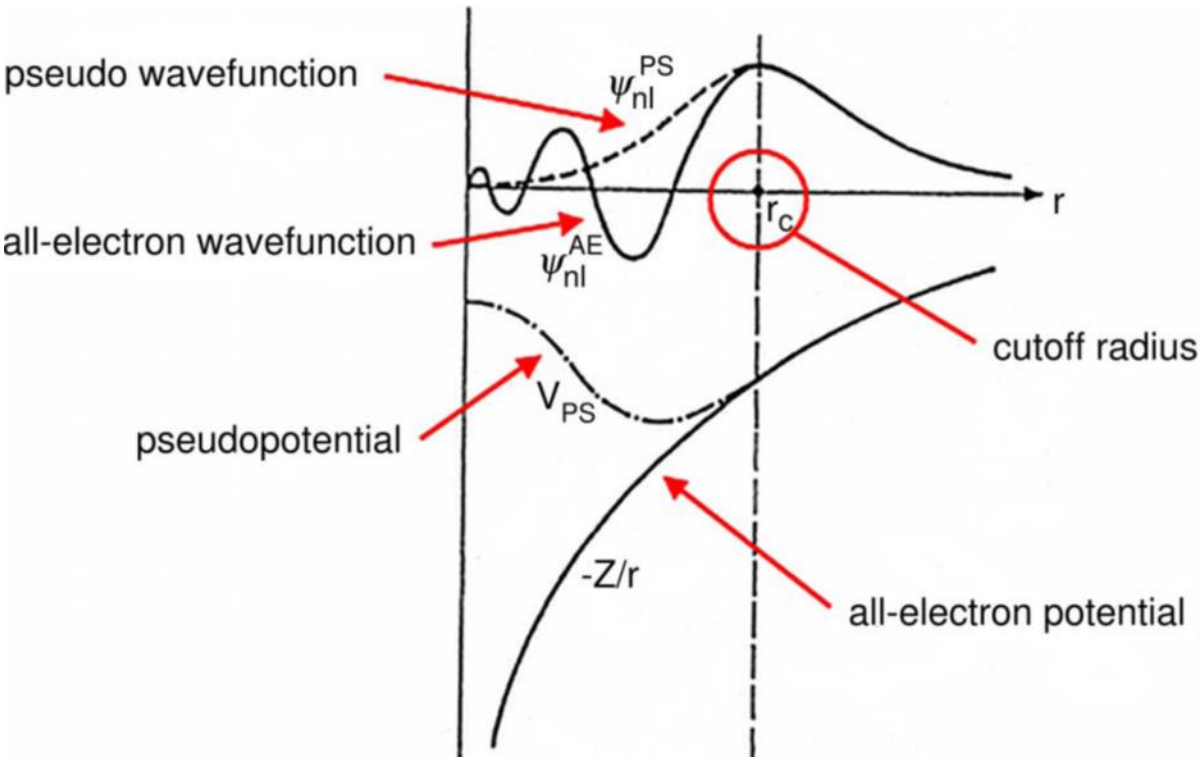

Figure 2-2: Schematic illustration of all-electron (solid lines) and pseudo-electron (dashed lines) potentials and their corresponding wave-functions [130].

The advantage of using pseudopotential approximation form factor can be determined by direct comparison with the energy gaps (known as empirical pseudopotential) from ab-initio calculations. It allows the electronic wave function to be expanded using a much smaller number of plane wave basis states and saves an enormous amount of computational time. The pseudo-potential has the form:

$$V_{NL} = \sum_{lm} |lm\rangle V_i \langle lm|, \tag{22}$$

where $|lm\rangle$ is the spherical harmonics and V_i is the pseudo-potential for angular momentum l, acting on the electronic wave-function. Most of the pseudo-potentials currently used in the electronic structure are generated from all electron atomic calculations. A pseudo-potential that uses the same potentials for all the angular momentum components of the wave-function is called a local pseudo-potential. The two types of pseudo-potentials are described briefly in the next two subsections.

2.5.3 Norm Conserving Pseudopotential

Norm conserving pseudo-potential is an example of a non-local pseudo-potential. Norm-conserving pseudo-potentials enforce the condition that, outside of a cut-off radius, the norm of each pseudo-wave-function is identical to its corresponding all-electron wave-function [131]. If the exchange-correlation energy is to be desired accurately, the pseudo wave function and the real wave function outside the core region must be identical in both their absolute magnitude. Hence, spatial dependence for two wave-functions to generate identical charge densities. The non-local pseudo-potential describes in detail the scattering from the ion core.

2.5.4 Ultrasoft Pseudopotentials

One aim of pseudo-potentials is to create pseudo functions that are smooth and yet accurate. Ultra-soft pseudo-potentials (USP) relax the norm-conserving constraint to reduce the basis-set size and was suggested by Vanderbilt [132]. In the USP scheme, the pseudo wave function can be as soft as possible within the core region. This is achieved by introducing a generalised orthonormality condition. The electron density should be augmented in the core region to recover the full electronic charge. The electron density is then subdivided into (i) a smooth part that extends throughout the unit cell and (ii) a hard part localised in the core region. Ultra-soft pseudo-potentials have another advantage besides being much softer than their norm-conserving counterpart.

2.6 K-sampling

Electronic states are allowed only at a set of k-points determined by the boundary conditions that apply to the bulk solid. The density of allowed k-points is proportional to the volume of the solid. A particle which leaves one surface of the crystal simultaneously enters the crystal at the opposite surface. The infinite numbers of electrons in the solid are accounted for by an infinite number of k-points and only a finite number of electronic states are occupied at each k-point. One of the difficulties associated with the use of plane-wave basis sets is that the number of basis states changes discontinuously with cut-off energy.

The Bloch theorem changes the problem of calculating an infinite number of wave functions into calculating a finite number of electronic states at each k-point. The electronic wave-functions at each k-point can be expanded in terms of a discrete plane-wave basis set. In principle, an infinite number of plane waves are required for such an expansion. The occupied states at each k-point contribute to the electronic potential in the bulk solid so that in principle an infinite number of calculations are needed to compute this potential. In this case, the electronic states at only a finite number of k-points are required to calculate the electronic potential and hence determine the total energy of the solid. However, the electronic wave-functions at k-points that are close to each other are very similar; therefore, the k-point summation can be efficiently carried out by an appropriate sampling.

To obtain accurate electronic potential, electronic density and total energy, efficient methods have been used to choose the finite sets of k-points. The two most common methods are those of Chadi and Cohen [133] and Monkhorst and Pack [134]. Using these methods, the number of these k-points necessarily depends on the material: for insulators, only a few points are needed as all bands are filled, while for metals more points are needed for the bands that cross the Fermi-level.

The computational cost of performing a very dense sampling of k space increases linearly with the number of k-points in the Brillouin zone (BZ). Density functional codes approximate these space integrals with a finite sampling of k-points. Special k-points schemes have been developed to use a few possible k-points for a given accuracy and reducing computational cost. The most commonly used scheme is by Monkhorst and Pack (Monkhorst and Pack, 1976) [134].

2.7 Universal Cluster Expansion

The cluster-expansion approach is a technique in quantum mechanics that systematically truncates the BBGKY hierarchy problem (the BBGKY hierarchy (Bogoliubov–Born–Green–Kirkwood–Yvon hierarchy, sometimes called Bogoliubov hierarchy) is a set of equations describing the dynamics of a system of many interacting particles) that arises when quantum dynamics of interacting systems is

solved. In statistical mechanics, the cluster expansion (also called the high-temperature expansion or hopping expansion) is a power series expansion of the partition function of a statistical field theory around a model that is a union of non-interacting 0-dimensional field theories. Cluster expansions originated in the work [135] unlike the usual perturbation expansion, it converges in some non-trivial regions when the interaction is small. The cluster expansion is a power series expansion of the partition function of a statistical field theory around a model that is a union of non-interacting of 0-dimensional field theories. Modern DFT methods can calculate material properties with reasonable to high precision (depending on the quality of the approximations to the exchange and correlation effects). Standard DFT applications are, however, restricted to unit cells of a few hundreds of atoms. If one wants to model an alloy with varying atomic concentrations and crystal structures a huge number of very large supercell would be needed if one would try to solve the problem using an abrupt force. Therefore, the process would be deemed fatal. A successful strategy to overcome this limitation is offered by the cluster expansion (CE) [136] when combined with Monte Carlo simulations

One significant class of problems in materials science comprises those that can be characterised, at the atomic level, as configurationally. Important configurational questions include order-disorder transitions, ground states (stable compounds in the solid part of the phase diagrams of crystalline metals and semiconductors), and segregation of defects in alloy interfaces and surfaces, or adsorption at surfaces. The new code, Universal Cluster Expansion (UNCLE), consolidates recent advances in the methodology and leverages one new development in the formalism itself. The fundamental goal of the package is to reduce the need for user intervention automating the method to reduce human error and judgment. The package extends standard cluster expansion formalism to the more complicated scenarios of ternary compounds, as well as surfaces, including adsorption and inequivalent sites. The sheer size of configurational space makes it impractical to explore any of these questions directly from an electronic structure theory (first-principles methods). But it is possible to map first-principles results onto a faster Hamiltonian. One example is the cluster expansion [136], which permits one to ‘extract’ the physics of atom-atom interactions from a set of first-principles, small-

unit-cell calculations and then model, in a practical way, unit cells with millions of atoms (as in Monte Carlo modelling), or explore tens of millions of different atomic configurations in different cell shapes (as indirect enumeration ground-state searches. The concept of CE is to describe every configuration dependent property of a system by a linear combination of interacting building blocks or figures. By configuration, one understands a distribution of atoms over a given lattice. Then the energy for a given configuration σ is written as a sum over pairs, triplets, quadruplets, and so on, the so-called figures or clusters. It was shown [136] that such an expansion exists if mathematically the expansion goes over every single configuration (i.e. atomic distributions). For practical reasons, the expansion should be limited to reasonably small clusters so that the expansion converges numerically. If the input of a convergent cluster expansion is provided by DFT calculations, then the accuracy of DFT calculations can be carried over to systems consisting of 10^4–10^6 atoms. Currently, UNCLE's format for structural information has been designed to match that of the first-principles code VASP of which communication has been established [137] [138] [139] [140] [141] and to adapt to the input of the FLAPW code FLAIR [142] [143] [144]. Many studies were made for binary alloy bulk systems, however, [145] [146] [147] [148] ternary systems (or binary systems with vacancies) [149] [150] are still rather scarce. Because they are complex hence effort (to set up the flowchart of the cluster expansion procedure) is needed.

2.7.1 Effective Cluster Interactions

A set of effective cluster interactions can be extracted and used in a Large-scale Monte Carlo simulations from an optimised cluster expansion to explore order-disorder phenomena and phase segregation processes as a function of temperature.

On a basic lattice various atoms, for example of type A and B, are distributed to define structure σ, a periodic configuration of A and B atoms. This configuration is described by the pseudo spin operator $\sigma_q = \pm 1$, which has the value +1 if atom A sits on site q or -1 if that atom is B (see Figure 2.1). Any physical property of the system, which is dependent on the atomic configuration, σ can now be described by a sum of spin products, as written in equation 35. An example for such a property is

the energy or enthalpy of formation, but also other observable properties can be cluster expanded such as tensorial quantities [151], Curie temperature [152] and density of states [153]. For fitting and finding the optimum set of figures, the energy or enthalpy of formation is much better suited because they should reach a minimum

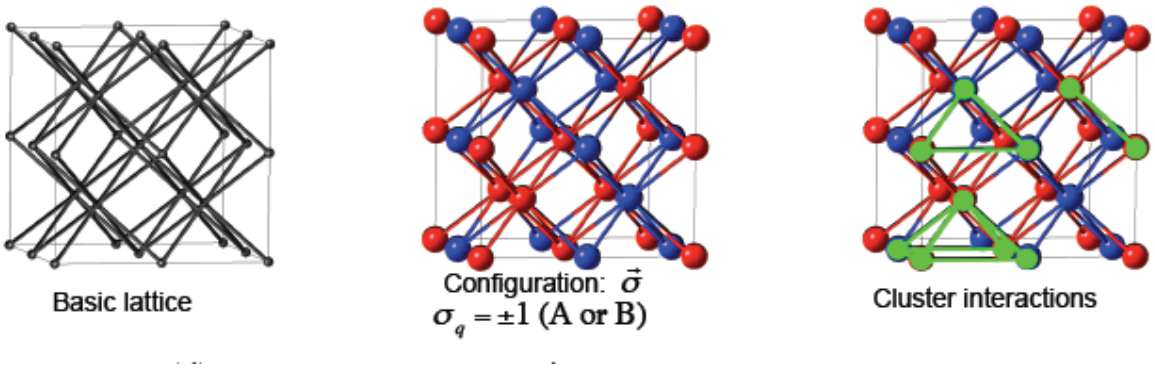

Figure 2-3: The diagram is decomposed into a set of truncating structures and clusters.

The energy (σ) associated with structure σ can be described by an expansion of cluster interactions and their respective interaction energies J by means of equation

$$E(\vec{\sigma}) = J_0 + J_1 \sum_i \sigma_i + \sum_{i>j} J_{ij}\sigma_i\sigma_j + \sum_{i>j>k} J_{ijk}\sigma_i\sigma_j\sigma_k + \cdots \quad (35)$$

The variable σ_i is the spin-like occupational variable to each site i of the parent lattice, which takes the value -1 or +1 depending on the type of atom occupying the site. The parametersJ_i in equation 35 are the so-called effective cluster interactions (ECI) or interaction energies, which are of the same dimension as the expanded property. In equation 35 J_0, the first term, serves as a constant value, configuration independent contribution. The second term is concentration dependent and is a sum over all N sites of structure σ with onsite energy J_1 times the pseudo spin operator σ at each site i. Further terms describe the cluster the distance between pairs and three-body interactions, for example two-body interactionsJ_{ij} or three-body interaction J_{ijk}. A particular arrangement of spin of the parent lattice is called a configuration and can be represented by a vector σ containing the value of the occupation variable for each site in the parent lattice. They contain spin products $\sigma_i\sigma_j$ … over all f vertices of a cluster times is an effective cluster interaction energy $J_{ij\ldots}$ summed up over all the possible ways that the cluster can be placed on the

lattice of structure σ. Furthermore the interaction energies or effective cluster interactions representing the contribution of each group of atom to $E(\sigma)$. In practise, an atom cluster expansion is known to converge rapidly but it is necessary to know which effective cluster interactions (ECI) are most important for a given material. To conduct the cluster expansion this it is applicable to formulate again equation 35 into a more compressed form;

$$E(\vec{\sigma}) = \sum_{C \epsilon \vec{C}} J_c \pi_c(\vec{\sigma}) \quad (36)$$

Therefore, the cluster expansion equation sums up the product of cluster C's interaction energy J_c with the correlation function,

$$\prod_c(\vec{\sigma}) = N^{-1} \sum_{i=1}^{N} \sum_{k \epsilon C} \prod_{v \epsilon f} \sigma_v \quad (37)$$

a sum over all the possible ways a cluster C with f $\vec{}$ vertices can be placed on the N sites of the structure. In the correlation function, the spin product $\sigma 1 \ldots \sigma$f goes over all f vertices of the cluster. Only symmetry inequivalent clusters are now considered and clusters included in an expansion can be collected by the vector C = {C1… Cn}.

2.7.2 Structures Selection

The initial step in the UNCLE approach is to define the pool of figures. Although symmetrically the amounts of distinct figures are limited by the input structures, even the list may contain far more figures than is required to form accurate cluster expansion. The approach is to choose a 'cut-off radius,' taking all figures smaller than the cut-off. Because the importance of figures generally decreases as the number of vertices increases, we specify smaller cut-offs for figures with more vertices [154].

A very important task of a convergent CE is to guarantee and to avoid biasing the training set and associated effective interaction energies. To prevent a wrong interpretation of the whole system by choosing the wrong input, UNCLE uses the chosen figure set to fit the energy of other structures. New structures can now be

designed and if they lie energetically below the existing ground state line they are recalculated by DFT, providing a new set of input structures. Then, a new set of figures is fitted and the procedure repeated. Such an iterative approach has the advantage that a reliable ground state line can be achieved together with a figure set which yields accurate results. The basic idea is to consider structures and clusters that will best approximate the finite set of energies at hand. The three-body and four-body clusters and other compact many-body clusters are added in the expansion.

2.7.3 Cluster Expansion Flowchart

In order for the expansion to be useful, it must be truncated to a relatively small number of terms without losing the expansion's predictive power. Choosing which figures to retain is the most critical step of the cluster expansion method. A minimisation using genetic algorithm was first used for the CE by Hart et al. [155]. In this approach, the figure list is represented as a binary string. However, the evolutionary approach based on a genetic algorithm (GA) has proven to be the most effective approach to select the figures [156]. The set of figures selected by the GA results in a cluster expansion that has better predictive power than if selected using other approaches. The details of the algorithm, which is implemented in UNCLE, have been described in [157] [155]. A figure used is marked by the value 1, otherwise, the value is 0. Furthermore, the interaction energies are also represented as a binary string. The combination of both binary strings, including figures used and their interaction energies, is now the genetic ‘DNA’ of a solution, who’s fitness is described by the CVS. A higher CVS compared to other solutions means, that this solution has a lower fitness.

Now, a ‘population’ of n_{pop} different solutions is created, in which the fitness of every individual solution is calculated. Of those n_{pop} individuals only the fittest n_{fit} ($0 < n_{fit} < n_{pop}$) individuals are selected to survive to the next iteration process. The other $n_{pop} - n_{fit}$ solutions are replaced by ‘descendants’ of the surviving fittest ‘parent’ solutions. Their ‘DNA’ is generated by two different processes as shown in Figure 2-5:

• In the crossover, the ‘DNA’ of the ‘offspring’ is created by mixing the ‘DNA’ of two randomly selected ‘parent’ solution. Thereby the ‘DNA’ of one ‘parent’ solution is

used up to the crossover point. After that point, the 'DNA' of the second 'parent' is used.

• In mutation, a random binary bit of the 'DNA' string is flipped from one state to the other, i.e. 1 ⇒ 0 or 0 ⇒ 1.

Note, that one may replace all surviving 'parent' solutions with the 'children', as long as only the fittest 'parent' solutions are used to create them. Therefore the basic principle is illustrated in Figure 2-5.

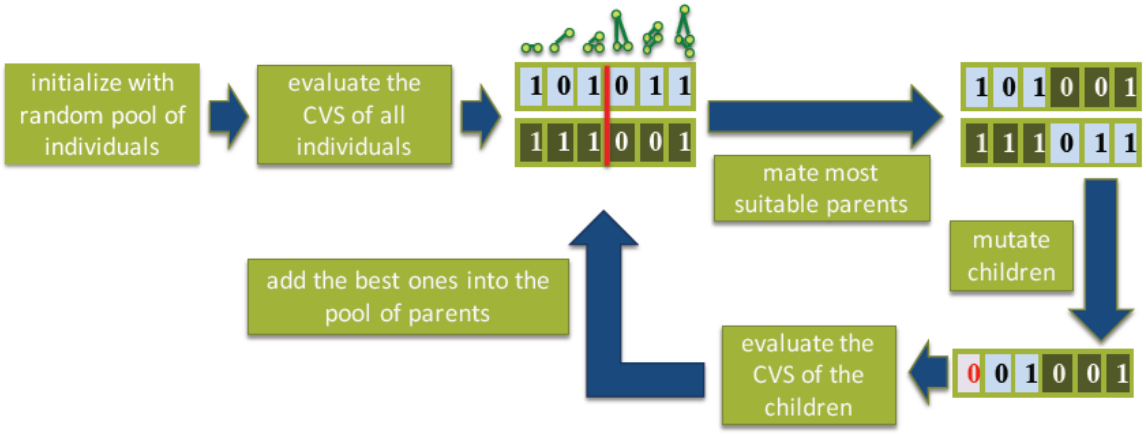

Figure 2-4: Illustration of the Genetic Algorithm.

The figure above shows mutation, in an illustration of crossover given, two 'parent' solutions marked red and green are used to manufacture a 'child' solution. Which helps with the safety identification of the relevant figures that need to be included in the Cluster Expansion-sum. The process is stochastic in nature meaning that an identical training set yields slightly different results if the genetic algorithm is repeated. A random bit in the binary string is flipped into the opposite state. Thus, the fitness of the new 'population' created by this process can be re-evaluated and the procedure repeated until the results are obtained with a very small CVS. However this procedure will always find a minimum and it also remains unclear, if a local or global minimum will be found. It is then advisable to perform a number of separate CE and use the end product with the lowest CVS as the final solution. Therefore universal cluster expansion can be set up to do the procedure automatically by performing a number of steps sequentially and only save the best-yielded solution at the end.

2.7.4 Input Energies ($E_{i\sigma}$) for the Cluster Expansion

When the genetic algorithm has converged a set of figures is selected to describe the best system. This set predicted all the DFT derived ground state energies of the starting input set and resulted in the lowest SC_V. Structures, which were not members of the input set of the GA run, should now be predicted sufficiently correct. Now, the ECIs –as derived from the fitting are taken to describe all possible structures of the system on the given parent lattice. If the enthalpy of formation of one of these structures is below the ground state line as defined by the DFT input data– this structure is included in an enlarged input set. As a consequence, its formation enthalpy is calculated by DFT and added it to the list of input structures. With this enlarged input set a new GA is done. This procedure is repeated until no new ground states are predicted by the CE. As a result, the stable structures of the system are obtained and the final ground state line.

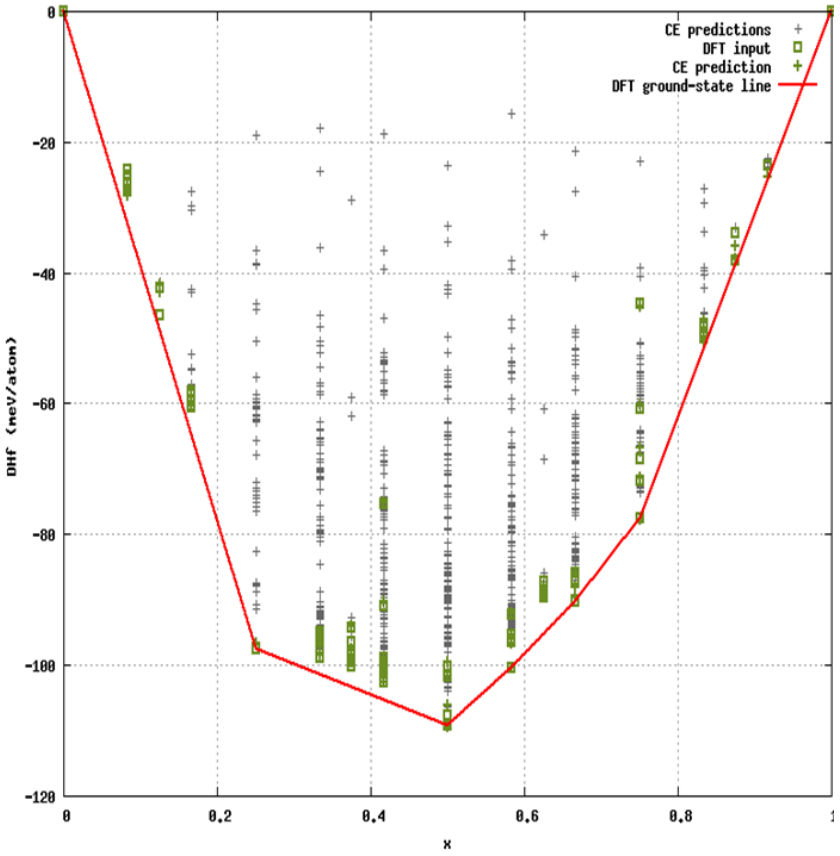

Figure 2-5: Ground-state line of the binary $LiNi_2O_4$-$LiMn_2O_4$ systems for an fcc-parent lattice.

At the red line is the defined Dft grounded-state line, where lies the structures with the lowest formation energies, the green blocks denote the DFT results taken as an input for the CE and the green crosses represent the energies predicted by CE.

2.7.4.1 Miscible Constituents

When models with miscible constituents have structures with the more negativeΔH_f, (thermodynamically stable, ordered structures) which are close to the ground states or on the Dft grounded state line at a given concentration, are deemed important and the cluster expansion should be most accurate for those. In order to accomplish this, those structures predicted by the cluster expansion to be more beneficial (with a lower ΔH_f) and does not form part of the training set are added to the training set. Therefore, it is done iteratively until no new structures are predicted by cluster expansion to be more favourable than those already included in the training set. It is then at this point that the cluster expansion has converged and from all structures considered by the cluster expansion the thermodynamically stable ones have been identified.

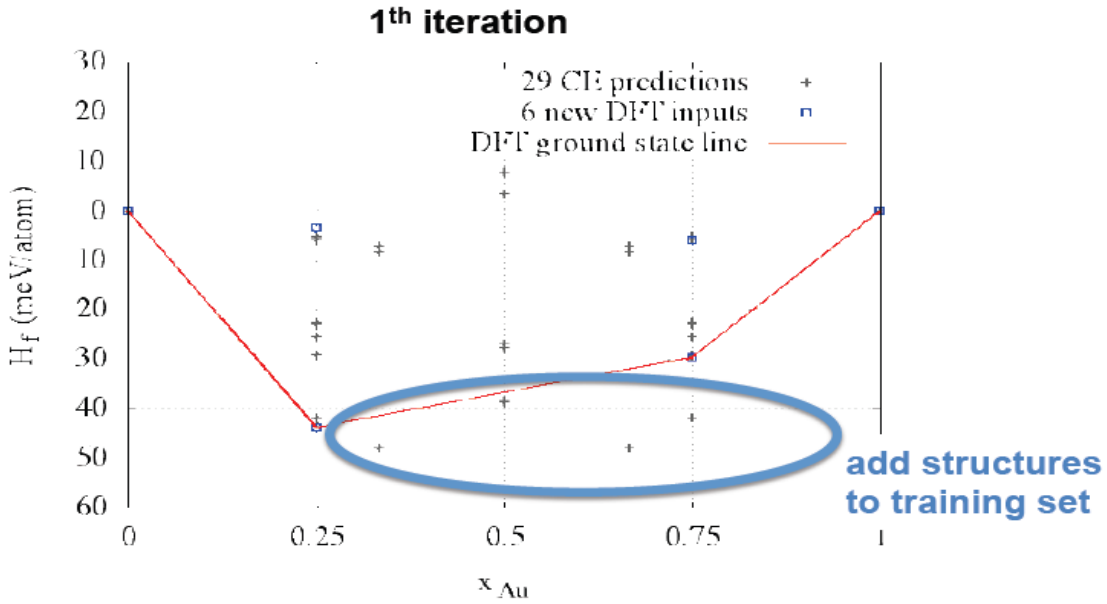

Figure 2-6: A Binary ground state diagram illustrating miscible constituent

2.7.4.2 Miscibility Gap

When a model is a phase separating, no stable ordered structures exist apart from the two pure phases and all structures are of equal importance to the cluster expansion. Therefore, the selection process of structures to be added to the training set has to improve the quality of the cluster expansion for all structures considered, irrespective of their formation energies ΔH_f.

The stochastic nature of the genetic algorithm is then used to determine how good (or bad) the energies of the structures predicted by the cluster expansion. Then the multiple cluster expansions are performed using an identical training set. The energy of all considered structures are then predicted by these multiple J's and a standard deviation of the predicted energies is evaluated. Structures with the highest standard deviation are those whose description by the cluster expansion is the worst. Therefore, these are added iteratively to the training set.

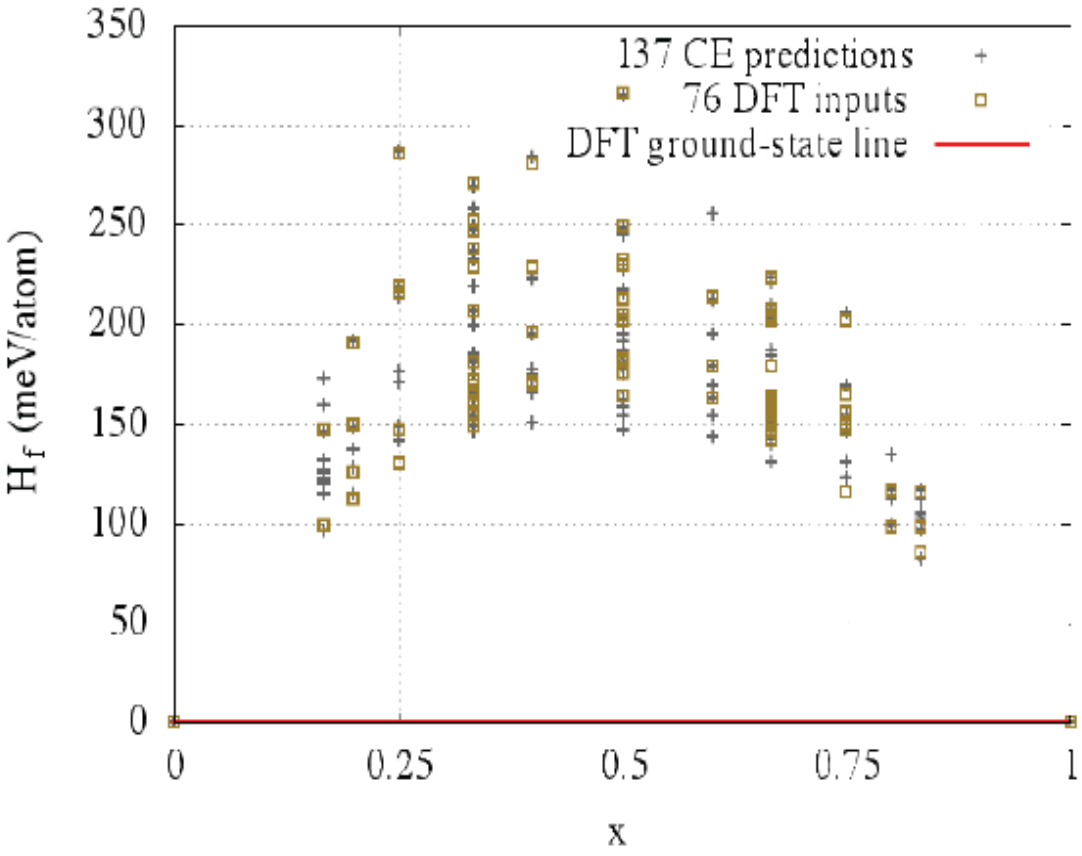

Figure 2-7: A Binary ground state diagram illustrating a miscibility gap

2.7.5 Ternary Systems Expansion

Recently, first-principles electronic structure calculations are used to compute the phase stability of ordered binary compounds in which the A and B atoms are defined with respect to a given underlying lattice. For the $LiNi_2O_4$–$LiMn_2O_4$ system, it is well known that the ordering of defects plays a fundamental role to understand the structure and stability within the $LiNi_2O_4$–$LiMn_2O_4$ phase. In a binary CE approach, the desired property of the system can be determined by using the spin product as a basis (see equation 52). In a ternary CE, the spin product is conveniently replaced by an orthogonal basis set which is constructed by Chebyshev polynomials $\Theta_n$of order$n$, for which their arguments are the spin variables [154],

$$\Theta_0 = 1, \quad \Theta_1(S_i) = \sqrt{3/2} * S_i \quad \Theta_2(S_i) = \sqrt{2} - 3/\sqrt{2} * S_i^2 \tag{38}$$

From now on, we will use the term “figure” instead of “cluster”. The spin product of a figure f used in equation (52) for the binary case is now replaced by the product of polynomials on each lattice site which is occupied by spinS_i;

$$\Pi_{f,s}(\sigma) = \Theta_{S_1}(S_1) \cdot \Theta_{S_2}(S_2) \cdot \ldots \cdot \Theta_{S_n}(S_n). \tag{39}$$

The vector *s* has components$S_j\ \varepsilon\ \{1; 2\}$, which designate the order of the polynomial. The number of factors n is equal to the number of lattice sites or vertices

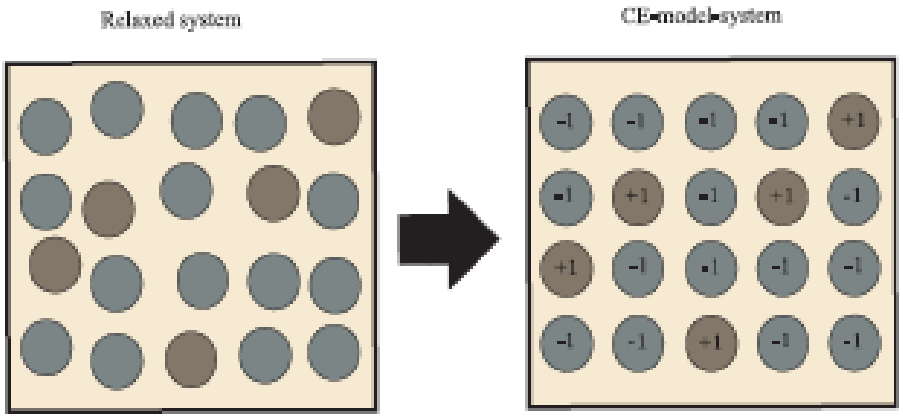

Figure 2-8: Schematic picture of mapping a physical configuration [158].

Figure 2-8 shows a schematic picture with relaxed structure (left panel) with a given atomic occupation (circles with different colours) onto the virtual lattice (right panel) and a decomposed into the clusters. The atom types in the CE fit are defined as the spin variable$S_i = -1, +1$. A basic lattice type (e.g. bcc) should be chosen for both of

the systems. Structural relaxations (see left panel) are allowed if they are not too large: the CE converges also for the given set of relaxed structures, see discussion in the text which belong to a figure$f$. By making use of Θ_{S_j} each figure can now be described by a different basis. For example, the correlation function of the figure with one vertex $\Pi_{1,s}$ describes two different characteristics:

- $\Pi_{f,(1)}$ Describes correlations only between atom types with spin -1 and 1, since the atoms with $S_i = 0$ do not contribute because the Chebyshev polynomial of the first order is zero. If atoms are labelled by A, B,C and their occupation variables are -1,0,+1 in respective order, then only correlations between A and C atoms are described.
- $\Pi_{f,(2)}$ describes correlations between all three atoms, because the Chebyshev polynomial of second order is different from zero for $S_i = 0$ and $|S_i| = 1$

In a ternary system, the maximum number of figures with k vertices or lattice sites is

3^k possibilities. This can be reduced if clusters are equivalent because of symmetry. Summing over all figures$f$, the Hamiltonian has now the form;

$$E(\sigma) = J_0 + \sum_f J_f \cdot \Pi_{f,s}(\sigma) \tag{40}$$

with the configuration dependent spin products Π and the configuration *independent* effective cluster interaction energies J. The main task of the CE consists in getting the effective cluster interactions $J_f(ECI)$ connected to each figure$f$, as sketched in figure 2.3. The correlation functions can now be symmetrized for a set of symmetry equivalent figures,$\overline{\Pi}_F(\sigma)$

$$\overline{\Pi}_F(\sigma) = \frac{1}{ND_F} \sum_{f \varepsilon F} \Pi_f(\sigma) \tag{41}$$

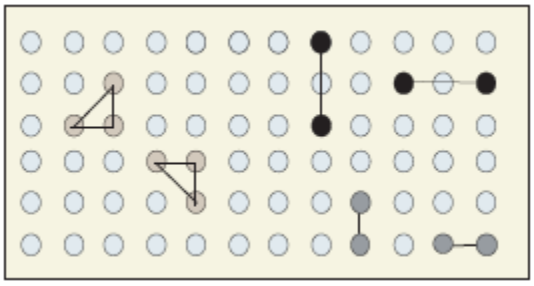

Figure 2-9: Example of figures in a two-dimensional lattice. Two duplets and triplets are shown in two different but symmetry equivalent arrangements [158].

where D_F is the number of symmetry operations by which the clusters $f \varepsilon F$ are related. Now, the summation runs over all F symmetrized spin products. For the sake of normalisation one, divides by the number of lattice sites *N* as used in the actual CE.

The energy of a certain configuration σ is now decomposed by the expansion;

$$E(\sigma) = N \sum_F D_F J_F \overline{\Pi}_F(\sigma) \quad (42)$$

Because of the given lattice the correlations $\overline{\Pi}_F$ are known and can be constructed. What is not known are the ECIsJ_F.The main task is now to calculate the ECIs. This is done by DFT calculations for the configuration dependent property of interest (e.g. the formation energy E_{DFT}) for suitably selected compounds with a given structure and fitting these results to the corresponding CE for each configuration (=compound). The quality of the CE strongly depends on the quality of the fitting, for which sophisticated self-consistent procedures were developed [159]. These fitting procedures are based on a least square fit;

$$\Sigma^{N_\sigma} |E_{DFT}(\sigma) - N\Sigma^{N_F} D_F J_F \Pi_F|^2 = min. \quad (43)$$

2.8 Monte Carlo Method

The Monte Carlo method has had a considerable history in physics. As far back as 1949 a review of the use of Monte Carlo simulations using ‘modern computing machines’ was presented by Metropolis and Ulam (1949). In addition to giving examples, they also emphasized the advantages of the method. Now, Monte Carlo simulations are reaching into areas that are far afield of physics. In a Monte Carlo simulation, the aim is to imitate the ‘time dependence’ of a model for which modification, or growth, does not proceed in some extreme predefined manner (e.g. according to Newton’s equations of motion). But preferably in a stochastic manner which was generated during the simulation, which depended on a sequence of random values. The simulation will not give corresponding findings with a second and different sequence of random numbers, but will produce values in agreement with those obtained from the initial sequence to within some ‘statistical error’. Monte Carlo methods consider only positions, as outlined by Ungerer when applied to systems at thermodynamic equilibrium [160]**.** The contribution of velocities to the partition function is determined analytically. Compared with Equilibrium Molecular dynamics, Monte Carlo methods also allow building statistical ensembles at thermodynamic equilibrium, but they do not address the dynamic properties of matter such as diffusion, viscosity or thermal conductivity. In requital, they may address important changes in the configuration space, such as the withdrawal or insertion of molecules in the system, which would be difficult to address with Molecular dynamics. Therefore, they are the privileged way to simulate adsorption with the Grand Canonical ensemble or fluid phase equilibrium with the Gibbs ensemble.

The Uncle code performs simulations either within the canonical or the grand canonical ensemble. Like the calculation of the input structures’ correlations for the cluster expansion, the determination of the starting energy of the Monte Carlo cell is done within the *g*-representation provided by the SNF. Inside UNCLE there is an implementation of a Monte Carlo simulation [161] from the Metropolis algorithm [162]. The Monte Carlo cell is thus represented by the tensor *G*. Changing the atomic occupation of a site corresponds to changing the corresponding integer value of one element of *G*. In a Monte Carlo simulation, the calculation of the energy

changes due to changes in the occupation (atom swaps) can be computed efficiently as only the energy contribution of those interactions 'touched' by the swapped sites needs to be evaluated.

The tensor *G* is the only large entity stored at runtime, requiring only *one byte* per site within the Monte Carlo cell; the correlations do *not* have to be stored at runtime. The minimal memory footprint allows for Monte Carlo cells of billions of sites, CPU time, rather than memory, becoming the limiting factor. A parallel implementation is underway to take advantage of this approach. Since the accuracy of a Monte Carlo estimate depends upon the thoroughness with which. This is computationally very demanding for ternary cases. Therefore, ECI would become temperature-dependent and with that also the whole CE.

Monte Carlo simulation is a numerical method for calculating the partition function (Z) of a model (i.e. Ising model) on a large lattice based on simulating the thermal fluctuations from one state to the other. In thermal Monte Carlo simulation for phase diagram calculations, the usual goal is basically the calculation of the expectation value $\langle Q \rangle$ of observable quantity Q. Therefore, our expectation value being the free energy or grand-canonical potential required for calculating the phase diagram. The quantity $\langle Q \rangle$ is calculated by averaging over all states μ of that system, where we weigh each state with its own Boltzmann probability. The expectation value is given by:

$$\langle Q \rangle = \frac{1}{Z} \sum_{\mu} Q_{\mu} e^{-\beta E_{\mu}} = \frac{\sum_{\mu} Q_{\mu} e^{-\beta E_{\mu}}}{\sum_{\mu} e^{-\beta E_{\mu}}} \tag{44}$$

where Q_{μ} are the observable quantities of states μ and $\beta = 1/kT$, where k is the Boltzmann constant. To determine $\langle Q \rangle$ accurately, we need to make an estimate of Q such that for a given number M of states we have:

$$Q_M = \frac{\sum_{i=1}^{M} Q_{\mu i} P_{\mu i}^{-1} e^{-\beta E_{\mu i}}}{\sum_{j=1}^{M} P_{\mu j}^{-1} e^{-\beta E_{\mu j}}} \tag{45}$$

where Q_M is the estimator of Q and P is the probability distribution that needs to be chosen to generate M states that will give an accurate estimate of $\langle Q \rangle$. However, the number of states required in the simulation should be chosen carefully and it is not possible to know which states are important to give the equilibrium solution of $\langle Q \rangle$ accurately or give accurateQ_M, similarly it is, impossible to calculate the partition function directly. Therefore, we use the "importance sampling" technique to choose the good states or distribution from which it is to simulate one's random variables [163]. The states are thus picked out in such a way that the probability that a state μ get chosen is$P_\mu = Z^{-1} e^{-\beta E_\mu}$. Thus, substituting the probability distribution P_μ into and then our estimator for$\langle Q \rangle$, (Eq.46), is,

$$Q_M = \frac{1}{M} \sum_{i=1}^{M} Q_{\mu i}. \tag{46}$$

This expression works well especially for a certain number of states particularly the lowest-lying states at low temperature. However, the exact set of states required for the calculation can be obtained through a "Markov process". The process generates new states ν from the initial state μ of a given system where the accompanying probability is the transition probability $P(\mu \to \nu)$and should satisfy the following three conditions, namely (1) no vary with time (2) only depended on the properties during the initial and final states, not on any passed states in the system (3) then over all final states the sum of the transition probabilities must be equal to unity [163] [164],

$$\sum_\nu P(\mu \to \nu) = 1. \tag{47}$$

A Monte Carlo simulation will repeat the process and generate a "Markov chain" of states $\mu, \nu,$etc., which appear with probability given by the Boltzmann distribution, and the process is termed "coming to equilibrium" or equilibration of the system [163]. In order to achieve the accurate representation of the Markov process, two other important conditions such as "ergodicity" (i.e. starting from any chosen state it should be possible to reach any other state of the system) and "detailed balance" (i.e. the transition rate from one state to another must be equal to the rate of the reverse process) are applied [163] [164]. As a result, the condition for the ratio of the transition probability that gives a Boltzmann equilibrium distribution is written as:

$$\frac{P(\mu \to \nu)}{P(\nu \to \mu)} = \frac{P_\nu}{P_\mu} = e^{-\beta(E_\nu - E_\mu)} \quad (48)$$

where $P_\mu$and $P_\mu$are the occupation probabilities of states μ and ν, with energies E_μ and E_ν, respectively. However, to improve the overall efficiency of the Monte Carlo algorithm, we still need to ensure that the acceptance ratio is high. The acceptance ratio determines the probability of moving from an initial state μ to a new stateν, provided that ν was generated from μ. Therefore, in order to achieve this condition, we use the more efficient algorithm, "Metropolis algorithm" [162]. Within the Metropolis algorithm, new states ν are chosen repeatedly, and then accepted or rejected randomly according to the acceptance probability$A(\mu \to \nu)$, where the set of selection probabilities $g(\mu \to \nu)$ for each possible transition from one state to another,$(\mu \to \nu)$ and acceptance probabilities $A(\mu \to \nu)$ are chosen such that the condition of the ergodicity and detailed balance are satisfied respectively [163]. The Metropolis Monte Carlo method is summarized as follows [164];

1. Start with a system in a randomly chosen state μ and evaluate the energyE_μ.
2. Generate a new state ν by making a random, ergodic change toμ, and evaluateE_ν.
3. If $E_\nu - E_\mu \leq 0$ then accept the new stateν. If $E_\nu - E_\mu > 0$ then accept the new state with probability$e^{-\beta(E_\nu - E_\mu)}$.
4. Return to step 2 and repeat until equilibrium is reached. That is the microstate occupancies follow a Boltzmann distribution.

2.9 Computer Codes

2.9.1 CASTEP Code

CASTEP (Cambridge Sequential Total Energy Package) is a software package which uses density functional theory to provide a good atomic-level description of all manner of materials and molecules [165] [166]. CASTEP can give information about total energies, forces and stresses on an atomic system, as well as calculating optimum geometries, band structures, optical spectrum, phonon spectra and much more. It can also perform molecular dynamics simulations. However, it uses density functional theory (specifically, using plane waves and pseudo-potentials) to solve approximately the Schrödinger equation for periodic systems of atoms, yielding the total energy, atomic forces and internal stresses in the system, as well as interesting electronic properties (the electron wave function, charge density distribution density of electronic states, etc.). The electronic relaxation is achieved by minimisation of the total energy. The minimisation is achieved using the technique called band-by-band, where each wave function is optimised independently, or by modern all band method.

CASTEP uses special k-points sampling for integration over the Brillouin zone and Fast Fourier Transformation (FFT) to evaluate matrix elements [133] [134] [167] [168]. It also uses wave function symmetrisation for a crystal with point group symmetry higher than $P\bar{1}$ and for metallic systems, it introduces partial occupancies for levels close to the Fermi energy. It uses both the local density approximations and the generalised gradient approximation for the exchange correlation energy functional and it is also used ultra-soft pseudo-potential as put forward by Vanderbilt as well as norm conserving potential [132].

2.9.2 MedeA-UNCLE

The MedeA-Universal Cluster Expansion (UNCLE) package allows you to set up, construct and automatically converges a cluster expansion for bulk systems with a partial disorder on some or all sub-lattices. The UNCLE software was developed by Stefan Müller, currently at the Technical University of Hamburg, and Gus Hart at the

Brigham-Young University in Salt Lake City, Utah and their co-workers [Uncle]. Accurate (ab-initio) calculations of a relatively small number of supercells are the basis on which the effective cluster interactions are determined. Maintaining the predictive power and accuracy of first-principles DFT methods. MedeA-UNCLE allows the determination of the following factors; the stable multi-component crystal of structures and the rank metastable of structures by the enthalpy of formation. It automatically performs ground-state searches and applies genetic algorithms or compressive sensing to explore configuration space. The as such derived effective cluster interactions map the ab-initio results onto a much simpler Hamiltonian which allows large-scale Monte Carlo simulations on systems with up to millions of atoms. The code can perform a complete CE-fit using a genetic algorithm and predict the ground states of systems containing up to three and more elements. For deriving results for temperatures $T \neq 0$ Monte Carlo simulations are implemented (as discussed in section 2.13). By this, configurationally entropies are considered. The working scheme for a cluster expansion is sketched in Figure 2-7.

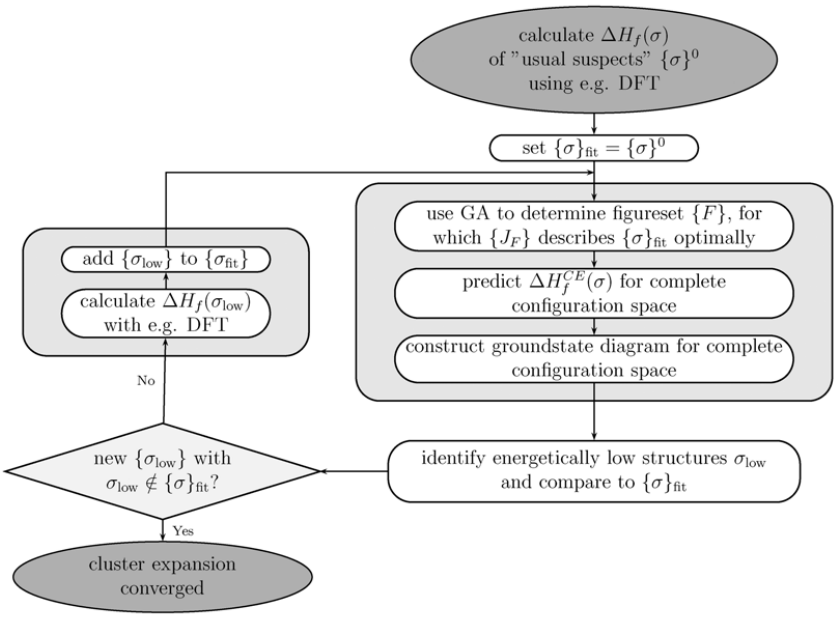

Figure 2-10: Self-consistent working plan as used by UNCLE for the cluster expansion for finding new input structures [169].

The following key benefit within the software that's incorporated in the MedeA is as follows:

1. Simulate structures containing millions of atoms with DFT accuracy
2. Accommodating operation in MedeA
3. Workflow-based on machine control of cluster expansion clarification
4. The adequate approach of many input systems
5. In-build graphical assessment and visualization
6. Break-up and restart complex calculations

Extend and expand existent Cluster Expansions

2.9.3 Virtual Crystal Approach

The CASTEP approach for dealing with disorder in first principle calculations is the so called virtual crystal approximation (VCA). The "virtual crystal" (VC) approach is a tractable way of studying configurationally disordered systems; the potentials which represent atoms of two or more elements are averaged into a composite atomic potential. This approach has the advantage that a single configuration with a smaller unit cell represents the disordered system. However, due to the different local environment of the virtual atom, some properties may not be reproduced [170]. The material properties of solid-solutions and alloys have been widely studied in both experimentally and computationally. Ferroelectric ceramics correspond to a typical material class for which most of the realistic applications are implemented by solid solutions.

To use such material systems within first principle methods, there exists two ways: super-cell and virtual crystal approach (VCA), regarding the advantages and shortcomings of both methods. The former can give correct results but requires more computational resources compared with the latter. The issue of correctness is related to the fact that the SC method can describe the local interaction between two atoms which consist of the virtual atom but VCA method cannot do that. It is vivid that the effectiveness of the calculation relates to the fact that the supercell may contain many unit cells compared with the primitive unit cell of the VCA method.

In the year 2000, several modern VCA approaches were developed with their own advantages and shortcomings. Hence, there are mainly two issues considered: the capability of treating the heterovalent atoms and accuracy of the calculation. The simplest VCA approach will be the simple mixing of the pseudo-potentials [170] [171]. In practice, this is performed through the averaging of the matrix elements in reciprocal space (Fourier momentum space). The advantage is simple but it is not sufficiently precise in some cases. The reason for the incorrectness is mixing of only the potentials. Ramer and Rappe developed more accurate VCA approach through performing the averaging at the level of atomic calculation, where the averaging of eigenvalues of valence orbitals, Coulomb nuclear potentials, core-charge densities and wave functions are performed. The CASTEP approach for dealing with disorder in first principle calculations is the so called virtual crystal approximation. The basic ideas of the workable VCA implementation for DFT methods can be expressed as:

$$V_{ext}(r, r') = \sum_i \sum_{\infty} \omega' \, v_{ps}^{\alpha}\left(r - RI\alpha^{r'} - RI\alpha\right), \tag{49}$$

where the total external potential V_{ext} is the sum of the nonlocal potentials of each atomic species, α, taken with the weights, ω, of the component atoms in the mixture atom. This approach can be used to study any composition in a solid solution [172] [173] [174].

2.9.4 Site Occupancy Disorder Program

SOD is a box of programs and tools for computer modelling site-disordered solids by reducing the number of site-occupancy configurations. During the calculation, it takes advantage of the crystal symmetry of the lattice. The SOD program works in combination with codes like VASP (input files for VASP calculations), GULP and other programs for simulations of systems with periodic boundary conditions (etc. evaluate the configuration energies). Finally, there is a program that uses the Boltzmann's statistics to take the results from those calculations and obtain thermodynamic quantities [175]. The SOD is a non-periodic occupation of lattice sites in a crystal system and ubiquitous phenomenon in solid-state chemistry. There are relevant examples namely which are metallic alloys, mineral solid solutions, and

synthetic non-stoichiometric compounds. Although experimental research of these specified materials applying diffraction techniques or other methods developed for the study of periodic crystals only gives averaged information of their properties, thus mapping the complexity of long-range patterns of site-occupancy configurations into a small crystal unit cell with ill-defined (fractional) site occupancies [175]. By the evaluation of the relative stabilities of configurations using simple energetic criteria, computer-modelling techniques are well fitted to make important contributions to the investigation of site-occupancy disorder in solids [176] [177] [178] [179] [180] [181] [182] [183] [184] [185].

There have been the employment of various computational strategies to this end that has involved the analysis of the energies of different site-occupancy configurations in supercells of the structure. One of the obvious and yet important restrictions of supercells approach is computational cost. There are still other glitches which are namely; (i) the analysis and minimisation of large supercells energy which can be very costly, even if with the employment of interatomic potential methods rather than quantum-mechanical techniques; and (ii) the number of possible configurations increases effectively and reaching very high values rapidly, with respect to the size of the supercell. However, the two limitations make it very complex to do a direct study of a complete configurational ensemble for any supercells apart from a very small one, usually insufficient, simulation cell [175]. There are strategies to deal with the above-mentioned problems, one common way to deal with the first of the problem is the usage of simple parametric interaction models consisting of energy contributions for each pair of atom types in the nearest-neighbour (NN) or the ext.-nearest-neighbour (NNN) sites. As a result, the reproduction of these energies obtained using quantum-mechanical or interatomic potential methods in small supercells because of the fitted parameters of these interaction models. These simple interaction models perform remarkably to the study of covalent solid solutions and of the same-charge cation or anion distributions in ionic systems. However, when the site-occupation configurations differ in their charge distributions, as is the case in many ionic solid solutions, the effect of the long-range electrostatic interactions cannot simply be incorporated into NN and NNN potentials and should be evaluated explicitly.

The second problem is even more difficult to solve, which is relating to the number of configurations. There is one approach used by certain authors (e.g. [183] [184] [185]), using the Monte Carlo method, before the samples are being accepted or rejected in the ensemble according to the Metropolis algorithm [162]. It is then possible to obtain a representative set of configurations, which can be considerably reduced as to the complete configurational space. An alternative approach is to take advantage of the system symmetry by reducing the number of configurations. Since the symmetry are related, identical and possible to limit the configurational space to the symmetrical in equivalent configurations only [186] [187] and other some alternative methods were discussed by Todorov *et al* [185].

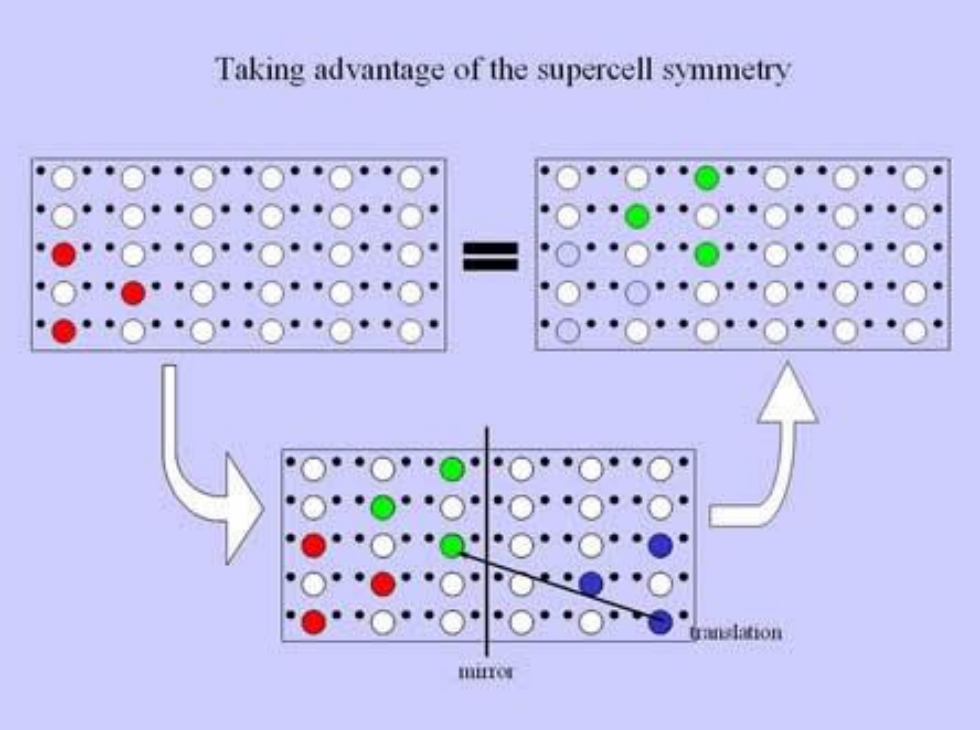

Figure 2-11 Illustration of identical configurations related by an isometric transformation [175].

2.9.4.1 Configurational statistics

We illustrate how to obtain the thermodynamic properties associated with the configurational disorder that resulted from the calculations in the reduced configurational space. Then summarize the equations for configurational statistics in the complete space of all configurations. If all site-occupancy configurations are

in thermodynamic equilibrium at temperature *T,* each configuration *n* (labelled with an index n) in the complete space (*n* = 1. . . *N*) is described in this approximation by a Boltzmann-like probability which is calculated from the energy E_n.

$$P_n = \frac{1}{Z}\exp(-E_n/k_BT) \quad (50)$$

where $k_B = 8.6173 \times 10^{-5}\ eVK^{-1}$ is Boltzmann's constant (it is formally equivalent to use the gas constant *R* instead, and expressing the molar energies of supercells, but we follow here the usual notation in statistical mechanics in terms of k_B), E_n is the energy of that configuration and

$$Z = \sum_{n=1}^{N} \exp(-E_n/k_BT) \quad (51)$$

is the partition function, and k is the total number of configurations with the given composition in the supercell. Now, we can calculate the energy of the system in configurational equilibrium as the average:

$$E = \sum_{n=1}^{N} P_nE_n \quad (52)$$

In evaluating the thermodynamic stability of a disordered solid at a given temperature, the energy and the configurational multiplicity of the system should be considered, while the configurational free energy E_n can be obtained from the partition function as

$$F = -k_BT\ln\mathrm{Z} \quad (53)$$

The difference per temperature unit between the average energy and the free energy defines the configurational entropy which is simply

$$S = \frac{E-F}{T} \quad (54)$$

In the case of a perfectly ordered system, in which one non-degenerate configuration has much lower energy than the rest, both the energy and the free energy of the system are identical to the energy of that configuration, and the

configurational entropy is zero. Alternatively, for a totally disordered system of *N* configurations, all with identical energies, the configurational entropy reaches a maximum value:

$$S_{max} = k_B \ln N \tag{54}$$

the configurational entropy calculated by equation (above) can take any value between zero and S_{max}, depending on the temperature and on the energy distribution of the configurations. It is possible to calculate this vibrational entropy term,S_{vib} by standard lattice dynamical procedures [188], and thus to replace the energy, E_n of each configuration by its corresponding Helmholtz free energy term: $F_n^{vib} = E_n$ - TS_{vib}. Now with the translation of the above equations to the reduced configurational space. The probability $\tilde{P}_m$ of an independent configuration *m* (*m* = 1. . . *M*) with degeneracy _*m* occurring is:

$$\tilde{P}_m = \frac{1}{Z}\Omega_m \exp(-E_m/k_B T) = \frac{1}{Z}\exp\left(\tilde{E}_m/k_B T\right) \tag{55}$$

and the introduction of reduced energy:

$$\tilde{E}_m = E_m - TS_m \tag{56}$$

and seen as temperature-dependent free energy associated with the degeneracy entropy [186] [187]:

$$S_m = k_B \ln \Omega_m \tag{57}$$

The introduction of this degeneracy entropy allows us to take into consideration the effect of the configuration degeneracy and make direct comparisons of independent configurations via the reduced energies, which comprise of both the energetic and the degeneracy information. It is clear, from the previous equations that if two independent configurations have the same energy, the one with higher degeneracy will have higher degeneracy entropy, which in turn lowers its reduced energy$\tilde{E}_m$,

resulting in a higher probability of appearance for that configuration. The energy and the partition function can therefore be calculated in the reduced space as

$$E = \sum_{m=1}^{M} \tilde{P}_m E_m \tag{58}$$

and

$$Z = \sum_{m=1}^{M} exp\ \exp\left(-\tilde{E}_m / \mathrm{k_B T}\right) \tag{59}$$

which allows the calculation of the configurational entropy via equation (9). Finally, in the equations above, *T* is the temperature at which the configurations are in equilibrium. However, cation exchange is often inhibited by high activation barriers, and thermodynamically equilibrium, except at high temperatures, should not be expected.

2.9.4.2 Average voltage for spinel cathode materials

The discovery of an open-cell voltage (OCV) was discovered eighteen years ago by Ceder and his co-workers for a Li-ion battery [189]. The guest ions can be inserted into and be removed from the host network reversibly. The equilibrium voltage difference between the two electrodes depends on the difference of the Li chemical potential between the anode and cathode. It is also referred to as the open-circuit voltage for a Li-intercalation reaction which is given by;

$$V(x) = \frac{\mu_{Li}^{Cathode} - \mu_{Li}^{Anode}}{zF} \tag{60}$$

where *F* is the Faraday constant, open-circuit voltage of the cell, z is the charge (in electrons) transported by lithium in the electrolyte and *e* is the magnitude of each electron charge. For the case of Li+ ions being the charge carrier, z in unity. The first term in the numerator ($\mu_{Li}^{Cathode}$) is a function of Li-content. Equation (102) was simply integrated between compositions $Mn_{2-2x}Ni_{2x}O_4$ and $LiMn_{2-2x}Ni_{2x}O_4$, where the average OCV was determined over a full charge/discharge cycle. Therefore the classical Nernst equation for the average OCV was obtained [189];

$$\bar{V} = \frac{-\Delta G_r}{(x_2 - x_1)F} \quad (61)$$

where ΔG_r is the Gibbs free energy. The well-known expression for the Gibbs free energy is the following:

$$\Delta G_r = \Delta E_r + P\Delta V_r - T\Delta S_r \quad (62)$$

where ΔG_r is the change in the Gibbs free energy, ΔE_r is the change in internal energy, P is the pressure, ΔV_r is the volume change, T is the temperature, and, finally, ΔS_r is the entropy change.

Here the order of 10^{-5} electron volts is of term $P\Delta V$ and in contrast ΔE_r is of the order of 3-4 eV per molecule. Lastly, the term $T\Delta S_r$ is of the order of thermal energy which is also much less thanΔE_r. Hence, we conclude that the changes in the Gibbs free energy are approximately equal to the changes in internal energy.

$$\Delta G_r \approx \Delta E_r \quad (63)$$

Consequently, *ΔGr* is the Gibbs free energy for the following reaction:

$Mn_{2-2x}Ni_{2x}O_4$ (cathode) + Li (anode) → $LiMn_{2-2x}Ni_{2x}O_4$ (cathode) (64)

However, the average voltage for the complete discharge is obtained from the difference in Gibbs free energy between the lithiated ($LiMn_{2-2x}Ni_{2x}O_4$) and delithiated ($Mn_{2-2x}Ni_{2x}O_4$) states (and Gibbs free energy of pure Li) [190] [191]. In that case, the average voltage is given by

$$\bar{V} = -\frac{1}{F}[G_{\mathrm{LiMn2-2xNi2xO4}} - G_{\mathrm{Mn2-2xNi2xO4}} - G_{Li}] \quad (65)$$

At 0 K, the Gibbs free energies can be approximated by the total energies (E). When G (or E) expressed in electron-Volts (e/V) and the voltage in Volts (V), the prefactor of 1/e drops out and the average voltage is written as,

$$\bar{V} = -[E_{\mathrm{LiMn2-2xNi2xO4}} - E_{\mathrm{Mn2-2xNi2xO4}} - E_{Li}] \quad (66)$$

Where the average voltage of an intercalation compound is directly related to the energies of the charged and discharged process, then voltage changes with respect to each structure of either state. Then the average voltage is calculated from each lowest energy structures at lithiated and delithiated states or between the lowest energy state at the lithiated structure and a higher energy structure at the delithiated state, e.g., by removing Li from the $LiMn_{2-2x}Ni_{2x}O_4$ structure. Since all the lithiated oxides have normal structure as the lowest energy structure, we calculate voltages considering the normal structures at the lithiated state. On the other hand, at the delithiated state, the normal structure is not always the preferred structure and the voltage-calculation depends on which structure is used for the delithiated state [192].

2.10 Theoretical Background for Calculated Properties

2.10.1 Pressure

The pressure is calculated in a computer simulation via the viral theorem of Claussius. The viral theorem is defined as the expectation value of the sum of the product of the coordinates of the particles and forces acting on them. It is written as:

$$W = \sum x_i \, p_{xi}, \quad (67)$$

where the xi is the coordinate and p_{xi} is the first derivative of the momentum along the coordinate. The viral state that is equal to $-3NK_BT$. In an ideal gas, forces are those due to interactions between the gas and the container and are this case the viral theorem is equal to -3PV. These results can be obtained from:

$$PV = NK_BT, \quad (68)$$

Forces between the particles in a real gas and liquid affect the viral hence the pressure. The total viral for a system equals the sum of an ideal gas part (-3PV) and the contribution due to interactions between the particles. The result obtained is:

$$P = \frac{1}{V}\left[Nk_BT - \frac{1}{3K_BT}\sum_{i=1}^{N}\sum_{j=i+1}^{N} r_{ij}f_{ij}\right], \quad (69)$$

The forces are calculated as part of molecular dynamics simulation, and so little additional effort is required to calculate the viral and thus the pressure.

2.10.2 Electronic Properties

The number of states at each energy level, which is available to be occupied, is called the density of states (DOS). A zero DOS of an energy level means that no states can be occupied. It is a useful mathematical concept allowing integration with respect to the electron energy to be used instead of the integration over the Brillouin zone. In addition, the DOS is often used for quick visual analysis of the electronic structure. Characteristics such as the width of the valence band, the energy gap in insulators and the number and intensity of the main features are helpful in qualitatively interpreting experimental spectroscopic data. The closest band above the bandgap is called the conduction band, and the closest band beneath the bandgap is called the valence band. In a metal or semimetal, the Fermi level is inside of one or more allowed bands. In semimetals, the bands are usually referred to as "conduction band" or "valence band" depending on whether the charge transport is more electron-like or hole-like, by analogy to semiconductors. In many metals, the bands are neither electron-like nor hole-like, and often just called "valence band" as they are made of valence orbitals [193]. The band gaps in a metal's band structure are not important for low energy physics since they are too far from the Fermi level.

DOS analysis can also help to understand the changes in electronic structure caused by, for example, external pressure. Therefore, a high DOS for an energy level represents that many states are available for occupation. DOS delivers invaluable information about the bonding within solid and in the classification of

materials as metallic, semiconductor or insulator. Metals and semimetals have non-localised electrons and no gap (separation between the valance band and conduction band). The distinction between semiconductors and insulators is a matter of convention. Semiconductors are regarded as a type of insulator with a narrow bandgap. Insulators having a larger bandgap, usually greater than 3eV, are not considered semiconductors and generally do not exhibit semi-conductive behaviour under practical conditions. In a scenario where parabolic relation, such as applied to free electrons, or to the electron in solid with an isotropic parabolic band structure, the energy is related to the wave vector as $\varepsilon = \frac{\hbar}{2m} k^2$. Accordingly, the densities of state in the three dimensions are as follows,

$$D(\varepsilon) = \frac{1}{2\pi^2}\left(\frac{2m}{\hbar^2}\right)^{3/2}\varepsilon^{1/2}, \tag{70}$$

Although DFT seems to systematically underestimate the bandgap in insulator and Semiconductors by about 30-40%, it is successful in reporting the shape of the DOS.

So, more accurate methods are based on linear or quadratic interpolations of band energies between the reference points in the Brillouin zone. The most popular and reliable technique, which is based on the tetrahedron interpolation, is unfortunately ill suited to the Monkhorst-Pack grid of special points. This method is based on the linear interpolation in parallelepipeds formed by the points of the Monkhorst-Pack set, followed by the histogram sampling of the resultant set of band energies. Therefore, CASTEP programme [130], [194] is a first principle quantum mechanical code for performing electronic structure calculations.

2.10.3 Elastic Properties

It's a constant or a coefficient that expresses the degree to which material possesses elasticity. In an elastic material that has been subjected to a strain below its elastic limit, the elastic constant is the ratio of the unit stress to the corresponding unit strain. The mechanics of solid bodies, considered as continuous media, form the content of the theory of elasticity. The main problem in estimating elastic constants from first principles is not only the requirement of accurate methods for

calculating the total energy but also the complicated heavy computations involved in the calculation of elastic constants [195].

From the perspective of materials physics, the elastic constants C_{ij}contain some of the more important information that can be obtained from ground state total energy calculations. Hence a given structure cannot exist in a stable or metastable phase unless its elastic constants obey certain relationships. Elastic properties of a solid are important because they relate to various fundamentals of solid-state properties, such as the equation of state, phonon spectra, etc. [195]. A given crystal structure cannot exist in a stable or metastable phase unless its elastic constants obey certain relationships. The C_{ij}also determines the response of the crystal to external forces, as characterised by the bulk modulus, shear modulus, Young's modulus and Poisson's ratio plays an important role in determining the strength of a material [196].

Many first-principles calculations of the electronic structure and the total energy of solids have been carried out since the development of high speed computers (Pickett, 1985). Hence the use of periodic boundary conditions assume the existence of a single crystal, so all elastic constants can be determined by direct computation. The calculated C_{ij} can then be used to check the experimental bulk and shear moduli, if available and to calibrate model calculations. In addition, the elastic constants can be used to check the phase stability of proposed compounds [196]. Elastic properties determine the stiffness of a crystal against the external strain, so they are important for understanding the structure stability and the strength of materials such as bulk modulus, shear model, Young's modulus and Poisson's ratio [197]. First-principles calculations can then be used to predict the existence and properties of new materials.

Elastic constants are physical properties of crystals to relate the mechanical response to the material deformation (*i.e.* stress and strain) within the elastic regime. A isotropic material which obeys Hooke's law, where strain is linearly proportional to stress, there are only two independent elastic constants, those of stress and strain. The elastic properties of such materials are defined by elastic moduli, notably

the bulk modulus, shear modulus, Young's modulus, Lamé's constant, and Poisson's ratio. Seismic wave velocities are governed by the elastic moduli and the densities of the media through which they travel. A system is said to be elastic if any deformations caused by external forces will spontaneously and completely disappear once the external forces are removed. Hence the unit cell is created by changing the Bravais lattice vectors **R = (a, b, c)** of the undisturbed unit cell to **R′ = (a', b', c')** using a strain matrix **e**

$$R' = R\begin{bmatrix} 1+e_{xx} & \frac{1}{2}e_{xy} & \frac{1}{2}e_{xz} \\ \frac{1}{2}e_{yx} & 1+e_{yy} & \frac{1}{2}e_{yz} \\ \frac{1}{2}e_{zx} & \frac{1}{2}e_{zy} & 1+e_{zz} \end{bmatrix}, \quad (71)$$

.

hence a change of the total energy of the crystal,

$$U = \frac{E_{tot}-E_0}{V_o} = \frac{1}{2}\sum_{i=1}^{6}\sum_{j=1}^{6} C_{ij}\, e_i e_j, \quad (72)$$

with the sum, overall i and all j so that each cross term appears twice. E_0 is the total energy of the unstrained lattice, V_o is the volume of the undistorted cell and the C_{ij} are the elements of the elastic constant matrix with a notation that follows standard convention. Both is i and j run from 1…6 in the sequence {xx, yy, zz, yz, xz, xy}. The tensor of elasticity has 36 elements and the elastic behaviour of a completely asymmetric material is specified by 21 independent elastic constants, while for an isotropic material, the number is 2.

To calculate the elastic constants is one simple way of validating a potential model. There are two methods to compute elastic constants: one is to monitor (Virial) stress and the other is to monitor strain energy as a function of the applied strain. Conceptually, the two approaches are equivalent accept that stress is a linear function of strain and the strain energy is a quadratic function of strain. The methods will be explained to get three independent elastic constants (C_{11}, C_{12} and C_{44}) for the cubic crystal materials and to estimate the three independent elastic constants,

C_{11}, C_{12}, and C_{44}. Each representing three equal elastic constants (C_{11}= C_{22}= C_{33}, C_{12}= C_{23}= C_{31} and C_{44}= C_{55} =C_{66}).

The application is to illustrate the behaviour in which the stiffness matrix elements may be obtained from strain fields of the form (equation 70). If the applied strain is exx = e with all other ei = 0, the energy change would be$U = {C_{11}e^2}/{2}$. This allows a unique determination of C_{11}. If $e_{yz} = e_{zy} = e/2$, with all other strain components being zero, then $U = C_{44}e^2/2$, then we have an independent determination of C_{44}. The bulk modulus, B, is the response to a uniform compression so applying the strain field $e_{xx} = e_{yy} = e_{zz} = e$ allows the computation of B via the relation$U = Be^2/2$. Similarly, the shear modulus can be calculated by using the strain field $e_{zz} = e; e_{xx} = e_{yy} = -{e}/{2}$, where upon$U = 3C'\,{e^2}/{2}$. Hence, the elastic constant C_{12} is easily determined by using one or other of the elastic relations. From the first-principles calculated elastic constants, one may get bulk modulus B, shear modulus G and the anisotropic factor A and using schemes such as Reuss (lower bound), Voigt (upper bound) or Hill averaging [198]. The B/G ratio was also discovered as early as 1954 by Pugh, based on an analysis of the ratio of bulk modulus to shear modulus of pure metals [199].

$$B = \frac{1}{2}(c_{11} + 2c_{12}), \tag{73}$$

$$G = \frac{1}{2}\left[\frac{C_{11}-C_{12}+3C_{44}}{5} + \frac{5C_{44}(C_{11}-C_{12})}{4C_{44}+3(C_{11}-C_{12})}\right], \tag{74}$$

$$C' = \frac{1}{2}(c_{11} - c_{12}), \tag{75}$$

and

$$A = \frac{(2c_{44}+c_{12})}{c_{11}}, \tag{76}$$

where *E* is the Young modulus, *G* shear modulus, *B* bulk modulus, *C'* tetragonal shear modulus and anisotropy factor *A.* The Zener anisotropy factor A measures

the degree of anisotropy in solid [200] and calculated using equation 32. It takes the value of 1 for an isotropic material by making provision a measure of the degree of elastic anisotropy when the A values are smaller or greater than unity. Hence applying the following relations provides a useful independent check on the accuracy of the computation. A symmetry-general formulation of the calculation of elastic constants from total energy calculations is given by Le Page and Saxe [201].

2.10.4 Energy of formation

For the study of the relative stability and calculation of binary alloy phase diagram, it is convenient to consider the cluster expansion of the energy of formation,

$$E_f(\sigma) = E_0(\sigma) - xE(A) - (1-x)E(B), \tag{77}$$

where *E(A)* and *E(B*) are the equilibrium total energies of *A* and *B* in a given underlying lattice (fcc or bcc), and x is the atomic concentration of A in σ. The cluster expansion of *E(A)* and *E(B)* is given by,

$$E(A) = \sum_K \sum_{\alpha K} m_{\alpha K} J_{\alpha K}, \tag{78}$$

and

$$E(B) = \sum_K \sum_{\alpha K} m_{\alpha K} J_{\alpha K} (-1)^K. \tag{79}$$

where $m_{\alpha K}$ is the multiplicity of the geometrically different clusters _K and $J_{\alpha K}$ are the expansion coefficients.

Now, consider a cluster expansion for a crystal that has only one lattice site in the primitive unit cell of the underlying lattice (e.g. fcc and bcc). The expansion coefficient J_0 that correspond to the empty cluster $\Phi_0 = 1$ will remain constant for the entire system. However, the expansion coefficient J_1 coupled to the point-cluster $\Phi = \frac{1}{N_0}\sum_{n-1}^{N_0} \sigma_n$ is the same for all lattice sites. Thus inserting $E(\sigma) = \sum_\alpha m_\alpha J_\alpha \Phi_\alpha(\sigma)$ and $\Phi_\alpha(\sigma) = \frac{1}{N_\alpha} \sum_{cluster} \sigma_1 \sigma_2 \ldots \sigma_{n\alpha}$ into (80)

$$\sigma_i = \begin{cases} +1 \; if \; site \; i \; is \; occupied \; by \; A, \\ -1 \; if \; site \; is \; occupied \; by \; B, \end{cases} \tag{81}$$

and assuming that $x = \; C_A = \frac{1+\Phi_1}{2}$, we have

$$\langle E_f(\sigma) \rangle = \; \Sigma_K \sum_{\alpha K} m_{\alpha K} J_{\alpha K} \left[\Phi_{\alpha K} - \frac{1+(-1)^K}{2} \Phi_0 - \frac{1-(-1)^K}{2} \Phi_1 \right]. \tag{82}$$

Therefore, the contribution of the clusters α_0 and α_1 to $E_f(\sigma)$ vanishes identically. This suggests that $E_f(\sigma)$ is independent of the empty- and the point-cluster, therefore the empty- and the point-cluster cannot appear in the cluster expansion of$E_f(\sigma)$.

2.10.5 Phonons

In this section, the first principle calculations based on the DFT were performed using the VASP code [141] [138]. The calculated results were obtained using the generalised gradient approximation (GGA) exchange correlation functional of Perdew, Burke and Ernzerhof (PBE) and projector augmented wave method [202] [113]. The Kohn-Sham orbitals were expanded using different plane wave cut-off energies for each configuration as shown in Table 5-3. Then followed by the Brillouin zone integrations carried out using the Monkhorst-Pack k-point mesh [134] with different grid sizes for each configuration as shown in Table 5-3.

In this section, the first principle calculations based on the DFT were performed using the VASP code [144] [141]. The calculated results were obtained using the generalised gradient approximation (GGA) exchange correlation functional of Perdew, Burke and Ernzerhof (PBE) and projector augmented wave method [203] [91]. The Kohn-Sham orbitals were expanded using different plane wave cut-off energies for each configuration as shown in Table 5-3. Then followed by the Brillouin zone integrations carried out using the Monkhorst-Pack k-point mesh [118] with different grid sizes for each configuration as shown in Table 5-3. It was Soviet a physicist Igor Tamm who introduced the concept of phonons in the year 1932. The phonon name originates from the Greek word φωνή (phonē), which construe to sound or voice due to the rise of the sound of the long-wavelength phonons. Shorter-

wavelength higher-frequency phonons give rise to heat. Detailed knowledge of a quantum mechanical description of an elementary lattice vibrational motion in which a lattice of atoms uniformly oscillate at a single frequency [204]. The fundamental thermodynamic functions of internal and free energy, entropy, heat capacity as well as non-linear properties such as thermal expansion and heat conduction are to a considerable extent obtained by the vibrations of the constituent atoms in the lattice. However, the quantum theory of lattice dynamics is well developed and it is proven to be one of the most successful theories of solid-state physics [205].

In regard to the existent of density functional theory and the progress with numerical methods for solving quantum physical equations together with the emergence of improved software and substantial year-on-year improvement in computing power have combined to make accurate materials simulations not only possible but almost routine. Therefore, describing the interatomic interactions in crystals and molecules based on quantum mechanics. For calculating the phonon dispersion on an ab-initio level three different techniques for *ab initio* evaluation of vibrational properties have been developed, mainly two approaches are used, namely the linear response approach [206] [207] [208] [209] [210] and the direct method [211] [212]. They are as follows: (i) direct methods based on total energy changes or forces calculated for atoms displaced from their equilibrium position, (ii) analytical calculation of force constants based on a perturbative expansion around the equilibrium geometry and (iii) Fourier transform of the atomic velocity autocorrelation function obtained from a molecular dynamics trajectory [213]. Direct methods (option (i)) require the inspection of total energy and forces for the equilibrium geometry as well as some distorted geometries from which the force matrix constant can be assembled [214]. The method of inter-planar force constants is perpendicular to the directions that displaced within elongated supercell [215], hence the determination of the phonon dispersion curves along with specific high symmetry directions in reciprocal space. The techniques for selecting suitable supercells and atomic displacements, assembling force constant matrices from the calculated forces and calculating phonon dispersion relations via Fourier transform are well documented [211] [212] [216]. The perfect crystal environment should be sufficiently large to ensure that interactions of the perturbation with all its translational symmetry equivalent copies are small, which usually requires construction of suitable supercells. Therefore, the

most general direct approach to lattice dynamics based on the ab initio evaluation of forces on all atoms that are produced by a set of finite displacements of a few atoms within an otherwise perfect crystal [217].

2.10.5.1 Phonon dispersion and polarization vectors

The frequencies $\omega^2(k,j)$ of phonon modes j are calculated by diagonalization of the super cell dynamical matrix for each wave vector k along a specified path through the Brillouin zone, thus creating phonon dispersion curves.

$$D(k).e(k,j)\omega^2(k,j)e(k,j) \tag{83}$$

The irreducible representations of all phonon modes at the $\Gamma(0,0,0)$ the point can be calculated, providing, in addition, Raman and infrared activities of the modes. The complex polarization vectors satisfy the orthonormality relations,

$$\sum_j e_i^*(k,j;\mu).e_l(k,j;v) = \delta_{i,l}\delta_{\mu,v} \tag{84}$$

$$\sum_i \sum_j e_i^*(k,j;\mu).e_l(k,j;\mu) = \delta_{i,j} \tag{85}$$

The polarization vector $e(k,j;\mu)$s defined for the wave vector k being at the origin of reciprocal space differ from the conventional polarization vector $e(k_\tau;\mu)$ that is defined for the wave vector k_τ pointing from the centre of a given Brillouin zone labelled by the reciprocal vectorτ. Because of $k = \tau + k_\tau$ the relation between the differently defined polarization vectors is,

$$e(k,j;\mu) = e(k,j;\mu)exp\left[-2\pi\tau.r_\mu\right] \tag{86}$$

Therefore, the usage of the polarization vectors implies that the displacements caused by a particular phonon and its intensity can be calculated. Assuming the amplitude Qk and phase $0 \leq \varphi_k \leq 1$ of the displacement wave, the displacements $U(n,\mu)$ of atoms (n,μ) for a given wave vector k and the phonon branch j are given by the following equation:

$$F^{(s)}(k,j) = \frac{1}{k^2}\left|\sum_{\mu}\frac{e(k,j;\mu)}{\sqrt{M_{\mu}}}\right|^2 \quad (87)$$

and can be applied to remove unessential phonon branches originating from back folding or to estimate relative intensities of all modes in varying Brillouin zones.

The MedeA-Phonon module [216] is focused on the general direct approach to lattice dynamics and is designed to work independently of a specific underlying code for deriving forces and total energies. Together with the VASP, a fully automatic and highly parallel procedure is embedded in MedeA.

2.10.6 Heats of Formation

The standard heat of formation of a compound is the change of enthalpy during the formation of 1 mole of the compound from its constituent elements, with all substances in their standard states at 1 atmosphere (1 atm or 101.3 kPa). The heats of formation of compounds and associated entropies provide the basis for understanding and constructing phase diagrams. Knowledge of these quantities gives the prospect of disentangling which of the observed phases might occur upon varying the means of fabrication. Types of models, the heat of formation $\Delta H_i(\vec{\sigma})$ are evaluated for all structures in the training set. It is defined:

$$\Delta H_i(\vec{\sigma}) = \frac{E_{DFT}(\vec{\sigma}) - \sum n_i(\vec{\sigma}) E^i_{DFT}}{\sum n_i(\vec{\sigma})} \quad (88)$$

Wherein $E_{DFT}(\vec{\sigma})$ describes the DFT total energy of the structure$\vec{\sigma}$, $n_i(\vec{\sigma})$ is the number of atoms of atomic species i contained in $\vec{\sigma}$, and E^i_{DFT} denotes the DFT total energy of the pure phase of atomic species i. The sums go over all type of atoms contained in the structure$\vec{\sigma}$.

Chapter 3

Structural Properties and Pressure Dependence

In this chapter, we present and discuss results based on the ab-initio calculations performed on spinel $LiMn_2O_4$ and doped $LiNi_xMn_{2-x}O_4$ the (structural parameters, bond length and the equation of states). DFT has provided a convenient first principle framework for studying the convergence test (cut-off, k-points and convergence parameters), structural parameters (lattice parameters, volume, bond length, and total energy) of different concentrations and compared with experimental results. A summary of the method used is given and finally, results are presented. The structural properties and pressure dependence calculations were performed using computer code CASTEP and are discussed in this chapter. The effect of pressure on different systems is discussed, with pressure ranging from 10 GPa to 50 GPa, which is discussed in detail in chapter 2. All of the work done in this study will focus on the first-principles energy calculations optimised at a uniform cut-off energy to determine the total energy of various structures. The approximation used called GGA-PBE which was designed to be more robust and accurate [113] and the Brillouin-zone for the surface model were represented by a Monkhorst-Pack scheme for the generation at a uniform k-points.

3.1 Convergence Test

3.1.1 Energy Cut-off

To determine the appropriate cut-toff energy for the spinel $LiMn_2O_4$, single-point energy calculations were performed for different kinetic energy cut-offs at the default number of k-points for each system within GGA-PBE. The ultra-soft pseudo-potentials, which require significantly less computational resources than the norm-conserving potentials [218], were used. Energy cut-off is an important parameter in PWP calculations since it determines the number of plane waves required in a calculation. Different values of energy cut-off were calculated until constant minimum energy is obtained, thus the energy becomes stable and the cut-off energy

that corresponds to the minimum total energy is recorded. The energy cut-off of 500eV is found to be appropriate for GGA-PBE. The graphs of total energy versus energy cut-off are shown in Figure 3.1. The maximum of iterations used is 300 for the spinel $LiMn_2O_4$. In all optimisations, the tolerance in total energy and pressure change before self-consistency was 2.0×10^{-5}eV/atom and 0.1GPa respectively. The RMS tolerance for the atom displacement was restricted to 0.002Å. Hence Mishra and Ceder in their study on the structural stability of lithium manganese oxides have stressed the use of GGA [74].

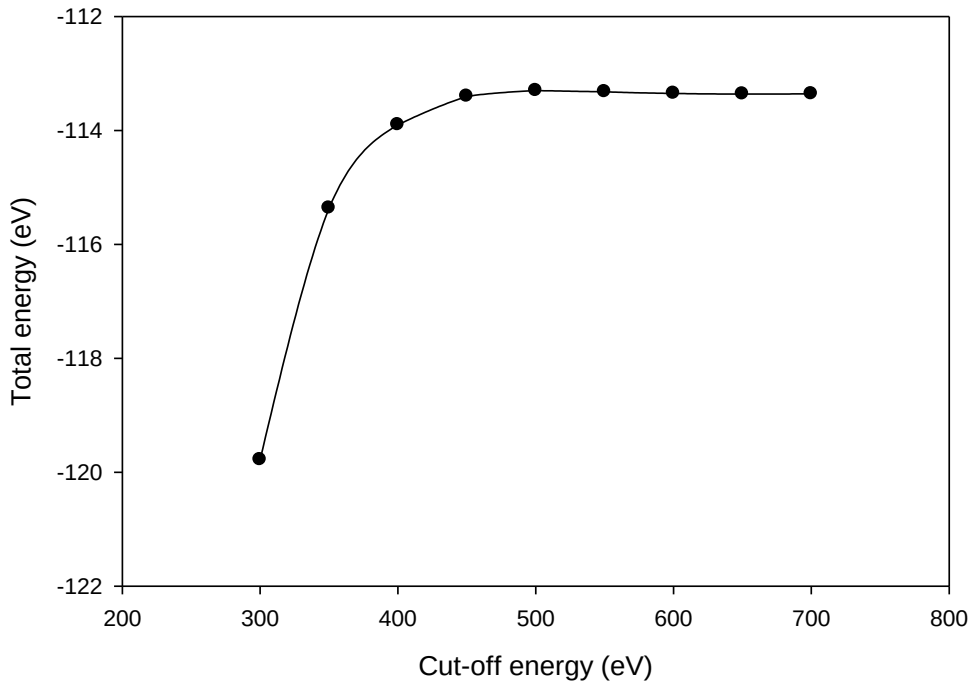

Figure 3-1: Total energy versus energy cut-off for spinel $LiMn_2O_4$ structure.

3.1.2 K-points

It is important to determine an accurate number of k-points to use in PWP calculations for a speedy convergence coupled with an accuracy of the total energy. The greatest possible accuracy is achieved from the number of k-points which were used by P. Hohenberg and W. Kohn, Kohn and L. J. Sham [219]. The Monkhohorst-Pack scheme of the k-points sampling was used to select an optimal set of special k-points used [220] [106]. The number of k-points was determined by running SCF calculations for different k-points. The k-points mesh parameters that gave the

minimum total energy of the system was chosen and used in all calculations. The k-points mesh parameter was chosen to be 5x5x5 and for spinel $LiMn_2O_4$. All the calculations presented in this dissertation were obtained using 500 (eV) cut-off energy and 5x5x5 k-points.

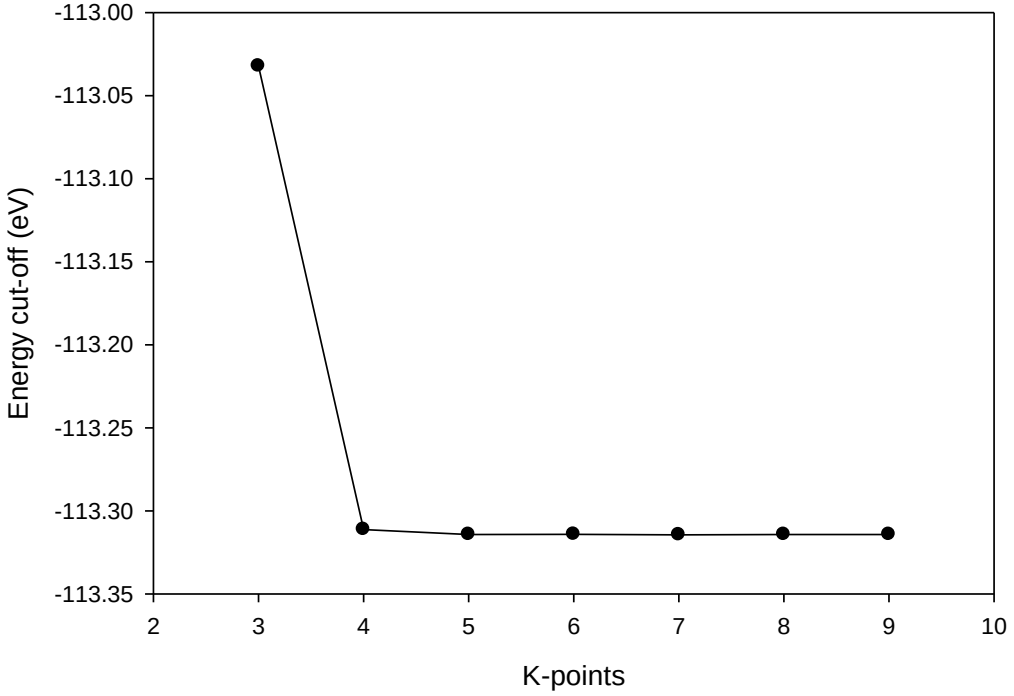

Figure 3-2: Energy cut-off against variation of the number of k-points.

3.2 Structural Properties

The structural properties of pure and nickel doped $LiMn_2O_4$ are structures at 0GPa are listed in Table 3-1. Shown in the table are lattice parameters, volume, energy and bond lengths for $LiMn_2O_4$ and doped systems. The spinel structure of the conventional cell containing 56 atoms is compared with an experimental lattice constant 8.241 (Å) [221] and the structure was optimised using the method discussed in chapter 1 allowing the structure to change. Geometry optimisation gives the equilibrium lattice parameters and relaxed internal lattice parameters which can be compared with experimental results. The deviation between the experimental results and our calculated results is 0.8% $LiMn_2O_4$ and 1.3%

$LiNi_{0.5}Mn_{1.5}O_4$for lattice parameter for Gurpreet Singh et al. [221] and J.H Kim et al [133]. Hence the results in Table 3-1 are in good agreement with studies done by Gurpreet Singh et al. [221] and J.H Kim et al. [222].

3.2.1 Structural Properties of $LiMn_2O_4$ and $LiNi_xMn_{2-x}O_4$

Table 3-1: Calculated and experimental structural parameters, of $LiMn_2O_4$ and $LiNixMn_{2-x}O_4$ ($0 \leq x \leq 2$) structures.

Systems	Lattice Parameters (Å)		Volume ($Å^3$)	Energy/atom (eV)
	Calculated	Experimental		
$LiMn_2O_4$	8.174	8.241 [221]	546.107	-463.653
$LiNi_{0.25}Mn_{1.75}O_4$	8.158		542.852	-517.168
$LiNi_{0.5}Mn_{1.5}O_4$	8.068	8.172 [223]	525.130	-579.073
$LiNi_{1.75}Mn_{1.25}O_4$	8.158		542.855	-517.168
$LiNi_{0.875}Mn_{1.125}O_4$	8.043		520.362	-652.217

We compared the calculated lattice parameters obtained from a conventional structure and doped structures using a GGA-PBE approximation. We observed a decrease with respect to the lattice parameters (calculated), volume and energy when the system was doped with different nickel concentrations. In Table 3-1 it is apparent that the lowest total energy occurs at a volume of 520.362 ($Å^3$) and at a lattice constant 8.043 (Å) of the system with the highest nickel concentration $LiNi_{0.875}Mn_{1.125}O_4$. As indicated in Table 3-1 the pure $LiMn_2O_4$ and doped $LiNi_{0.5}Mn_{1.5}O_4$ with both calculated and experimental lattice a, volume and energy show the effect of the nickel content in both systems. The lattice parameters decrease with an increasing nickel concentration, excluding the $LiNi_{0.25}Mn_{1.75}O_4$ and $LiNi_{1.75}Mn_{1.25}O_4$ systems which have the same lattice parameters, volume and energy. The energy and volume of the systems also decrease with the increasing nickel concentration. Table 3-2 gives the bond length of the systems and it is revealed that the bond length decreases with an increasing nickel concentration. The Mn-O bond length in spinel $LiMn_2O_4$ (un-optimised) was found to be different after optimisation; four different kinds of bond length were obtained in

$LiMn_2O_4$:$d_1^{Mn-O} = 2.173Å$, $d_1^{Mn-O} = 3.523Å$ $d_1^{Mn-O} = 4.483Å$ $d_1^{Mn-O} = 6.233Å$. d_1^{Mn-O} is in good agreement experimental and literature results for all the systems. The percentage difference between the calculated literature and experimental results is 1.5%, 1.3%, 1.4%, 0.4%, 1.2% and 6.1% respectively for $LiMn_2O_4$ and $LiNi_{0.5}Mn_{1.5}O_4$.

Table 3-2: Calculated and experimental bond length of $LiMn_2O_4$ and $LiNixMn_{2-x}O_4$ structures.

Bond Length				
Systems	Mn-O (Å)	Mn(Ni)-O (Å)	Literature	Experiments
$LiMn_2O_4$	1.967		1.937 [47]	1.940 [224]
$LiNi_{0.25}Mn_{1.75}O_4$		1.947		
$LiNi_{0.5}Mn_{1.5}O_4$		1.940	(a)1.969 [225] (b)1.947 [225]	(a)1.917 [224] (b)2.062 [225]
$LiNi_{1.75}Mn_{1.25}O_4$		1.947		
$LiNi_{0.875}Mn_{1.125}O_4$		1.911		

3.3 Pressure Dependence

3.3.1 Equation of State

The most prominent use of an equation of state is to correlate densities of gases and liquids to temperatures and pressures. One of the simplest equations of state for this purpose is the ideal gas law, which is roughly accurate for weakly polar gases at low pressures and moderate temperatures. However, this equation becomes increasingly inaccurate at higher pressures and lower temperatures and fails to predict condensation from a gas to a liquid. At present, there is no single equation of state that accurately predicts the properties of all substances under all conditions. In addition, there are also equations of state describing solids, including the transition of solids from one crystalline state to another.

Calculations were performed for various pressures ranging from 10GPa to 50GPa in steps of 10. The equation of state (EOS) of all compositions is given in Figure 3.4 shows the GGA-PBE simulation results. Compressibility of all compositions is illustrated by the change in relative volume with pressure. The calculations were considered converged when the residual forces were less than 0.05eV/A, the displacement of atoms during the geometry optimisation steps were less than 0.002A and the residual bulk stress was less than 0.1GPa. The pressure variations of the bond length, volume and normalisation lattice parameters V/V_0, and a/a_0 are computed and displayed in Figures 3-5. They are observed to be decreasing with increasing pressure. The prediction of the volume of a system indicates how accurate the system is being modelled. Presently the are no experimental results to compare with.

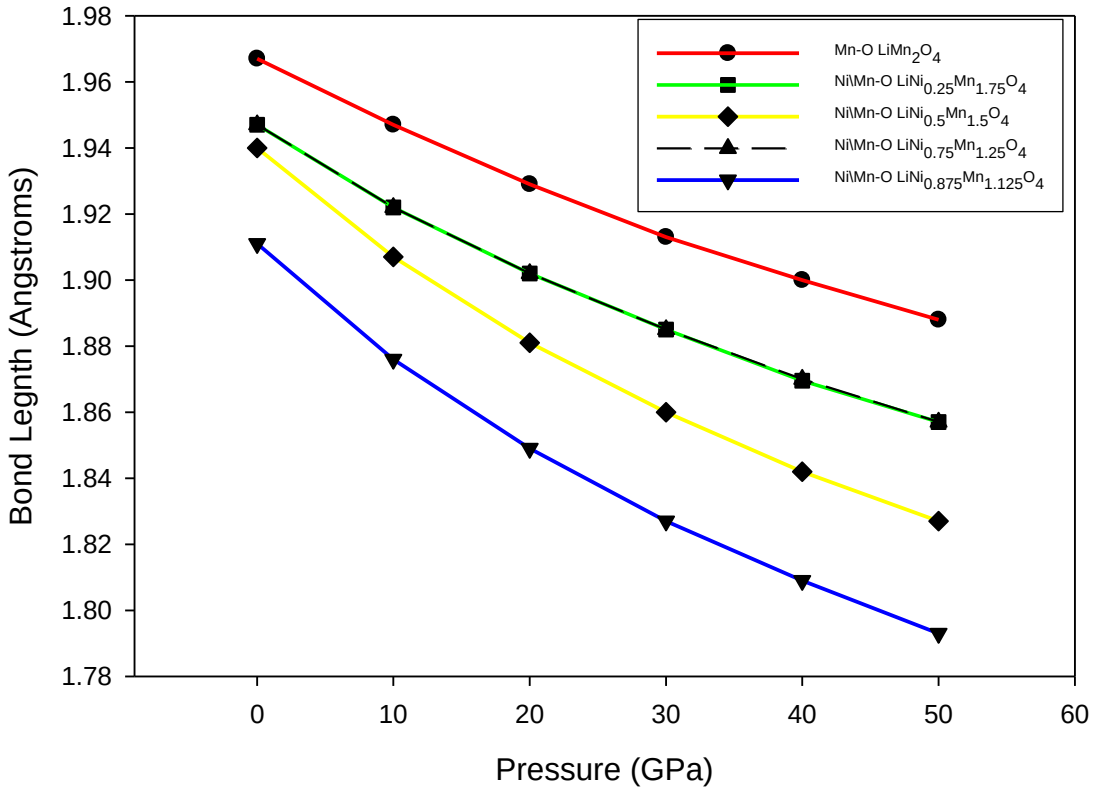

Figure 3-3: The spinel $LiMn_2O_4$ and $LiNi_xMn_{2-x}O_4$ bond length versus pressure graph were a different kind of shapes represents a structure and only $LiNi_{0.25}Mn_{1.75}O_4$ and $LiNi_{0.75}Mn_{1.25}O_4$ have the same shape.

The different compositions are represented by different colours (red, green, yellow, blue and black). All four graphs follow the same trend and two graphs of

$LiNi_{0.25}Mn_{1.75}O_4$ (green) and $LiNi_{0.75}Mn_{1.25}O_4$ (blue) follow the same decrease point to point. The graph with the $LiNi_{0.5}Mn_{1.5}O_4$ (yellow) colour nearly has the same starting point at 1.94 $Å^3$ and blue and green is 1.942 $Å^3$. Then starts decreasing in volume with increasing pressure. The graphs depict a volume decrease with increasing pressure. The graph also indicates that the bond length of the structures would go through changes due to transformation because of pressure.

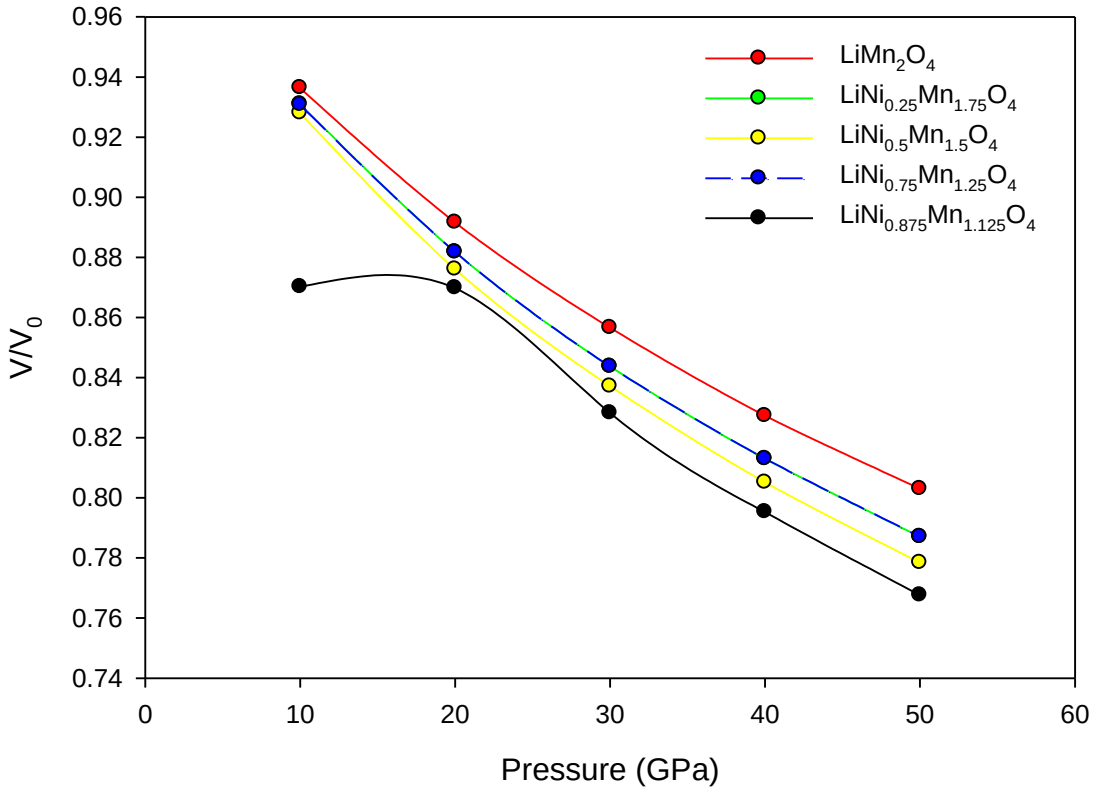

Figure 3-4: The calculated equation of states for $LiMn_2O_4$ (red), $LiNi_{0.25}Mn_{1.75}O_4$ (green), $LiNi_{0.5}Mn_{1.5}O_4$ (yellow), $LiNi_{1.75}Mn_{1.25}O_4$ (blue) and $LiNi_{0.875}Mn_{1.125}O_4$ (black). The circles represent the calculated values and the solid lines represent the curve fit.

The different compositions are represented by different colours (red, green, yellow, blue and black). The first four graphs follow the same trend and differ slightly ranging between 0.94 and 0.92Å. $LiNi_{0.875}Mn_{1.125}O_4$ shows a slight constant movement between 10 and 20 GPa and with a volume of 0.86 Å, then starts decreasing in volume with increasing pressure. The graphs depict a volume decrease with increasing pressure. The graph also indicates that the shape of the structure would go through changes due to transformation because of pressure.

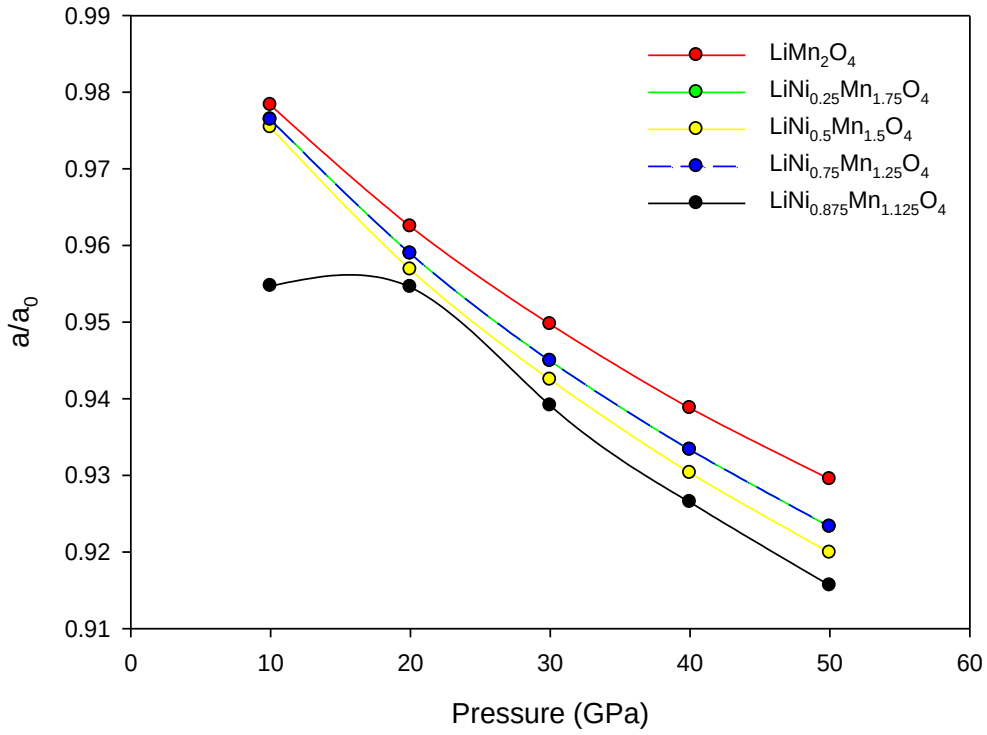

Figure 3-5: The calculated equation of states for $LiMn_2O_4$ (red), $LiNi_{0.25}Mn_{1.75}O_4$ (green), $LiNi_{0.5}Mn_{1.5}O_4$ (yellow), $LiNi_{1.75}Mn_{1.25}O_4$ (blue) and $LiNi_{0.875}Mn_{1.125}O_4$ (black). The circles represent the calculated values and the solid lines represent the curve fit.

The different compositions are represented by different colours (red, green, yellow, blue, and black). The five graphs follow the same trend with a slight difference with respect to the nickel concentration. The $LiNi_{0.875}Mn_{1.125}O_4$ indicates the start of a drastic decrease from 20GPa and a volume of 0.95Å. The lower values of pressure correspond to the high values of the lattice parameters and the increase in the nickel concentration corresponds to the decrease in the lattice parameters as shown in Figure 3-5.

Chapter 4

Electronic and Mechanical Properties

The density of states describes the number of different states at a particular energy level that electrons are allowed to occupy. It allows one to determine the general distribution of states as a function of energy, stability of the material and can also evaluate the nature of the material. In this chapter, we discuss electronic properties, i.e., calculated total density states and partial density states of spinel $LiMn_2O_4$ and doped $LiNi_xMn_2O_4$ where x= 0.25, 0.5, 0.75 and 0.875. Firstly, in this chapter; the spinel $LiMn_2O_4$ and doped $LiNi_xMn_2O_4$ DOS/PDOS shows that the states are distinguished into two patterns; the valence band and the conduction band. Although aspects of pseudo and band gaps are necessary to stability, where the shift of the E_f Fermi with respect to the gaps plays an essential role in verifying stability and change of coordination within the system. We note that the total and partial DOS in this chapter show no opening (pseudogap or band gap) near the Fermi level (E_f).

We also discuss the mechanical properties of spinel $LiMn_2O_4$ and doped $LiNi_xMn_2O_4$ where x= 0.25, 0.5, 0.75 and 0.875. We also determine the effect of pressure (10 and 50GPa) on mechanical properties of structures under study. Furthermore, the bulk modulus *B* is calculated to measure the resistance of volume change under pressure, while shear modulus *G* describing the resistance to shape change caused by shearing force and the elastic anisotropy *A*.

4.1 Electronic Properties

It has been indicated, that the electronic structure of $LiMn_2O_4$ is governed by a strong hybridisation between the Mn-*d* and the O-*p* states whereas the lithium atoms are substantially ionised in the spinel structure. The spinel $LiMn_2O_4$ has an equal number of Mn^{3+} and Mn^{4+} ions which are anti-ferromagnetically aligned. The electronic properties help in understanding the classification of the material under three main phases, i.e., metals, semiconductors and insulators. The type of

materials is determined by the size and existence of the energy gap between the highest occupied orbitals (valence band) and the lowest unoccupied orbitals (conduction band). A high density of states DOS at a specific energy level means that there are many states available for occupation and a zero DOS means that no states can be occupied at the energy level. In semiconductors and insulators, the gap is present, which happens to be larger for insulators. In metals, the occupied and unoccupied orbitals overlap, therefore no gap between the bands is noted.

The relation between structural stability and the behaviour of the electronic density of states near the Fermi energy can be formalised by a Jones-type analysis [226] Structural instabilities in metals are typically related to details of the Fermi surface. A Jones-type analysis then states that the structural energy difference between any two lattices at the same atomic volume is given by:

$$\Delta U = \Delta U_{band} = \Delta \left[\int^{E_f} En(E) dE \right] \tag{89}$$

where $n(E)$ is the electronic density of state per atom, E_f is the Fermi energy and when the number of states per unit energy range $n(E)$ is known, we can obtain the Fermi energy immediately as a function of the number of electrons per atom. The difference in the band energyΔU_{band}, is calculated under the constraint that the potential within the Wigner-Seitz (WS) spheres remain unchanged on going from one structure-type to another. The band energy difference equation allows us to perform a Jones-type analysis that links the relative stability of the two structures to the relative behaviour of the corresponding DOS. This link results from the relationship between the Fermi energy, E_f and the number of valence electrons. Band gaps are essentially left over ranges of energy not covered by any band, a result of the finite widths of the energy bands. The bands have different widths, with the widths depending upon the degree of overlap in the atomic orbitals from which they arise. Two adjacent bands may simply not be wide enough to fully cover the range of energy. For example, the bands associated with core orbitals (such as 1s electrons) are extremely narrow due to the small overlap between adjacent atoms. As a result, there tend to be large band gaps between the core bands. Higher bands

involve larger and larger orbitals with more overlap, becoming progressively wider and wider at high energy so that there are no band gaps at high energy.

From the DOS, we can deduce the nature of the compositions and predict the stability or instability of the systems. In the next sections, we present the results of the calculated DOS of nickel doped spinel $LiNi_xMn_{2-x}O_4$ (x= 0.25, 0.5 and 0.875) which will give us more information on the studied compositions.

This section discusses the partial density of states (PDOS) for pure and doped spinel structures. PDOS gives the atomic contribution of an element. Considering the projections over atomic orbitals, the sequence of the peaks appearing from the valence band to the conduction band can be interpreted as discussed below.

The total DOS of pure and doped spinel is the contribution of Li, Mn_{2-x}, Ni_x and O_4; hence it is important to understand the way electrons are allocated for individual atoms in the systems. The band structure is a good way to visualise the wave vector-dependence of the energy states, the band-gap, and the possible electronic transitions. The actual transition probability depends on how many states are available in both the initial and final energies. For the $LiMn_2O_4$ system, the first peak in the valence band corresponds to d-orbital and there are no maximum peaks in the conduction band. Lithium shows s-orbital it is dominated by d-orbitals in the low energy band and a small contribution of the d-orbital in the high energy band for all the compositions. For all compositions at approximately -2eV a contribution of d-orbital is shown. Hence all the compositions appear to be metallic at 0GPa.

In this section, we discuss TDOS and PDOS for an un-doped system $LiMn_2O_4$ that is shown in Figure 4-1. For the TDOS three peaks are distinguishable in the valence band at -6, -4 and a broad peak at -2 eV (labelled I-III) whereas the fourth peak is at the Fermi-level (0eV) and labelled IV. The contributions from the Li-2s in the valence band corresponds to peaks in the TDOS. The peaks between -6 and -1 eV originate from the 3p orbitals of the oxygen PDOS and are dominated by three broad peaks, corresponding to peaks I, II and III in the TDOS. There is also a small 3s state in the valence band contribution between -7 and -5 eV. The Mn PDOS shows

a very small valence band contribution concentrated between -6 and -2 eV which consists mainly of 2s and 3p states, followed by a moderate contribution between -6 and -2 eV which consist of 3d states. The O PDOS displays most of the peaks in the TDOS which are a result of the O 2p states. The sharply increasing Peak IV is dominated by 3d states of Mn atoms, with some contribution from 3p states of O atoms and little contributions from the 2s states of Li atoms. The shallow peaks in the conduction band and the sharp peaks in the valence band consist of states derived from a mixture of Mn 3d and O 2p. Moreover, the figure shows that the system is metallic because there is no pseudo-gap or bandgap at the Fermi-level.

The calculated total and partial electronic density of states (TDOS/PDOS), shown in Figure 4-2, indicate that the low nickel concentration in the $LiNi_{0.25}Mn_{1.25}O_4$ does not affect significant changes. As a result, the (TDOS and PDOS) has a similar outcome as that of undoped $LiMn_2O_4$.The calculated TDOS and PDOS of $LiNi_{0.25}Mn_{1.75}O_4$ shows four peaks which are distinguishable in the valence band at -6, -4, -2 and another apex at the Fermi level 0 eV (labelled I-IV). The Li PDOS is dominated by 2s states with peaks at -6, -4 and 0 eV in the valence band, corresponding to peaks in the TDOS. The O PDOS is dominated by 3p states with three broad peaks between -6 and -2 eV, corresponding to peaks I, II and III in the TDOS and a small peak at the Fermi-level. The Ni/Mn PDOS shows little contribution in the valence band between -6 and -2 eV which consists mainly of 2s and 3p states, then a small contribution between -6 and -2 eV which consist of 3d states. The O PDOS displays most of the peaks in the TDOS with considerable contributions from the 3d states of the Mn atoms. Peak II is O 2p in nature, with peak II and III also mainly O 2p. Peak IV at the Fermi-level is mostly Ni/Mn 3d with some Li 2s and O 3p states. Hence it is important to note that the contribution of Mn 3d is approximately 90% at the Fermi level. In conclusion, the TDOS/PDOS of $LiNi_{0.25}Mn_{1.25}O_4$ shows no indication of a pseudo-gap or bandgap at the Fermi-level, indicating the structure as metallic.

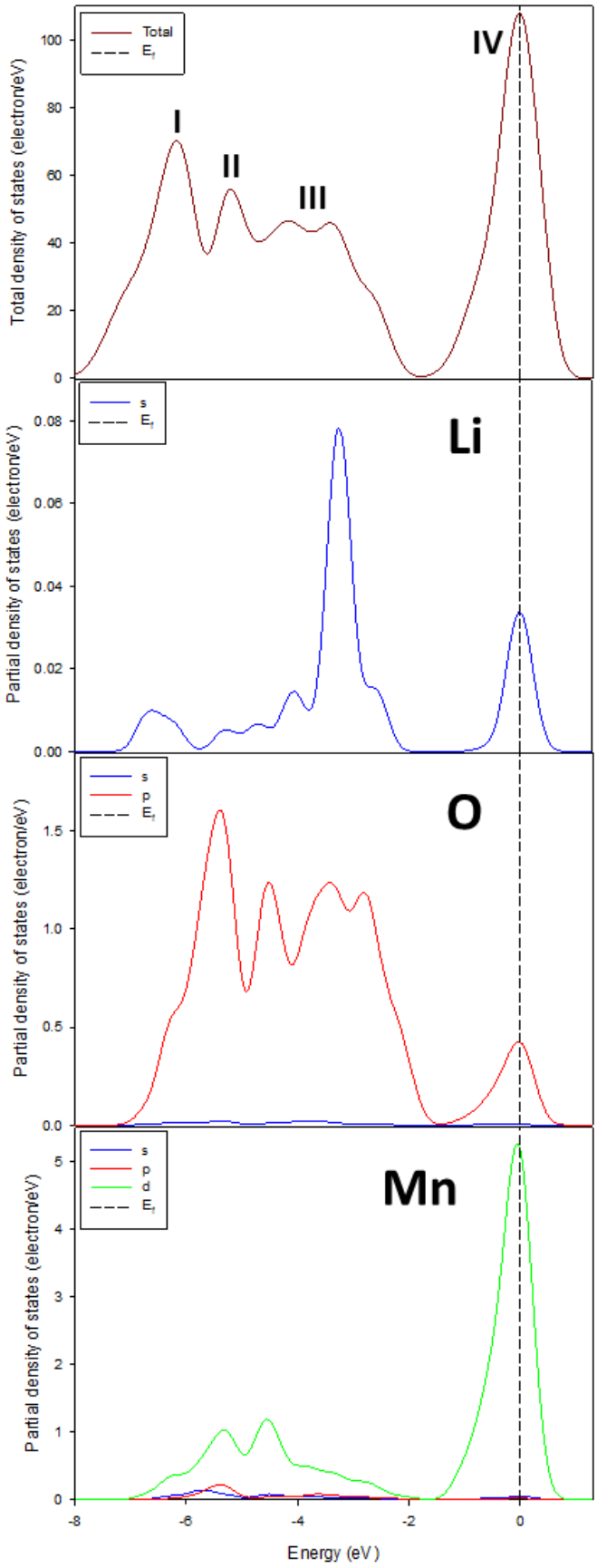

Figure 4-1: Partial density of states (PDOS) at 0GPa, showing Li, Mn and O contributions for $LiMn_2O_4$ structure. The Fermi energy is set as the energy zero (E_f).

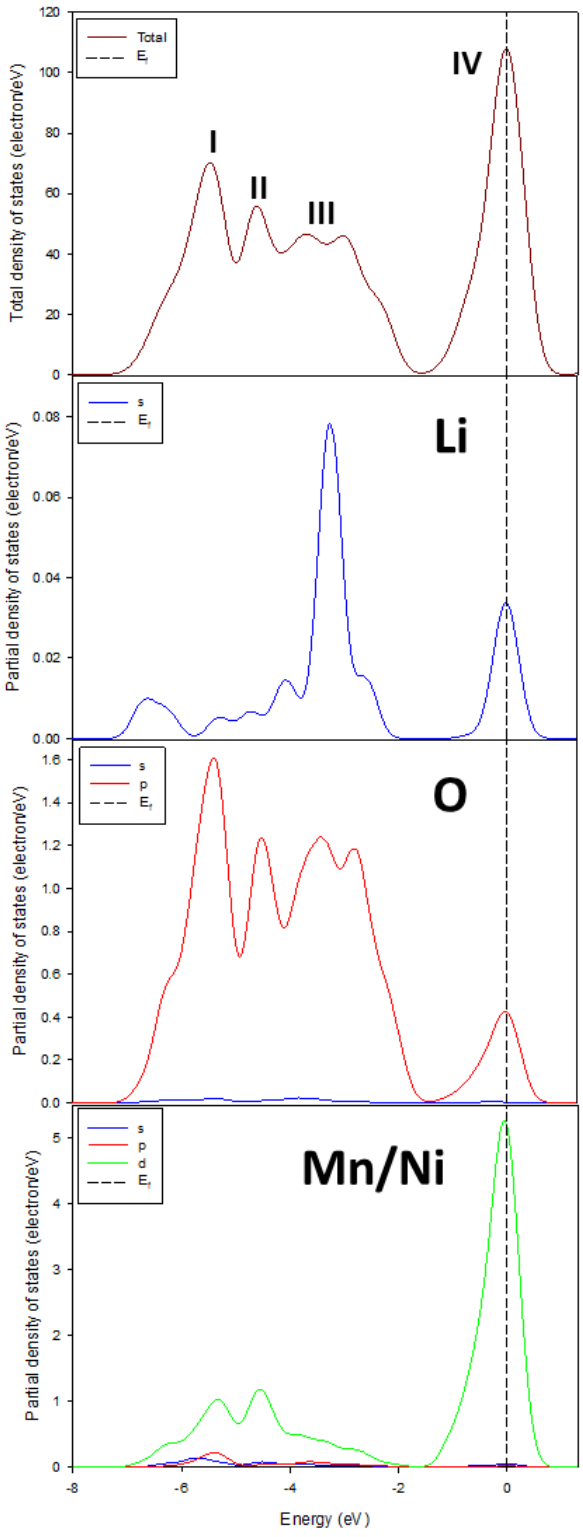

Figure 4-2: Partial density of states at 0 GPa, depicting Li, Mn, Ni and O contributions for $LiNi_{0.25}Mn_{1.75}O_4$. The Fermi energy is set as the energy at zero (E_f).

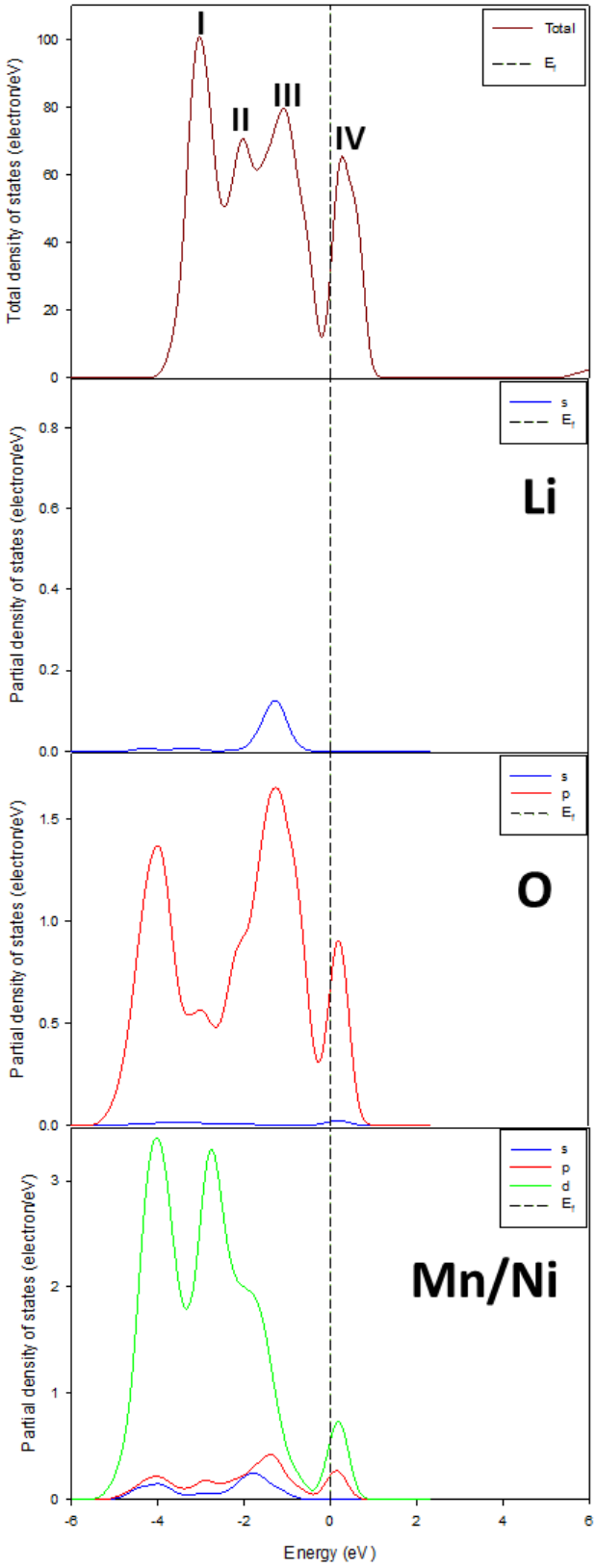

Figure 4-3: Partial density of states (PDOS) at 0GPa, showing Li, Mn, Ni and O contributions for $LiNi_{0.5}Mn_{1.5}O_4$ structure. The Fermi energy is set as the energy at zero (E_f).

The calculated total and partial electronic density of states (DOS/PDOS) for $LiNi_{0.5}Mn_{1.5}O_4$ are shown in Figure 4-3. Three peaks are distinguishable in the valence band at -4, -2 and -1 (labelled I-III). The Li PDOS is dominated by 2s states with peaks between -2 and 0 eV in the valence band, corresponding to peak III in the TDOS. The O PDOS is dominated by 3p states with three broad peaks between -6 and -2 eV, corresponding to peaks I, II and IV in the TDOS and a small peak at the Fermi-level. There are also little contributions of Li 2s in the valence band. The Ni/Mn PDOS shows little contributions between -6 and -2 eV in the valence band which consists mainly of 2s and 3p states, then sharp peaks contribution between -5 and 0 eV with a contribution of the 3d states. The O PDOS displayed most of the peaks in the TDOS by the 3d state. The electronic states of peak IV at the Fermi level is a result of the contribution of Mn-3d, Ni-3d and O-2p states. Therefore, the Figure 4-3 shows that the system is metallic at 0GPa and the Fermi level has shifted closer to the pseudo-gap as compared to that of $LiNi_{0.25}Mn_{1.75}O_4$.

The calculated total and partial density of states (DOS/PDOS) for $LiNi_{0.75}Mn_{1.25}O_4$ are shown in Figure 4-4. For this system, two peaks are distinguishable in the valence band at -4 and -1 eV and the other cutting at 0 eV (labelled I-III). The Li PDOS is dominated by 2s states with peaks between -3 and -1 eV and the other peak cutting at the Fermi level overlapping to the conduction band from the valence band. The O PDOS is dominated by 3p states with two broad peaks between -4 and -1 eV, corresponding to peaks I and II in the TDOS and a another at the 0 eV (Fermi-level) corresponding to peak III in the TDOS. There is also the minimum contribution of Li 2s in the valence band. The Mn/Ni PDOS shows very small peaks in the valence band contribution concentrated between -4, -2 and 0 eV which consists mainly of 2s and 3p states, then a broad peak contribution between -4 and -1 eV which consist of 3d states. The O PDOS displays most of the peaks in the valence band of the DOS. Peak III at the Fermi-level is mostly Ni/Mn 3d with some Li 2s and O 3p states. In comparison to all the other figures, there is a shift of the peaks from the valence band to conduction band due to the increase of the nickel concentration.

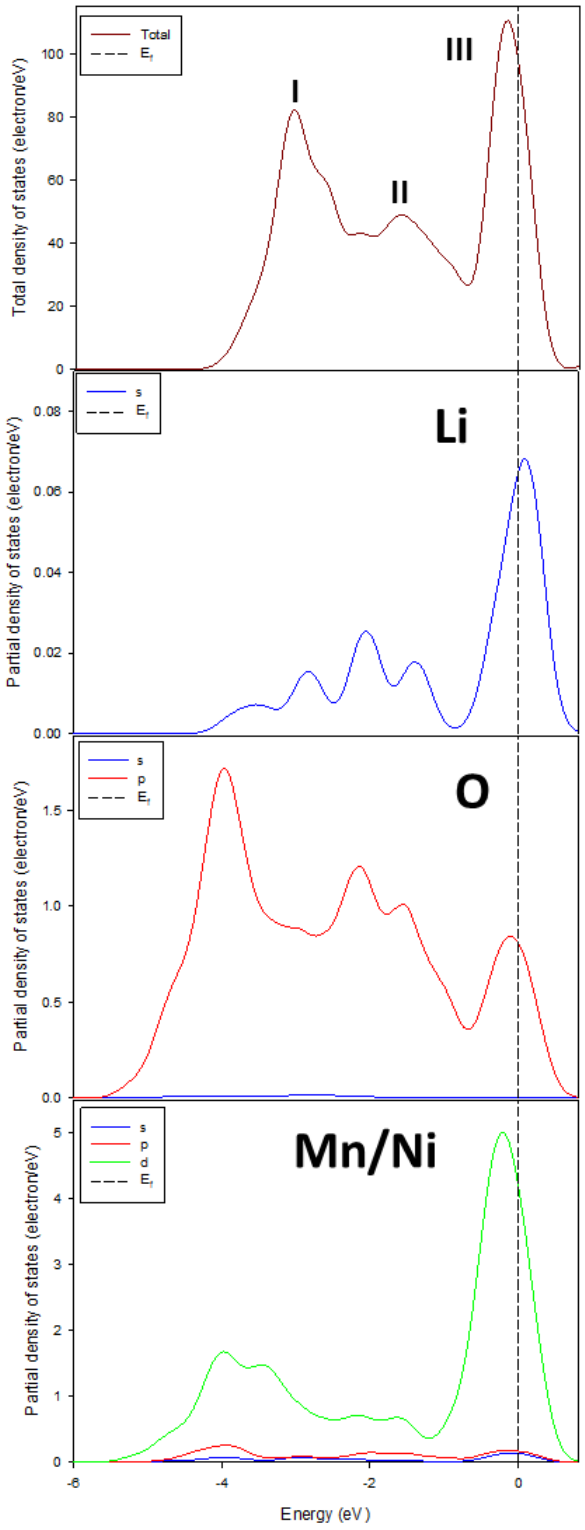

Figure 4-4: Partial density of states (PDOS) at 0GPa, depicting Li, Mn, Ni and O contribution for $LiNi_{0.75}Mn_{1.25}O_4$. The Fermi energy is set as the energy zero (E_f).

Although $LiNi_{0.75}Mn_{1.25}O_4$ concentrations gave the same results in terms of energy and lattice parameters as $LiNi_{0.25}Mn_{1.75}O_4$, their density of states graphs is different.

There is a slight difference in terms of the peak positions since the Fermi level intersects the TDOS for $LiNi_{0.75}Mn_{1.25}O_4$ on the right, and closer to the top of the main peak. This shows that the system is metallic at 0GPa and relatively unstable compared to $LiNi_{0.5}Mn_{1.5}O_4$ since the pseudo-gap.

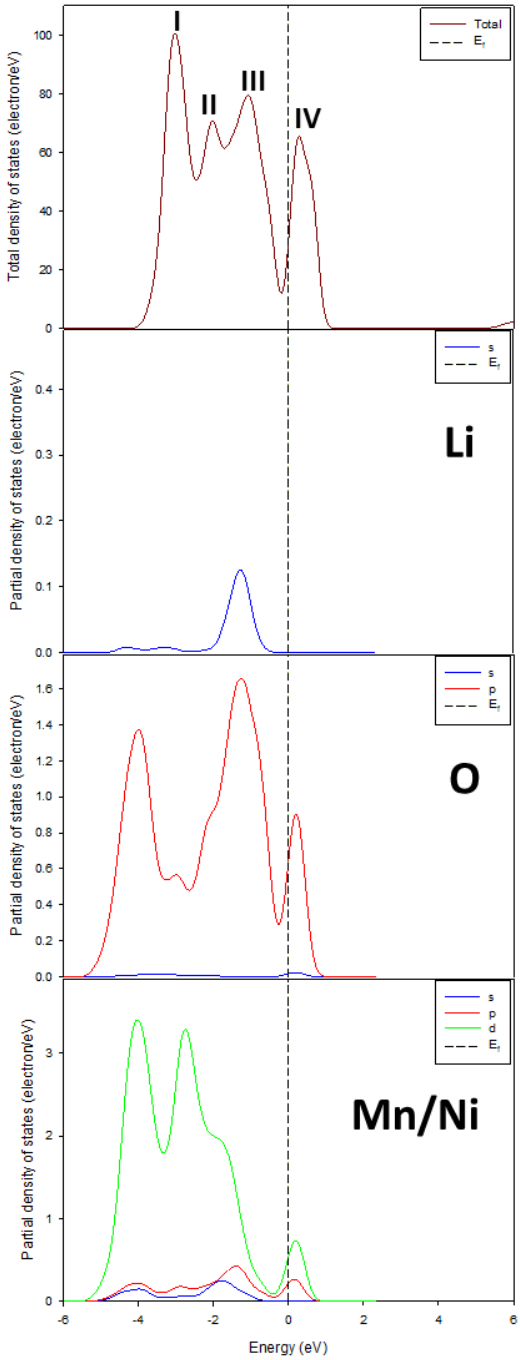

Figure 4-5: Partial density of states (PDOS) at 0GPa, showing Li, Mn, Ni and O contributions for $LiNi_{0.875}Mn_{1.125}O_4$ structure. The Fermi energy is set as the energy zero (E_f).

The calculated total and partial density of states (DOS/PDOS) for $LiNi_{0.875}Mn_{1.125}O_4$ are shown in Figure 4-5. Three peaks are distinguishable in the valence band at -4, -2, -1 eV (labelled I-III) and one peak cutting at 0 eV Fermi-level (labelled IV). The conduction band displays a peak between 0 and +2 eV labelled IV. The Li PDOS is dominated by 2s states with a peak positioned at -1 eV in the valence band, corresponding to the peak III in the TDOS. The O PDOS is dominated by 3p states with two peaks at -4 and -1 eV, corresponding to peaks in the TDOS and a peak overlapping at the Fermi-level. There are also minimum contributions of Li 2s in the conduction band. The Ni/Mn PDOS shows a small contribution in the valence band concentrated between -4, -3, -2, and -1 eV which consists mainly of 2s and 3p states, then two peaks contribution between -4 and -2 eV which consist of 3d states. The majority of the peaks of O and Ni/Mn PDOS are shown in the TDOS. Small peaks corresponding to IV at the Fermi-level is mostly Ni/Mn 3d with some Li 2s and O 3p states concentration. The bottom of the conduction band and the top of the valence band both consist of states derived from mixtures of Mn 3d and O 2p. As it has been observed in other concentrations, 0GPa shows no availability of a pseudo-gap or bandgap at, the Fermi-level.

In this section, we discuss DOS and PDOS for the three systems ($LiMn_2O_4$, $LiNi_{0.5}Mn_{1.5}O_4$ and $LiNi_{0.875}Mn_{1.125}O_4$) at a pressure of 10 GPa and 50GPa. The calculated total and partial electronic density of states (DOS/PDOS) for $LiMn_2O_4$ at 10GPa are shown in Figure 4-6. Four peaks are distinguishable in the valence band at -6, -5, and 4 and between 1 and 0 eV which is very close to Fermi level (labelled I-IV). The Li PDOS is dominated by 2s states with peaks at -3, and 0 eV in the valence band, corresponding to peak III in the TDOS. The Mn PDOS shows a very broad peak in the valence band contribution concentrated between -6 and -2 eV which consists mainly of 2s and 3p states, then followed by a peak contribution at 0 eV which consist of 3d states corresponding to peak VI in the TDOS. The O PDOS is dominated by 3p states with three peaks between -6 and -2 eV, corresponding to peaks I, II and III in the TDOS. The O PDOS displays most of the peaks in the TDOS. Peak II is O-2p in nature, with peak III and IV also mainly O-2p. The peak at the Fermi-level (0eV) in the O-2p has a short peak and that could be an indication of the type of impact oxygen is having in the system.

4.1.1 Partial Density of States

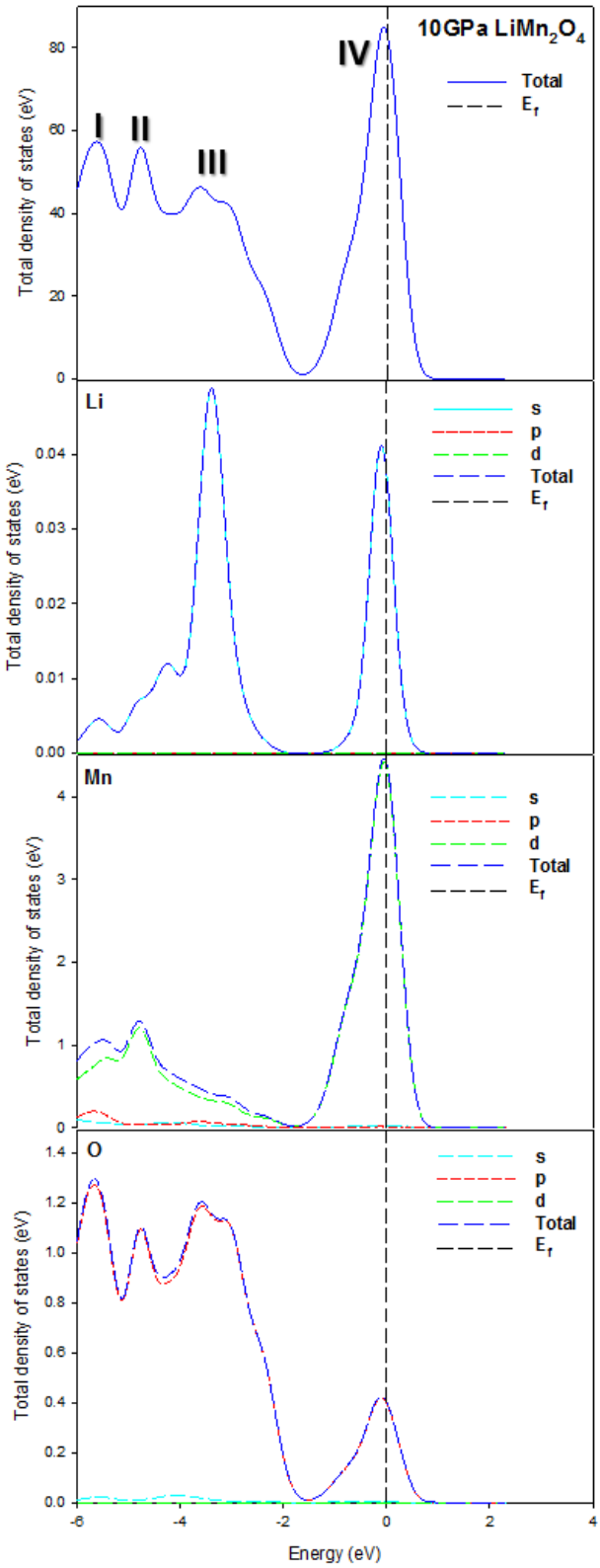

Figure 4-6: Partial density of states (PDOS) at 10 GPa, showing Li, Mn, Ni and O contribution for $LiMn_2O_4$ structures and their orbitals (s-cyan, p-red, d-green and total-blue). The Fermi energy is set as the energy at zero (E_f-black).

Peak IV is mostly Mn 3d with some Li 2s and O 3p states. The bottom of the conduction band and the top of the valence band both consist of states derived from mixtures of Mn 3d and O 2p. There is an indication of a slight shift of the peak at the Fermi level and that could be because of pressure added as compared to the system at 0GPa. The total and partial density of states of $LiMn_2O_4$ is shown in Figure 4-6 together with the total density of states (TDOS). The Figure 4-6 shows the total and partial density of states of Li-2s and Mn-3d, which are the nearest neighbours in LiM_2O_4. The shapes of the Li-2s and Mn-3d bands do not differ. Three peaks are distinguishable in the lower energy at -6,-4 and 0 eV (labelled I-III). The Li PDOS is dominated by Li-2s states with peaks at -4, and 0 eV in the lower energy and 0eV corresponding to peak III. The Mn PDOS shows a very broad peak in the lower energy contribution concentrated from -6 and -2 eV which consists mainly of Li-2s, Mn-3d and O-3p states, then followed by a long peak contribution at 0 eV which consist of Mn-3d states corresponding to peak III. The O PDOS is dominated by O-3p states with three peaks between -6 and -2 eV, corresponding to peaks I, II and III in the TDOS. The O-3p PDOS displays most of the peaks. The peak at the Fermi-level (0eV) in the O-2p has a short peak and that could be an indication of the type of impact oxygen is having in the system. Peak III is a contribution of Li-2s and Mn-3d states. The bottom of the higher energy and the top of the lower energy both consist of states derived from mixtures of Li-2s, Mn-3d and O 2p. The slight shift of the peak at the Fermi level at the TDOS to the lower energy could be a result of pressure added as compared to the system at 0GPa.

The total partial density of states of $LiNi_{0.5}Mn_{1.5}O_4$ is shown Figure 4-8 together with the total density of states (TDOS). The shapes of the Li-2s and Mn-3d bands do not differ drastically. Four peaks are distinguishable in the lower energy at -6, -4 and 1 eV (labelled I-III) and one peak in the higher energy between 0 and 2eV (IV) of TDOS The Li PDOS is dominated by Li-2s states with small broad peaks between -4 and -1 in the lower energy. The high peak at 0eV in the Li-2s corresponds to peak III in the TDOS slightly shifting from the Fermi-level. The Mn PDOS shows peaks in the lower energy contribution concentrated between -4 and -2 eV consisting mainly of Li-2s, Mn-3d and O-3p states and make up the peaks (I and II).

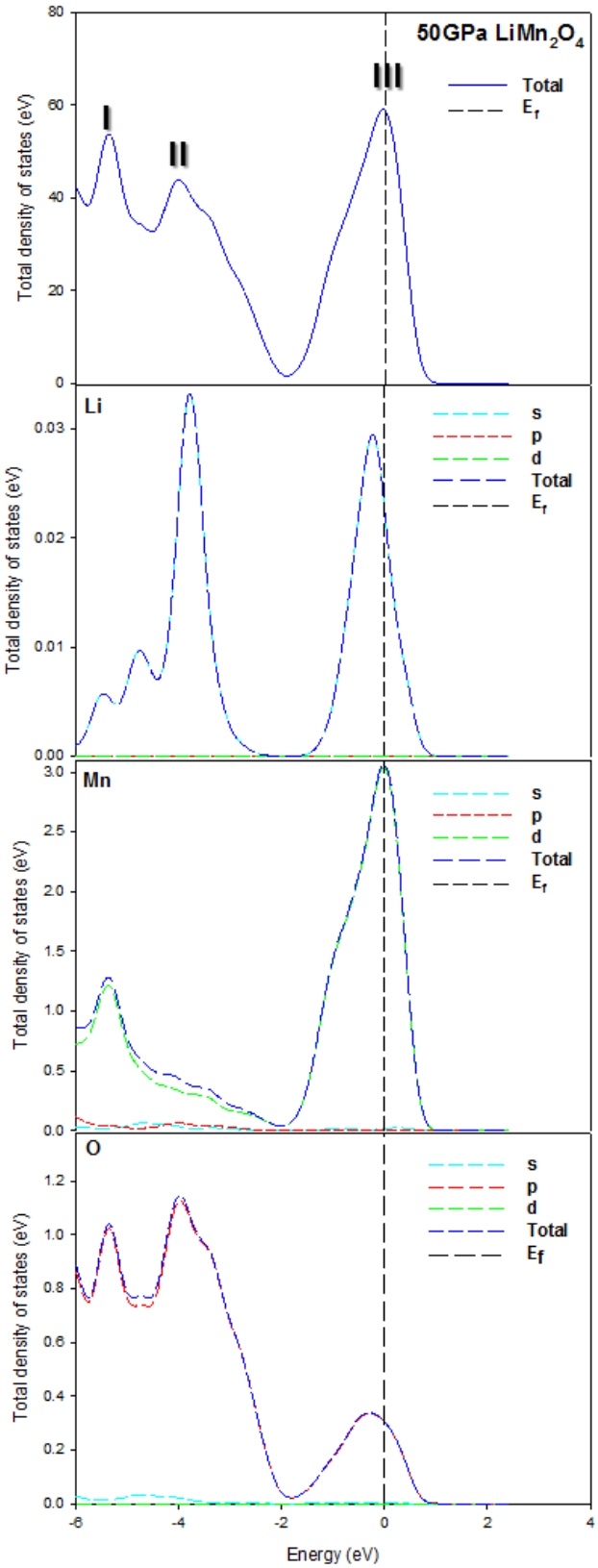

Figure 4-7: Partial density of states (PDOS) at 50 GPa, with Li, Mn, Ni and O contribution for $LiMn_2O_4$ structures and their orbitals (s-cyan, p-red, d-green and total-blue). The Fermi energy is set as the energy at zero (E_f-black).

It is then followed by a high peak contribution at 1 eV which consists of Mn-3d states corresponding to peak III in the TDOS and shifting away from the Fermi level to the lower energy region. One peak of Mn-3d occurs in the higher energy between 0 and 2eV and could be the combination of the increase of pressure and the nickel concentration. The O PDOS is dominated by O-3p states with three peaks between -5 and -3 eV, corresponding to peaks I, II and III in the TDOS. The O-3p PDOS displays most of the peaks in the TDOS. The peak at the Fermi-level (0eV) in the O-2p has an increased peak and shifting slightly from the Fermi level to the lower energy. One peak of O-3p occurs in the higher energy between 0 and 2eV. There is a slight shift of the peak at the Fermi level at the TDOS to the lower energy could be a result of pressure and the nickel concentration added in the system. There is a change with the PDOS and TDOS with the increase in pressure compared to the system at 0GPa.

Figure 4-9 shows the total partial density of states of $LiNi_{0.5}Mn_{1.5}O_4$ together with the total density of states (TDOS). The total partial density of states of Li-2s and Mn-3d is shown in Figure 4-9, which are the nearest neighbours in $LiNi_{0.5}Mn_{1.5}O_4$. The picks of the Li-2s and Mn-3d bands do not differ too much. Three peaks are distinguishable in the valence band at -4,-2 and -1 eV (labelled I-III) and one peak in the conduction band between 0 and 2eV (IV). The Li PDOS is dominated by Li-2s states with small broad peaks between -4 and -1 in the valence band. The highest peak at 0eV in the Li-2s corresponds to peak III which is slightly shifted from the Fermi-level. The Mn PDOS shows peaks in the valence band contribution concentrated between -4 and -2 eV consisting mainly of Li-2s, Mn-3d and O-3p states and make up the peaks (I and II). It is then followed by a high peak contribution at -1 eV which cuts at the Fermi-level and corresponds to peak III. The peak shifts away from the Fermi level to the valence band. One peak of Mn-3d occurs in the conduction band between 0 and 2eV and could be the combination of the increase of pressure and the nickel concentration. The O PDOS is dominated by O-3p states with three peaks between -5 and -3 eV, corresponding to peaks I, II and III in the TDOS. The O-3p PDOS displays most of the peaks in the TDOS.

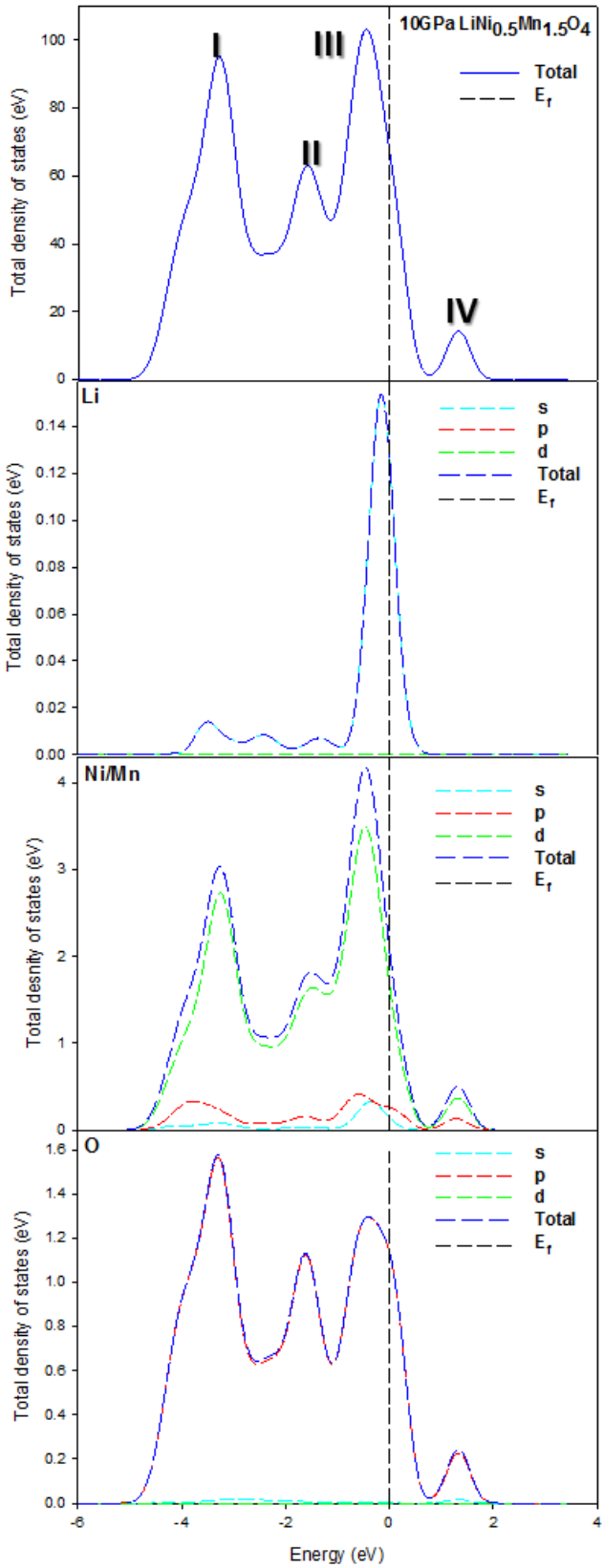

Figure 4-8: Partial density of states (PDOS) at 10 GPa, with Li, Mn, Ni and O contribution for $LiNi_{0.5}Mn_{1.5}O_4$ structure and their orbitals (s-cyan, p-red, d-green and total-blue). The Fermi energy is set as the energy at zero (E_f-black).

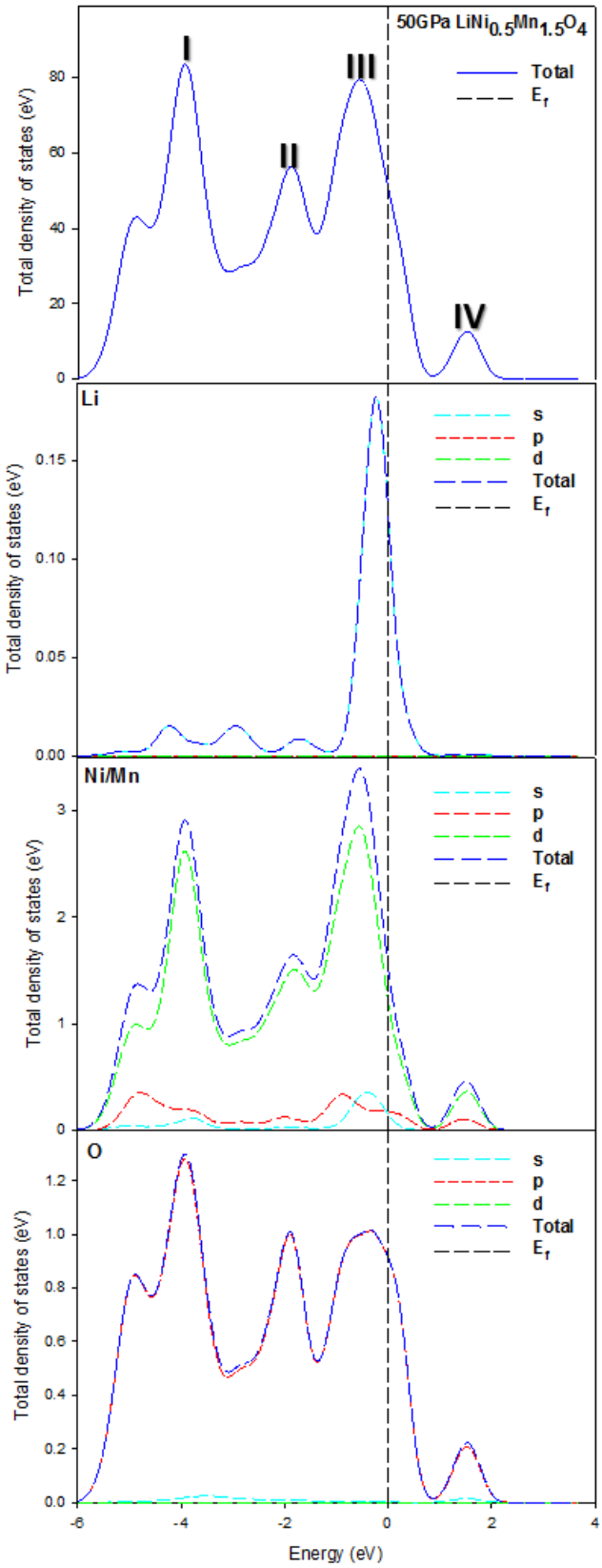

Figure 4-9: Partial density of states (PDOS) at 50 GPa, showing Li, Mn, Ni and O contribution for $LiNi_{0.5}Mn_{1.5}O_4$ structure and their orbitals (s-cyan, p-red, d-green and total-blue). The Fermi energy is set as the energy at zero (E_f-black).

The peak at the Fermi-level (0eV) in the O-2p has an increased peak and shifting slightly from the Fermi level to the lower energy. One peak of O-3p occurs in the higher energy between 0 and 2eV. There is a slight shift of the peak (III) at the Fermi level at the TDOS to the lower energy could be a result of pressure and the nickel concentration added in the system. There is no change with the PDOS and TDOS regardless of the increase in pressure as compared to 40GPa $LiNi_{0.5}Mn_{1.5}O_4$.

The total density of states (TDOS) and partial density of states of $LiNi_{0.875}Mn_{1.125}O_4$ are shown in Figure 4-10. Three peaks are distinguishable in the lower energy at -6, -4, -2 and one between 0 and 2eV (labelled I-IV). The Li PDOS is dominated by Li-2s states with small broad peaks between -6 and -4 in the lower energy. The highest peak is at -2eV in the Li-2s which has shifted drastically from the Fermi-level to the lower energy as the pressure increases and nickel concentration as compared to 40GPa $LiNi_{0.875}Mn_{1.125}O_4$. The Mn PDOS shows three (3) peaks in the lower energy contribution concentrated from -6, -4 and -2 eV consisting mainly of Li-2s, Mn-3d and O-3p states and make up the peaks (I and III). It is then followed by a small peak contribution in the high energy which consists of Mn-3d states corresponding to peak IV in the TDOS. The O PDOS is dominated by O-3p states with three peaks at -6 and -2 eV, corresponding to peaks I, II and IV in the TDOS. The peak in the O-2p is dissecting the Fermi level from the high energy. The pressure from 50GPa $LiNi_{0.75}Mn_{1.25}O_4$ to 0-10GPa $LiNi_{0.875}Mn_{1.125}O_4$ has not produced significant results regardless of the different compositions.

Figure 4-11 b is the total partial density of states of $LiNi_{0.875}Mn_{1.125}O_4$ and shows the contribution of each element. Three peaks are distinguishable in the lower energy at -6, -4, -2 and one between 0 and 2eV (labelled I-IV). The Li PDOS is dominated by Li-2s states with two small peaks between -6 and -4 in the lower energy. The highest peak is at -2eV in the Li-2s which is shifting away from the Fermi-level. The Mn PDOS shows three (3) peaks in the lower energy contribution concentrated from -5, -4 and -2 eV consisting mainly of Li-2s, Mn-3d and O-3p states and make up the peaks (I and IV).

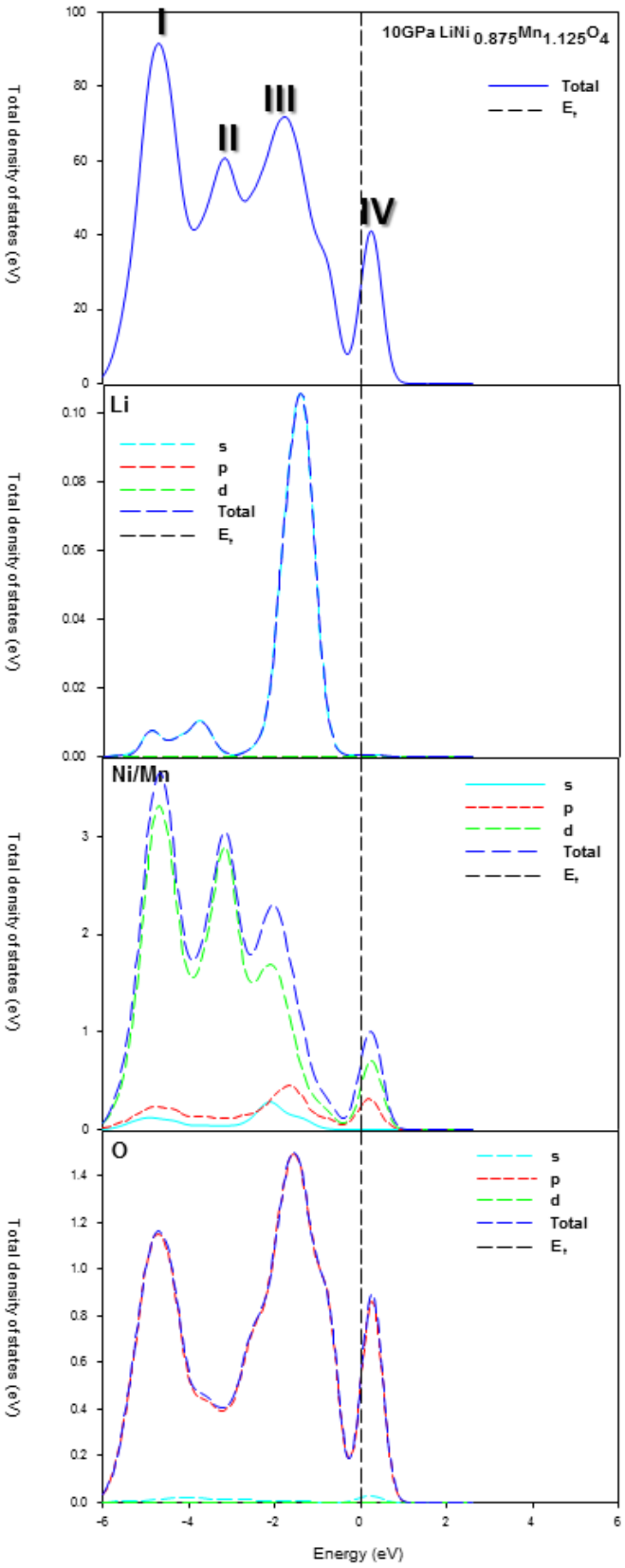

Figure 4-10: Partial density of states (PDOS) at 10 GPa, showing Li, Mn, Ni and O contribution for $LiNi_{0.875}Mn_{1.125}O_4$ structures and their orbitals (s-cyan, p-red, d-green and total-blue). The Fermi energy is set as the energy at zero (E_f-black).

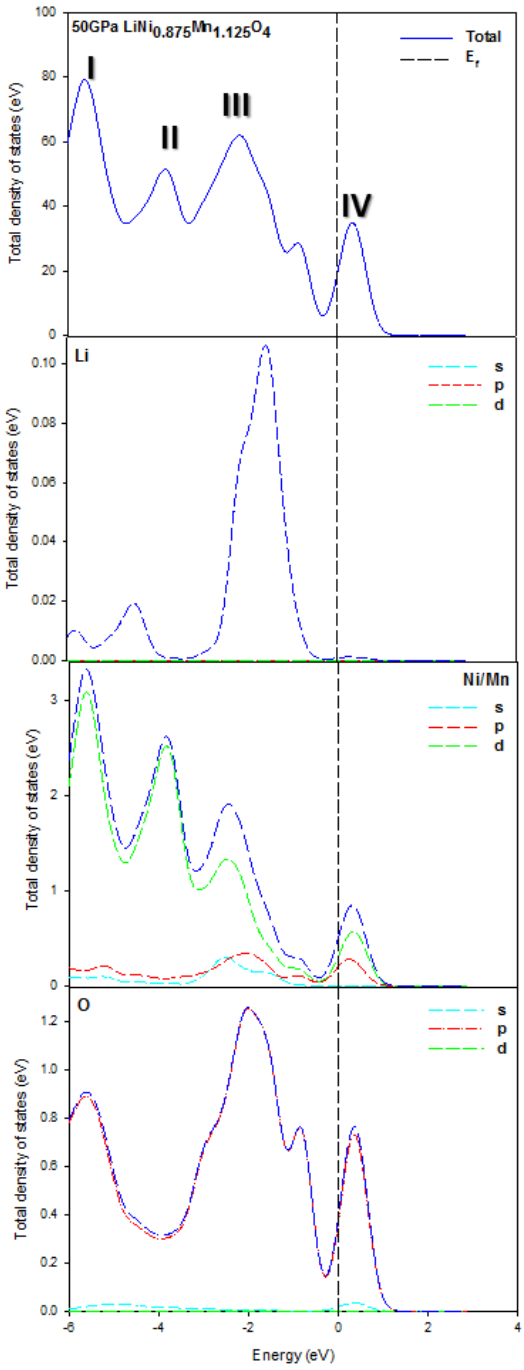

Figure 4-11: Partial density of states (PDOS) at 50 GPa, with Li, Mn, Ni and O contribution for $LiNi_{0.875}Mn_{1.125}O_4$ structures and their orbitals (s-cyan, p-red, d-green and total-blue). The Fermi energy is set as the energy at zero (E_f-black).

It is then followed by a small peak contribution in the high energy which consists of Mn-3d states corresponding to peak IV in the TDOS. The O PDOS is dominated by O-3p states with three peaks at -6 and -2 eV, corresponding to peaks I, II and IV in the TDOS.

The peak in the O-2p is dissecting the Fermi level from the high energy.

4.2 Total Density of States

To better examine the differences in the studied crystal structures, we plot the density of states (DOS) for $LiMn_2O_4$, $LiNi_{0.25}Mn_{1.75}O_4$, $LiNi_{0.5}Mn_{1.5}O_4$, $LiNi_{0.75}Mn_{1.25}O_4$, and $LiNi_{0.875}Mn_{1.125}O_4$ in Figure 4-12. The DOS show the contribution of states from the $LiMn_2O_4$ and nickel doped $LiMn_2O_4$ atoms and these contributions are analysed from the partial density of states. Figure 4-12 gives the total density of states for $LiMn_2O_4$ and nickel doped $LiMn_2O_4$ structures. The DOS is expressed in the number of states per atom per energy interval. In this section, the DOS of $LiMn_2O_4$ and doped $LiNi_xMn_2O_4$ crystal structures were plotted against each other to compare their phase stabilities. Figure 4-12 shows overlapping of peaks (with respect to all the compositions) from the valence band to the conduction band. As a result, the compositions show metallic behaviour since there is no visibility of a bandgap or pseudo-gap. In terms of the stability of the composition's, we focused on the highest peak at the Fermi-level.

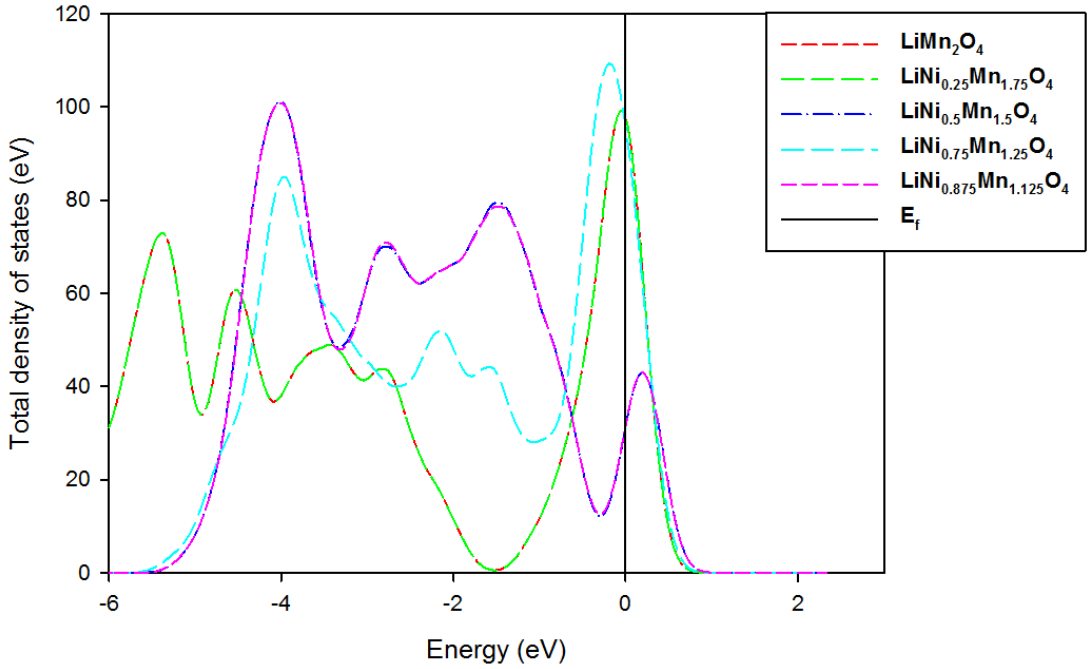

Figure 4-12: Total densities of states for various concentrations at 0 GPa give the total density of states for $LiMn_2O_4$ and doped $LiNi_xMn_{2-x}O_4$ structures. The Fermi energy is set as the energy zero (E_f).

4.2.1 Total Density of States at Different Pressure

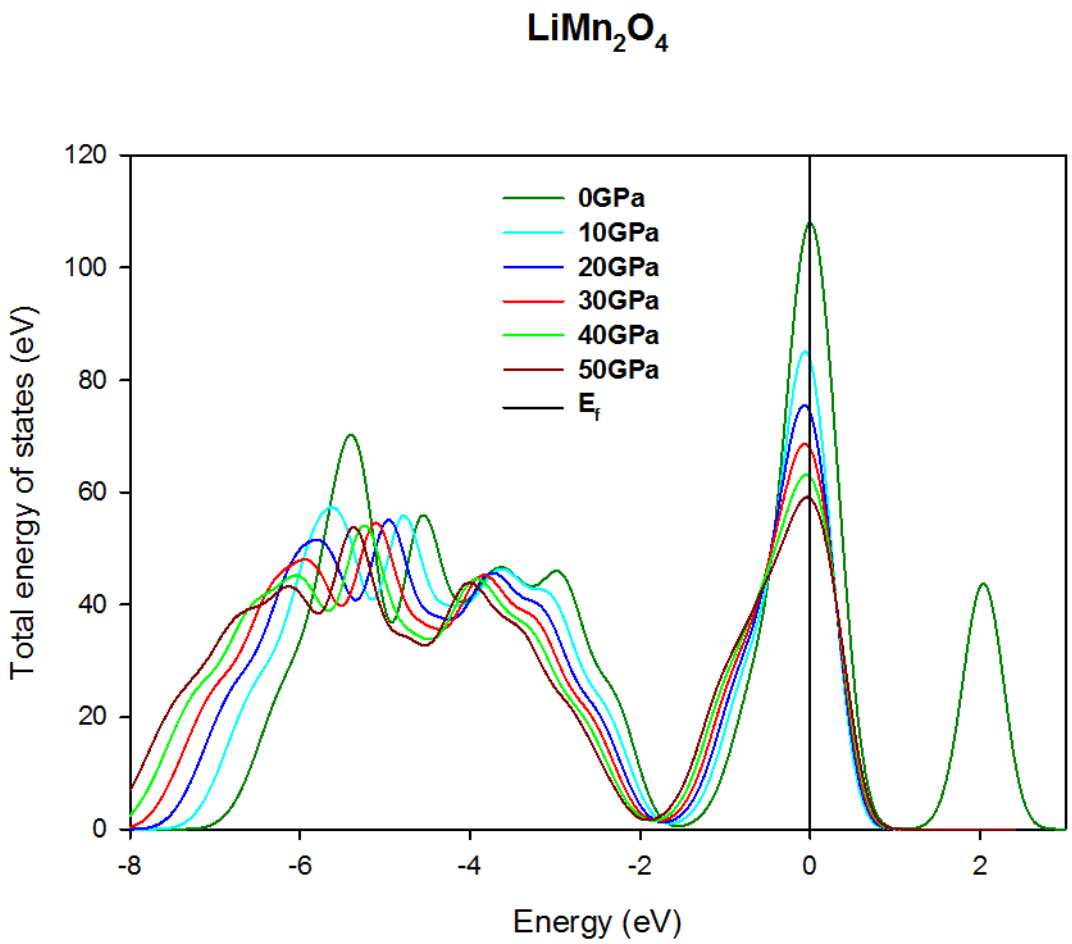

Figure 4-13: Total densities of states of $LiMn_2O_4$ for various pressures values. The 0GPa is represented by dark green, 10GPa light blue, 20GPa dark blue, 30GPa red, 40GPa light green and 50GPa maroon. The Fermi energy is set as the energy zero (E_f).

Figure 4-13 illustrate the behaviour of $LiMn_2O_4$ when subjected to various pressures from 0GPa to 50GPa and the Fermi level. The increase in pressure on $LiMn_2O_4$ shows a decrease in the height of the peaks at the Fermi level. The pressure was increased from 0GPa until 50GPa to see the effect on the structure and the behaviour at the Fermi-level. The 50GPa has the least number of states at the Fermi-level making it more stable at that pressure. The more pressure is increased the less density of states at the Fermi-level and an indication of the peaks shifted away from the Fermi level more to the valence band.

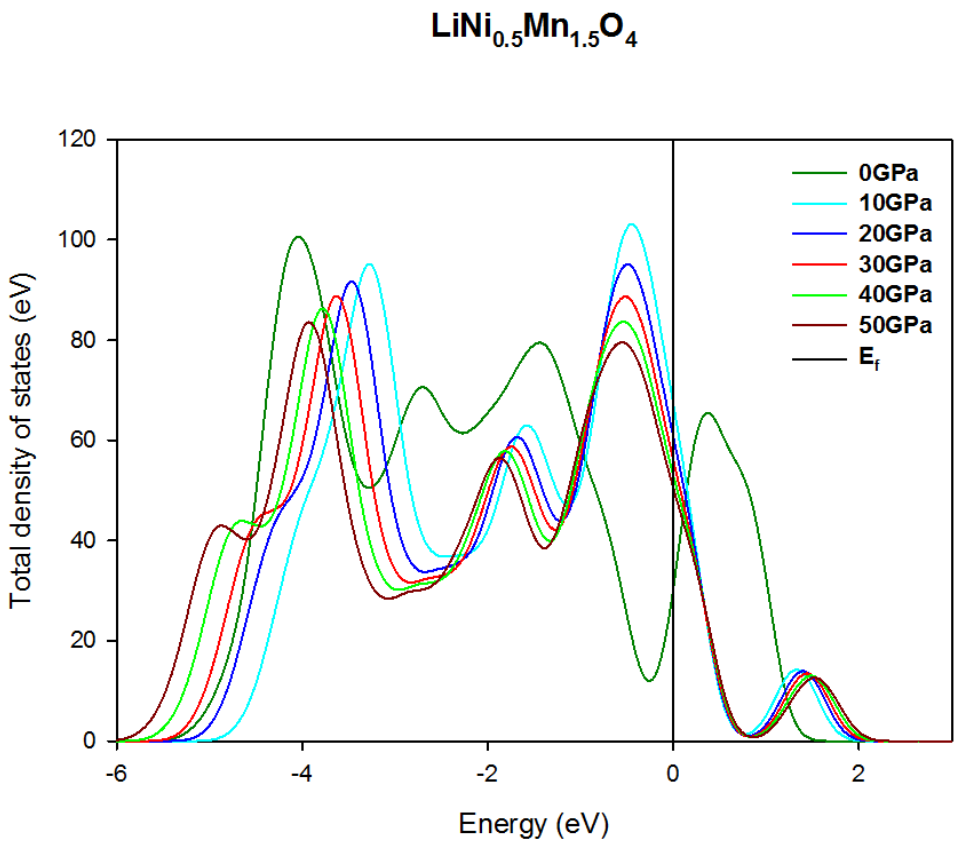

Figure 4-14: Total densities of states of $LiNi_{0.5}Mn_{1.5}O_4$ for various pressures values. The 0GPa is represented by dark green, 10GPa light blue, 20GPa dark blue, 30GPa red, 40GPa light green and 50GPa maroon. The Fermi energy is set as the energy zero (E_f).

The pressure was increased from 0GPa to 50GPa to see the effect on the structure and its behaviour at the Fermi-level. Increasing pressure on our systems decreases the volume of the systems and thus increases its density although the effect on the densities is small. Figure 4-14 shows that apart from the effect of the increase in pressure, the nickel concentration also has an impact as compared to the un-doped $LiMn_2O_4$. Hence the peaks are not at the Fermi level but cut at the Fermi level. The increased pressure produced less density of states we have at the Fermi-level. There is a decreasing trend with the increase in pressure to the system from 10 until 50GPa. Due to the pressure applied to the system the peaks (10GPa, 20GPa 30GPa 40GPa and 50GPa) lie between -2 and 0eV and not at the Fermi-level as compared to the peaks in Figure 4-13.

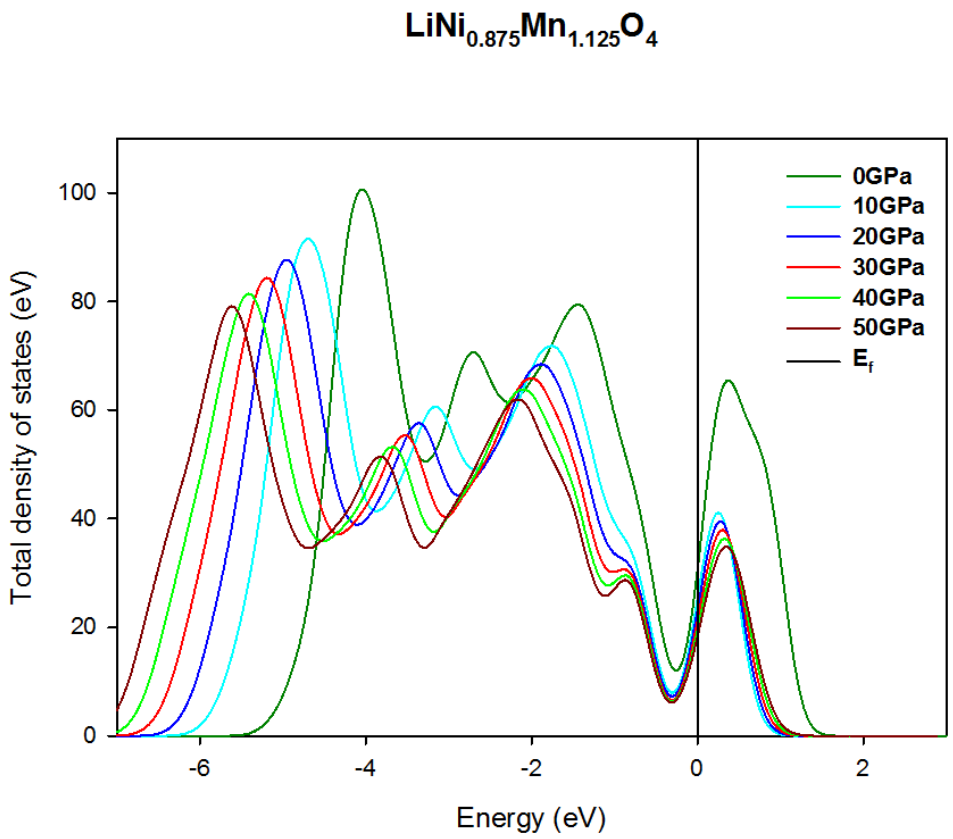

Figure 4-15: Total densities of states of $LiNi_{0.875}Mn_{1.125}O_4$ for various pressures values. The 0GPa is represented by dark green, 10GPa light blue, 20GPa dark blue, 30GPa red, 40GPa light green and 50GPa maroon. The Fermi energy is set as the energy zero (E_f).

Figure 4-15 illustrates the behaviour under the increasing pressure and an increase in a nickel concentration $LiNi_{0.875}Mn_{1.125}O_4$. The pressure was increased from 0GPa until 50GPa to see the effect on our structure and the behaviour at the Fermi-level. Increasing the pressure on our systems decreases the volume of the systems and thus increases its density hence the effect on the densities is small. The more we increase the pressure the less density of states we have at the Fermi-level. There is a decreasing trend with the increase in pressure of the system from 0 until 50GPa. All the peaks cut at the Fermi-level to the valence band moving away from the Fermi-level to the conduction band. All the peaks are present in the conduction band between 0 and +2eV due to the increased nickel concentration together with the increasing pressure.

4.3 Elastic Properties

There are three independent single-crystal elastic constants of a cubic crystal (C_{11}, C_{44} and C_{12}). The elastic moduli are determined using the following expressions: the bulk modulus *B*, shear modulus *G,* young modulus E, anisotropic factor *A*, tetragonal shear modulus, *C'* and the *B/G* ratio. The bulk modulus *B* is a measure of resistance to volume change under pressure, young modulus E describing the relative stiffness of a material, while shear modulus *G* describes the resistance to shape change caused by shearing force; whereas the elastic anisotropy, *A* has an important implication in engineering science. If the material is completely isotropic, the value of A will be 1, while values smaller or larger than 1 measure the degree of elastic anisotropy.

The calculated elastic properties of the following compositions: $LiMn_2O_4$, $LiNi_{0.25}Mn_{1.75}O_4$, $LiNi_{0.5}Mn_{1.5}O_4$, $LiNi_{0.875}Mn_{1.125}O_4$ and $LiNi_{1.75}Mn_{0.25}O_4$ are listed in Table 4-1. It is well known that *B*, *C'* and C_{44} must be positive for a structure to remain mechanically stable. It's a general fact that the larger the shear modulus, the more pronounced its directional bonding between atoms. Apart from *B/G* is significant, it was recently found that the *C'* is also very significant on the mechanical properties of materials [139].

Therefore, the results in Table 4-1 indicate that our structures generally satisfy stability conditions of a cubic crystal at 0GPa and an increase in the nickel concentration does not implicate negative values of the bulk modulus, shear modulus and tetragonal shear modulus. The bulk modulus *B* is in reasonable agreement with previously calculated value. The calculated values of *A* show that our structure is approaching unity ($A \approx 1$) which indicates that the structure becomes isotropic.

The stability against small deformations can be studied by considering the elastic properties and the calculated elastic properties of $LiMn_2O_4$ at various pressures are listed in Table 4-2. It has been recently found that the *C'* is also very significant on the mechanical properties of materials [227].

Table 4-1: The elastic constants with calculated C_{11}, C_{44} and C_{12} (GPa), Bulk modulus *B,* Young modulus E, Shear modulus *G, B/G,* Anisotropy *A* and tetragonal shear modulus *C'* of $LiMn_2O_4$ at 0 GPa with a strain of 0.002.

	$LiMn_2O_4$	$LiNi_{0.25}Mn_{1.75}O_4$	$LiNi_{0.5}Mn_{1.5}O_4$	$LiNi_{0.75}Mn_{0.25}O_4$	$LiNi_{0.875}Mn_{1.125}O_4$
C_{11}(GPa)	155.206	167.989	149.368	167.83	102.919
C_{12}(GPa)	103.509	91.146	109.593	90.006	83.246
C_{44} (GPa)	7.316	41.254	31.191	44.448	38.328
B (GPa)	120.741	116.760	122.851	115.948	89.803
$B_{(Calc)}$	133 [228]				
E (GPa)	42.460	107.993	74.608	112.984	73.453
$E_{(Calc)}$	92 [229]		124 [229]		
G (GPa)	14.729	40.121	26.669	42.234	26.932
$G_{(Calc)}$	77.0 [228]				
C'	25.849	38.421	19.888	38.912	9.837
B/G	8.198	2.910	4.0606	2.745	3.334
A	0.761	1.034	1.151	1.066	1.554

Therefore, the results in Table 4-1 indicate that our structures satisfy conditions of a cubic crystal at 0GPa and an increase in the nickel concentration does not implicate negative results of the bulk modulus, shear modulus and tetragonal shear modulus. The bulk modulus, *B,* and shear modulus, G, of $LiMn_2O_4$ is in good agreement with the calculated value. There has been experimental finding which are in range with our finding of (42 GPa) for the fully intercalated $LiMn_2O_4$ with E ranging from 10-200 GPa due to different experimental techniques used [230] [231] [232] [233] [234]. The calculated values of *A,* from $LiMn_2O_4$ to $LiNi_{0.75}Mn_{0.25}O_4$, are approaching unity ($A \approx 1$) which indicates that they are becoming isotropic, with the exception of $LiNi_{0.875}Mn_{1.125}O_4$.

The stability against small deformations can be studied by considering the elastic properties and the calculated elastic properties of $LiMn_2O_4$ at various pressures are

listed in Table 4-2. It has been recently found that the *C′* is also very significant on the mechanical properties of materials [227].

Table 4-2: Calculated elastic constants *B*, *G*, *B/G*, anisotropy *A* and tetragonal C' of $LiMn_2O_4$ at various pressure.

$LiMn_2O_4$ Elastic Constants (GPa)						
Pressure(GPa)		10	20	30	40	50
	C_{11}	250.861	216.5954	260.6196	287.372	353.7856
	C_{44}	28.64205	29.91637	30.76665	32.69235	31.99567
	C_{12}	167.3776	198.8269	261.8913	305.5424	330.8306
	B	195.2054	204.7497	261.4674	299.4856	338.4822
	G	33.88191	21.50353	18.20565	15.98133	23.78841
	B/G	5.761345	9.52168	14.36188	18.73972	14.22887
	C′	41.7417	8.88427	-0.63585	-9.0852	11.47751
	A	0.895562	1.194206	1.240983	1.290756	1.115992

The calculated value of *C′* is negative for $LiMn_2O_4$ at 30 and 40GPa, thus indicating that the composition is not stable at 30 and 40GPa. The bulk modulus of the composition measured the composition's resistance to uniform compression, as a result, there is an increase in the bulk modulus when pressure is applied to $LiMn_2O_4$. The shear modulus increases monotonically with the applied pressure. The *B/G* increases with the increasing bulk modulus and increasing pressure then decrease at 50GPa. Therefore, the material becomes ductile since the structure at different pressure has a greater *B/G* as compared to the Pugh proposed *B/G* ratio. The composition is isotropic when values are smaller or larger than 1 to measure the degree of elastic anisotropy, hence $LiMn_2O_4$ structure satisfies the condition for the system to be isotropic with increasing pressure.

The calculated elastic properties of $LiNi_{0.25}Mn_{1.75}O_4$ are displayed in Table 4-3 and the conditions indicate that $LiNi_{0.25}Mn_{1.75}O_4$ is sensitive to the applied pressure. For a cubic material, it is well known that *B*, *G* and C_{44} must be positive for a structure to remain mechanically stable. The calculated value of *C′* is positive for $LiNi_{0.25}Mn_{1.75}O_4$ 10, 20, 30 and 50GPa, thus indicating that the composition is stable.

Table 4-3: Calculated elastic constants *B, G, B/G*, anisotropy *A* and tetragonal *C*' of $LiNi_{0.25}Mn_{1.75}O_4$ at various pressure.

$LiNi_{0.25}Mn_{1.75}O_4$ Elastic Constants (GPa)						
Pressure(GPa)		10	20	30	40	50
	C_{11}	223.937	197.789	243.858	266.795	357.388
	C_{44}	34.555	28.684	25.141	23.681	17.421
	C_{12}	121.473	153.173	236.158	290.668	338.930
	B	155.628	168.045	238.725	282.710	345.083
	G	41.226	26.133	16.625	9.434	14.145
	B/G	3.775	6.430	14.310	29.968	24.397
	C'	51.232	22.307	3.810	-11.937	9.229
	A	0.851	1.064	1.175	1.267	1.046

Then *C'* becomes negative at 40GPa, indicating that the composition is unstable as observed from the calculations shown in the Table above. The bulk modulus of the composition measured the composition's resistance to uniform compression, as a result, there is an increase in the bulk when pressure is applied to $LiNi_{0.25}Mn_{1.75}O_4$ at all pressure values. While the shear modulus decreases with the increasing pressure from 10 until 30GPa and begins to increase at 50GPa. The critical value, which separates ductile and brittle materials, is about 1.75 [227]. Table 4-3 shows that the calculated values of *B/G* increase with increasing pressure until 40GPa then begins decreasing at 50GPa, and the ductility and brittleness of $LiNi_{0.25}Mn_{1.75}O_4$ indicate instability under high pressure. The composition is completely isotropic when *A*=1, hence regarding the values in Table 4-3 the compositions satisfies the condition for the system to be isotropic with the increase in pressure.

In Table 4-4, we listed elastic constant ($C_{11,}$ C_{44} and C_{12}) and bulk modulus *B*, shear modulus *G*, *B/G* ratio, C' and anisotropy *A* under a range of pressure values (10-50GPa). The calculated elastic properties of $LiNi_{0.5}Mn_{1.5}O_4$ listed in Table 4-4 indicate that $LiNi_{0.5}Mn_{1.5}O_4$ is extremely sensitive to applied pressure.

Table 4-4: Calculated elastic constants *B, G, B/G*, anisotropy *A* and tetragonal *C'* of $LiNi_{0.5}Mn_{1.5}O_4$ at various pressure

$LiNi_{0.5}Mn_{1.5}O_4$ Elastic Constants (GPa)						
Pressure(GPa)		10	20	30	40	50
	C_{11}	178.862	217.796	155.244	203.285	263.439
	C_{44}	23.795	21.121	40.679	10.909	10.902
	C_{12}	172.275	227.374	80.354	243.984	334.944
	B	172.275	224.181	105.318	230.419	311.109
	G	16.253	10.757	39.385	-1.595	-7.760
	B/G	10.599	20.840	2.674	-144.492	-40.091
	C'	3.293	-4.789	37.445	-20.351	-35.752
	A	1.229	1.238	1.042	1.308	1.354

It is also seen that the elastic constants $C_{11,}$ C_{12} and bulk modulus *B* increase monotonically with the applied pressure. However, when pressure increases C_{44} fluctuates and attains values of 10.909 and 10.902 GPa at 40 and 50GPa respectively. The shear modulus, *G,* shows fluctuations and becomes negative with values of -1.59468 and -7.76006GPa at 40 and 50 GPa pressure respectively. Therefore, indicating the mechanical instability of $LiNi_{0.5}Mn_{1.5}O_4$ at the two pressure values. The tetragonal shear modulus *C'* generally decreases with pressure reflecting negative values at 20 40 and 50 GPa, and an anomalous positive value at 30 GPa. Table 4-4 shows that the calculated values of *B/G* fluctuate with increasing pressure and $LiNi_{0.5}Mn_{1.5}O_4$ shows brittleness at 40GPa (1.75>-144.492) and at 50GPa (1.75>-144.492) and ductility is indicated from 10-30GPa. There is a gradual departure from isotropy with pressure, except at 30 GPa which is near isotropic as indicated in Table 4-4. On the whole it may be surmised that at 30 GPa $LiNi_{0.5}Mn_{1.5}O_4$ show a different mechanical behaviour from other pressures.

The calculated elastic properties of $LiNi_{0.75}Mn_{1.25}O_4$ listed in Table 4-5, obey mechanical stability conditions for a cubic system. It is apparent that the elastic constants C_{11} and C_{44} increase monotonically whereas C_{12} and the bulk modulus increases when pressure is enhanced. The calculated value of *C'* is positive for $LiNi_{0.75}Mn_{1.25}O_4$ at 10 and 50GPa and appear negative from 20-40GPa.

Table 4-5: Calculated elastic constants *B*, *G*, *B/G*, anisotropy *A* and tetragonal *C'* of $LiNi_{0.75}Mn_{1.25}O_4$ at various pressures

$LiNi_{0.75}Mn_{1.25}O_4$ Elastic Constants (GPa)						
Pressure (GPa)		10	20	30	40	50
	C_{11}	254.225	223.916	247.343	249.559	320.576
	C_{44}	35.964	26.971	27.425	24.292	19.985
	C_{12}	123.283	198.107	247.249	301.625	328.297
	B	166.931	206.710	247.271	284.261	325.723
	G	47.767	21.344	16.474	4.162	10.447
	B/G	3.495	9.685	15.011	68.299	31.171
	C'	28.059	-11.666	-27.141	-39.369	160.288
	A	0.768	1.126	1.221	1.403	1.149

For a cubic material, it is well known that *B, C'* and C_{44} must be positive for a structure to remain mechanically stable. Hence it may be concluded that an increase in pressure renders $LiNi_{0.75}Mn_{1.25}O_4$ owing to the negative tetragonal shear modulus. Table 4-5 indicate ductility, as the values obtained, are >1.75. The composition is isotropic when pressure is enhanced and the condition is satisfied. On the whole it is observed that mechanical properties change significantly at 50 GPa compared to other pressures.

It is further noted from Table 4-6 that elastic constants $C_{11,}$ C_{12} and the bulk modulus B, for $LiNi_{0.875}Mn_{1.125}O_4$, increase monotonically with pressure, except at 40 GPa for C_{11}, whereas C_{44} reduces with increasing pressure. However, when the pressure increases *G* decreases and behave anomalously at 40 GPa. The calculated value of *C'* is positive for $LiNi_{0.875}Mn_{1.125}O_4$ from up to 30GPa, thus indicating that the composition is stable, and subsequently tends negative above this pressure, hence showing mechanical instability. This can be observed from the table below that the *B/G* increase with the increasing bulk modulus and begins to show inconsistency from 40-50GPa. The composition is closer to isotropy at lower pressure values and deviates at 40GPa (2.283).

Table 4-6: Calculated elastic constants *B*, *G*, *B/G*, anisotropy *A* and tetragonal C' of $LiNi_{0.875}Mn_{1.125}O_4$ at various pressure

$LiNi_{0.875}Mn_{1.125}O_4$ Elastic Constants (GPa)						
Pressure (GPa)		10	20	30	40	50
	C_{11}	168.189	207.205	223.585	175.205	232.885
	C_{44}	49.625	46.221	46.097	44.529	33.477
	C_{12}	144.261	182.109	216.631	310.949	310.358
	B	152.243	190.474	218.949	265.701	284.534
	G	34.559	32.752	29.049	-0.431	4.592
	B/G	4.405	5.816	7.537	-616.018	61.964
	C'	11.951	12.548	3.477	-67.872	-38.737
	A	1.448	1.325	1.381	2.283	1.620

On the whole it can be concluded that anomalous behaviours and instabilities of various compositions of $LiNi_xMn_{2-x}O_4$ are observed at different pressures. A composition with the best mechanical properties in the range 0-50 GPa, is $LiNi_{0.25}Mn_{1.75}O_4$, followed by $LiNi_{0.875}Mn_{1.125}O_4$, particularly as attested by the shear modulus *C'* and the isotropy *A*. It can further be deduced that the stability of the latter, as shown by electronic properties, does not change much with pressure variation. Although the well-studied $LiNi_{0.5}Mn_{1.5}O_4$ indicates both electronic and mechanical instabilities at high pressures, it is quite stable at 0 and 10 GPa as compared to other compositions.

Chapter 5

Cluster Expansion Phase Stability Predictions

In this chapter, we present and discuss results from the universal cluster expansion code, implemented in cluster expansion formalism used to investigate nickel doped LMO phase stabilities.

5.1 Structural Predictions

The method determines stable multi-component crystal structures and ranks metastable structures by the enthalpy of formation while maintaining the predictive power and accuracy of first-principles density functional methods. The ground-state phase diagram generated various structures with different concentrations and symmetries. This fitting scheme ran for a maximum number of iterations, adding a maximum of 5 structures in each iteration, and starting from an initial training set of five structures. The iterations continue until the energies of all structures are predicted by the cluster expansion which is higher than the energy calculated for the structure of the ground state line at each sampled concentration. The iterations continued until the standard deviation of 95% of the structures were within 5 meV of the cross-validation score (CVS). Therefore, the cross-validation score indicates how well the energies of the structures of the stable phases in the training set compare with each other. However, systematic errors will not be displayed. Lastly, the properties of all structures identified on the binary diagram are characterised by calculating heats of formation, elastic properties to determine mechanical properties, electronic stability from their density of states and phonons calculations to illustrate vibrational properties of the generated structures of stable phases.

Figure 5-1 shows a binary diagram that is an isotropic volume optimisation binary ground state-diagram and the structure being non-magnetic. The alternative to f
ull structural optimisation is to optimise the volume of the structure isotropically where both minimisation stages volume are optimised isotropically. Then to counter the issue with the anomalous DFT total energy values we increased the accuracy in the VASP flowchart, by increasing the plane-wave basis cut off from 300eV to 400eV

in the GGA stage and decreased the k-spacing from 0.5 to 0.35 in the second minimisation stage. The isotropic volume optimisation calculation yielded miscible constituents (see Figure 5-1), implying that the generated phases close to the ground states with the lowest $\Delta \boldsymbol{Hf}$ at a given concentration should be stable. The highlighted red line corresponds to density functional theory ground state systems and the structures that are on the DFT ground state line (red) are thermodynamically stable. The binary diagram produced 62 new structures of stable phases from which only six structures are stable. The stable structures obtained from the binary diagram in Figure 5-1 have different space groups, different lattice parameters, the same Wyckoff positions and a different energy of formations. Therefore, the isotropically optimised structures has a cross validation score of 1.1 meV which is an indication of a good cluster expansion because it has CVS lesser than 5 meV per active position.

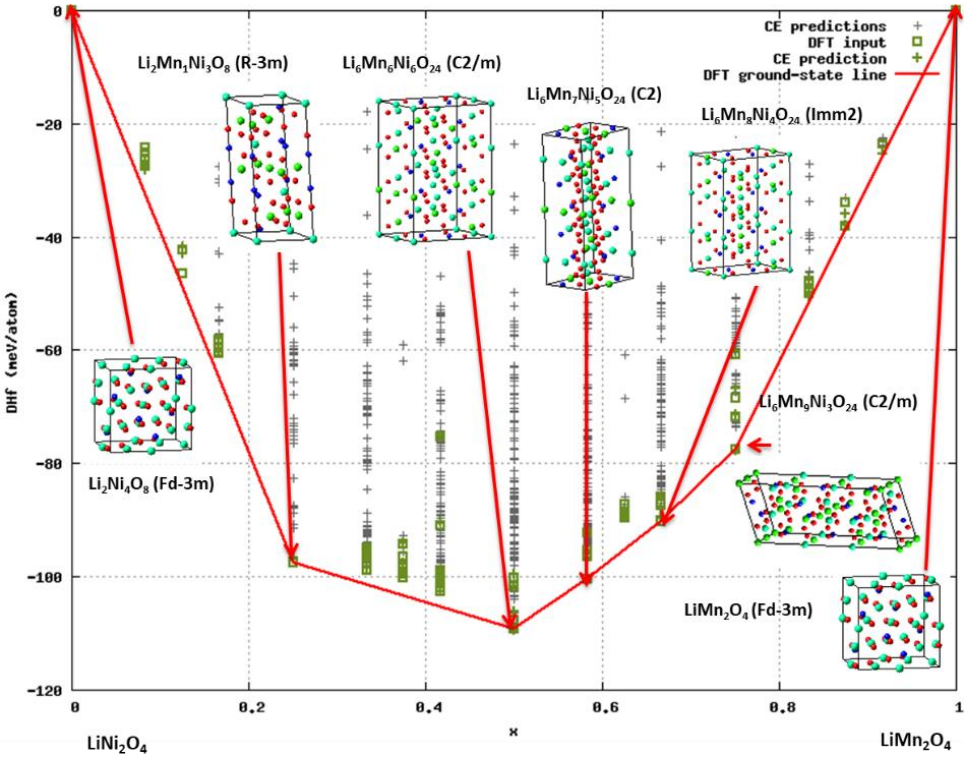

Figure 5-1: An isotropic volume optimised binary ground state-diagram of $(LiNiMnO_4)_8$ with a cross-validation score of 1.1 meV. The grey line is the CE predictions (-), the green line is the (-) DFT input and the red line is the DFT ground-state line (-).

Figure 5-2 shows a binary diagram that has been fully optimised with the structure being non-magnetic. The full optimised binary ground state diagram produced 77 new structures where only 8 are stable. We utilised the same plane-wave basis cut off of 400eV in the GGA stage and the k-spacing of 0.35 in the second minimisation stage of the flowchart that yielded Figure 5-1. The structures shown in Figures 5-2 are miscible constituents, implying that the generated phases close to the ground states having the lowest ΔH_f at a given concentration should be stable. The highlighted red line corresponds to density functional theory ground state systems and the structures that are on the DFT ground state line (red) are thermodynamically stable. The stable structures in Figure 5-2 have different space groups, different lattice parameters, the same Wyckoff positions and different energies of formation. Therefore, the fully optimised calculation produced a cross validation score of 13 meV which is an indication of a bad cluster expansion because the CVS is greater than 5 meV per active position. However, structures produced by binary ground state diagram in Figure 5-2 would not be taken into consideration because of the high cross validation score. The high error could be due to large Mn concentrations as compared to the isotropically optimised binary ground state diagram. Consequently, there is a necessity to limit Mn concentration to the occupancy of 0.8.

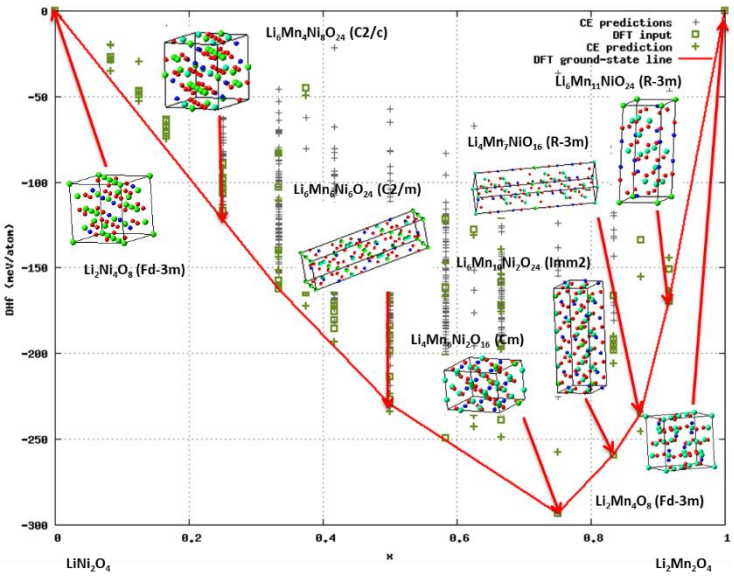

Figure 5-2: Full optimised binary ground state diagram of $(LiNiMnO_4)_8$ and cross-validation score of 13 meV. The grey and green crosses (**+** and **+**) are CE's predicted structures, the green block (▫) is the DFT input and the red line (-) is the DFT ground-state line.

The undoped systems ($LiMn_2O_4$ and $LiNi_2O_4$) which are randomly mixed to produce structures of stable phases are also predicted as stable structures on the DFT ground state line (red). The other structures ($LiMnNiO_4$, $LiMn_{1.2}Ni_{0.8}O_4$, $LiMn_{1.3}Ni_{0.7}O_4$, $LiMn_{1.5}Ni_{0.5}O_4$) have different lattice parameters where the values for a, b and c are not equal. The table shows that $LiMn_2O_4$, $LiMn_{0.5}Ni_{1.5}O_4$ and $LiMn_{1.3}Ni_{0.7}O_4$ have the lowest energies as compared to the other structures due to the low nickel concentration. The isotropically optimised binary diagram predicted a cathode material of composition $LiMn_{1.5}Ni_{0.5}O_4$ shown in Table 5-1 which is consistent with theoretical and experimental findings [235].

Table 5-1: The most stable phases as predicted by the isotropically optimised binary diagram.

Stable Structures	Lattice Parameters (Å)	Space group	Energy(eV/atom)
$LiNi_2O_4$	a=b=c=5.666	Fd-3m	-20.169
$LiMn_{0.5}Ni_{1.5}O_4$	a=b=c=5.661	R-3m	-24.103
$LiMnNiO_4$	a =5.662, b =8.008, c =9.808	C2/m	-22.853
$LiMn_{1.2}Ni_{0.8}O_4$	a =5.663, b =8.009, c =9.809	C2	-23.273
$LiMn_{1.3}Ni_{0.7}O_4$	a =5.663, b =8.009, c =9.809	Imma	-23.691
$LiMn_9Ni_{0.5}O_4$	a =5.664, b =8.011, c =9.811	C2/m	-24.109
$LiMn_2O_4$	a=b=c=5.671	Fd-3m	-25.319

The energy difference between the two ground-state lines, i.e. for full structural optimisation (atomic and cell parameters) and isotropic volume optimisation, is quite large as shown in Figure 5-3. The large energy changes in Figure 5-3 seem to be due to changes in positions of oxygen atoms. This indicates that another structure might be more stable at higher Mn concentrations (x (Mn)>0.5). The cross-validation score is lower for the isotropic volume optimisation ground state diagram, of magnitude 1.1meV while significantly high for full optimisation ground state diagram, equal to 13 meV. When cross-validation score is high, it becomes a poor measure of predictive accuracy and it implies that the structural stability is not well predicted by the cluster expansion.

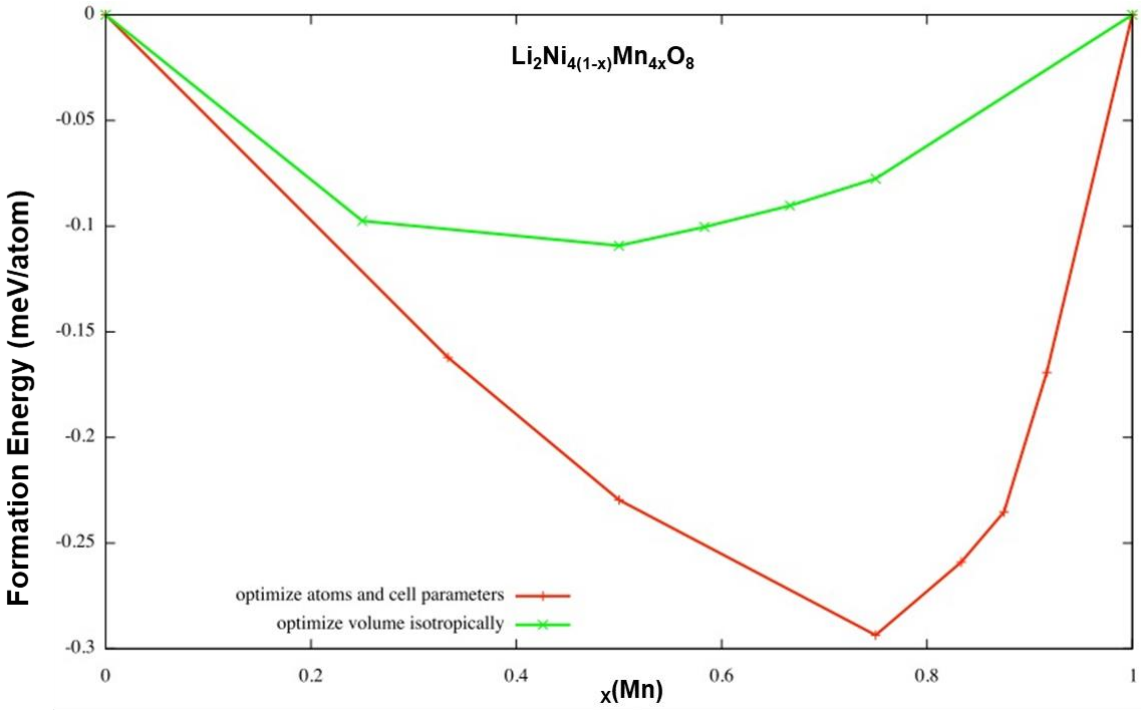

Figure 5-3: Comparison of a fully optimised binary ground state diagram and isotropically optimised binary ground state diagram.

Figure 5-4 shows the errors of a fully optimised binary ground state diagram of $(LiNi_2Mn_2O_4)_8$ between cluster expansion and DFT. It shows the errors of each structure's energy of a nickel and manganese concentration. Optimising atomic positions and cell parameters resulted in large unforeseeable energy changes that the cluster expansion cannot predict. If positive results are achieved, then various properties for the most stable structures on the ground state line can be calculated. With this approach, cluster expansion allows the identification and a study of the stable ground state structures. Curtailing the concentration range did not improve the final CVS by much (from 13 meV/atom to 12 meV/atom). Therefore, the best next step in this work was to use the isotropic cluster expansion to probe the properties of the predicted structures. However, based on high values of CVS after relaxations and errors of each structure between cluster expansion and DFT as shown in Figure 5-4, it would be trivial to perform Monte Carlo simulation as all summarised errors by the CVS will be transferred to the Monte Carlo simulations.

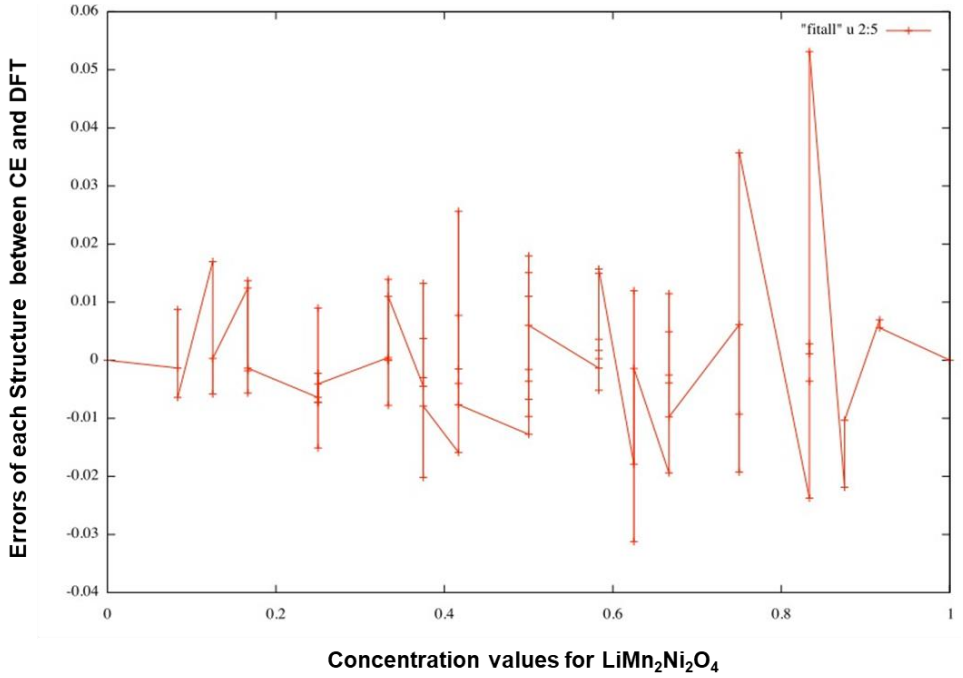

Figure 5-4: Errors of a fully optimised binary ground state diagram of $(LiNi_2Mn_2O_4)_8$ between cluster expansion and DFT.

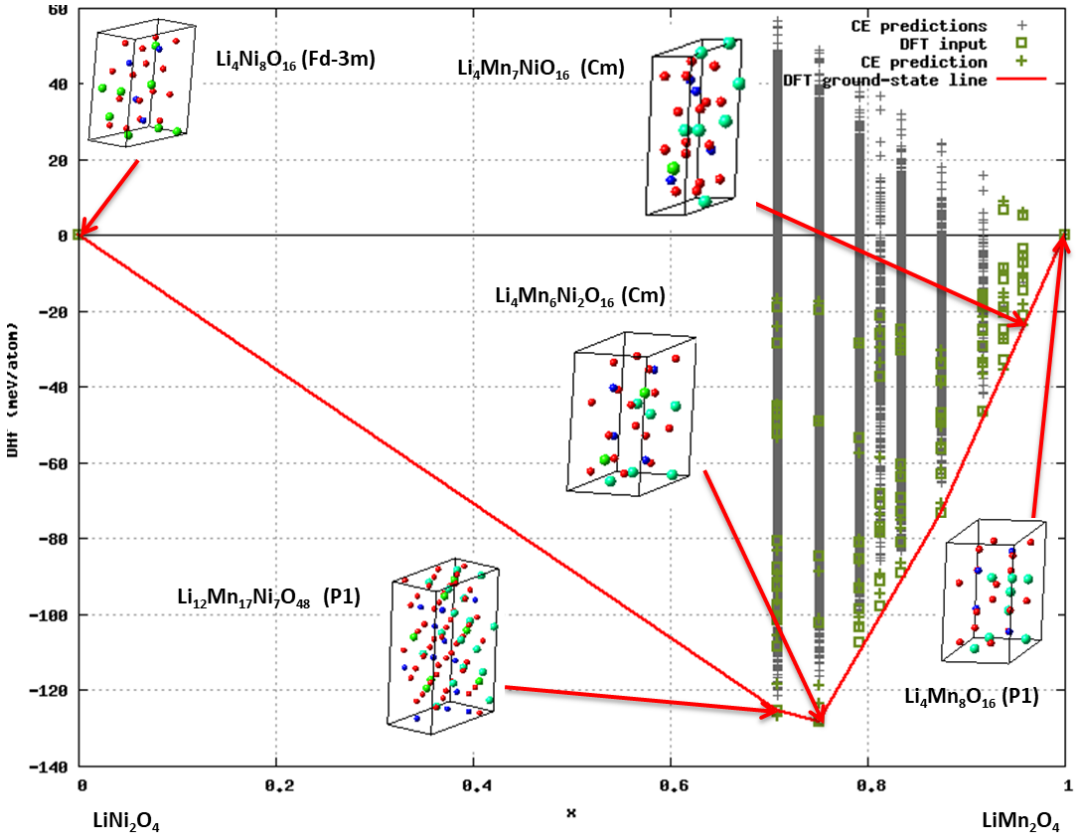

Figure 5-5: Full optimisation binary ground state diagram with the occupancy of Mn0.8 and Ni 0.33 Ni-doped $(Li(Mn_{1-x}Nix)_2O_4$ heats of formation for different unit cells and a suitable cross-validation score of 1.4 meV. The grey and green crosses (**+** and **+**) are CE's predicted structures, the green block (▫) is the DFT input and the red line (-) is the DFT ground-state line.

The full optimised binary ground state diagram produced 48 new structures from which only 5 structures on the DFT ground-state line are stable. The same plane-wave basis cut off of 400eV in the GGA stage and the k-spacing of 0.35 in the second minimisation stage as in Figure 5-1 were used. To be able to obtain results in Figure 5-5, we created active sites that must be defined to perform CE simulation and created double occupancies on the Ni and Mn consisting of 6 sites. The occupancies were limited on both Ni and Mn so that a CE around the stoichiometry of (Mn, occupancy=0.81), Ni (Ni, occupancy=0.31) 16d sites. The occupancies were set as 0.81 for Mn and 0.31 for Ni and CE was then performed in the set concentration range of 0.81 and 0.31. The cluster expansion produced a CVS of 1.4 meV/atom. As a result, there were no major structural instabilities since both cell parameters and atomic positions were fully optimised. Figure 5-5 shows only a small portion of the $LiNi_2O_4$ on the concentration range that is considered by the CE because of the maximum occupancy of Ni being limited to 0.31. The figure also shows the CE predictions, DFT input and CE predictions on the side of the $LiMn_2O_4$ where the occupancy is 0.81. The five (5) stable structures produced are presented on the DFT ground-state line (red) are $LiNi_2O_4$, $LiMnNi_{1.4}O_4$, $LiMn_{1.5}Ni_{0.5}O_2$, $LiMn_{1.75}Ni_{0.25}O_4$ and $LiMn_2O_4$ with different space groups, different lattice parameters, the same Wyckoff positions and different energy of formations.

Table 5-2 shows the structures of stable phases as predicted by the full optimisation binary ground state diagram with the occupancy limited to Mn0.8 and Ni0.33 Ni-doped $(Li(Mn_{1-x}Nix)_2O_4$. The structures in Table 5-2 have different lattice parameters and their energies are close to the ground state line, therefore considered thermodynamically stable. Consequently, the structures were used further to calculate mechanical properties because of the low cross-validation score of 1.4 meV. The five systems are triclinic structures and have different lattice parameters. The undoped systems ($LiMn_2O_4$ and $LiNi_2O_4$) are predicted as part of the most stable structure candidates. There is a notable energy difference between $LiNi_2O_4$ and $LiMn_2O_4$ where the other three structures of energy is marginally different. Although Table 5-1 ($LiMn_{1.5}Ni_{0.5}O_4$ =-24.109 eV/atom) and Table 5-2 ($LiMn_{1.5}Ni_{0.5}O_4$ =-24.334 eV/atom) were optimised differently they have an energy difference of 0.227 eV/atom. Therefore, the fully optimised binary diagram with double occupancy

for Mn (0.81) and Ni (0.31) predict that $LiMn_{1.5}Ni_{0.5}O_4$, in Table 5-2, is a promising cathode material in agreement with theoretical and experimental findings [235].

Table 5-2: The most stable phases as predicted by full optimisation ground state diagrams with occupancies of Mn (0.81) and Ni (0.31).

Stable Structures	Lattice Parameters (Å)	Space group	Energy (eV/atom)
$LiNi_2O_4$	a=5.614, b=5.654, c=9.801	Cm	-20.149
$LiMn_{1.4}Ni_{0.6}O_4$	a=5.449, b=14.307, c=10.110	P1	-24.104
$LiMn_{1.5}Ni_{0.5}O_4$	a=5.381, b=5.412,=c=10.184	Cm	-24.336
$LiMn_{1.75}Ni_{0.25}O_4$	a=5.438, b=5.456, c=9.875	Cm	-24.958
$LiMn_2O_4$	a=5.474, b=5.534, c=9.678	Cm	-25.561

5.2 Elastic Properties

The structural and elastic property calculations in this section are based on DFT as implemented in the Vienna ab initio simulation package (VASP) within a plane wave basis set [236] [237] [138] [238]. The accurate calculation of elasticity is important to have an insight into the mechanical stability and elastic properties of solids. The calculations were performed at 0K temperature, since temperature-related differences in the C_{ij} are likely to be at a minimum. The following structures: $LiNi_2O_4$, $LiMn_{1.4}Ni_{0.6}O_4$, $LiMn_{1.5}Ni_{0.5}O_4$, $LiMn_{1.75}Ni_{0.25}O_4$, and $LiMn_2O_4$, (shown in Figure 5-5) were obtained from the cluster expansion embedded in VASP. The components of the elasticity tensor, C_{ij}, were computed from the first derivatives of the stresses computed in VASP, rather than from the second derivatives of the total energy with respect to strain, following the least-squares method of Le Page and Saxe *et al*. [239] [240]. Therefore, the method averts the numerical difficulties often encountered with evaluations of the second derivatives of the total energy with respect to strain and reduces the number of VASP calculations. The values were computed simultaneously rather than as independent sums. C_{ij} is sensitive to the k-point mesh, and this required a series of test convergence calculations for each structure to obtain k-point and cut-off energy of each unique C_{ij} for each material.

Due to the sensitivity of theC_{ij}, the stable structures presented in Table 5-3 were computed using different k-points and cut-off energies listed in Table 5-3. The cut-off energy increase with each configuration and some are greater than the other.

The Brillouin zone integrals used followed the Monkhorst Pack scheme for each configuration listed in Table 5-3 [134]. Since there are no magnetic moments in the respective structures, non-magnetic calculations were considered using 'normal' precision and user-defined plane-wave cut-off energies for each structure. The electronic iterations convergence is $1.00\mathrm{E}^{-05}\,\mathrm{eV}$ using the normal (blocked Davidson) algorithm and reciprocal space projection operators. $LiMn_{1.5}Ni_{0.5}O_4$ and $LiMn_2O_4$ structures have the same energy cut-off but different k-points. It could all be because the two structures have the same number of 28 atoms and the same positioning in the octahedral 16d site. Using first-order Methfessel-Paxton [137] smearing with a width of 0.2 eV is small to avoid the result in wrong total energy, as a result, the small smearing parameters required a large k-point mesh (as indicated in Table 5-3). The accuracy of computed materials properties such as equilibrium lattice parameters, binding energies and elastic moduli depend on a variety of computational parameters (e.g. k-points and cut-off energies), most importantly the quality of plane-wave basis sets and the density of k-meshes for integrations in reciprocal space. The convergence module automates the process of determining optimal parameter settings in VASP [141] [138] for achieving the desired level of accuracy in the calculations of the structures in Table 5-3.

Table 5-3: Convergence parameters via geometry optimisation for each unique C_{ij} in each material.

Compositions	Cut-off energy (eV)	k-points
$LiMn_{0.5}Ni_{1.5}O_4$ (isotropic)	526.481	6x5x5
$LiNi_2O_4$	828.398	8x9x5
$LiMn_{1.4}Ni_{0.6}O_4$	910.739	6x3x4
$LiMn_{1.5}Ni_{0.5}O_4$	883.292	5x6x3
$LiMn_{1.75}Ni_{0.25}O_4$	899.034	7x7x4
$LiMn_2O_4$	883.292	5x5x3

Table 5-4 shows the symmetrised elastic constants C_{11}, C_{12}, C_{13}, C_{33} and C_{44} and anisotropy of tetragonal $LiMn_{0.5}Ni_{1.5}O_4$ structure. Besides the pure phase, there is only one structure to consider from the isotropic CE, $LiMn_{0.5}Ni_{1.5}O_4$ R-3m, the one structure that was optimised separately.

The C_{ij} were calculated at 0 K and we note that all the independent elastic constants for $LiMn_{0.5}Ni_{1.5}O_4$ are positive. Both Laue classes of the hexagonal crystal system, as well as the tetragonal (I) class (4/mmm), have the same form for the elastic matrix [241]. $LiMn_{0.5}Ni_{1.5}O_4$ is of the tetragonal (I) class which have 6 independent elastic constants (C_{11}, C_{12}, C_{13}, C_{33} and C_{44}). The tetragonal $LiMn_{0.5}Ni_{1.5}O_4$ becomes mechanically stable because the structure satisfies the necessary and sufficient Born mechanical stability criteria for tetragonal and which are,

i.e.: $\frac{1}{3}(C_{12} + 2C_{13}) < B_0 < \frac{1}{3}(2C_{11} + C_{33})$ (90)

and their eigenvalues being positive which further proves the mechanical stability of the tetragonal structure. The value of A = 1 for a completely isotropic material, if A is smaller as indicated in Table 5-4 or greater than one, it shows that the tetragonal structures are anisotropic (A>1).

Table 5-4: The unique C_{ij} for the tetragonal structure.

Tetragonal	
Elastic Constants (GPa)	$LiMn_{0.5}Ni_{1.5}O_4$
C_{11}	212.4
C_{12}	99.87
C_{13}	85.12
C_{14}	25.02
C_{33}	263.1
C_{44}	55.94
A	0.99

Table 5-5 shows the symmetrised elastic constants C_{ij} and anisotropy of triclinic $LiNi_2O_4$, $LiMn_{1.4}Ni_{0.6}O_4$, $LiMn_{1.5}Ni_{0.5}O_4$, $LiMn_{1.75}Ni_{0.25}O_4$, and $LiMn_2O_4$ structures. The triclinic structures in Table 5-5 systems have 21 independent elastic constants, with low-symmetries and all their respective eigenvalues being positive, that the triclinic structures in Table 5-5 are mechanically stable. Although it is sometimes possible to obtain negative off-diagonal elastic coefficients in structures that are structurally stable. Tourmaline "Schorl" is, for example, a well-known structure where the C_{14} elastic coefficient is negative and Table 5-5 showing C_{14} being negative. Monoclinic and triclinic systems are said to impose no restrictions on the individual lattice parameters, have 13 and 21 independent elastic constants respectively [241] [242]. The structure satisfies the necessary and sufficient Born mechanical stability criteria for triclinic and which are,

i.e.:$C_{11} > 0, C_{22} > 0, C_{33} > 0, C_{44} > 0, C_{55} > 0,\ C_{66} > 0$ (91)

The value of A = 1 for a completely isotropic material, if A is smaller as indicated in Table 5-5 or greater than one, it shows that the triclinic structures are anisotropic (A>1). This suggests that the $LiNi_2O_4$, $LiMn_{1.4}Ni_{0.6}O_4$, $LiMn_{1.5}Ni_{0.5}O_4$, $LiMn_{1.75}Ni_{0.25}O_4$, and $LiMn_2O_4$ structures mechanically stable at absolute zero temperature. A closer look at the magnitudes of the various elastic constants of the triclinic systems in Table 5-5 allude to these being near tetragonal or even cubic.

The elastic properties of the present conditions are studied using stress-strain and energy-strain methods within the framework of Density Functional Theory. The strong compositional dependence of the elastic properties is predicted as Young's modulus, E, and Shear modulus, G, exhibit fluctuating compositional trends, while bulk modulus, B, remains almost constant. The averaged bulk (*B*), shear (*G*), and Young's (*E*) moduli and Longitudinal (L) moduli and Poisson's ratio (v) are obtained. The elastic properties of the present conditions are studied using stress-strain and energy-strain methods within the framework of Density Functional Theory. The strong compositional dependence of the elastic properties is predicted as Young's modulus, E, and Shear modulus, G, exhibit fluctuating compositional trends, while bulk modulus, B, remains almost constant. The averaged bulk (*B*), shear (*G*), and

Young's (*E*) moduli and Longitudinal (L) moduli and Poisson's ratio (v) are obtained by inputting the C_{ij} into Reuss's lower bound, Voigt's upper bound, and Hill's homogenisation schemes [203].

Table 5-5: The unique C_{ij} for the triclinic structures (GPa).

Triclinic Systems					
Elastic Constants (GPa)	$LiNi_2O_4$	$LiMn_{1.5}Ni_{0.5}O_4$	$LiMn_{1.75}Ni_{0.25}O_4$	$LiMn_2O_4$	$LiMn_{1.4}Ni_{0.6}O_4$
C_{11}	212.4	250.5	228.3	234.3	296.4
C_{12}	95.23	96.7	118.2	124.5	126.3
C_{13}	83.57	98.1	111.9	115.6	123
C_{14}	-18.55	-16.61	-23.37	-23.93	-21.66
C_{15}	-0.03	0.01	-0.02	-0.06	2.28
C_{16}	-0.14	0.11	-0.06	0.11	-0.46
C_{22}	213	266.3	251.9	234.2	295.1
C_{23}	82.85	96.74	97.36	122.6	124.3
C_{24}	17.14	21.11	28.2	17.71	20.34
C_{25}	0.01	-0.07	0	-0.09	-0.08
C_{26}	-0.09	0.14	-0.05	-0.03	-2.84
C_{33}	223.2	288.6	281.6	248	327.3
C_{34}	-0.03	0.01	7.35	8.86	0.16
C_{35}	-0.02	0	-0.01	0.08	1.35
C_{36}	-0.12	0.27	0.12	0	1.49
C_{44}	45.8	54.48	0.12	48.31	58.27
C_{45}	0.02	-0.02	0.12	-0.04	-0.26
C_{46}	0.02	-0.05	0.12	-0.02	0.91
C_{55}	46.99	58.1	0.12	39.53	56.46
C_{56}	-17.23	-18.19	0.12	-16.28	-19.03
C_{66}	59.4	82.46	0.12	48.99	88.78
A	0.78	0.71	0	0.88	0.69

The related quantities, such as the Bulk modulus and Poisson's ratio have been calculated within the Voight-Reus-Hill approximation [243]. First, the Reuss (lower) [244] and Voight (upper) [245] bounds, for the bulk (B) and for the Shear (G) moduli have been evaluated, corresponding to crystalline values at uniform stress and uniform strain respectively. The Young's modulus, E, and shear modulus, G, change smoothly and increase or decrease relative to the amount of Ni concentration. Both show almost a linear dependence on the composition in contrast to an almost practically constant value of B. A criterion proposed by Pugh's suggests that material will be brittle if its G/B > 0.5, if not then it is ductile. However, the materials shown in Table 5-6 are ductile because of the G/B < 0.5. The Frantsevich's rule also states that the mechanical property of material will be dominated with brittleness when Poisson's ratio v < 0.33; if v > 0.33, the mechanical property of the material mainly exhibits ductile nature and it is indicated in Table 5-6.

Table 5-6: The calculated Bulk Modulus B, Shear modulus G. Young's

Moduli E, Longitudinal and L B/G of all stable compositions.

Compositions	Bulk moduli (GPa)	Shear moduli (GPa)	Young's moduli (GPa)	Longitudinal moduli (GPa)	G/B
$LiMn_{0.5}Ni_{1.5}O_8$	136.2	55.47	146.4	210.1	0.4
$LiNi_2O_4$	130.2	52.87	139.7	200.7	0.4
$LiMn_{1.5}Ni_{0.5}O_4$	157.1	64.64	170.4	243.3	0.4
$LiMn_{1.75}Ni_{0.25}O_4$	185.3	80.21	210.1	292.3	0.4
$LiMn_2O_4$	160.2	47.04	128.5	222.9	0.3
$LiMn_{1.4}Ni_{0.6}O_4$	184.9	72.57	192.5	281.7	0.4

5.3 Electronic Properties

The aim of computational chemistry is to understand the importance of chemical bonds. Figures 6-6 to 6-10 show the total density of states and partial density of states of isotropic and fully optimised structures. The DOS calculations were computed using the non-magnetic GGA-PBE at 0K temperature. The density of states facilitates the characterisation of chemical bonds in the context of the solid-state. As a periodic solid has a large number of atoms, the discrete energy levels related to the different atoms are similar, which results in the formation of continuous bands. The energy bands can be analysed from the DOS, which is in correspondence to the number of states available to electrons per unit cell at a specified energy. There are two kinds of bands: the valence band which is on the negative side of the Fermi level (E_f) and corresponds to the occupied states, and the conduction band which is on the positive side of the Fermi level and corresponds to the unoccupied states. This section discusses the partial density of states for Ni-doped spinel structures yielded from a binary diagram. The PDOS were calculated using cut-off energies and k-points from Table 5-3. The DOS can be projected onto atomic orbitals which gives the projected DOS (PDOS). The PDOS are useful to investigate the atomic states involved in the formation of the chemical bonds. The intensity and position of the PDOS bands provide information on the different electronic interactions occurring in the system such as a charge transfer, ionic or covalent interactions.

5.3.1 $LiMn_{0.5}Ni_{1.5}O_4$ Isotropic Volume Optimisation

Figure 5-6 shows the total (top) and partial density of states (below) of $LiMn_{0.5}Ni_{1.5}O_4$ at ambient pressure (0GPa) and the black dashed line represents the Fermi energy which is used as the zero of the energy scale. The Li PDOS shows that the valence band region of Li is divided into two parts, the first part (-19 to -7 eV) and the second part (-7 to 0 eV) gap characterised by the contributions of 2s, corresponding to a peak in the TDOS of the same energies. The Mn and Ni PDOS shows a very broad peak in the valence band contribution concentrated between -6 and -2 eV which consists mainly of 3p and 3d states, then followed by a peak contribution at 0 eV which consist of 3d states corresponding to a peak in the TDOS. The O PDOS is dominated by 3p states with small peaks between -6 and -1 eV. The

Fermi energy is located in the band interval of (-22 to 5) spanning the energy interval (-0.038:0.032) eV. The mixture of Mn (0.5) and Ni (1.5) is responsible for the dispersed peaks at the Fermi level and the gap near the Fermi level. However, there is no pseudogap or bandgap at the Fermi suggesting that the $LiMn_{0.5}Ni_{1.5}O_4$ system is metallic and electronically stable.

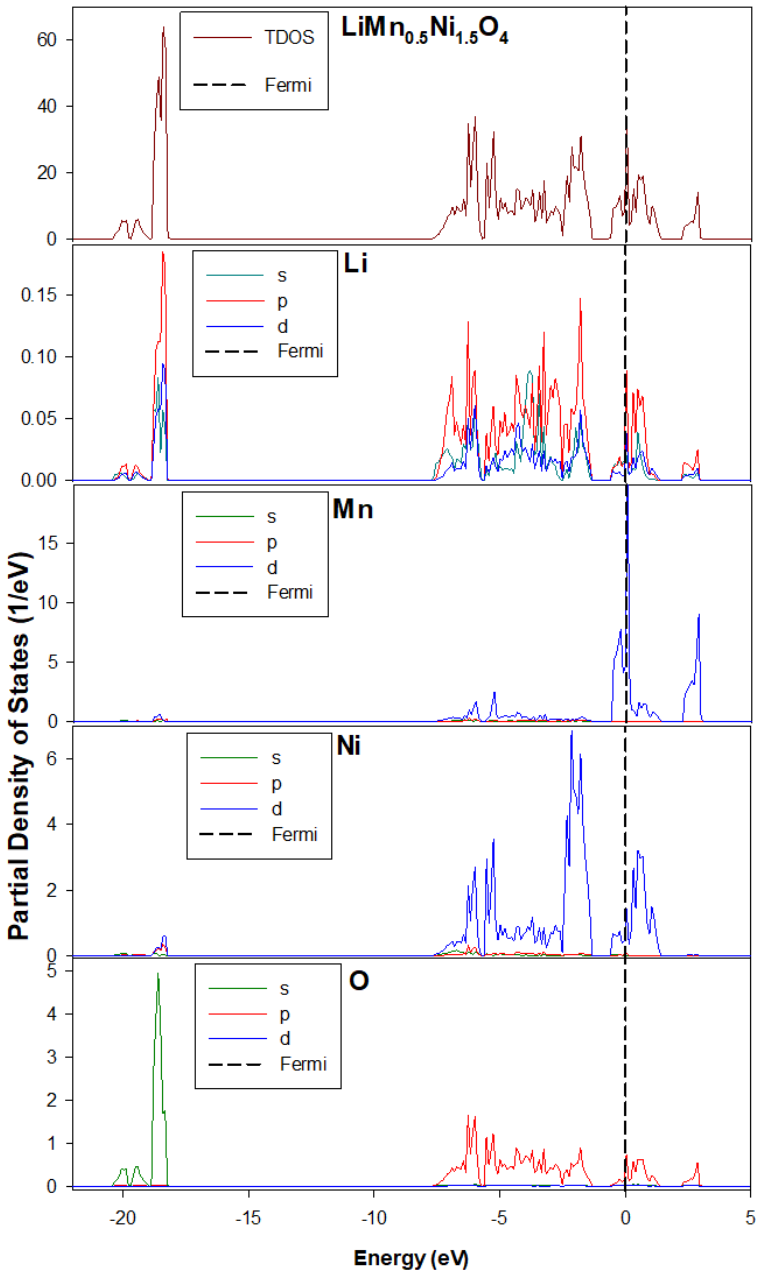

Figure 5-6: A partial density of states (PDOS), showing Li, Ni, Mn and O contribution for $LiMn_{0.5}Ni_{1.5}O_4$ structures and their orbitals (s-orange, p-red, d-blue) and total density of states (brown). The Fermi energy is set as the energy at zero (Fermi-black).

5.3.2 $LiNi_2O_4$ Full Optimisation

Figure 5-7 shows the total (top) and partial density of states (below) of $LiNi_2O_4$ at ambient pressure (0GPa) and the dashed line represents the Fermi energy which is used as the zero of the energy scale. The k-points of 9x9x5 and cut-off energy of 828.398eV were used to calculate PDOS and DOS. The Li PDOS shows that the valence band is divided into two parts, ranging from (-20 to -6 eV) and (-6 to 0 eV) respectively. The gap is characterised by the contributions of 2s, corresponding to a gap in the TDOS of the same energies. The conduction band shows the sharp peak between the 5eV and 10 eV. The Ni PDOS shows a very broad peak in the valence band contribution concentrated between -6 and -1 eV which overlaps into the conduction band between 0 eV and 1 eV. The peak consists mainly of 3p and 3d states, then followed by a peak contribution at 0 eV (Fermi) which consist of 3d states corresponding to a peak in the TDOS. The O PDOS is dominated by 3p states with small peaks between -6 and -2 eV. The Fermi energy is located in the band interval of (-22 to 10.1) spanning the energy interval (-0.058:0.184) eV. The partial density of states at the Fermi level was mainly due to the contributions of Ni-3d and O-2p states. It could also be found that the concentrations of the electronic holes increased, the Fermi level shifted and the DOS around the Fermi level was increased compared with pure $LiMn_{0.5}Ni_{1.5}O_4$. Therefore $LiNi_2O_4$ system shows metallic behaviour and is electronically stable because it does not exhibit pseudo-gap or bandgap at the Fermi.

5.3.3 $LiMn_{1.5}Ni_{0.5}O_4$ Full Optimisation

The total density of states (top) and partial density of states (below) of $LiMn_{1.5}Ni_{0.5}O_4$ at ambient pressure (0GPa) are presented by Figure 5-8. From Figure 5-8, it is interesting to note that the Mn-3d and Ni-3d are mainly dispersed in the narrow band near the Fermi level (dashed line). So to improve the electrochemical performance of $LiNi_2O_4$, Mn site was doped with $Ni_{0.5}$ concentration for the electronic structures of Ni is similar to Mn. To analyse the electronic distribution nearby the Fermi level, the partial density of states of Ni, Mn, O and Li atoms are represented as shown in Figure 5-8. We used the k-points of 5x6x3 and cut-off energy of 883.292 eV to calculate PDOS and DOS. The Mn and Ni PDOS show dispersed peaks in the

valence band contribution concentrated between -6 and -1 eV which consists mainly of 3p and 3d states.

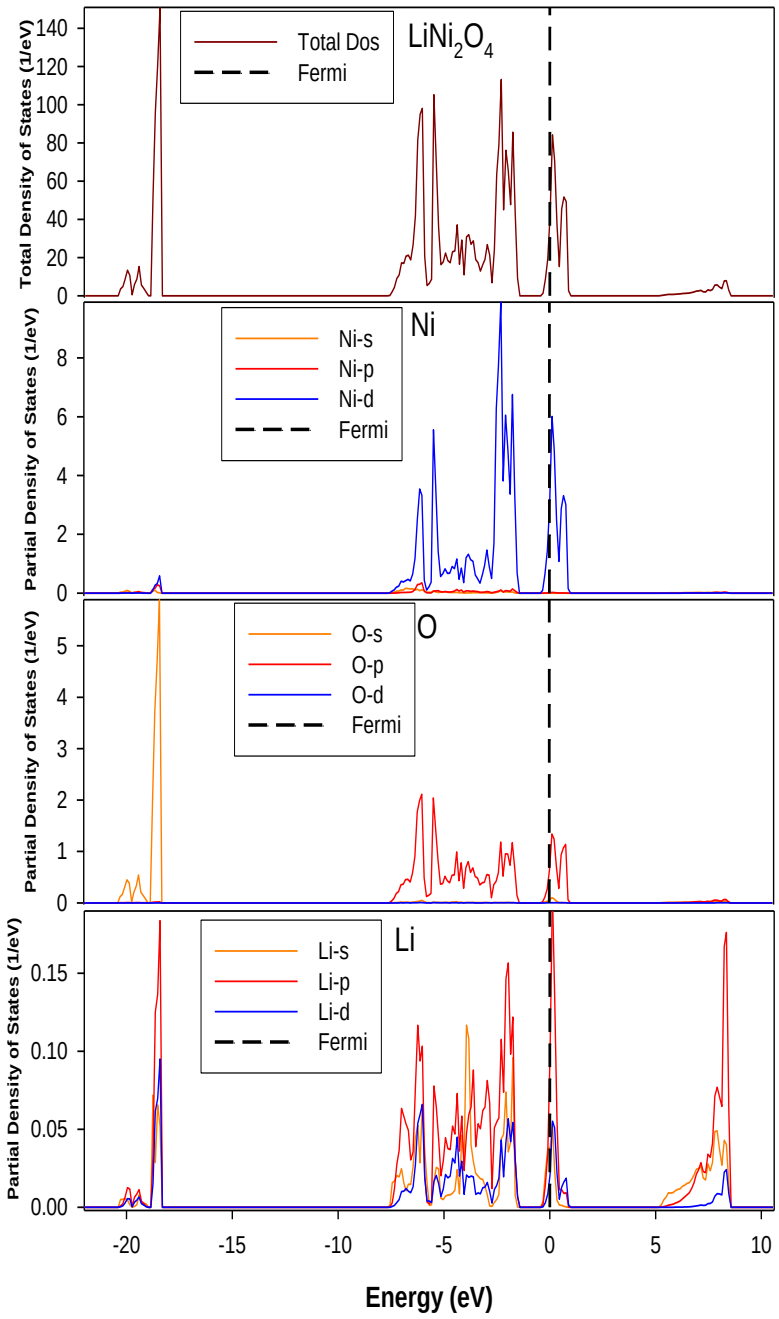

Figure 5-7: The density of states, showing Li, Ni and O contribution for $LiNi_2O_4$ structures and their orbitals (s-orange, p-red, d-blue and total-brown). The Fermi energy is set as the energy at zero (Fermi-black).

Then followed by the peaks contribution at 0 eV (Fermi) which consist of 3d states corresponding to a peak in the TDOS. The Li PDOS shows that the valence band region of Li has two parts, the (-20 to -6 eV) and the (-6 to 0 eV) gap characterised

by the contributions of 2s, corresponding to a gap in the TDOS of the same energies. The O PDOS is dominated by 3p states with small dispersed peaks between -6 and -2 eV and shows minimum contribution in the TDOS. The conduction band in the TDOS is dominated by the Mn and Ni, whereas Li and O have a minimum contribution. The Fermi energy is located in the band interval of (-22 to 4.9) spanning the energy interval (-0.035:0.014) eV. However, the mixture of the Mn (1.5) and Ni (0.5) shows more dispersed peaks (DOS/PDOS) at the Fermi as compared to Figure 5-7. In summary, the graph shows no pseudogap or bandgap at the Fermi suggesting that the $LiMn_{1.5}Ni_{0.5}O_4$ system has metallic attributes and is electronically stable.

5.3.4 $LiMn_{1.75}Ni_{0.25}O_4$ Full Optimisation

In Figure 5-9, we plotted the density of states (top) and partial density of states (below) against the one-electronic energy, relative to the Fermi level. The k-points of 7x7x3 and cut-off energy of 899.034 eV to calculate PDOS and DOS was used. As was expected the pure $LiMn_{1.75}Ni_{0.25}O_4$ spinel structure feature sharp peaks in the partial density of states plot. This is explained by the high symmetry of the lattice. The increase of Mn concentration compared with Ni significantly reduce the symmetry, and density of states plot has a more continuous form. The Li PDOS shows shallow peaks dispersed at the Fermi level. The valence band region of Li is divided into two parts, the (-17 to -7 eV) and there is also the (-7 to 0 eV) gap characterised by the contributions of 2s which corresponds to a gap in the TDOS of the same energies. The Mn and Ni PDOS show a very broad peak in the valence band contribution concentrated between -6 and -1 eV which consists mainly of 3p and 3d states. Then followed by the peaks contribution at 0 eV (Fermi) which consist of 3d states corresponding to a peak in the TDOS. The O PDOS is dominated by 3p states with small peaks in the valence band between (-7 to -2 eV) and conduction band between (0 to 4 eV). The O PDOS have two segments in the valence band between -20 to -18 eV and --7 to 0 eV. The conduction band in the TDOS is dominated by the Mn (1.75) and Ni (0.25) with the contribution of Li and O being minimum. The mixture of the Mn and Ni shows a decrease in the total density of states at the Fermi as compared to Figure 5-8.

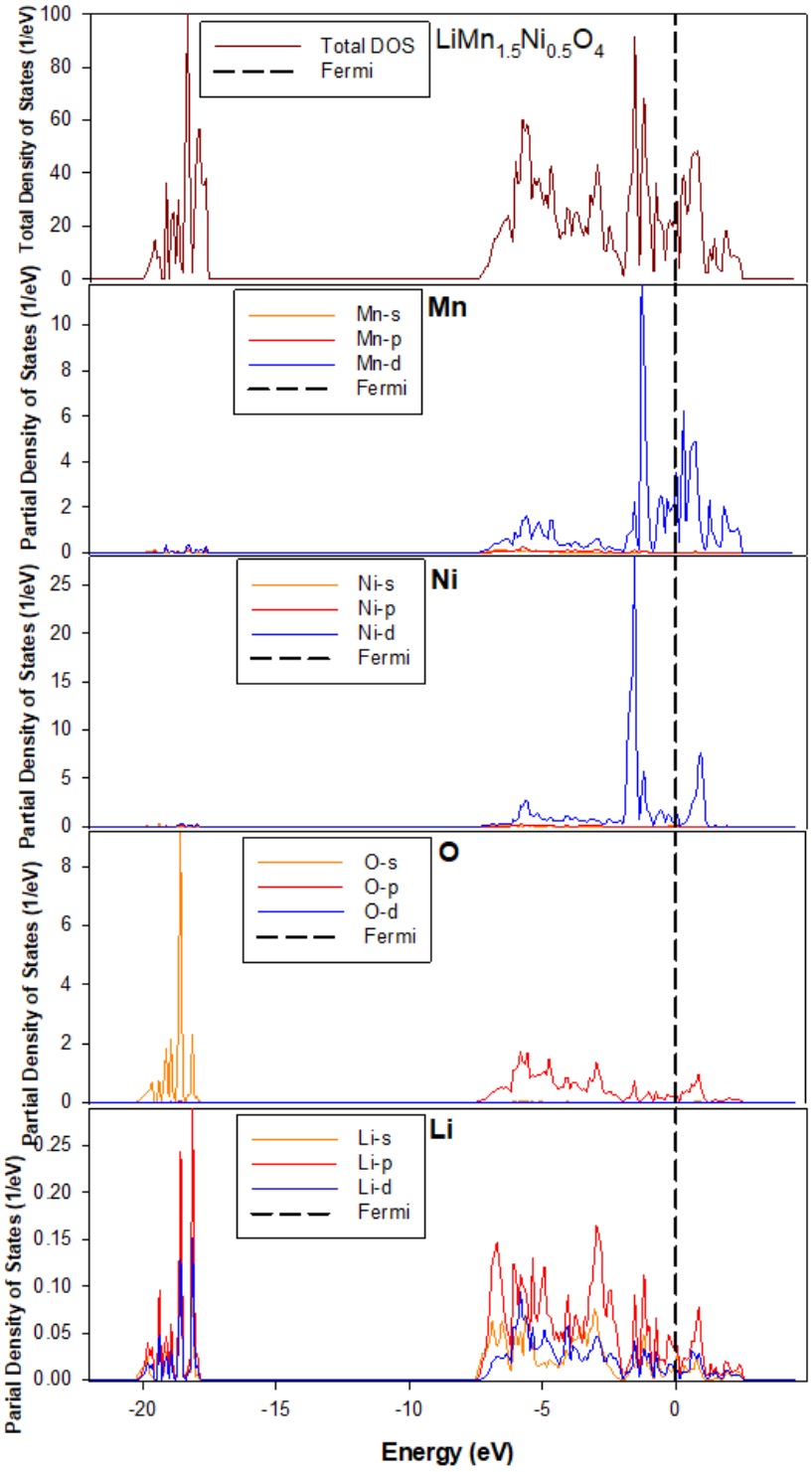

Figure 5-8: A partial density of states (PDOS), showing Li, Ni, Mn and O contribution for $LiMn_{1.5}Ni_{0.5}O_4$ structures and their orbitals (s-orange, p-red, d-blue and total-brown). The Fermi energy is set as the energy at zero (Fermi-black).

The conduction band in the TDOS is dominated by the Mn (1.75) and Ni (0.25) with the contribution of Li and O being minimum. The mixture of the Mn and Ni shows a

decrease in the total density of states at the Fermi as compared to Figure 5-8. The Fermi energy is located in the band interval (-20 and 4.8) spanning the energy interval (-0.066:0.075) eV. The non-existence of pseudogap or bandgap at the Fermi suggests that the $LiMn_{1.75}Ni_{0.25}O_4$ system is metallic and electronically stable.

5.3.5 $LiMn_2O_4$ Full Optimisation

The electron density of states (DOS) (top) and the projected electron density of states (below) (PDOS) of $LiMn_2O_4$ is presented in Figure 5-10. From Figure 5-10, it is engaging to see that the Mn-3d is mainly dispersed in the valence band at the Fermi level. Then Figure 5-10 was obtained using different k-points of 5x5x3 and cut-off energy of 883.292 eV as compared to Figure 5-7. Figure 5-10 with Mn-3d shows a gap at -1eV and Figure 5-7 with Ni-3d shows a gap closer to the Fermi. The Li PDOS shows that the valence band region of Li is divide into two parts, the first part (-17 to -7 eV) and the second part (-7 to 0 eV) gap characterised by the contributions of 2s, corresponding to a gap in the TDOS of the same energies. The Li PDOS shows that the conduction band ranges from 0 to 1 eV. The Mn PDOS show dispersed peaks in the valence band and conduction band with the contribution concentrated between -6 and 2 eV which consists mainly of 3p and 3d states. Figure 5-10 shows more dispersed peaks contribution at 0 eV (Fermi) which consist of 3d states corresponding to a peak in the TDOS as compared to Figure 5-7. The O PDOS is dominated by 3p states with small peaks between -7 and -2 eV. The conduction band in the TDOS shows significant contributions the Mn-3d and the minimum contributions coming from Li and O. The Fermi energy of the TDOS is dispersed and dominated by the Mn-3d located in the band interval (-20 to 4.8) spanning the energy interval (-0.031:0.033) eV. Figure 5-10 shows no pseudo gap or bandgap at the Fermi which suggests that the $LiMn_2O_4$ system is metallic and electronically stable.

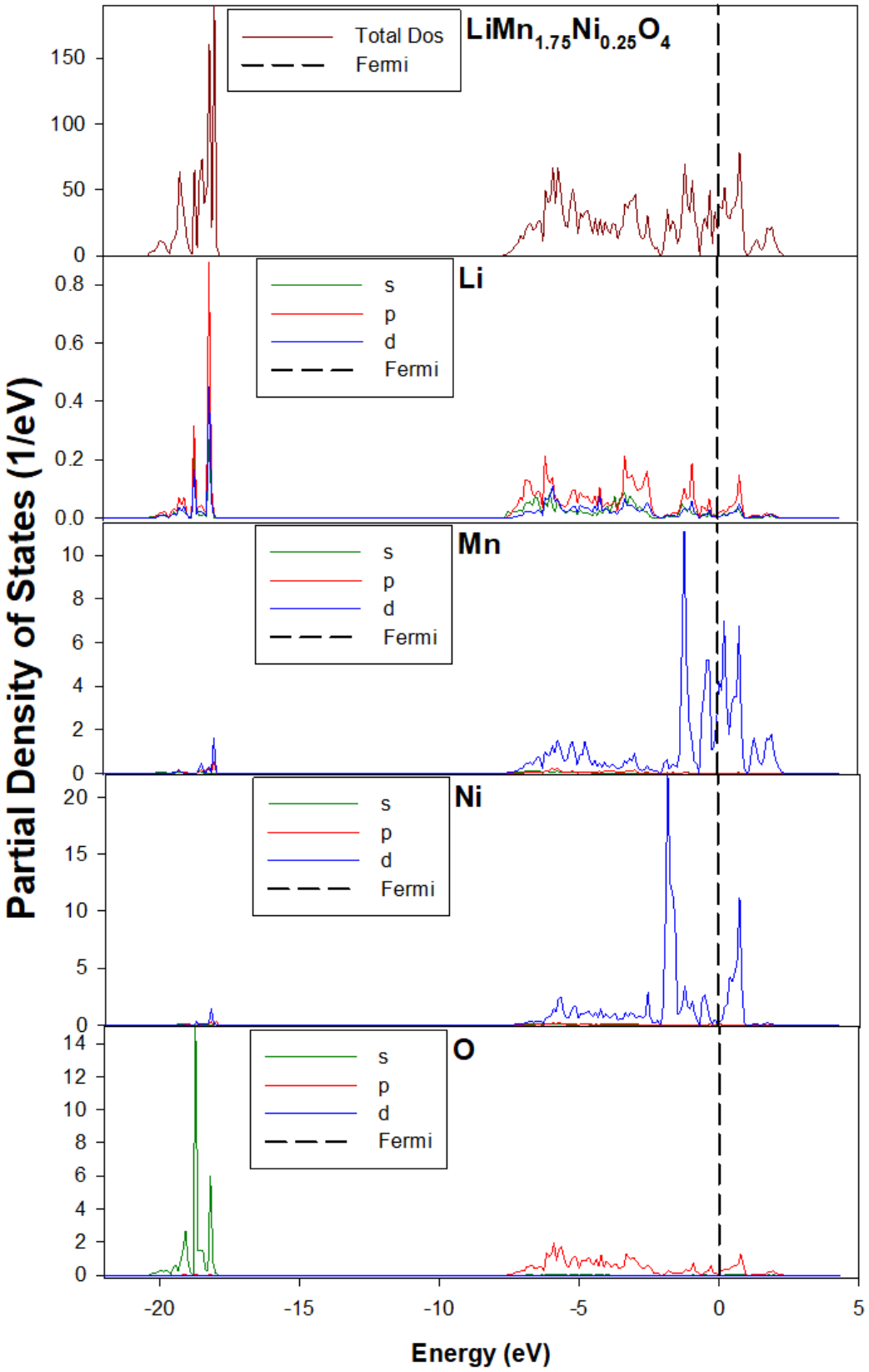

Figure 5-9: A partial density of states (PDOS), showing Li, Ni, Mn and O contribution for $LiMn_{1.75}Ni_{0.25}O_4$ structures and their orbitals (s-orange, p-red, d-blue and total-brown). The Fermi energy is set as the energy at zero (0 eV).

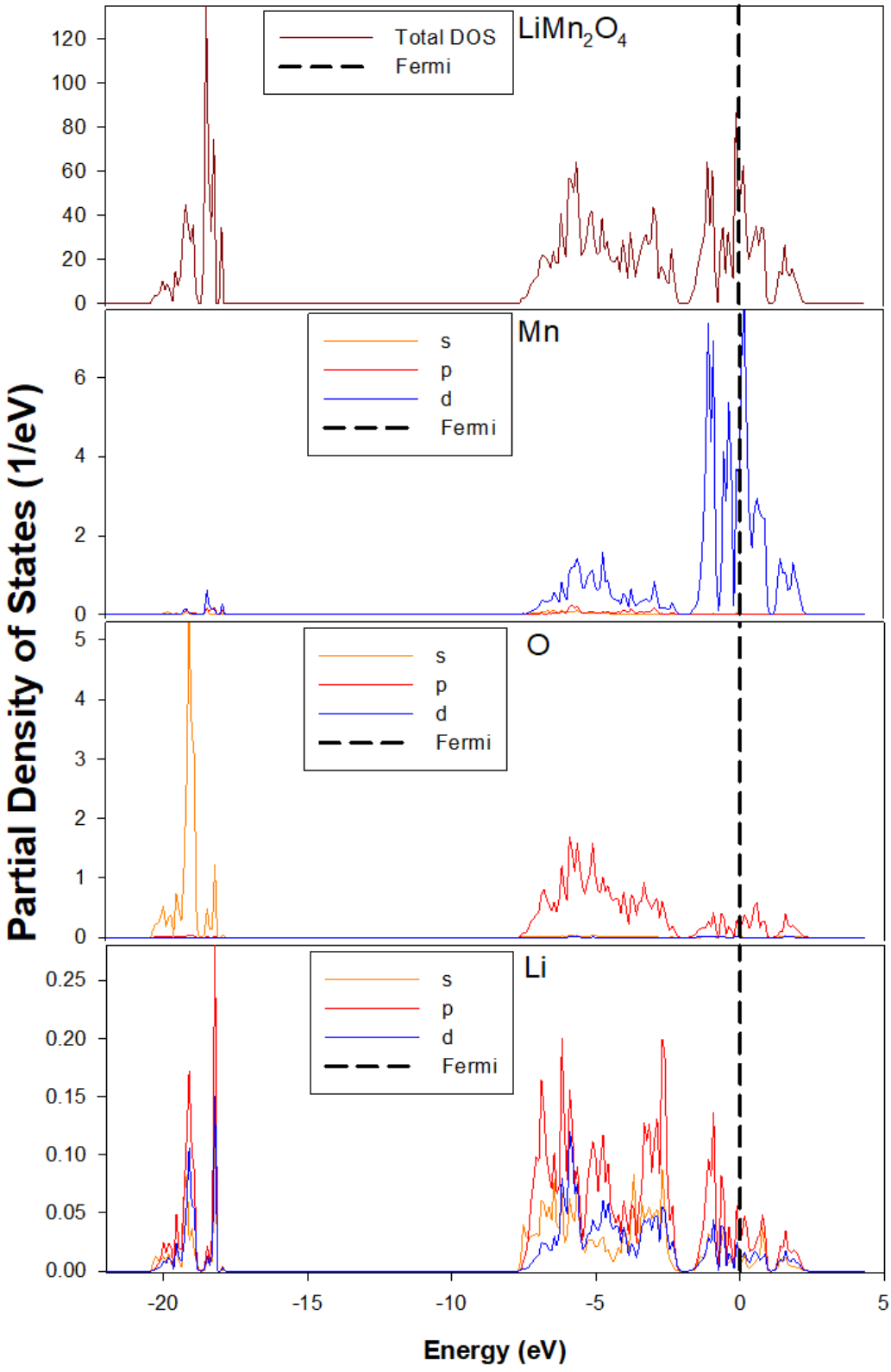

Figure 5-10: A partial density of states (PDOS), showing Li, Mn and O contribution for $LiMn_2O_4$ structures and their orbitals (s-orange, p-red, d-blue and total-brown). The Fermi energy is set as the energy at zero (Fermi-black).

5.4 Phonons

Phonons are described as lattice vibrations that draw an analogy between quanta of lattice vibration energy in a similar manner to photon representing a quantum of electromagnetic radiation. The theory behind phonons explains the phenomena of most solid-state such as stability, specific heat, melting, thermal and electrical conductivity, etc., which cannot be explained with static lattice theory [246].

The dispersion relations of propagation wave exhibit two types of phonons, namely an upper branch (optical branch) and a lower branch (acoustical branch). For the optical branch (in the long-wavelength limit) the two atoms in the unit cell move opposite to each other and the light mass amplitude is greater. For acoustical branch (in the long-wavelength limit) the displacement of both atoms has the same amplitude, direction and phase. The phonon dispersion and density of states (PHDOS) were obtained from the MEDEA-PHONON module, which implements a direct approach of harmonic approximation [216]. The VASP software follows a numerical method to evaluate the vibrational frequencies of all the systems that are discussed in the section, where the atoms are displaced in the direction of each Cartesian coordinate. The direct approach to lattice dynamics is based on the *ab-initio* evaluation of forces on all atoms produced by a set of finite displacements of a few atoms within respective crystal structures. The VASP code was used to make the force calculations with the supercell approach and the resulting data imported into the PHONON program. The calculation explores the full Brillouin zone and accounts for an interaction range of about 10 Angström. The asymmetric atoms are displaced by +/-0.02Å. Therefore, the calculated frequencies (THz) provide important information about the materials identification and analysis of their vibrational modes. As it is already been seen in the elastic properties and the phonon dispersion calculations show that the generated structures [$Li_2MnNi_3O_8$ ($LiMn_{0.5}Ni_{1.5}O_4$) $Li_4Ni_8O_{16}$ ($LiNi_2O_4$), $Li_{12}Mn_{17}Ni_7O_{48}$ ($LiMn_{1.42}Ni_{0.58}O_4$), $Li_4Mn_6Ni_2O_{16}$ ($LiMn_{1.5}Ni_{0.5}O_4$), $Li_4Mn_7NiO_{16}$ ($LiMn_{1.75}Ni_{0.25}O_4$) and $Li_4Mn_8O_{16}$ ($LiMn_2O_4$)] illustrate vibrational stability since there are only imaginary modes visible below the zero frequency in the phonon calculations as discussed in the next section.

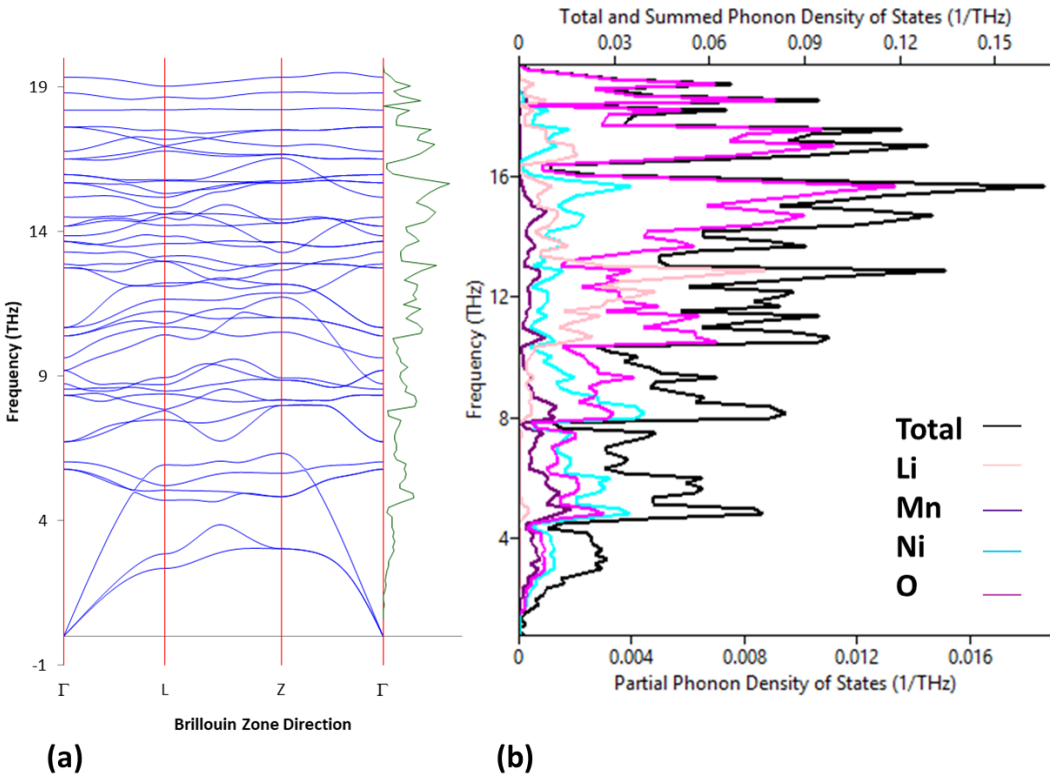

Figure 5-11: (a) Phonon dispersion spectrum (left panel) and (b) the corresponding phonon density of states (right panel) of configuration $LiMn_{0.5}Ni_{1.5}O_4$ (R-3m).

Figure 5-11 shows the phonon dispersion spectrum along with the high-symmetry points in irreducible BZ and the corresponding vibrational total and partial phonon density of states (PHDOS) for $LiMn_{0.5}Ni_{1.5}O_4$ (R-3m). The partial phonon density of states above contributed from Li, Mn, Ni and O are represented by different colours; light peach, violet, turquoise and purple. Phonon dispersion curves and density of states in Figure 5-11 are obtained from the structures of stable phases of an isotropic volume optimised binary ground state-diagram in Figure 5.1. The $LiMn_{0.5}Ni_{1.5}O_4$ (R-3m) supercell contains (56 atoms) and used k-points and cut-off energy in Table 5-3 to calculate phonon dispersion curves in Figure 5-11. At the Gamma point (Γ), normal modes correspond to a collective vibration of all atoms in the acoustic region of the $LiMn_{0.5}Ni_{1.5}O_4$ (R-3m) structure. The frequency of 19THz is observed along with the Γ point in the optical branches of the phonon vibrations. The acoustic modes are located below about 0–9THz and the optical modes lie above that particular range. Therefore Figure 5-11a, shows no soft modes phonons vibrations along the Brillouin Zone (BZ) direction, indicating that the structure dynamically stable at 0GPa. Figure 5-11b shows the total and partial density of

states for $LiMn_{0.5}Ni_{1.5}O_4$ (R-3m) and the contribution of each element into the phonon vibrations. The higher frequency region (about >8 THz) in Figure 5-11b is dominated by the displacement of O and Li. The lower frequency region about 0-8THz is dominated by Ni atoms followed by O and Mn atom. The Li atom contribution becomes lesser towards 0THz and ends before 4THz. However, PHDOS does not show any negative frequency overlapping at the 0 frequency or along any BZ direction, hence confirming the stability of this system. At 0GPa Figure 5-11a, the phonon dispersion curve displays soft frequency vibrations along the high symmetry direction in the Γ (0, 0, 0) which shows the vibrational stability of the structure.

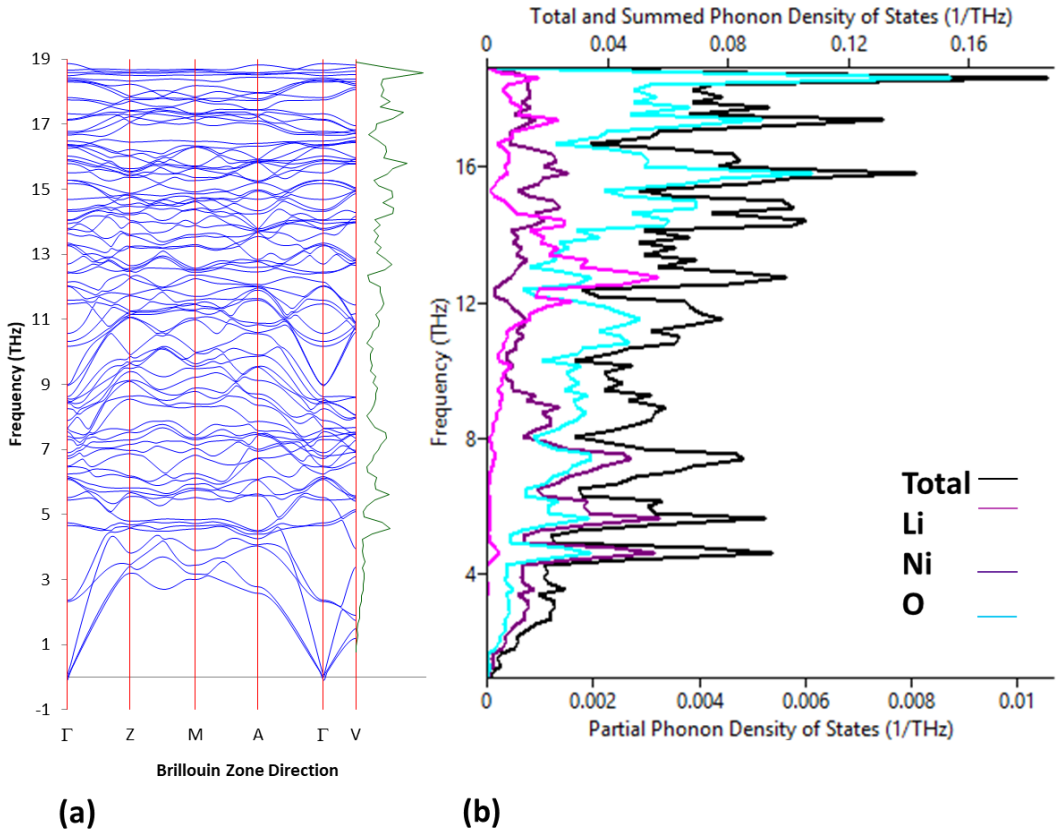

Figure 5-12: (a) Phonon dispersion spectrum (left panel) and (b) the corresponding phonon density of states (right panel) of configuration $LiNi_2O_4$ (Cm).

Figure 5-12 displays the phonon dispersion curves and partial phonon density of states (PHDOS) for $LiNi_2O_4$ (Cm) calculated along with several symmetry directions at zero pressure and zero Kelvin conditions. The partial phonon density of states above contributed from Li, Mn, Ni and O are represented by different colours; violet,

turquoise and purple Phonon dispersion and density of states in Figure 5-12 are obtained from the fully optimised (occupancy of Mn0.8 and Ni 0.31) binary diagram shown in Figure 5.5. We observe dispersed phonon modes (acoustic and optics branches) in the dispersion relations, this is in accordance with a primitive cell with 56 atoms. The frequency of 19(THz) is observed along with the Γ point in the optical branches of the $LiNi_2O_4$ (Cm). The gamma point (Γ) and normal modes correspond to a collective vibration of all atoms in the acoustic region of the system. The acoustic modes are located below about 0–5THz and the optic modes that lie above that particular range. In Figure 5-12a, no soft modes of the phonon vibrations along the Brillouin Zone (BZ) direction are observed, indicating the vibrational stability of the structure. Also shown in Figure 5-12b is the total and partial density of states of $LiNi_2O_4$ (Cm). The higher frequency region (about >8 THz) is dominated by the displacement of O and Li. The lower frequency region ranges from 0-5THz and is dominated by Ni atoms followed by O atoms, whereas Li atoms contribution becomes lesser towards 0THz and ends just after 4THz. However, the corresponding phonon density of states (right panel) does not show any negative frequency overlapping at the 0 THz point or along any BZ direction. It confirms the vibrational stability of $LiNi_2O_4$ (Cm) structure in the acoustic region along with the gamma point (Γ). $LiNi_2O_4$ (Cm) depicts that all the frequencies are positive showing the stability of the structure.

Figure 5-13 shows the calculated phonon dispersion relations and the corresponding vibrational total and partial phonon density of states (PHDOS) of $LiMn_{1.42}Ni_{0.58}O_4$ (Cm). The partial phonon density of states contributed from Li, Mn, Ni and O are represented by different colours; light peach, violet, turquoise and purple. Phonon dispersion relations and density of states in Figure 5-13 are obtained from the structures of stable phases from Figure 5-5. The k-points of 6x3x4 and cut-off energy of 910.739 eV containing (56 atoms) of supercells were used to calculate the phonon dispersion curves in Figure 5-13. The phonon dispersion spectrum of the $LiMn_{1.4}Ni_{0.5}O_4$ (Cm) phases were calculated along with the G-F-Q-Z-G directions and the phonon partial density of states (PHDOS) of $LiMn_{1.4}Ni_{0.5}O_4$ (Cm) structure. At the gamma point (Γ), normal modes correspond to a collective vibration of all atoms in the acoustic region of the $LiMn_{1.4}Ni_{0.5}O_4$ (Cm) structure.

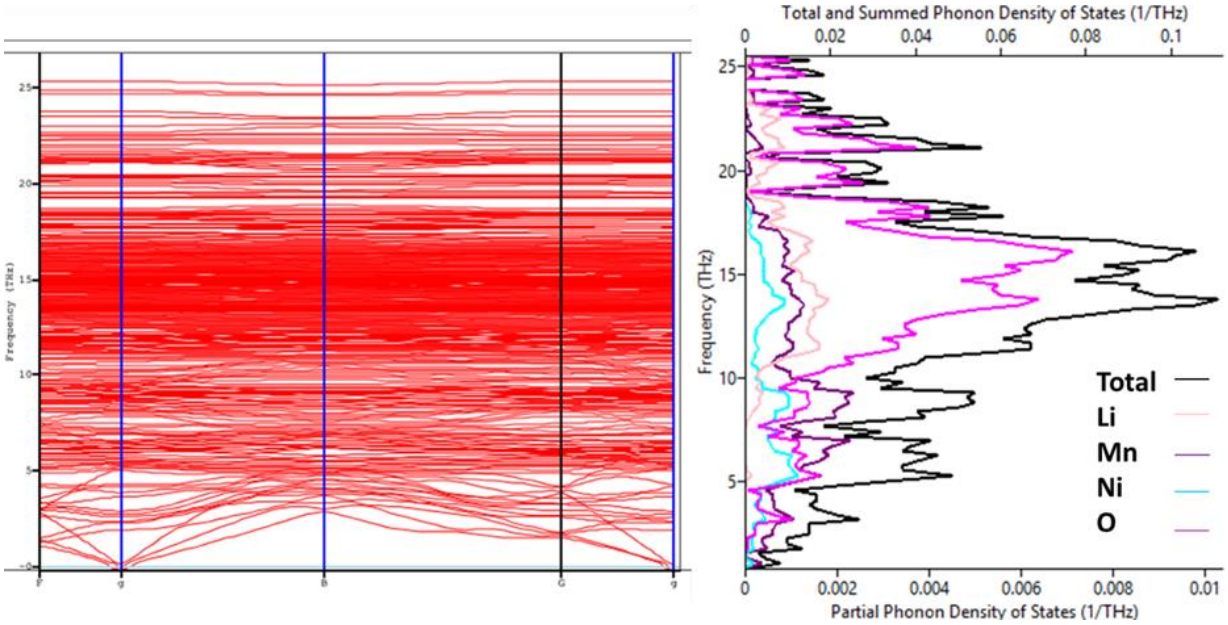

Figure 5-13: ((a) Phonon dispersion spectrum (left panel) and (b) the corresponding phonon density of states (right panel) of configuration $LiMn_{1.4}Ni_{0.5}O_4$ (Cm).

The highest frequency of 25(THz) is observed along with the Γ point in the optical branches of the $LiMn_{1.4}Ni_{0.5}O_4$. The acoustic modes are located below about 0–5THz and the optic modes lie above that particular range in Figure 5-13a. Therefore, Figure 5-13a shows no soft mode phonons vibrations along the Brillouin Zone (BZ) direction, indicating the vibrational stability of the system. Figure 5-13b shows the total and partial density of states of $LiMn_{1.4}Ni_{0.5}O_4$ (Cm) structure. Hence, in combination with the part phonon state density diagram presented in Figure 5-13b, the total DOS can be classified into two regions. The higher frequency region (about >10 THz) has a major contribution to the displacement of O. There are higher peaks that indicate that the lattice vibrations are very strong. The lower frequency region ranges from 0-5THz is dominated by Ni/Mn atoms and the dominance of the O frequency fades towards 0THz. The Li atom contribution becomes lesser towards 0THz and ends at 5THz. However, PHDOS does not show any negative frequency at 0THz or along any BZ direction. The curves of the strong peaks in the state density diagram correspond to the smoothing curves of the phonon dispersion spectra in the corresponding frequency range. In summary, the phonon spectrum in Figure 5-13 has no soft modes along with the symmetry directions indicating the dynamical stability. The curves of the strong peaks in the state density diagram

correspond to the smoothing curves of the phonon dispersion spectra in the corresponding frequency range.

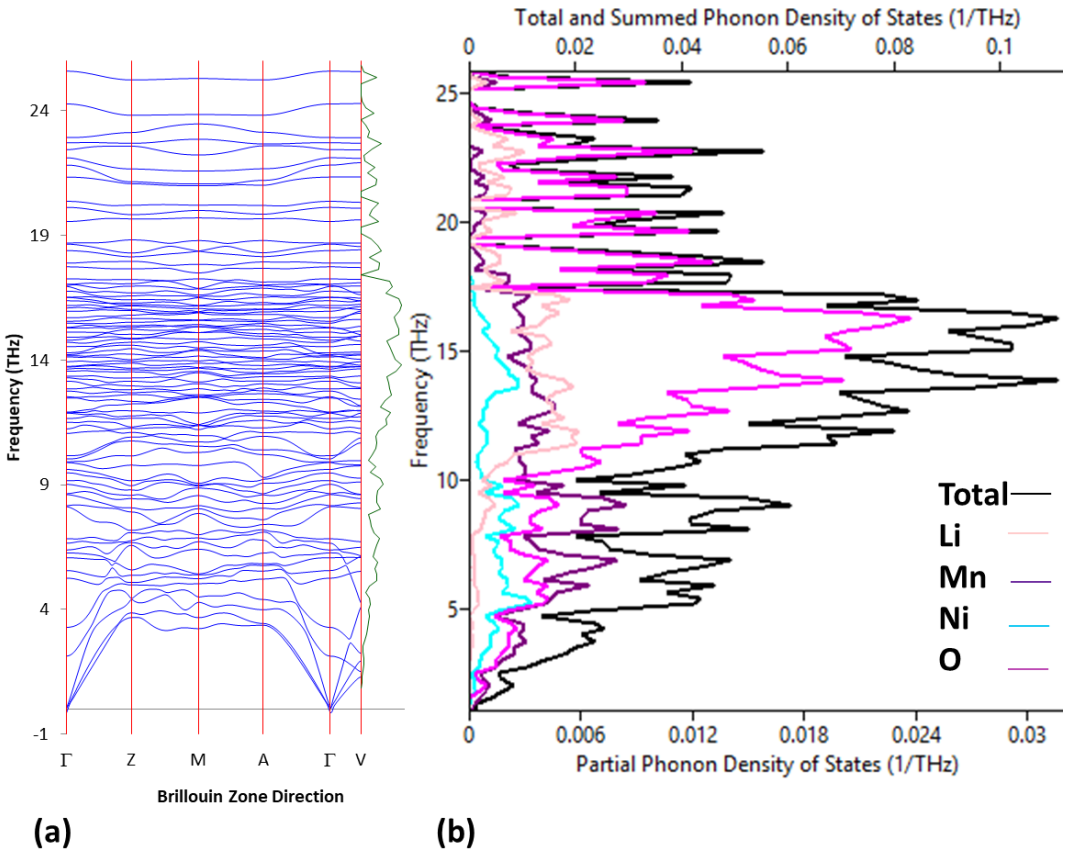

Figure 5-14: (a) Phonon dispersion spectrum (left panel) and (b) the corresponding phonon density of states (right panel) of configuration $LiMn_{1.5}Ni_{0.5}O_4$ (Cm).

The phonon band structure and phonon partial density of states (PDOS) of the Cm phase are shown in Figure 5-14. The partial phonon density of states above contributed from Li, Mn, Ni and O are represented by different colours; light peach, violet, turquoise and purple. Phonon calculations established the dynamical stability of the Cm phase of $LiMn_{1.5}Ni_{0.5}O_4$ in the view of the absence of imaginary frequencies. The low-frequency modes below this gap are mostly associated with the Mn, Ni and O atoms. A dispersed phonon spectrum exists between 9THz and 19THz, which divides the phonon spectrum structure into two major regions. The low-frequency region of the Cm phases from 0-9THz and the high-frequency region reaches approximately 25 THz. The O atom vibrations above the dispersed phonon

spectrum dominate the high-frequency region. The Li, Mn and Ni atoms slightly contribute to this region (19 to 25 THz). At the gamma point (Γ), normal modes correspond to a collective vibration of all atoms in the acoustic region of the following $LiMn_{1.5}Ni_{0.5}O_4$ (Cm) structure. The acoustic modes are located below about 0–5THz and the optic modes lie above that particular range. Figure 5-14b shows the total and partial density of states of $LiMn_{1.5}Ni_{0.5}O_4$ (Cm) structure and reveals that the lower frequency region about 0-9THz is dominated by Mn and O atoms, followed by the Ni atom, where Li atoms contribution becomes less towards 0 THz. However, PHDOS does not show any negative frequency overlapping at the 0 THz point or along any BZ direction, hence confirming the vibrational stability of $LiMn_{1.5}Ni_{0.5}O_4$ (Cm) structure in the acoustic region along with gamma point.

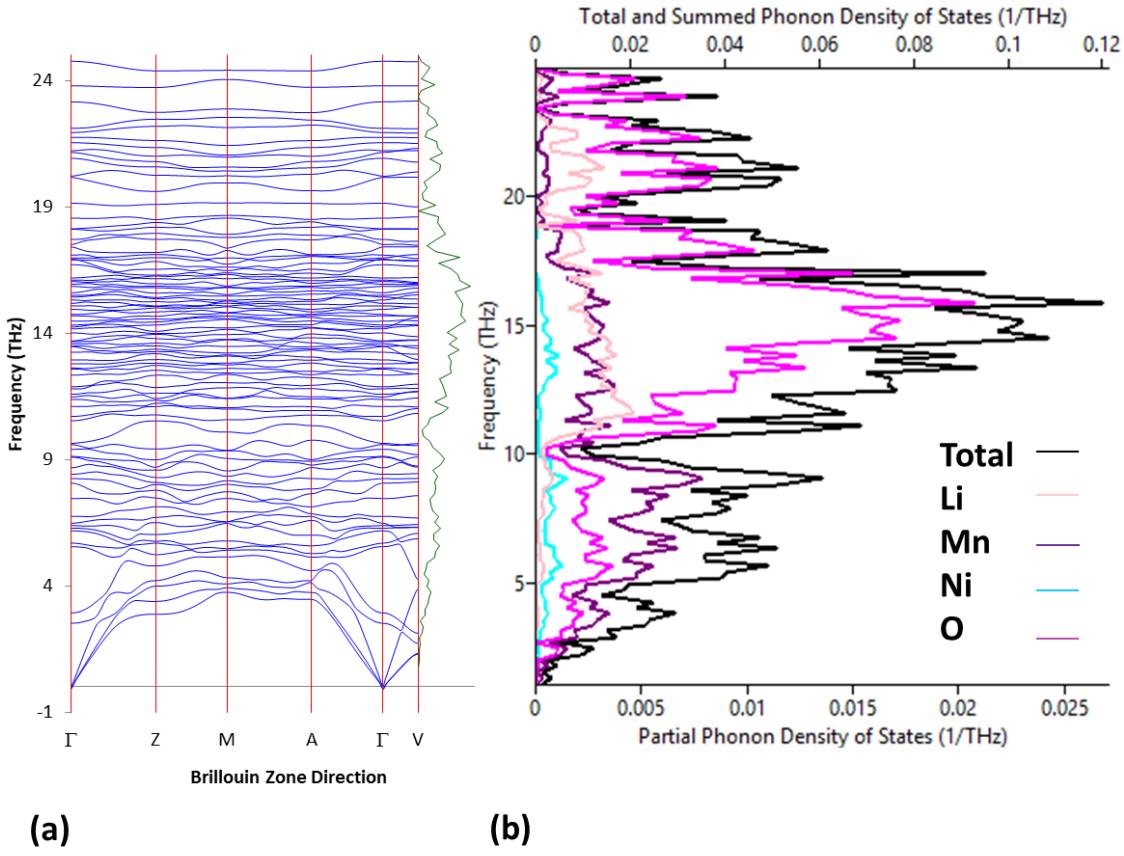

Figure 5-15: (a) Phonon dispersion spectrum (left panel) and (b) the corresponding phonon density of states (right panel) of configuration $LiMn_{1.75}Ni_{0.25}O_4$ (Cm).

Phonon spectrum and partial density of states are shown in Figure 5-15. The partial phonon density of states above contributed from Li, Mn, Ni and O are represented

by different colours; light peach, violet, turquoise and purple. No imaginary frequencies are found at a wave vector in the whole BZ for all studied phase at equilibrium volume. The crystal structure of the phases contains 56 atoms, showing no gap in the phonon branches. Phonon dispersion curves and density of states in Figure 5-15 are obtained from the structures of stable phases from a full optimised binary diagram in Figure 5.5. In the optic region (19-25THz), the main contribution to the phonon spectrum comes from the dynamics of O atoms due to its smallest mass. The strong overlap exists between acoustic and some low-frequency optical phonon branches. At the gamma point (Γ), normal modes correspond to a collective vibration of all atoms in the acoustic region of the $LiMn_{1.75}Ni_{0.25}O_4$ (Cm) structure. However, most phonon bands in Z, M and A directions are rather flat. Therefore Figure 5-15a shows no soft mode phonons vibrations along the Brillouin Zone (BZ) direction indicating the vibrational stability of the structure stable at 0GPa. Figure 5-15b shows the total and partial density of states of $LiMn_{1.75}Ni_{0.25}O_4$ (Cm) structure. The lower frequency region about 0-10THz is dominated by Mn and O atoms and a minimum contribution of Ni being lesser towards 0 THz. The phonon partial density of states does not show any negative frequency overlapping at the 0 THz point or along any BZ direction, confirming the vibrational stability of the phonon spectrum along with gamma point (Γ).

Phonon dispersion curves and the density of states in Figure 5-16 are obtained from the Binary diagram shown in Figure 5.5. The partial phonon density of states above contributed from Li, Mn, Ni and O are represented by different colours; violet, turquoise and purple. The phonon dispersions in the supercell are shown in Figure 5-16. We used 7x7x4 plane-wave basis set and the 899.034 eV cut-off energy-containing (56 atoms) to calculate the phonon dispersion in Figure 5-16. The figure above of the phonon dispersion curves contains the highest number of high-symmetry points of the Brillouin zone: Γ-Z, Z-M, M-A, A- Γ and Γ-V and the corresponding vibrational total and partial phonon density of states (PHDOS) for $LiMn_2O_4$ (Cm). The gamma point (Γ), corresponds to collective phonon vibrations of all atoms in the acoustic region of the $LiMn_2O_4$ (Cm) structure. Then the acoustic modes ranging from 0–4THz and the optic modes range being above that particular range.

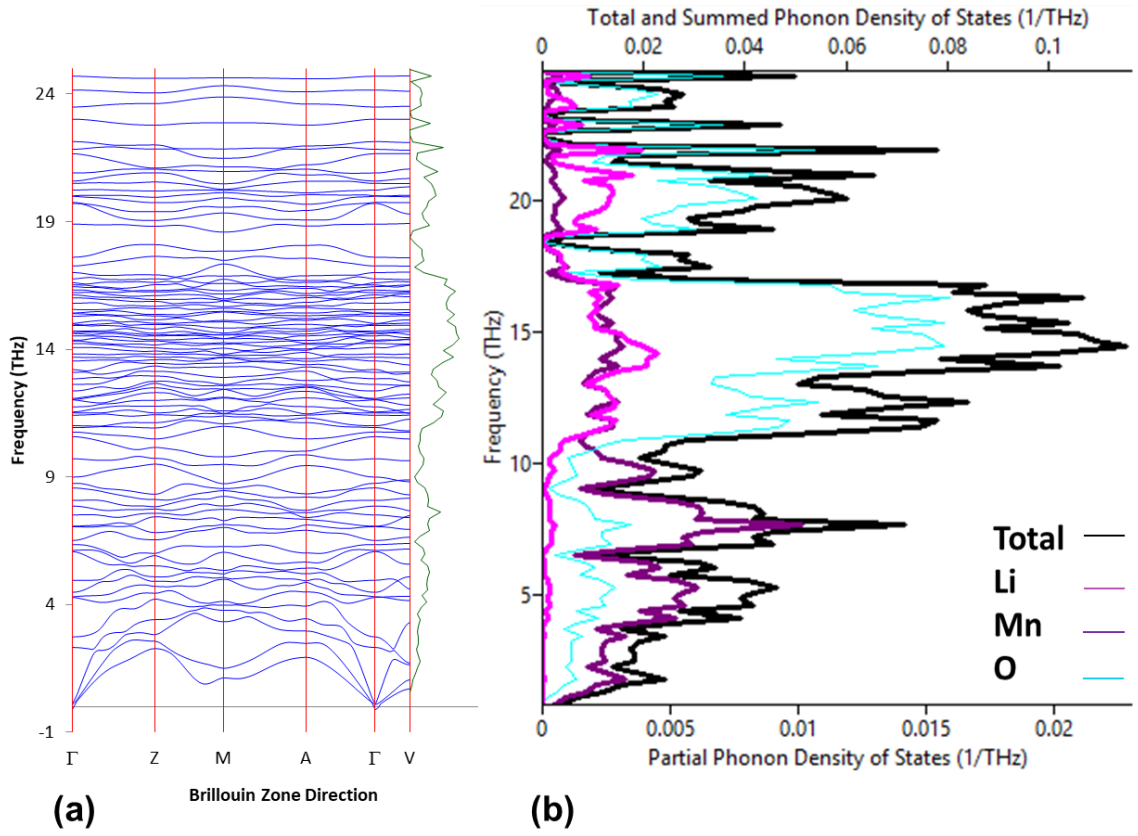

Figure 5-16: (a) Phonon dispersion spectrum (left panel) and (b) the corresponding phonon density of states (right panel) of configuration $LiMn_2O_4$ (Cm).

The frequency of 25(THz) is observed along with the Γ point of the optical branches of the system. Figure 5-16a shows no soft mode phonons vibrations along the Brillouin Zone (BZ) direction indicating the vibrational stability of the system. Figure 5-16b shows the total, partial density of states and each element contribution in confirming the findings of Figure 5-16a. The lower frequency region from 0-10THz is dominated by Mn and O atoms and the minimum Li atoms contribution fading towards 0 THz. Therefore, PHDOS does not show any negative frequency along any BZ direction and is in agreement with Figure 5-16a, confirming that the $LiMn_2O_4$ (Cm) structure is dynamically stable.

Chapter 6

Site-occupancy disorder

In this chapter, we present and discuss the computational study of the $Li(Mn_{1-x}Ni_x)_2O_4$ solid solution using the site-occupancy disorder program. We used the program to generate a complete configurational space and the inequivalent configurational subspace for each spinel $Li(Mn_{1-x}Ni_x)_2O_4$ composition. The chapter also reports on the mixing thermodynamics and average voltage of lithium intercalation for all the Ni concentrations and their dependence on the temperature for the most energetically stable composition.

6.1 Structure Description and Calculation

The cation ordering was determined based on the configurational entropy. The approach presented also shows that moderate Ni doping of the $LiMn_2O_4$ leads to a substantial change in the average voltage of lithium intercalation, suggesting an attractive route for tuning the cathode properties of this spinel. Then, the calculations were carried out using the spin-polarised density functional theory (DFT) and using the Vienna *Ab-initio* Simulation Package (VASP) [138] [236] [137]. The following functionals were employed the Perdew, Burke, and Ernzerhof corrected for solids (PBE_{sol}) functional [113], included the long-range dispersion corrections via the semi-empirical method of Grimme with the Becke and Johnson damping [D3-(BJ)) [247] [248]. The cut-off for the kinetic energy of the plane wave basis 730 eV was set and the effective Hubbard parameters of U_{eff} = 4.0 eV for Mn and 5.5 eV [249]) for Ni [124]. A *Γ*-centred ***k***-point mesh with a uniform spacing of. 0.16 $Å^{-1}$ was adopted for the Brillouin-zone integrations [134].

The site occupancy disorder (SOD) code was used to generate the symmetry-adapted ensemble of configurations within the disordered $Li(Mn_{1-x}Ni_x)_2O_4$ solid solution and carry out the thermodynamic analysis [248]. Within this approach, SOD produced complete configurational space for each Ni concentration in a 1x1x1 supercell of the spinel conventional cubic unit cell, followed by the reduction to the

subspace of the symmetrically inequivalent configurations. The configurations were constructed via atomic substitutions in $LiMn_2O_4$, using the group of symmetry operators of the space group $Fd\bar{3}m$ (No. 227) of the parent structure. There are two configurations that were considered equivalent if they can be interconverted following an isometric transformation. Table 7-1 displays the prohibitively large total number of configurations (*N*) for each Ni concentration in the complete configuration space, which can be reduced by more than two orders of magnitude to the symmetrically inequivalent configurations (*M*) in the reduced configurational space. It is worth noting that only those cell with compositions containing an even number of Ni atoms were chosen in order to further reduce the number of simulations.

Table 6-1: Total number of configurations (M) and the number of symmetrically inequivalent configurations (N) for each nickel concentration in $LiMn_{2-2x}Ni_{2x}O_4$.

Cell composition	*x*	*N*	*M*
$Li_8Mn_{16}O_{32}$	0.0000	1	1
$Li_8Mn_{14}Ni_2O_{32}$	0.1250	120	3
$Li_8Mn_{12}Ni_4O_{32}$	0.2500	1820	22
$Li_8Mn_{10}Ni_6O_{32}$	0.3750	8008	65
$Li_8Mn_6Ni_{10}O_{32}$	0.6250	8008	65
$Li_8Mn_4Ni_{12}O_{32}$	0.7500	1820	22
$Li_8Mn_2Ni_{14}O_{32}$	0.8750	120	3
$Li_8Ni_{16}O_{32}$	1.0000	1	1

From the subspace of the symmetrically inequivalent configurations, we have used statistical mechanics to estimate the thermodynamic properties. We have assumed a Boltzmann-like distribution for the estimation of the occurrence probability $\tilde{P}_m$ at a temperature T of each inequivalent configuration m of energy E_m according to the equation:

$$\tilde{P}_m = \frac{\Omega_m}{Z} \exp(-E_m/k_B T), \tag{92}$$

where Ω_m represents the degeneracy or number of times that a given configuration is repeated in the complete space of all configurations, m can take integer values from 1 to$M$, k_B is the Boltzmann constant and the configurational partition function

$$Z = \sum_{m=1}^{M} \Omega_m \exp(-E_m/k_{\mathrm{B}}T) \quad (93)$$

ensures that the sum of the probabilities of the complete configurational space is equal to 1.The Helmholtz free energy of mixing ΔF_{mix} of the solid solution was obtained as

$$\Delta F_{\mathrm{mix}} = F[\mathrm{Li(Mn_{1-x}Ni_x)_2O_4}] - (1-x)F[\mathrm{LiMn_2O_4}] - xF[\mathrm{LiNi_2O_4}] \quad (94)$$

where the configurational free energies $F = -k_B T \ln Z$ (95)

were calculated directly from the partition function. The equilibrium geometries and energies of all configurations in the reduced configurational space of the $Li(Mn_{1-x}Ni_x)_2O_4$ solid solution was obtained from the DFT calculations. The results indicate that usually, only one configuration is more stable than the rest for the entire Ni concentration range, suggesting a large degree of order within the $LiMn_2O_4$-$LiNi_2O_4$ system.

6.2 Mixing of thermodynamics

In this section, the mixing of enthalpies of nickel-doped spinel ($Li(Mn_{1-x}Ni_x)_2O_4$; where $0 \leq x \leq 1$ were considered. The $E[(Li(Mn_{1-x}Ni_x)_2O_4]$ is the average lattice energy $Li(Mn_{1-x}Nix)_2O_4$ calculated during the thermodynamics of mixing and $E[LiMn_2O_4]$ and $E[LiNi_2O_4]$ are lattice energies for the manganese and nickel respectively. Figure 6-1 shows the mixing of enthalpies of the $Li(Mn1\text{-}xNi_x)_2O_4$ system. Both curves have negative values of ΔF_{mix} , which indicates the formation of stable solid solutions. The most energetically stable structure has the lowest energy of ΔF_{mix} at both 300 and 1000K at the intermediate cell composition of $Li_8Mn_{12}Ni_4O_{32}$ which agrees with experimental findings that $LiNi_{0.5}Mn_{1.5}O_4$ is the most promising and attractive material because of its acceptable stability, good cyclic property and relatively high capacity [69].

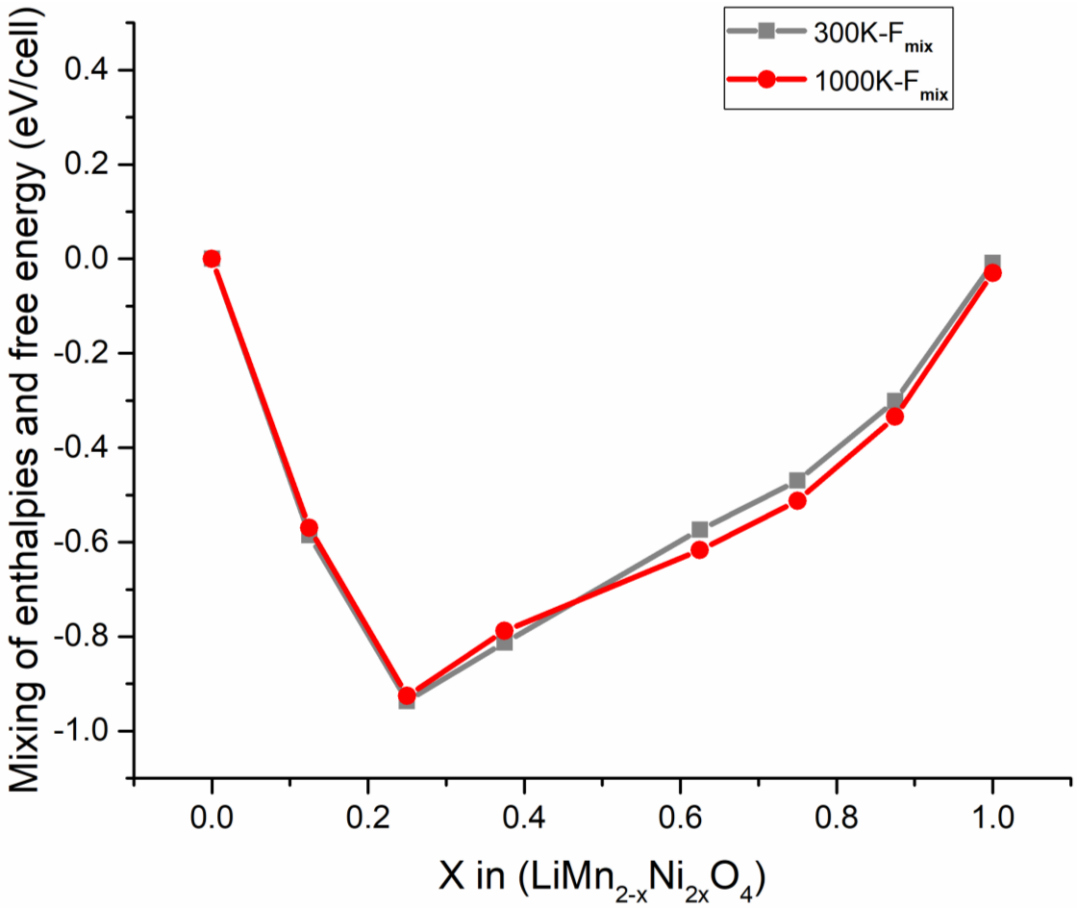

Figure 6-1: Calculated mixing of enthalpies for Ni-doped ($Li(Mn_{1-x}Ni_x)_2O_4$ solid solution for different unit cells. The solid lines are the free energy of mixing (ΔF_{mix}).

The calculations on the ordered cell composition of $Li_8Mn_{12}Ni_4O_{32}$ ha a lower energy and its weight as compared to the other 21 configurations with the probability above 99% at 300 K and 85% at 1000 K. It could be all due to the magnetic interactions which play a crucial role in the thermodynamics of mixing of these solid solutions, especially at different temperatures. Therefore, there have been various studies reported on $Li(Mn_{1-x}Ni_x)_2O_4$; such as synthetic method, thermal stability, effects of ordered and disordered local structure, cation ordering, particle size, and composition change [250] [251] [252] [253] [254]. Figure 6-1 also shows a minimum difference of ΔF_{mix} where all configurations enter with the same weight in energy, and with the introduction of temperature. Also, it shows the presences of low-energy cation arrangements. In conclusion Figure 6-1 is a miscible constituent because of the negative ΔF_{mix} structures, hence the existence of thermodynamically stable structures $Li_8Mn_{12}Ni_4O_{32}$ ($LiMn_{1.5}Ni_{0.5}O_4$) with the lowest energy. The graph also shows that x = 0.25, equivalent to 0.5 Ni atoms per formula unit has the lowest energy at any temperature.

6.3 Configurational Entropies

In Figure 6-2 we have plotted the variation of the configurational entropy of the solid solution for $LiMn_{0.25}Ni_{0.75}O_4$ with $0 \leq x \leq 1$ as calculated in the supercell at different temperatures. The composition x=0 and x=1 correspond to the Ni4+ substitution of any of the 16 equivalent Mn4+ in the supercell, therefore all the 16 configurations are equivalent as shown in Figure 6-2 and the configurational entropy shows an increasing progression with respect to temperature. However, for the paring of the x values (shown in Figure 6-2) of the nickel concentration, there are similarities in an increasing progression and the shape with the increasing temperature except when x=0.25 and x=0.75 where their shapes differ and there exist bigger entropy difference as compared to other nickel concentration paring. There are several experimental works done on the investigation of Ni and Mn ordering in $LiMn_{1.5}Ni_{0.5}O_4$ samples by annealing at 973.15 K [251]. The variation of the configurational entropy of the $LiMn_{2x-2}Ni_{2x}O_4$ system in Figure 6-2 with increasing temperature indicates ordering from 300K and a possible disordering at a higher temperature (at above 1000 K) due the existent of a full configurational equilibrium.

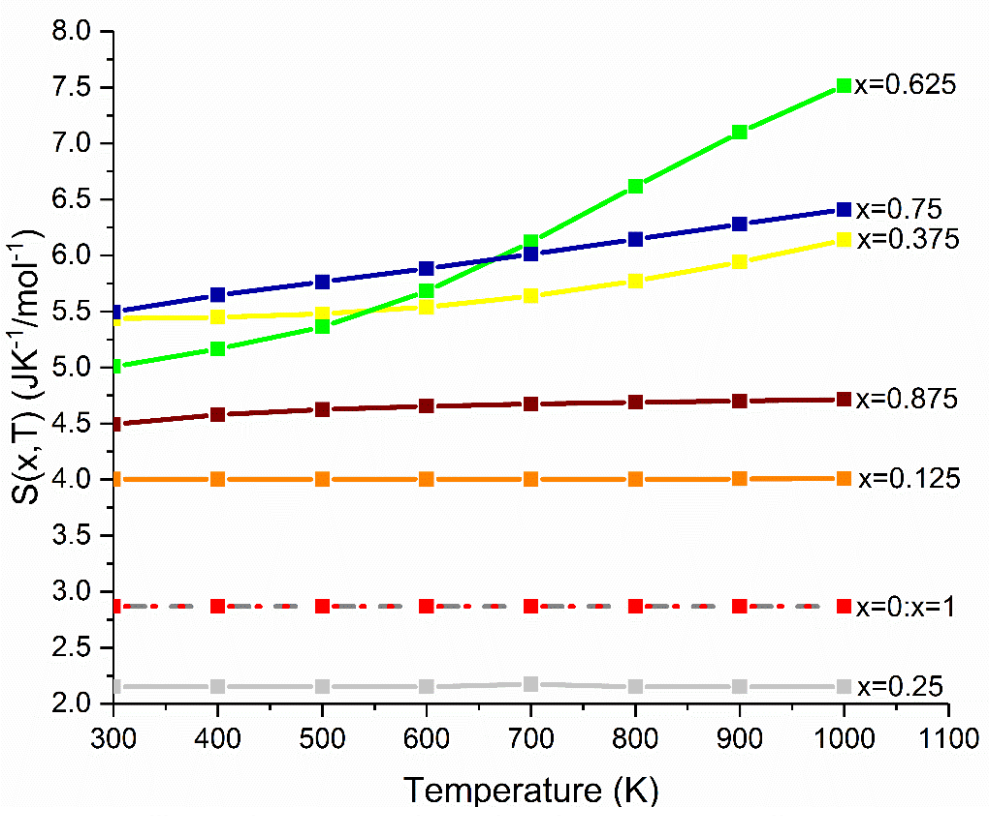

Figure 6-2: An illustration of configurational entropy for different temperatures calculated in a supercell.

6.4 Average voltage Intercalation

The fully lithiated and de-lithiated forms of the nickel-manganese oxide spinel were modelled starting from the conventional cubic unit cell, while the body-centred cubic (bcc) lithium was simulated using the asymmetric unit cell. For simplicity, the normal cation arrangement for the spinel phases was used, where Li is confined to the tetrahedral positions and Mn as well as Ni is limited to occupy the octahedral holes, ignoring the partial inversion degree x = 0.30 reported experimentally [175]. It has been indicated that although all lithiated transition metal oxides are stable in the normal spinel structure, the stability preference changes with the discharging process. Thermodynamically, during the discharging process transition metal oxides should transform to the lowest energy structures of the corresponding binary oxides. Since the thermodynamic ground state is often prohibited by kinetic limitations [192]. For spinel crystal structure, along with the tetrahedral 8a sites and the octahedral 16d sites, there are octahedral 16c sites which are vacant for an ideal spinel. However, the delithiated transition metal oxides often have transition metal atoms in these non-spinel sites (16c), as it was seen in case of Ni, Ti, Cr, Mn and Fe [192]. Instead of attaining the thermodynamic ground state, kinetically, it is more realistic than a spinel-related lowest energy state is accessed by the delithiated oxide. We considered the lowest energy one among these structures to be the possible ground state accessible to the delithiated oxide Figure 6-3.

The equation (96) is used to obtain Figure 6-3 and it indicates that the total energy of three compounds is required to predict the average intercalation voltage. Then the insert is the average voltage as a function of the configurational equilibrium temperature at T= 0K and the intercalation voltage for lithium [255] relates to the aspects of the electronic structure.

$$V = [E(Li(Mn_{1-x}Ni_x)_2O_4) - E(Mn_{2-2x}Ni_{2x}O_4) - E(Li)] \quad (96)$$

The figure below shows the average intercalation voltage of ordered low energy structures of the inequivalent configurations (N). The Li^+ intercalated into tetrahedral sites are energetically more stable for Li-rich compositions, as they share a face with Li^+ on the Mn/Ni site in the cubic transition metal. Figure 6-3 shows how the

average voltage of intercalation of $Li(Mn_{1-x}Ni_x)_2O_4$ is directly related to the energies of the end state (charging and discharging), where the highest average voltage is 4.866 V at x =0.25 of the nickel concentration. There have been several investigations on the spinel-structured $LiMn_{1.5}Ni_{0.5}O_4$ (LMNO)

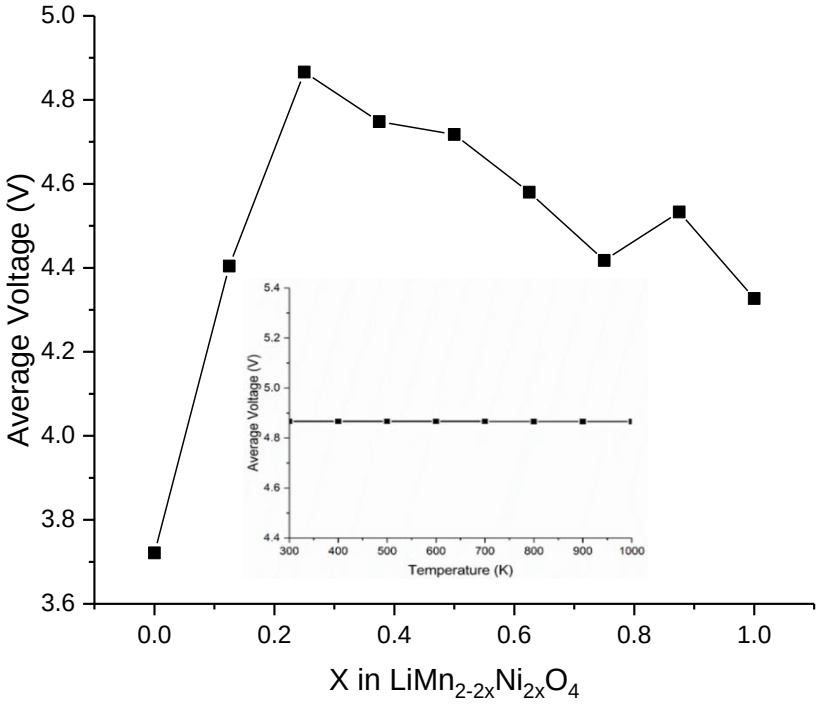

Figure 6-3: Calculated average voltage as a function of inversion degree. In the insert, the average voltage of the stable composition ($LiMn_{1.5}Ni_{0.5}O_4$).

which has attracted great attention, due to its higher working voltage (4.7 V) in comparison with the commercialised cathodes such as $LiFePO_4$ (3.4 V), $LiCoO_2$ (3.9 V) and $LiMn_2O_4$ (4.1 V) [256] [257] and which are lower than the calculated $LiMn_{1.5}Ni_{0.5}O_4$ voltage of (4.866 V) shown in Figure 6-3. The energetically stable spinel structure $LiMn_{1.5}Ni_{0.5}O_4$ has an average voltage of 4.866 V which agrees well with the 5 V spinel cathode $LiMn_{1.5}Ni_{0.5}O_4$ that has high operating voltage (~4.8 V) [258] [259]. However, from the stable composition of $LiMn_{1.5}Ni_{0.5}O_4$, the structure has a probability that is greater than zero. The inserted diagram in Figure 6-3 shows that there is no change in the average voltage when the temperature increases.

Chapter 7

Conclusions and Recommendations

7.1 Conclusions

$LiMn_2O_4$ is ideal as a high-capacity Li-ion battery cathode material by its low toxicity, low cost, and the high natural abundance of Mn. Among several cathode materials, the spinel structure has attracted considerable attention for secondary lithium-ion batteries due to its high intrinsic safety, low cost and high voltage (4.7 V vs. Li/Li+) [260] [261] [262]. There has been numerous investigations that proposed Ni as a suitable dopant to improve the structural stability, electrochemical performance of the $LiMn_2O_4$ materials, the average lithium intercalation voltage and the thermodynamics of the Ni incorporation, where $LiMn_{2-x}Ni_xO_4$ spinel has a concentration range $0 \leq x \leq 2$. Therefore, making lithium nickel manganese oxide (LNMO, $LixNi_{0.5}Mn_{1.5}O_4$) an attractive high-potential cathode material for high energy lithium-ion batteries due to its high operating potential around 4.7 V vs. Li/Li+ [61] [263], its high rate capability, structural stability and the absence of cobalt [264]. To meet the ongoing pressing demands of electric vehicles (EVs), the LMNO offers a stable spinel crystalline structure and good cycling durability during charge or discharge of the battery [265]. In contrast to conventional cathode materials (e.g., $LiCoO_2$ and $LiMn_2O_4$), LNMO and its derivatives have good rate capability, low cost, and high safety characteristics; moreover, providing 20% more energy density due to their high voltage [266].

However, the implementation of LNMO electrodes still faces several deterrent issues. Firstly, the flat potential where the voltage is invariant with state of charge (SOC) during charge or discharge processes and LMNO materials exhibiting relatively low discharge capacities of ~110–130 mAhg_1 [267] [268] [269] [270] [271] [272]; Secondly, the LMNO materials are still unsatisfactory for the commercial application due to the intrinsic slow ionic diffusivity and low electronic conductivity [269] [270] [271]. Thirdly, the crystal structure of LMO is severely degraded after a few operational cycles of lithiation and de-lithiation due to the strong Jahn-Teller

(JT) distortions of the octahedrally coordinated high-spin Mn^{3+} cation, especially below the Verwey-like temperature of T_V = 283.5 K [273]. In order to address some of these impediments, the current study has addressed the thermodynamics of the Ni incorporation in $LiMn_2O_4$. In this thesis, three computational modelling approaches on the study of $LiMn_{2-x}Ni_xO_4$ spinel via tuning of the Ni concentration from 0≤x≤2.have been employed, i.e. the VCA approach, cluster expansion and site occupancy disorder methods.

Firstly we used the density functional theory methods to investigate structural and electronic properties, pressure dependence and mechanical stability. The calculations were performed using the well-established total energy CASTEP code in conjunction with the Virtual Crystal Approximation, which is an approach for dealing with disordered systems in first-principles calculations. Solid solution VCA was applied to generate various concentrations of Ni doped $LiMn_2O_4$ in the range 0≤x≤2. The GGA-PBE approach implemented in DFT was successfully used to investigate the above-mentioned properties.

The calculated lattice parameters for spinel's $LiMn_2O_4$ and $LiNi_{0.5}Mn_{1.5}O_4$ are in good agreement with experimental and literature results [221] [223]. In addition, structural parameters for $LiNi_{0.25}Mn_{1.75}O_4$, $LiNi_{0.75}Mn_{1.25}O_4$ and $LiNi_{0.875}Mn_{1.125}O_4$ were predicted. The Mn-O bond lengths were measured from the ground state structures with an average value of 1.9 Å, which is in good agreement with previous studies [224] [225]. Such studies showed that the shortening of the average chemical bond length of Mn(Ni)–O in $LiNi_{0.5}Mn_{1.5}O_4$ increases the mean chemical bond energy and enhances structural stability. Hence, the $LiNi_{0.5}Mn_{1.5}O_4$ system has a high cycling performance as compared to $LiMn_2O_4$. In the current study nickel doped systems are predicted to be stable with a smaller Mn(Ni)-O bond length. It was further observed that the bond length reduces with an increase in pressure. Also, the variation in bond lengths with applied pressure was computed. This gives an account of the behaviour of relative lattice constant (a) and (a/a_0) which increases as the pressure decreases. The two systems with different nickel/manganese ratio, i.e., $LiNi_{0.25}Mn_{1.75}O_4$ and $LiNi_{0.75}Mn_{1.25}O_4$ predicted the same results in terms of both

structural properties and energetics. This suggests further investigations on different compositions with related atomic weight percentages.

Furthermore, the total density of states was calculated to study the stability of pure and nickel doped spinel $LiMn_2O_4$. The total density of states at the Fermi-level indicated that the peaks of all the compositions are overlapping from the valence to the conduction band. Thus, all compositions are metallic in their ground state, since there is no band gap from the valence band to the conduction band. Similarly, partial densities of states have been calculated and predicted all the compositions to be metallic. The introduction of the dopant Ni/Mn-3d in the 4 systems has an influence on the Li-2s and O-3p, hence their contribution becomes significant. As observed with structural properties, these two systems $LiNi_{0.25}Mn_{1.75}O_4$ and $LiNi_{0.75}Mn_{1.25}O_4$, showed similar electronic properties. Pressure dependences of the density of states revealed that the highest peaks for $LiNi_{0.5}Mn_{1.5}O_4$ and $LiNi_{0.875}Mn_{1.125}O_4$ are intercepted by the Fermi level and move away from it. It is worth noting that when pressure is applied to the $LiNi_{0.5}Mn_{1.5}O_4$ system, the behaviour of the electrons is not influenced. This affirms that this composition is the most stable as reported in the literature.

The mechanical properties of spinel and nickel doped $LiMn_2O_4$ were successfully calculated. The calculated bulk, Young and shear moduli for pure spinel $LiMn_2O_4$ and $LiNi_{0.5}Mn_{1.5}O_4$ are, at 0 GPa, are in agreement with the literature results [228] [229]. In addition for a cubic system to be mechanically stable, such moduli should be positive. The results showed that the predicted elastic properties at 0GPa are mechanically stable. However, when pressure is applied to the system, there is inconsistency in terms of stability. At 40 and 50GPa $LiNi_{0.5}Mn_{1.5}O_4$ and $LiNi_{0.875}Mn_{1.125}O_4$ appear to be mechanically unstable. Consequently, the B/G ratio showed brittleness at 40 and 50GPa for both $LiNi_{0.5}Mn_{1.5}O_4$ and $LiNi_{0.875}Mn_{1.125}O_4$ systems. While the tetragonal shear modulus *C'* is consistently negative for all the compositions.

Secondly, cluster expansion formalism was used to investigate nickel doped LMO phase stabilities, as implemented in the UNCLE code. The method determines

stable multi-component crystal structures and ranks metastable structures by the enthalpy of the formation while maintaining the predictive power and accuracy of first-principles density functional methods. The ground-state phase diagram generated various structures with different concentrations and symmetries. The isotropically volume optimised and fully optimised structures produced the cross-validation score of 1.1 meV and 1.4 meV, which is an indication of a good cluster expansion since it is less than 5 meV per active position. The mechanical, electronic and vibrational properties of all identified structures on the isotropically optimised volume and fully optimised binary diagram were calculated to depict their stability. Mechanical properties of the mixture, $LiNi_2O_4$-$LiMn_2O_4$, were successfully calculated for isotropic optimised volume. The $LiMn_{0.5}Ni_{1.5}O_4$ (isotropic) is found to be tetragonal (I) with 6 independent elastic constants (C_{11}, C_{12}, C_{13}, C_{33} and C_{44}). The tetragonal $LiMn_{1.5}Ni_{0.5}O_4$ becomes mechanically stable because the structure satisfies the necessary and sufficient Born mechanical stability criteria for tetragonal and the structure is anisotropic (A>1). Mechanical properties of the mixture, $LiNi_2O_4$-$LiMn_2O_4$, were also successfully calculated for full optimisation. The triclinic structures $LiNi_2O_4$, $LiMn_{1.4}Ni_{0.6}O_4$, $LiMn_{1.5}Ni_{0.5}O_4$, $LiMn_{1.75}Ni_{0.25}O_4$ and $LiMn_2O_4$ in Table 5-5 are mechanically stable and anisotropic (A>1). However, the structures shown in Table 5-6 are ductile owing to the G/B < 0.5. The non-existence of band gaps at the Fermi level for all structures showed that the $LiMn_{0.5}Ni_{1.5}O_4$ (isotropic), $LiNi_2O_4$, $LiMn_{1.4}Ni_{0.6}O_4$, $LiMn_{1.5}Ni_{0.5}O_4$, $LiMn_{1.75}Ni_{0.25}O_4$ and $LiMn_2O_4$ systems are metallic. As already illustrated by the elastic properties, the phonon dispersion calculations show that the generated structures ($LiMn_{1.4}Ni_{0.6}O_4$, $LiNi_2O_4$, $LiMn_{1.4}Ni_{0.6}O_4$, $LiMn_{1.5}Ni_{0.5}O_4$, $LiMn_{1.75}Ni_{0.25}O_4$, and $LiMn_2O_4$) have no negative values along the gamma direction and the phonon density of states also depict no soft modes below the 0 THz. Consequently all structures can be regarded as being vibrationally stable.

Lastly, we employed density functional theory calculations with a Hubbard Hamiltonian (DFT+*U*) to investigate the thermodynamics of mixing of the $Li(Mn_{1-x}Ni_x)_2O_4$ solid solution with the range of $0 \leq x \leq 1$. The site occupancy disorder (SOD) code was used to generate the symmetry-adapted ensemble of configurations within the disordered $Li(Mn_{1-x}Ni_x)_2O_4$ solid solution and to carry out the thermodynamic

analysis. All configurations were constructed via atomic substitutions in $LiMn_2O_4$, by using the group of symmetry operators of the space group $Fd\bar{3}m$ (No. 227) of the parent structure. Site-occupancy disorder was employed successfully to find stable structures and $LiMn_{1.5}Ni_{0.5}O_4$ was depicted as most stable. The results indicate that any small change in the tuning of the Ni concentration, achieved via temperature change during the thermodynamics of mixing and controlling of the lithium intercalation is reflected in the properties of the stable structure. The most energetically stable structure showed the lowest energy of ΔF_{mix} at both 300 and 1000K at an intermediate Ni composition of $LiMn_{1.5}Ni_{0.5}O_4$ which agrees with experimental findings that $LiNi_{0.5}Mn_{1.5}O_4$ is the most promising and attractive material because of its acceptable stability, good cyclic property and relatively high capacity. The configurational entropy showed an increasing progression with respect to temperature. However, for the pairing of the x values of the nickel concentration, there are similarities in an increasing progression and the shape with the increasing temperature except when x=0.25 and x=0.75, where their shapes differ and there exists larger entropy difference as compared to other nickel concentration pairing. The variation of the configurational entropy of the $LiMn_{2x-2}Ni_{2x}O_4$ system showed an increasing temperature which indicated ordering from 300K and a possible disordering at a higher temperature (above 1000 K) due the existent of a full configurational equilibrium. The connection between Li^+ average intercalation voltage and the equilibration temperature for the cation distribution illustrated different voltage values and the most stable system $LiMn_{1.5}Ni_{0.5}O_4$ with an average voltage of 4.866 V. The results further attest to a stable system, showing that there is no much change in the average voltage when the temperature increases. The findings indicate a possible route for controlling the charging and discharging process for the stable nickel doped spinel.

7.2 Recommendations

Density functional theory was used to investigate various properties of spinel $LiMn_2O_4$ and most importantly various concentrations of nickel doped $LiNi_xMn_{2-x}O_4$. Virtual crystal approach proved to be a successful tool in metal doping, in this case by generating systems with various concentrations of nickel into spinel $LiMn_2O_4$. The universal cluster expansion code proved to be a success in generating new stable

phases. The study and different approaches give a vivid understanding of structural, electronic and mechanical properties of the spinel systems. Lastly, the site-occupancy disorder program indicated that any small change in the tuning of the Ni concentration, achieved via temperature change during the thermodynamics of mixing and controlling of the lithium intercalation will be reflected in the properties of the stable structure. Previous studies showed that the performance of battery materials can be improved by doping those materials with different divalent and trivalent elements. Particularly, doping spinel $LiMn_2O_4$ with various elements tends to stabilise the structure and improve its cyclability. Replacing manganese with other elements controls manganese dissolution and reduces Jahn-Teller deformation. Experimental studies on multivalent spinel doping are complicated since the transition metal elements can exhibit different oxidation states between 2+ and 4+. Moreover, the Mn ions are embedded in the 16*d* octahedral positions and hold an effective 3.5+ oxidation state, with the 3*d* itinerant electrons moving from the Mn^{3+} to the Mn^{4+} cations, which renders them equivalent. Furthermore, most experimental studies on $LiNi_xMn_{2-x}O_4$ were confined to the case of $x \leq 0.2$. This work laid a foundation from which a better understanding of the spinel $LiMn_2O_4$ doping can be built. Most importantly, the study opens a window on spinel co-doping. Thus, different elements, such as nickel and cobalt can be introduced simultaneously to the spinel system with various atomic weights. This will include investigating systems such as $LiCo_{0.01}Al_{0.05}Mn_{1.94}O_4$, $LiCo_{0.01}Ni_{0.05}Mn_{1.94}O_4$ etc. Listed below are some of the possible future investigations on this subject:

- Use VCA to dope spinel with other elements such as Co, Cr, Fe, Co, Ni, Al, Mg, etc. and investigate their properties. The effects of doping can be complicated because of the interrelations between doping elements and structural morphology. The investigations will include predicting properties (such as electronic and mechanical properties) that are not possible or difficult to obtain experimentally. These investigations could be extended to co-doping, whereby two different elements are introduced to the system simultaneously.

- Use the site-occupancy disorder to investigate surface properties of a yielded stable structure.

- Use UNCLE Code to further determine the stability of spinel $LiMn_2O_4$ and nickel doped $LiMn_2O_4$. Uncle is a code for constructing cluster expansions for arbitrary lattices with minimal user input. Doping plays a vital role in structural stability and improves cyclability. Furthermore, Monte Carlo simulations could be investigated for stable compositions.

- Derive Buckingham potential model of the Ni-doped system using the Forcefields Optimiser which allows to create, optimize, and validate Forcefields based on first-principles derived training information.

- Studies of discharge for certain identified stable structures of $LiNi_xMn_{2-x}O_4$ will be of great interest.

References

[1] R.V. Noorden, “The rechargeable revolution: A better battery,” *Nature,* vol. 507, pp. 26-28, 2014.

[2] G.J. Xu, Z.H. Liu, C.J. Zhang, G.L. Cui and L.Q. Chen, “Strategies for improving the cyclability and thermo-stability of $LiMn_2O_4$-based batteries at elevated temperatures,” *J. Mater. Chem. A,* vol. 3, pp. 4092-4123, 2015.

[3] F.G. Mao, W. Guo and J.M. Ma, “Research progress on design strategies, synthesis and performance of $LiMn_2O_4$-based cathodes,” *RSC Adv.,* vol. 5, pp. 105248-105258, 2015.

[4] M. Armand and J.M. Tarascon, “Building better batteries,” *Nature,* vol. 451, pp. 652–657, 2008.

[5] J.M. Tarascon and M. Armand, “Issues and challenges facing rechargeable lithium batteries,” *Nature,* vol. 414, pp. 359-367, 2001.

[6] G. Berckmans, M. Messagie, J. Smekens, N. Omar, L.Vanhaverbeke and J. Van Mierlo, “Cost Projection of State of the Art Lithium-Ion Batteries for Electric Vehicles Up to 2030,” *Energies,* vol. 10, pp. 1-20, 2017.

[7] F.K. Dokan, H. Sahan, S. S. Veziroglu, N.A. Tas, A. Aydin and S. Patat, “The Effect of Multiple Cation (Al, Si, Ti, Co) Doping on Electrochemical Performance of $LiMn_2O_4$ Cathode Active Material,” *Acta Physica Polonica, A,* vol. 123, pp. 365-367, 2013.

[8] C. Luo, Investigation on the Phase Stability and Defect Structure of Li-Mn-O and Li-Me-Mn-O Spinel (Me=Mg, Ni, Co), Germany: Publikationsserver der RWTH Aachen University, 2005, pp. 1-110.

[9] C. Zhang, X. Liu, Q. Su, J. Wu, T. Huang and A. Yu, “Enhancing Electrochemical Performance of $LiMn_2O_4$ Cathode Material at Elevated Temperature by Uniform Nanosized TiO_2 Coating,” *ACS Sustainable Chem. Eng.,* vol. 5, pp. 640-647, 2017.

[10] J.O. Besenhard, Editor, Handbook of battery Materials, Weinheim: Wiley-VCH, 1999.

[11] D. Linden and T.B. Reddy, Editors, Handbook of Batteries, 3rd Ed ed., New York: McGraw-Hill, 2001.

[12] D. Deng, “Li-ion batteries: Basics, progress, and challenges,” *Energy Sci. Eng.,* vol. 3, pp. 385-418, 2015.

[13] J.B. Goodenough and Y. Kim, “Challenges for Rechargeable Li Batteries,” *Chem. Mater.,* vol. 22, pp. 587-603, 2010.

[14] W.C. Chang, Understanding the capacity fade mechanisms of spinel manganese oxide cathodes and improving their performance in lithium ion batteries, Texas at Austin: The university of texas at austin, 2007, pp. 1-147.

[15] T.F. Fuller, M. Doyle and J. Newman, “Simulation and Optimization of the Dual Lithium Ion Insertion Cell,” *J. Electrochem. Soc.,* vol. 141, pp. 1-10, 1994.

[16] G.L. Xu, Q. Wang, J.C. Fang, Y.F. Xu, J.T. Li, L. Huang, and S.G. Sun, “Tuning the structure and property of nanostructured cathode materials of lithium ion and lithium sulfur batteries Gui-Liang,” *J. Mater. Chem. A,* vol. 2, pp. 19941-19962, 2014.

[17] T. Ohzuku, M.Kitagawa and T.Hirai, “Electrochemistry of manganese-dioxide in lithium nonaqueous cell,” *J. Electrochem. Soc.,* vol. 137, pp. 769-775, 1990.

[18] A.D. Robertson, S.H. Lu, W.F. Averill, and. W.F. Howard Jr, “M^{3+} -Modified LiMn2O4 spinel intercalation cathodes: I. Admetal effects on morphology and electrochemical performance,” *J. Electrochem. Soc.,* vol. 144, pp. 3500-3505, 1997.

[19] D.H. Hu, S.X. Zhao, Y.F. Deng and C.W. Nan, “Synthesis and electrochemical performance of rod-like spinel $LiMn_2O_4$ coated by Li−Al−Si−O solid electrolyte,” *J. Mater. Chem. A,* vol. 46, pp. 14729-14735, 2013.

[20] Y. Xia, M. Yoshio and H. Noguchi, “Improved electrochemical performance of $LiFePO_4$ by increasing its specific surface area,” *Electrochim. Acta,* vol. 52, pp. 240-245, 2006.

[21] M.C. Rao and O.M. Hussain, “Growth and characterization of vacuum evaporated WO_3 thin films for electrochromic device application,” *Research J. Chem. Sci.,* vol. 1, pp. 92-95, 2011.

[22] M.C. Rao, “Structure and properties of WO_3 thin films for electrochromic device application,” *J. Non-Oxide Glasses,* vol. 5, pp. 1-8, 2013.

[23] Y. Xia, Development of Low Cost Cathode Materials for Lithium-ion Batteries, Saga: Department of Energy and Materials Science Graduate School of Science and Engineering Saga University, 2008, pp. 1-126.

[24] R. Premanand A. Durairajan, B. Haran, R. White and B. Popov, “Studies on capacity fade of spinel-based Li-ion batteries,” *J. Electrochem. Soc.,* vol. 149, pp. A54-A60, 2002.

[25] L. Yang, M. Takahashi and B. Wang, “A study on capacity fading of lithium-ion battery with manganese spinel positive electrode during cycling,” *Electrochim. Acta,* vol. 51, pp. 3228-3234, 2006.

[26] S.T. Myung, S. Komaba and N. Kumagai, “Enhanced Structural Stability and Cyclability of Al-Doped $LiMn_2O_4$ Spinel Synthesized by the Emulsion Drying Method,” *J. Electrochem. Soc.,* vol. 148, pp. A482-A489, 2001.

[27] P. Arora, B.N. Popov and R.E. White, “Electrochemical investigation of Cobalt-doped $LiMn_2O_4$ as cathode material for Li-ion batteries,” *J. Electrochem. Soc.,* vol. 145, pp. 807-815, 1998.

[28] C.H. Lu and S.W. Lin, “Dissolution Kinetics of Spinel Lithium Manganate and its Relation to Capacity Fading in Lithium Ion Batteries,” *J. Mater. Res.,* vol. 17, pp. 1476-1481, 2002.

[29] L. Guohua, H. Ikuta, T. Uchida and M. Wakihara, “The spinel phase $LiM_yMn_{<2-y>}O_4$ (M=Co, Cr, Ni) as the cathode for rechrgeable lithium cells,” *J. Electrochem. Soc.,* vol. 143, pp. 178-182, 1996.

[30] Y. Ein-Eli and W.F. Howard Jr., “$LiCu_xIICu_yIIIMn_{[2-(x+y)]}III$, IV O4 : 5 V Cathode Materials,” *J. Electrochem. Soc.,* vol. 144, pp. L205-L207, 1997.

[31] H. Kawai, M. Nagata, H. Tukamoto and A.R. West, “A new lithium cathode $LiCoMnO_4$: Towards practical 5V lithium batteries,” *Electrochem. Solid-State Lett.,* vol. 1, pp. 212-214, 1998.

[32] Y.S. Lee, Y.K. Sun, S. Ota, T. Miyashita, and M. Yoshio, “Preparation and characterization of Nano-crystalline $LiNi_{0.5}Mn_{1.5}O_4$ for 5V cathode material by

Composite Carbonate Process," *Electrochem. Commun.,* vol. 4, pp. 989-994, 2002.

[33] R. Thirunakaran, K.T. Kim, Y.M. Kang and Y.L. Jai, "Cr^{3+} modified $LiMn_2O_4$ spinel intercalation cathodes through oxalic acid assisted sol–gel method for lithium rechargeable batteries," *Mater. Res. Bull.,* vol. 40, pp. 177-186, 2005.

[34] R. Thirunakaran, K.T. Kim, Y.M. Kang, C.Y. Seo and Y.L. Jai, "Adipic acid assisted, sol–gel route for synthesis of $LiCr_xMn_{2-x}O_4$ cathode material," *J. Power Sources,* vol. 137, pp. 100-104, 2004.

[35] G.G. Wang, J.M. Wang, W.Q. Mao, L.Q. Liu, J.Q. Zhang and C.N. Cao, "Structure and Electrochemical Performance of $LiNi_yCo_{0.1-y}Mn_{1.9}O_4$ Cathode Materials Prepared by a Precipitation Method," *Acta Phys-Chim. Sin,* vol. 21, pp. 1285-1290, 2005.

[36] S.J. Bao, W.J. Zhou and Y.Y. Liang, et al., "Enhancement of the electrochemical properties of $LiMn_2O_4$ through chem-ical substitution," *Mater. Chem. Phy.,* vol. 95, pp. 188-190, 2006.

[37] S.H. Park, Y.S. Lee, and Y.K. Sun, "Synthesis and electro-chemical properties of sulfur doped-$Li_xMnO_{2-y}S_y$ materials for lithium secondary batteries," *Electrochem. Commun.,* vol. 5, pp. 124-128, 2003.

[38] T. Yi, X. Hu, D. Wang and H. Huo, "Effects of Al, F dual substitutions on the structure and electrochemical properties of lithium manganese oxide," *J Univ. Sci. Technol. B,* vol. 15, pp. 182-186, 2008.

[39] R. Dziembaj and M. Molenda, "Stabilization of the spinel structure in $Li_{1+\delta}Mn_{2-\delta}O_4$ obtained by sol-gel method," *J. Power Sources,* Vols. 119-121, pp. 121-124, 2003.

[40] D. Aurbach, M.D. Levi, K. Gamulski, B. Markovsky, G. Salitra, E. Levi, U. Heider, L. Heider and R. Oesten, "Capacity fading of $Li_xMn_2O_4$ spinel electrodes studied by XRD and electroanalytical techniques," *J. Power Sources,* Vols. 81-82, pp. 472-479, 1999.

[41] Y.Y. Xia, T. Sakai, T. Fujieda, X.Q. Yang, Z.F. Ma, J. McBreen and M. Yoshio, "Correlating capacity fading and structural changes in $Li_{1+y}Mn_{2-y}O_4$-delta spinel cathode materials - A systematic study on the effects of Li/Mn ratio and oxygen deficiency," *J. Electrochem. Soc.,* vol. 148, pp. A723-A729, 2001.

[42] Y. Ito, Y. Idemoto, Y. Tsunoda and N. Koura, “Relation between crystal structures, electronic structures, and electrode performances of $LiMn_{2-x}M_xO_4$,” *J. Power Sources,* vol. 119–121, pp. 733-737, 2003.

[43] Q.H. Wu, J.M. Xu, Q.C. Zhuang and S.G. Sun, “X-ray photoelectron spectroscopy of $LiM_{0.05}Mn_{1.95}O_4$ (M=Ni, Fe and Ti),” *Solid State Ion.,* vol. 177, pp. 1483-1488, 2006.

[44] A. Sakunthala, M.V. Reddy, S. Selvasekarapandian, B.V.R. Chowdari and P.C. Selvin, “Synthesis of compounds, Li $(MMn_{11/6})O_4$ (M= $Mn_{-1/6}$, $Co_{-1/6}$,$(Co_{1/12}Cr_{1/12})$,$(Co_{1/12}Al_{1/12})$,$(Cr_{1/12}Al_{1/12})$) by polymer precursor method and its electrochemical performance for lithium-ion batteries,” *Electrochim. Acta,* vol. 55, pp. 4441-4450, 2010.

[45] L.F. Xiao, Y.Q. Zhao, Y.Y. Yang, Y.L. Cao, X.P. Ai and H.X. Yang, “Enhanced electrochemical stability of Al-doped $LiMn_2O_4$ synthesized by a polymer-pyrolysis method,” *Electrochim. Acta,* vol. 54, pp. 545-550, 2008.

[46] H. Liu, J. Wang, X. Zhang, D. Zhou, X. Qi, B. Qiu, J. Fang, R. Kloepsch, G. Schumacher, Z. Liu, and J. Li, “Morphological Evolution of High-Voltage Spinel $LiNi_{0.5}Mn_{1.5}O_4$ Cathode Materials for Lithium-Ion Batteries: The Critical Effects of Surface Orientations and Particle Size,” *ACS Appl. Mater. Interfaces,* vol. 8, pp. 4661-4675, 2016.

[47] J. Shu, T. Feng, Y.M. Shui, Y. Wang, R.S. Zhu, X. Chu, F. Huang, D. Xu and L. Hou, “Comparison of electronic property and structural stability of $LiMn_2O_4$ and $LiNi_{0.5}Mn_{1.5}O_4$ as cathode materials for lithium-ion batteries,” *Compt. Mater. Sci.,* vol. 50, pp. 776-779, 2010.

[48] R. Santhanam and B. Rambabu, “Research progress in high voltage spinel $LiNi_{0.5}Mn_{1.5}O_4$ material,” *J. Power Sources,* vol. 195, pp. 5442-5451, 2010.

[49] H.M. Wu, J.P. Tu, X.T. Chen, Y. Li, X.B. Zhao and G.S. Cao, “Effects of Ni-ion doping on electrochemical characteristics of spinel $LiMn_2O_4$ powders prepared by a spray-drying method,” *J. Solid State Chem.,* vol. 11, pp. 173-176, 2007.

[50] L.Q. Zhang, T. Yabu and I. Taniguchi, “Synthesis of spherical nanostructured $LiM_xMn_{2-x}O_4$ (M= Ni^{2+} Co^{3+} and Ti^{4+}) via a single-step ultrasonic spray

pyrolysis method and their high rate charge-discharge performances," *Mater. Res. Bull.,* vol. 44, pp. 707-713, 2009.

[51] I. Taniguchi, D. Song and M. Wakihara, "Electrochemical properties of $LiM_{1/6}Mn_{11/6}O_4$ (M= Mn, Co, Al and Ni) as cathode materials for Li-ion batteries prepared by ultrasonic spray pyrolysis method," *J. Power Sources,* vol. 109, pp. 333-339, 2002.

[52] J.M. Amarilla, R.M. Rojas, F. Pico, L. Pascual, K. Petrov, D. Kovacheva, M.G. Lazarraga, I. Lejona and J.M. Rojo, "Nanosized $LiM_YMn_{2-Y}O_4$ (M=Cr, Co and Ni) spinels synthesized by a sucrose-aided combustion methodStructural characterization and electrochemical properties," *J. Power Sources,* vol. 174, pp. 1212-1217, 2007.

[53] J.M. Amarilla, K. Petrov, F. Pico, G. Avdeev, J.M. Rojo and R.M. Rojas, "Sucrose-aided combustion synthesis of nanosized $LiMn_{1.99-y}Li_yM_{0.01}O_4$ ($M=Al^{3+}$, Ni^{2+}, Cr^{3+}, Co^{3+}, y=0.01 and 0.06) spinelsCharacterization and electrochemical behavior at 25 and at 55°C in rechargeable lithium cells," *J. Power Sources,* vol. 191, pp. 591-600, 2009.

[54] K.S. Lee, S.T. Myung, H.J. Bang, S. Chung and Y.K. Sun, "Co-precipitation Synthesis of Spherical $Li_{1.05}M_{0.05}Mn_{1.9}O_4$ (M=Ni, Mg, Al) Spinel and Its Application for Lithium Secondary Battery Cathode," *Electrochim. Acta,* vol. 52, pp. 5201-5206, 2007.

[55] S.H. Wu and H.L. Chen, "The effects of heat-treatment temperature on the retention capacities of spinels prepared by the Pechini process," *J. Power Sources,* Vols. 119-121, pp. 134-138, 2003.

[56] X.M. Liu, Z.D. Huang, S.W. Oh, P.C. Ma, P.C.H. Chan, G.K. Vedam, K. Kang and J.K. Kim, "Sol-gel synthesis of multiwalled carbon nanotube-$LiMn_2O_4$ nanocomposites as cathode materials of Li-ion batteries," *Electrochim. Acta,* vol. 195, pp. 4290-4296, 2010.

[57] B.H. Kim, Y.K. Choi and Y.H. Choa, "Synthesis of $LiFe_xMn_{2-x}O_4$ cathode materials by emulsion method and their electrochemical properties," *Solid State Ion.,* vol. 158, pp. 281-285, 2003.

[58] W.S. Yang, Q.G. Liu, W.H. Qiu, S.G. Lu and L.L. Yang, “A citric acid method to prepare $LiMn_2O_4$ for lithium-ion batteries,” *Solid State Ion.,* vol. 121, pp. 79-84, 1999.

[59] K.M. Shaju, G.V. Subba Rao and B.V.R. Chowdari, “Li ion kinetic studies on spinel cathodes, $Li(M_{1/6}Mn_{11/6})O_4$ (M=Mn, Co, CoAl) by GITT and EIS,” *J. Mater. Chem.,* vol. 13, pp. 106-113, 2003.

[60] H.L. Wang, T.A. Tan, P. Yang, M.O. Lai and L. Lui, “High-rate performances of the Ru-doped spinel $LiNi_{0.5}Mn_{1.5}O_4$: effects of doping and particle size,” *J. Phys. Chem. C,* vol. 115, pp. 6102-6110, 2011.

[61] J.W. Fergus, “Recent developments in cathode materials for lithium ion batteries,” *J. Power Sources,* vol. 195, pp. 939-954, 2010.

[62] C. Bellitto, E.M. Bauer, G. Righini, M.A. Green, W.R. Branford, A. Antonini, M. Pasquali, “The effect of doping $LiMn_2O_4$ spinel on its use as a cathode in Li-ion batteries: neutron diffraction and electrochemical studies,” *J. Phys. Chem. Solids,* vol. 65, pp. 29-37, 2004.

[63] C. Sigala, A. Le Gal La Salle, Y. Piffard and D. Guyomard, “Influence of the Cr content on the Li deinsertion behavior of the $LiCr_yMn_{2-y}O_4$ $(0 \leqslant y \leqslant 1)$ Compounds: I. Separation of bulk and superficial processes at high voltage,” *J. Electrochem. Soc.,* vol. 148, pp. A812-A818, 2001.

[64] N. Hayashi, H. Ikuta and M. Wakihara, “Cathode of $LiMg_yMn_{2-y}O_4$ and $LiMg_yMn_{2-y}O_{4-\delta}$ spinel phases for lithium secondary batteries,” *J. Electrochem. Soc.,* vol. 146, pp. 1351-1352, 1999.

[65] E. Zhecheva, R. Stoyanova, M. Gorova, P. Lavela, J.L. Tirado, “Co/Mn Distribution and electrochemical intercalation of Li into $Li[Mn_{2-y}Co_y]O_4$ spinels, $0<y\leq 1$,” *Solid State Ion.,* vol. 140, pp. 19-33, 2001.

[66] C.H. Shen, R.S. Liu, R. Gundakaram, J.M. Chen, S.M. Huang, J.S. Chen and C.M. Wang, “Effect of Co doping in $LiMn_2O_4$,” *J. Power Sources,* vol. 102 , pp. 21-28, 2001.

[67] S. Mandal, R.M. Rojas, J.M. Amarilla, P. Calle, N.V. Kosova, V.F. Anufrienko, and J.M. Rojo, “High temperature co-doped $LiMn_2O_4$-based spinels, structural, electrical, and electrochemical characterization,” *Chem. Mater.,* vol. 14, pp. 1598-1605, 2002.

[68] C.P. Grey and N. Dupre, “NMR Studies of Cathode Materials for Lithium-Ion Rechargeable Batteries,” *Chem. Rev.,* vol. 104, pp. 4493-4512, 2004.

[69] H. Wang, H. Xia, M.O. Lai and L. Lu, “Enhancements of rate capability and cyclic performance of spinel $LiNi_{0.5}Mn_{1.5}O_4$ by trace Ru-doping,” *Electrochem. Commun.,* vol. 11, pp. 1539-1542, 2009.

[70] N. Amdouni, K. Zaghib, F. Gendron, A. Mauger and C.M. Julien, “, Magnetic properties of $LiNi_{0.5}Mn_{1.5}O_4$ spinels prepared by wet chemical methods,” *J. Magn. Magn. Mater.,* vol. 309, pp. 100-105, 2007.

[71] Y. Wei, K.B. Kim and G. Chen, “Evolution of the local structure and electrochemical properties of spinel $LiNi_xMn_{2-x}O_4$ ($0 \leq x \leq 0.5$),” *Electrochim. Acta,* vol. 51, pp. 3365-3373, 2006.

[72] T.F. Yi, Y.R. Zhu and R.S. Zhu, “Density functional theory study of lithium intercalation for 5V $LiNi_{0.5}Mn_{1.5}O_4$ cathode materials,” *Solid State Ion.,* vol. 179, pp. 2132-2136, 2008.

[73] S. Q. Shi, D. S. Wang, S. Meng, L. Q. Chen and X. J. Huang, “First-principles studies of cation-doped spinel $LiMn_2O_4$ for lithium ion batteries,” *Phys. Rev. B,* vol. 67, pp. 115130/1-115130/6, 2003.

[74] S.K. Mishra and G. Ceder, “Structural stability of lithium manganese oxides,” *Phys. Rev.,* vol. B59, pp. 6120-6130, 1999.

[75] A. Van der Ven, C. Marianetti, D. Morgan and G. Ceder, “Phase transformations and volume changes in spinel $Li_xMn_2O_4$,” *Solid State Ion.,* vol. 135, pp. 21-32, 2000.

[76] V. Massarotti, D. Capsoni, M. Bini, G. Chiodelli, C.B. Azzoni, M.C. Mozzati and A. Paleari, “Electric and magnetic properties of $LiMn_2O_4$- and Li_2MnO_3-Type oxides,” *J. Solid State Chem.,* vol. 131, pp. 94-100, 1997.

[77] M.M. Thackeray, “Manganese oxides for lithium batteries,” *Prog. Solid State Chem.,* vol. 25, pp. 1-71, 1997.

[78] G.G. Amatucci, C.N. Schmutz, A. Blyr, C. Sigala, A.S. Gozdz and D. Larcher, “Materials' effects on the elevated and room temperature performance of C/$LiMn_20_4$ Li-ion batteries,” *J. Power Sources,* vol. 69, pp. 1-25, 1997.

[79] S.H. Kang and J.B. Goodenough, “Li[Mn_2]O_4 Spinel Cathode Material Showing No Capacity Fading in the 3 V Range,” *J. Electrochem. Soc.,* vol. 147, pp. 3621-3627, 2000.

[80] D. Kovacheva, H. Gadjov, K. Petrov, S. Mandal, M.G. Lazarraga, L. Pascual, J.M. Amarilla, R.M. Rojas, P. Herrero and J.M. Rojo, “Synthesizing nanocrystalline $LiMn_2O_4$ by a combustion route,” *J. Mater. Chem.,* vol. 12, pp. 1184-1188, 2002.

[81] M.M. Thackeray, C.S. Johnson, A.J. Kahaian, K.D. Kepler, J.T. Vaughey, Y. Shao-Horn and S.A. Hackney, “Stabilization of insertion electrodes for lithium batteries,” *J. Power. Sources,* vol. 81–82, pp. 60-66, 1999.

[82] G. Amatucci, A.D. Pasquier, A. Blyr, T. Zheng and J.M. Tarascon, “The elevated temperature performance of the $LiMn_2O_{4/C}$ system: Failure and solutions,” *Electrochim. Acta,* vol. 45, pp. 255-271, 1999.

[83] Y.S. Lee and M. Yoshio, “Unique Aluminum Effect of $LiAl_xMn_{2-x}O_4$ Material in the 3 V Region. Electrochem,” *Electrochem. Solid-State Lett.,* vol. 4, pp. A85-A88, 2001.

[84] P. Aitchison, B. Ammundsen, D.J. Jones, G. Burns and J. Roziere, “Cobalt substitution in lithium manganate spinels: examination of local structure and lithium extraction by XAFS,” *J. Mater. Chem.,* vol. 9, pp. 3125-3130, 1999.

[85] D. Song, H. Ikuta, T. Uchida and M. Wakihara, “The spinel phases LiAlMnO(y50, 1/12, 1/ 9, 1/6, 1/3) and Li(Al,M) Mn O (M5Cr, Co) as the cathode for rechargeable lithium batteries,” *Solid State Ion.,* vol. 117, pp. 151-156, 1999.

[86] Y. Shao-Horn and R.L. Middaugh, “Redox reaction of cobalt, aluminum and titanium substituted lithium manganese spinel compounds in lithuim cells,” *Solid State Ion.,* vol. 139, pp. 13-25, 2001.

[87] L. Hernan, J. Morales, L. Sanchez, E. R. Castellon and M. A. G. Aranda, “Synthesis, characterization and comparative study of the electrochemical properties of doped lithium manganese spinels as cathodes for high voltage lithium batteries,” *J. Mater. Chem.,* vol. 12, pp. 734-741, 2002.

[88] Y.K. Sun, C.S. Yoon, C.K. Kim, S.G. Youn, Y.S. Lee, M. Yoshio and I.H. Oh, “Degradation mechanism of spinel $LiAl_{0.2}Mn_{1.8}O_4$ cathode materials on high temperature cycling,” *J. Mater. Chem.,* vol. 11, pp. 2519-2522, 2001.

[89] M.C. Tucker, J.A. Reimer and E.J. Cairns, “A 7Li NMR Study of Capacity Fade in Metal-Substituted Lithium Manganese Oxide Spinels,” *J. Electrochem. Soc.,* vol. 149, pp. A574-A585, 2002.

[90] D. Aurbach, M.D. Levi, E. Levi, H. Teller, B. Markovsky, G. Salitra, U. Heider and L. Heider, “Common electroanalytical behavior of Li intercalation processes into graphite and transition metal oxides,” *J. Electrochem. Soc.,* vol. 145, pp. 3024-3034, 1998.

[91] F. Orsini, A. Du Pasquier, B. Beaudoin, J.M. Tarascon, M. Trentin, N. Lagenhuizen, E. De Beer and P. Not, “In situ Scanning Electron Microscopy (SEM) observation of interfaces within plastic lithium batteries,” *J. Power Sources,* vol. 76, pp. 19-29, 1998.

[92] V. Blum and A. Zunger, “Mixed-basis cluster expansion for thermodynamics of bcc alloys,” *Phys. Rev. B,* vol. 70, pp. 155108-155117, 2004.

[93] W.D. Richards, S.T. Dacek, D.A. Kitchaev and G. Ceder, “Fluorination of Lithium-Excess Transition Metal Oxide Cathode Materials,” *Adv. Energy Mater.,* vol. 8, pp. 1701533, 2017.

[94] M.C. Warren, M.T. Dove and S.A.T. Redfern, “Ab initio simulations of cation ordering in oxides: application to spinel,” *J. Condens. Matter Phys.,* vol. 12, pp. L43-L48, 2000.

[95] M.C. Warren, M.T. Dove, E.J. Palin, A Bosenick, B .A. Guiton and S.A.T. Redfern, “Monte Carlo methods for the study of cation ordering,” *Mineral. Mag.,* vol. 65, pp. 221-248, 2001.

[96] S.D. Rocha and P. Thibaudeau, “Ab initio high-pressure thermodynamics of cationic disordered $MgAl_2O_4$ spinel,” *J. Condens. Matter Phys.,* vol. 15, pp. 7103-7115, 2003.

[97] M. C. Rao, “Advancements in Layered Cathode Materials for Lithium ion Batteries,” *J. Chem. Pharm. Res.,* vol. 8, pp. 450-456, 2016.

[98] T. ERIKSSON, $LiMn_2O_4$ as a li-ion battery cathode. From bulk to electrolyte interface, Sweden: Comprehensive summaries of Uppsala Dissertations from the Faculty of Science and Technology, 2001, pp. 1-58.

[99] S.T. Murphy , C.A. Gilbert , R. Smith , T.E. Mitchell and R.W. Grimes, “Non-stoichiometry in $MgAl_2O_4$ spinel,” *Philos. Mag.,* vol. 90, pp. 1297-1305, 2010.

[100] M.M. Thackeray, W.I.F. David, P.G. Bruce and J.B. Goodenough, “Lithium insertion into βMnO_2 and the rutile-spinel transformation,” *Mater. Res. Bull.,* vol. 18, pp. 461-472, 1983.

[101] D. Guyomard and J.M. Tarascon, “The carbon/$Li_{1+x}Mn_2O_4$ system,” *Solid State Ion.,* vol. 69, pp. 222-237, 1994.

[102] J.M. Tarascon, F. Coowar, G. Amatuci, F.K. Shokoohi and D.G. Guyomard, “The $Li_{1+x}Mn_20_{4/C}$ system materials and electrochemical aspects,” *J. Power Sources,* vol. 54, pp. 103-108, 1995.

[103] R.G. Vignale, “DFT in magnetic fields,” *Phys. Rev. Lett.,* vol. 59, pp. 2360-2363, 1979.

[104] P.Hohenberg and W. Kohn, “Inhomogeneous electron gas,” *Phys. Rev. B,* vol. 136, pp. 864-871, 1965.

[105] M. Levy, “Universal variational functionals of electron densities, first-order density matrices, and natural spin-orbitals and solution of the v-representable,” *Processes National Academic Science USA,* vol. 76, pp. 6062-6065, 1979.

[106] W. Kohn and L.J. Sham, “Fractional occupation in Kohn-Sham density-functional theory and the treatment of non-pure-state v-representable densities,” *Phys. Rev.,* vol. 140, pp. A1133-A1138, 1965.

[107] G. Chen and T.J. Richardson, “Thermal instability of olivine-type $LiMnPO_4$ cathodes,” *J. Power Sources,* vol. 195, pp. 1221-1224, 2010.

[108] W. Kohn and M.C. Holthausen, A Chemist’s Guide to Density Functional Theory, WILEY-VCH, 2001.

[109] A.J. Cohen, P. Mori-Sánchez, and W. Yang, “Challenges for Density Functional Theory,” *Chem. Rev.,* vol. 112, pp. 289-320, 2012.

[110] J.P. Perdew, “Density-functional approximation for the correlation energy of the inhomogeneous electron gas,” *Phys. Rev. B,* vol. 33, pp. 8822-8824, 1986.

[111] A.D. Becke, “Density-functional exchange-energy approximation with correct asymptotic behavior,” *Phys. Rev. A,* vol. 38, pp. 3098-3100, 1988.

[112] J.P. Perdew, and Y. Wang, “Accurate and simple analytic representation of the electron-gas correlation energy,” *Phys. Rev. B,* vol. 45, pp. 13244-13249, 1992.

[113] J.P. Perdew, K. Burke and M. Ernzerhof, “Generalized Gradient Approximation Made Simple,” *Phys. Rev. Lett.,* vol. 77, pp. 3865-3868, 1996.

[114] E. Wimrner, “Ab initio Methods for Surfaces and Interfaces: Status and Perspectives,” *J. Phys. IV France,* vol. 7, pp. c6-87, 1997.

[115] S. Ivanov, S. Hirata and R. Bartlett, “Exact Exchange Treatment for Molecules in Finite-Basis-Set Kohn-Sham Theory,” *Phys. Rev. Lett.,* vol. 83, pp. 5455-5458, 1999.

[116] T. Leung, C. Chan and B. Harmon, “Ground-state properties of Fe, Co, Ni, and their monoxides: Results of the generalized gradient approximation,” *Phys. Rev. B,* vol. 44, pp. 2923-2927, 1991.

[117] K. Terakura, T. Oguchi, A. Williams and J. Kübler, “Band theory of insulating transition-metal monoxides: Band-structure calculations,” *Phys. Rev. B,* vol. 30, pp. 4734-4747, 1984.

[118] G. Sawatzky and J. Allen, “Magnitude and Origin of the Band Gap in NiO,” *Phys. Rev. Lett.,* vol. 53, pp. 2339-2342, 1984.

[119] J. Zaanen, G. Sawatzky and J. Allen, “Band gaps and electronic structure of transition-metal compounds,” *Phys. Rev. Lett.,* vol. 55, pp. 418-421, 1985.

[120] A. Rohrbach, J. Hafner and G. Kresse, “Ab initio study of the (0001) surfaces of hematite and chromia: Influence of strong electronic correlations,” *Phys. Rev. B,* vol. 70, pp. 125426/1-17, 2004.

[121] G. Pacchioni, “Theory of point defects at the MgO surface. In: Woodruff, D.P. (Ed.), The Chemical Physics of Solid Surfaces - Oxide Surfaces,” *Elsevier B. V,* vol. 9, pp. 94-135, 2001.

[122] V.I. Anisimov, J. Zaanen and O.K. Andersen, “Band theory and Mott insulators: Hubbard U instead of Stoner I,” *Phys. Rev. B,* vol. 44, pp. 943-954, 1991.

[123] H. Ebert A. Perlov and V. Mankovsky, “Incorporation of the rotationally invariant LDA+U scheme into the SPR-KKR formalism: application to disordered alloys,” *Solid State Commun.,* vol. 127, pp. 443-446, 2003.

[124] S.L. Dudarev, G.A. Botton, S.Y. Savrasov, C.J. Humphreys and A.P. Sutton, “Electron-energy-loss spectra and the structural stability of nickel oxide: An LSDA+U study,” *Phys. Rev. B,* vol. 57, pp. 1505-1509, 1998.

[125] A. Rohrbach, J. Hafner and G. Kresse, “Electronic correlation effects in transition-metal sulfides,” *J. Phys. Condens. Matter,* vol. 15, pp. 979-996, 2003.

[126] G. Rollmann, A. Rohrbach, P. Entel and J. Hafner, “First-principles calculation of the structure and magnetic phases of hematite,” *Phys. Rev. B,* vol. 69, pp. 165107-165119, 2004.

[127] M.L. Cohen and V. Heine, “The fitting of pseudo-potentiasl to experimental data and their subsequent applications, Advances in research and applications,” *Solid State Phys.,* vol. 25, pp. 37-248, 1970.

[128] J.C. Phillips, “Energy-band interpolation scheme based on a pseudopotential,” *Phys. Rev.,* vol. 112, pp. 685-695, 1958.

[129] M.T. Yin and M.L. Cohen, “Theory of ab initio pseudopotential calculations,” *Phys. Rev. B,* vol. 25, pp. 7403-7412, 1982.

[130] M.C. Payne, M.P. Teter, D.C. Allan, T.A. Arias and J.D. Joannopoulos, “Iterative minimization techniques for ab Initio total energy calculations: Molecular dynamics and conjugate gradients,” *Rev. Mod. Phys.,* vol. 64, pp. 1045-1097, 1992.

[131] G.B. Bachelet, D.R. Hamann and M. Schlüter, “Pseudopotentials that work: From H to Pu,” *Phys. Rev. B,* vol. 26 (8), pp. 4199-4228, 1982.

[132] D. Vanderbilt, “Soft Self-Consistent Pseudopotentials in a Generalized Eigenvalue Formalism (Rapid Communications),” *Phys. Rev.,* vol. B 41, pp. 7892-7895, 1990.

[133] D.J. Chadi and M.L. Cohen, “Special Points in the Brillouin Zone,” *Phys. Rev. B,* vol. B 8, pp. 5747-5753, 1973.

[134] H.J. Monkhorst and J.D. Pack, “Special Points for Brillouin-zone Integrations,” *Phys. Rev. B,* vol. 13, pp. 5188-5192, 1976.

[135] J.E. Mayer and E. Montroll, “Molecular Distribution,” *J. Chem. Phys.,* vol. 9, pp. 2-16, 1941.

[136] J.M. Sanchez, F. Ducastelle and D. Gratias, “Generalized cluster description of Multicomponent systems,” *Physica A,* vol. 128, pp. 334-350, 1984.

[137] G. Kresse and J. Hafner, “Ab initio molecular dynamics for liquid metals,” *J. Phys. Rev. B,* vol. 47, pp. 558-561, 1993.

[138] G. Kresse and J. Furthmüller, “Efficient iterative schemes for ab initio total-energy calculations using a plane-wave basis set,” *Phys. Rev. B,* vol. 54, pp. 11169-11186, 1996.

[139] G. Kresse and D. Joubert, “From ultrasoft pseudopotentials to the projector augmented-wave method,” *Phys. Rev. B,* vol. 59, pp. 1758-1775, 1999.

[140] G. Kresse, J. Furthmüller, “Efficiency of ab-initio total energy calculations for metals and semiconductors using a plane-wave basis set,” *Comput. Mater. Sci.,* vol. 6, pp. 15-50, 1996.

[141] G. Kresse and J. Hafner, “Norm-conserving and ultrasoft pseudopotentials for first-row and transition elements,” *J. Phys. Condens. Matter,* vol. 6, pp. 8245-8257, 1994.

[142] E. Wimmer, H. Krakauer, M. Weinert and A.J. Freeman, “Full-potential self-consistent linearized-augmented-plane-wave method for calculating the electronic structure of molecules and surfaces: O_2 molecule,” *Phys. Rev. B,* vol. 24, pp. 864-75, 1981.

[143] M. Weinert, “Solution of Poisson’s equation: Beyond Ewald-type methods,” *J. Math. Phys.,* vol. 22, pp. 2433-2439, 1981.

[144] M. Weinert, E. Wimmer and A.J. Freeman, “Total-energy all-electron density functional method for bulk solids and surfaces,” *Phys. Rev. B,* vol. 26, pp. 4571-4578, 1982.

[145] M. Asta , D. de Fontaine, M. van Schilfgaarde, M. Sluiter, and M. Methfessel, “First-principles phase-stability study of fcc alloys in the Ti-Al system,” *Phys. Rev. B,* vol. 46, pp. 5055-5072, 1992.

[146] M. Asta, R. McCormack, and D. de Fontaine, “Theoretical study of alloy phase stability in the Cd-Mg system,” *Phys. Rev. B,* vol. 48, pp. 748-766, 1993.

[147] C. Colinet, A. Pasturel, D. Nguyen Manh, D.G. Pettifor and P. Miodownik, “Phase- stability study of the Al-Nb system,” *Phys. Rev. B,* vol. 56, pp. 552-565, 1997.

[148] K. Yuge, A. Seko, A. Kuwabara, F. Oba, and I. Tanaka, “First-principles study of bulk ordering and surface segregation in Pt-Rh binary alloys,” *Phys. Rev. B,* vol. 74, pp. 174202-174213, 2006.

[149] P.R. Alonso and G.H. Rubiolo, “Relative stability of bcc structures in ternary alloys with Ti50Al25Mo25 composition,” *Phys. Rev. B,* vol. 62, pp. 237-242, 2000.

[150] A. Van der Ven and G. Ceder, “Vacancies in ordered and disordered binary alloys treated with the cluster expansion,” *Phys. Rev. B,* vol. 71, pp. 054102-054107, 2005.

[151] A. van de Walle, “A complete representation of structure-property relationships and crystals,” *Nat. Mater.,* vol. 7, pp. 455-458, 2008.

[152] A. Franceschetti, S.V. Dudiy, S.V. Barabash, A. Zunger, J. Xu, and M. van Schilfgaarde, “First-Principles Combinatorial Design of Transition temperature in Multicomponent Systems: The Case of Mn in GaAs,” *Phys. Rev. Lett.,* vol. 97, pp. 047202-047201, 2006.

[153] H. Y. Geng, M. H. F. Sluiter, and N. X. Chen, “Cluster expansion of electronic excitations: Application to fcc Ni–Al alloys,” *J. Chem. Phys.,* vol. 122, p. p. doi:10.1063/1.1926276, 2005.

[154] J.M. Sanchez, F. Ducastelle and D. Gratias, “Generalized cluster description of multicomponent systems,” *Physica A,* vol. 128, pp. 334-350, 1984.

[155] G.L.W. Hart, V. Blum, J. Walorski and A. Zunger, “Evolutionary approach for determining first-principles hamiltonians,” *Nat. Mater.,* vol. 4, pp. 391-394, 2005.

[156] A. van de Walle and G. Ceder, “Automating First-Principles Phase Diagram Calculations,” *J. Phase Equilib.,* vol. 23, pp. 348-359, 2002.

[157] V. Blum, G. L. W. Hart, M. J. Walorski and A. Zunger, “Using genetic algorithms to map first-principles results to model Hamiltonians: Application to the generalized Ising model for alloys,” *Phys. Rev. B,* vol. 72, pp. 165113, 2005.

[158] G. Kastlunger, “First-principles study of the Fe-rich FexNiyAl1-x-y alloy system,” Magister der Naturwissenschaften (Mag. rer. nat.), 2011.

[159] D. Lerch, O. Wieckhorst, G.L.W. Hart, R.W. Forcade and S. Müller, “UNCLE: a Code for Constructing Cluster Expansions for Arbitrary Lattices with Minimal User-Input,” *Model. Simul. Mater. Sci. Eng.,* vol. 17, pp. 055003, 2009.

[160] Ph. Ungerer, B. Tavitian and A. Boutin, Applications of Molecular Simulation in the Oil and Gas Industry - Monte-Carlo Methods, Paris: France: Editions Technip, 2005.

[161] K. Binder and D. Heermann, Monte Carlo Simulation in Statistical Physics, Berlin: Springer-Verlag Berlin Heidelberg, 1978.

[162] N. Metropolis, A.W. Rosenbluth, M.N. Rosenbluth , A.H. Teller and E. Teller, “Equation of State Calculations by Fast Computing Machines,” *J. Chem. Phys.,* vol. 21, pp. 1087-1092, 1953.

[163] M.E.J. Newman and G.T. Barkema, Monte Carlo Methods in Statistical Physics, United States: Oxford University Press Inc., New York, 1999.

[164] J.A. Elliott, Introduction to Materials Modelling, London: Maney, 2005.

[165] V. Milman, B. Winkler, J.A. White, C.J. Pickard, M.C. Payne, E.V. Akhmatskaya and R.H. Nobes, “Electronic structure, properties, and phase stability of inorganic crystals: A pseudopotential plane-wave study,” *J. Quantum Chem.,* vol. 77, pp. 895-910, 2000.

[166] Accelrys Inc, “CASTEP users Guide,” San Diego: Accelrys Inc, 2001.

[167] J.D. Joannopoulos and M.L Cohen, “Electronic Properties of Complex Crystalline and Amorphous Phases of Ge and Si. I. Density of States and Band Structures,” *Phys. Rev.,* vol. B7, pp. 2644-2657, 1973.

[168] R.A. Evarestov and V.P. Smirnov, “Special points of the brillouin zone and their use in the solid state theory,” *Phys. Status. Solidi.,* vol. 119, pp. 9-40, 1983.

[169] D. Lerch, O. Wieckhorst, L. Hammer, K. Heinz and S. Müller, “Adsorbate cluster expansion for an arbitrary number of inequivalent sites,” *Phys. Rev. B,* vol. 78, pp. 121405(R), 2008.

[170] N.J. Ramera and A.M. Rappea, “Application of a new virtual crystal approach for the study of disordered perovskites,” *J. Phys. Chem. Solids,* vol. 61, pp. 315-320, 2000.

[171] N.J. Ramer and A.M. Rappe, “Virtual-crystal approximation that works: Locating a compositional phase boundary in $Pb(Zr_{1-x}Ti_x)O_3$,” *Phys. Rev. B,* vol. 62, pp. 743-746, 2000.

[172] D. Mazza, S. Ronchetti and A. Costanzo, “Atomistic simulations on mullite $Al_2(Al_{2+2x}Si_{2-2x})O_{10-x}$ in a variable range of composition,” *J. Eur. Ceram. Soc.,* vol. 28, pp. 367-370, 2008.

[173] D.J. Wilson, B. Winkler, E.A. Juarez-Arellanoa, A. Friedricha, K. Knorr, C.J. Pickard and V. Milmand, “Virtual crystal approximation study of nitrido silicates and oxonitridoaluminasilicates,” *J. Phys. Chem. Solids,* vol. 69, pp. 1862-1868, 2008.

[174] L. Bellaiche and D. Vanderbilt, “Virtual crystal approximation revisited: Application to dielectric and piezoelectric properties of perovskites,” *Phys. Rev.,* vol. B61, pp. 7877-7882, 2000.

[175] R. Grau-Crespo, S. Hamad, C.R.A. Catlow and N.H. de Leeuw, “Symmetry-adapted configurational modelling of fractional site occupancy in solids,” *J. Condens. Matter Phys.,* vol. 19, pp. 1-16, 2007.

[176] A. Bosenick, M.T. Dove, V. Heine and C.A. Geiger, “Scaling of thermodynamic mixing properties in garnet solid solutions,” *Phys. Chem. Miner.,* vol. 28, pp. 177-187, 2001.

[177] A. Bosenick, M.T. Dove, E.R. Myers, E.J. Palin, C.I. Sainz-Diaz, B.S. Guiton, M.C. Warren, M.S. Craig and S.A.T. Redfern, “Computational methods for the study of energies of cation distributions: applications to cation-ordering phase transitions and solid solutions,” *Mineral. Magn.,* no. 65, pp. 193-219, 2001.

[178] Z. Du, N.H. De Leeuw, R. Grau-Crespo, P.B. Wilson, J.P. Brodholt, M. Calleja and M.T. Dove, “A computational study of the structures and stabilities effect of Li-K solid solutions on of layered silicate materials - an application of the use of Condor pools in molecular simulation,” *Mol. Simul.,* vol. 31, pp. 339-347, 2005.

[179] R. Grau-Crespo, A. G.Peralta, A. R. Ruiz-Salvador, A. Gomez and R. Lopez-Cordero, “A computer simulation study of distribution, structure and acid strength of active sites in H-ZSM-5 catalyst,” *Phys. Chem. Chem. Phys.,* vol. 2, pp. 5716-5722, 2000.

[180] M.S. Islam, D.J. Driscoll, C.A.J. Fisher and P.R. Slater, “Atomic-Scale Investigation of Defects, Dopants, and Lithium Transport in the $LiFePO_4$ Olivine-Type Battery Material,” *Chem. Mater.,* vol. 17, pp. 5085-5092, 2005.

[181] M.S. Khan, M.S. Islam and D.R. Bates, “Cation doping and oxygen diffusion in zirconia: a combined atomistic simulation and molecular dynamics study,” *J. Mater. Chem.,* vol. 8, pp. 2299-2307, 1998.

[182] M.Y. Lavrentiev, N.L. Allan and J.A. Purton, “Beyond the point defect limit: solid solutions, phase diagrams and trace-element partitioning,” *Phys. Chem. Chem. Phys.,* vol. 5, pp. 2190-2196, 2003.

[183] M.Y. Lavrentiev, J.A. Purton and N.L. Allan, “Ordering in spinels-A Monte Carlo study,” *Am. Mineral.,* vol. 88, pp. 1522-1531, 2003.

[184] J.A. Purton, M. Yu. Lavrentiev and N.L. Allan, “Monte Carlo simulation of GaN/InN mixtures,” *J. Mater. Chem.,* vol. 15, pp. 785-790, 2005.

[185] I.T. Todorov, N.L. Allan, M. Yu. Lavrentiev, C.L. Freeman, C.E. Mohn and J.A. Purton, “Simulation of mineral solid solutions at zero and high pressure using lattice statics, lattice dynamics and Monte Carlo methods,” *J. Condens. Matter Phys.,* vol. 16, pp. S2751-S2770, 2004.

[186] R. Grau-Crespo, N.H. de Leeuw and C.R.A. Catlow, “The effect of cation coordination on the properties of oxygen vacancies in $FeSbO_4$,” *J. Mater. Chem.,* vol. 13, pp. 2848-2850, 2003.

[187] R. Grau-Crespo, N.H. de Leeuw and C.R.A. Catlow, “Distribution of Cations in $FeSbO_4$: A Computer Modeling Study,” *Chem. Mater.,* vol. 16, pp. 1954-1960, 2004.

[188] M.T. Dove, Introduction to Lattice Dynamics, New York: (Cambridge: Cambridge University Press), 1993.

[189] M.K. Aydinol, A.F. Kohan, G. Ceder, K. Cho and J. Joannopoulos, “Ab initio study of lithium intercalation in metal oxides and metal dichalcogenides,” *Phys. Rev. B,* vol. 56, pp. 1354-1365, 1997.

[190] C. Wolverton and A. Zunger, “Cation and vacancy ordering in Li_xCoO_2,” *Phys. Rev. B,* vol. 57, pp. 2242-2252, 1998.

[191] M. K. Aydinol, A. F. Kohan, G. Ceder, K. Cho and J. Joannopoulos, “Ab initio study of lithium intercalation in metal oxides and metal dichalcogenides,” *Phys. Rev. B,* vol. 57, pp. 1354-1365, 1997.

[192] J. Bhattacharya and C. Wolverton, “Relative stability of normal vs. inverse spinel for 3d transition metal oxides as lithium intercalation cathodes,” *Phys. Chem. Chem. Phys.,* vol. 15, pp. 6486-6498, 2013.

[193] T.S. Choy, J. Naset, J. Chen, S. Hershfield and C. Stanton., “In copper, for example, the effective mass is a tensor and also changes sign depending on the wave vector, as can be seen in the de Haas–van Alphen effect,” Bulletin of The American Physical Society, 2000. [Online]. Available: http://www.phys.ufl.edu/fermisurface/.

[194] M.D. Segall, P.J. D. Lindan, M.J. Probert, C.J. Pickard, P.J. Hasnip, S.J. Clark, and M.C. Payne, “First-principles simulation: ideas, illustrations and the castep code,” *J. Phys. Condens. Matter,* vol. 14, pp. 2717-2744, 2002.

[195] P. Ravindran, L. Fast, P.A. Korzhavyi, B. Johansson, J. Willis and O. Eriksson, “Density functional theory for calculation of elastic properties of orthorhombic crystals: Application to $TiSi_2$,” *J. Appl. Phys.,* vol. 84, pp. 4891-4904, 1998.

[196] D.A. Stewart, “Ab initio investigation of phonon dispersion and anomalies in palladium,” *New J. Phys.,* vol. 10, pp. 1-11, 2008.

[197] Q.J. Liu, Z.T. Liu, L.P. Feng and H. Tian, “First-Principles Study of Electronic Structure and Optical Properties of Tetragonal $PbMoO_4$,” *Comput. Mater. Sci.,* vol. 50, pp. 2822-2825, 2011.

[198] R. Hill, “The elastic behaviour of a crystalline aggregate,” *Proc. Phys. Soc. A,* vol. 65, pp. 349-54, 1952.

[199] S.F. Pugh, “Relations between the elastic moduli and the plastic properties of polycrystalline pure metals,” *Philos. Mag.,* vol. 45, pp. 823-43, 1954.

[200] C. Zener, Elasticity and An elasticity of Metals, Chicago: University of Chicago Press, 1948.

[201] Y. Le Page and P. Saxe, “Symmetry-general least-squares extraction of elastic coefficients from ab initio total energy calculations,” *Phys. Rev. B,* vol. 63, pp. 174103-174108, 2001.

[202] P. Bloechl, “Projector augmented-wave method,” *Phys. Rev. B,* vol. 50, pp. 17953-17979, 1994.

[203] G. Simmons and H. Wang, Single Crystal Elastic Constants and Calculated Aggregate Properties, Cambridge: The M.I.T. Press, 1971.

[204] S.H. Simon, The Oxford solid state basics (1st ed.), Oxford: Oxford University Press, 2013.

[205] F. Schwabl, Advanced Quantum Mechanics (4th ed.), Berlin: Springer, 2008.

[206] R.M. Martin, “Dielectric Screening Model for Lattice Vibrations of Diamond-Structure Crystals,” *Phys. Rev.,* vol. 186, pp. 871-884, 1969.

[207] J.C. Phillips, “Covalent Bond in Crystals. I. Elements of a Structural Theory,” *Phys. Rev.,* vol. 166, pp. 832-838, 1968.

[208] S. Baroni, P. Giannozi and A. Testa, “Green’s-function approach to linear response in solids,” *Phys. Rev. Lett.,* vol. 58, pp. 1861-1864, 1987.

[209] R.D. King-Smith and R.J. Needs, “A new and efficient scheme for first-principles calculations of phonon spectra,” *J. Phys. Condens. Matter,* vol. 2, pp. 3431-3444, 1990.

[210] X. Gonze, D.C. Allan and M. Teter, “Dielectric tensor, effective charges, and phonons in α-quartz by variational density-functional perturbation theory,” *Phys. Rev. Lett.,* vol. 68, pp. 3603-3606, 1992.

[211] G. Kresse, Furthmueller and J. Hafner, “Ab initio force constant approach to phonon dispersion relations of diamond and graphite,” *Europhys. Lett.,* vol. 32, pp. 729-734, 1995.

[212] W. Frank, C. Elsässer and M. Fähnle, “Ab initio Force-Constant Method for Phonon Dispersions in Alkali Metals,” *Phys. Rev. Lett.,* vol. 74, pp. 1791-1794, 1995.

[213] A. Rahman, “Correlations in the Motion of Atoms in Liquid Argon,” *Phys. Rev.,* vol. 136, pp. A405-A411, 1964.

[214] R. Mahlangu, “First principle study of Ti-Al and Pt-Ti alloys,” University of Limpopo, Polokwane, 2009.

[215] K. Kunc and R.M. Martin, “Ab Initio Force Constants of GaAs: A New Approach to Calculation of Phonons and Dielectric Properties,” *Phys. Rev. Lett.,* vol. 48, pp. 406-409, 1982.

[216] K. Parlinski, Z.Q. Li and Y. Kawazoe, “First-Principles Determination of the Soft Mode in Cubic ZrO_2,” *Phys. Rev. Lett.,* vol. 78, pp. 4063-4066, 1997.

[217] E. Deligoz, U.F. Ozyar and H.B. Ozisik, “Theoretical investigations on vibrational properties and thermal conductivities of ternary antimonides TiXSb, ZrXSb and HfXSb (X = Si, Ge),” *Philos. Mag.,* vol. 96, pp. 1712-1723, 2016.

[218] V. Milman, E.V. Akhmatskaya, R.H. Nobes, B. Winkler, C.J. Pickard and J.A. White, “Systematic ab initio study of the compressibility of silicate garnets,” *Acta Cryst.,* vol. B57, pp. 163-177, 2001.

[219] W. Kohn and L.J. Sham, “Self-consistent equations including exchange and correlation effects,” *Phys. Rev.,* vol. 140, pp. A1133, 1965.

[220] P. Hohenberg and W. Kohn, “Inhomogeneous Electron Gas,” *Phys. Rev.,* vol. 136, pp. B864-B871, 1964.

[221] G. Singh, S.L. Gupta, R. Prasad, S. Auluck, R. Gupta and A. Sil, “Suppression of Jahn–Teller distortion by chromium and magnesium doping in spinel $LiMn_2O_4$: A first-principles study using GGA and GGA+U,” *J. Phys. Chem. Solids,* vol. 70, pp. 1200-1206, 2009.

[222] J.H. Kim, S.T. Myung, C.S. Yoon, S.G. Kang and Y.K. Sun, “Comparative Study of $LiNi_{0.5}Mn_{1.5}O_{4-ä}$ and $LiNi_{0.5}Mn_{1.5}O_4$ Cathodes Having Two Crystallographic Structures: Fd-3m and $P4_332$,” *Chem. Mater.,* vol. 16, pp. 906-914, 2004.

[223] M. Aklalouch, J.M. Amarila, R.M. Rojas, I. Saadoune and J.M. Rojo, “Chromium doping as a new approach to improve the cycling performance at high temperature of 5V $LiNi_{0.5}Mn_{1.5}O_4$-based positive electrode,” *J. Power Sources,* vol. 185, pp. 501-511, 2008.

[224] M.W. Raja, S. Mahanty and R.N. Basu, “Multi-faceted highly crystalline $LiMn_2O_4$ and $LiNi_{0.5}Mn_{1.5}O_4$ cathodes synthesized by a novel carbon exo-templating method,” *Solid State Ion.,* vol. 180, pp. 1261-1266, 2009.

[225] X. Xiao-Gui, S. Jing-Qin, and S. Si-Qi, “Structural and magnetic properties of $LiNi_{0.5}Mn_{1.5}O_4$ and $LiNi_{0.5}Mn_{1.5}O_{4-\partial}$ spinels: A first principles study,” *Chin. Phys. B,* vol. 21, pp. 128202(1)-128202(7), 2012.

[226] H. Jones, “The phase boundaries in binary alloys, part 2: the theory of the α, β phase boundaries,” *Proc. Phys. Soc.,* vol. 49, pp. 250-257, 1937.

[227] Q.M. Hu and R. Yang, “Mechanical properties of structural materials from first-principles,” *Curr. Opin. Solid State Mater. Sci.,* vol. 10, pp. 19-25, 2006.

[228] Y. Qi, L.G. Hector Jr., C. James and K. Jin Kima, “Lithium Concentration Dependent Elastic Properties of Battery Electrode Materials from First Principles Calculations,” *J. Electrochem. Soc.,* vol. 161, pp. F3010-F3018, 2014.

[229] F.P. McGrogan, Y. Mi. Chiang and K.J. Van Vliet, “Effect of transition metal substitution on elastoplastic properties of $LiMn_2O_4$ spinel,” *J. Electroceram.,* vol. 38, pp. 215-221, 2016.

[230] M. Zhu, J. Park, and A.M. Sastry, “Fracture Analysis of the Cathode in Li-Ion Batteries: A Simulation Study,” *J. Electrochem. Soc.,* vol. 159, pp. A492-A498, 2012.

[231] W.H. Woodford, Y.M. Hiang and W.C. Carter, “Electrochemical Shock” of Intercalation Electrodes: A Fracture Mechanics Analysis,” *J. Electrochem. Soc.,* vol. 157, pp. A1052-A1059, 210.

[232] X. Zhang, A.M. Sastry and W. Shyy, “Intercalation-Induced Stress and Heat Generation within Single Lithium-Ion Battery Cathode Particles,” *J. Electrochem. Soc.,* vol. 155, pp. A542-A552, 2008.

[233] J. Christensen and J. Newman, “A mathematical model of stress generation and fracture in lithium manganese oxide,” *J. Electrochem. Soc.,* vol. 153, pp. A1019-A1030, 2006.

[234] J. Park, W. Lu and A.M. Sastry, “Numerical Simulation of Stress Evolution in Lithium Manganese Dioxide Particles due to Coupled Phase Transition and Intercalation,” *J. Electrochem. Soc.,* vol. 158, pp. A201-A206, 2011.

[235] R. Okamoto, K. Hayashi, S. Matsumoto, N. Suzuki and M. Terauchi, “Relationship between the crystal structures of $LiNi_{0.5}Mn_{1.5}O_4$ and $LiMn_{1.5}Ni_{0.45}Fe_{0.05}O_4$ and their internal resistances as cathode materials for lithium ion batteries,” *J. Solid State Electrochem.,* vol. 21, pp. 3301-3314, 2017.

[236] G. Kresse and J. Furthmuller, “Efficiency of ab-initio total energy calculations for metals and semiconductors using a plane-wave basis set,” *Comput. Mater. Sci.,* vol. 6, pp. 15-50, 1996.

[237] G. Kresse and J. Hafner, “Ab-Initio Molecular-Dynamics Simulation of the Liquid-Metal Amorphous-Semiconductor Transition in Germanium,” *Phys. Rev. B,* vol. 49, pp. 14251-14269, 1994.

[238] J. Hafner, “Ab-initio simulations of materials using VASP: Density-functional theory and beyond,” *J. Comput. Chem.,* pp. 2044–2078, 2008.

[239] Y. Le Page, P. Saxe and J.R. Rodgers, “Ab initio stiffness for low quartz and calcite,” *Phys. Status Solidi B,* pp. 1155-1161, 2002.

[240] Y. Le Page and P. Saxe, “Symmetry-general least-squares extraction of elastic data for strained materials from ab initio calculations of stress,” *Phys. Rev. B,* vol. 65, pp. 104104-104114, 2002.

[241] F. Mouhat and F.X Coudert, “Necessary and Sufficient Elastic Stability Conditions in Various Crystal System,” *Phys. Rev. B,* vol. 90, pp. 224104-1-224104-4, 2014.

[242] L. Kantorovich, Quantum Theory of the Solid State: An Introduction, London: Kluwer Academic Publishers, 2004.

[243] R. Hill, “The Elastic Behaviour of a Crystalline Aggregate,” *Phys. Soc.,* vol. 65, pp. 349-354, 1952.

[244] A. Reuss, “Berechnung der Fließgrenze von Mischkristallen auf Grund der Plastizitätsbedingung für Einkristalle,” *Z. Angew. Math. Mech.,* vol. 9, pp. 49-58, 1929.

[245] W. Voight, Lehrbuch der kristallphysik (mit ausschluss der kristalloptik), Berlin: Leipzig, Berlin, B.G. Teubner, 1928.

[246] H.S. Chen, “Anisotropy of Elasticity about Metal,” Metallurgy Industry Press, Beijing, 1996.

[247] S. Grimme, S. Ehrlich and L. Goerigk, “Effect of the damping function in dispersion corrected density functional theory,” *J. Comp. Chem.,* vol. 32, pp. 1456-1465, 2011.

[248] R. Grau-Crespo, S. Hamad, C.R.A. Catlow and N.H. de Leeuw, “Symmetry-adapted configurational modelling of fractional site occupancy in solids,” *J. Phys. Condens. Matter,* vol. 19, pp. 256201-256216, 2007.

[249] D. Santos-Carballal, A. Roldan, R. Grau-Crespo and N.H. de Leeuw, “First-principles study of the inversion thermodynamics and electronic structure of FeM_2X_4 (thio)spinels (M = Cr, Mn, Co, Ni; X = O, S),” *Phys. Rev. B,* vol. 91, pp. 195106-195113, 2015.

[250] M. Kunduraci and G.G. Amatucci, “Effect of Oxygen NonStoichiometry and Temperature on Cation Ordering in $LiMn_{2-x}Ni_xO_4$ ($0.50 \geq x \geq 0.36$) Spinels,” *J. Power Sources,* vol. 165, pp. 359-367, 2007.

[251] A. Sakunthala, M.V. Reddy, S. Selvasekarapandian, B.V.R. Chowdari and P. Christopher, “Synthesis of Compounds, $Li(MMn_{11/6})O_4$ (M = $Mn_{1/6}$, $Co_{1/6}$, ($Co_{1/12}Cr_{1/12}$), ($Co_{1/12}Al_{1/12}$), ($Cr_{1/12}Al_{1/12}$)) by Polymer Precursor Method and Its Electrochemical Performa,” *Electrochim. Acta,* vol. 55, pp. 4441-4450, 2010.

[252] E. Hu, S.M. Bak, J. Liu, X. Yu, Y. Zhou, S.N. Ehrlich, X.Q. Yang and K.W. Nam, “Oxygen-Release-Related Thermal Stability and Decomposition Pathways of $LixNi_{0.5}Mn_{1.5}O_4$ Cathode Materials,” *Chem. Mater.,* vol. 26, pp. 1108-1118, 2014.

[253] G.B. Zhong, Y.Y. Wang, X.J. Zhao, Q.S. Wang, Y. Yu and C.H. Chen, “Structural, Electrochemical and Thermal Stability Investigations on $LiNi_{0.5}$

$_xAl_{2x}Mn_{1.5-x}O_4$ (0 ≤ 2x ≤ 1.0) as 5 V Cathode Materials," *J. Power Sources,* vol. 216, pp. 368-375, 2012.

[254] J. Breger, K. Kang, J. Cabana, G. Ceder and C.P. Grey, "NMR, PDF and RMC study of the positive electrode material $Li(Ni_{0.5}Mn_{0.5})O_2$ synthesized by ion-exchange methods," *J. Mater. Chem.,* vol. 17, pp. 3167-3174, 2007.

[255] C.S. Barrett, "X-ray study of alkaline metal at low temperatures," *Acta Crystallogr.,* vol. 9, pp. 671-677, 1956.

[256] S. Hy, H. Liu, M. Zhang, D. Qian, B.J Hwang, and Y.S. Meng, "Performance and design considerations for lithium excess layered oxide positive electrode materials for lithium-ion batteries.," *Energy Environ. Sci.,* vol. 9, pp. 1931-1954, 2016.

[257] A. Kraytsberg and Y. Ein-Eli, "Higher, stronger, better... A review of 5 volt cathode materials for advanced lithium-ion batteries," *Adv. Energy Mater.,* vol. 2, pp. 922-939, 2012.

[258] K. Amine, H. Tukamoto, H. Yasuda and Y. Fujita, "Preparation and electrochemical investigation of $LiMn_{2-x}Me_xO_4$(Me: Ni, Fe, and x= 0.5, 1) cathode materials for secondary lithium batteries," *J. Power Sources,* vol. 68, pp. 604-608, 1997.

[259] Q. Zhong, A. Bonakdarpour, M. Zhang, Y. Gao and J.R. Dahn, "Synthesis and Electrochemistry of $LiNi_xMn_{2-x}O_4$," *J. Electrochem. Soc.,* vol. 205, pp. 205-213, 1997.

[260] Y.L. Ding, J. Xie, G.S. Cao, T.J. Zhu, H.M. Yu and X.B. Zhao, "Single-Crystalline $LiMn_2O_4$ Nanotubes Synthesized Via Template-Engaged Reaction as Cathodes for High-Power," *Adv. Funct. Mater.,* vol. 21, pp. 348-355, 2011.

[261] J. Liu, Z. Sun, J. Xie, H. Chen, N. Wu and B. Wu, "Synthesis and electrochemical properties of $LiNi0_{.5-x}Cu_xMn_{1.5-y}Al_yO_4$ (x= 0, 0.05, y= 0, 0.05) as 5 V spinel materials," *J. Power Sources,* vol. 240, pp. 95-100, 2013.

[262] S. Patoux, L. Daniel, C. Bourbon, H. Lignier, C. Pagano, F. Le Cras and S. Martinet, "High voltage spinel oxides for Li-ion batteries: From the material research to the application," *J. Power Sources,* vol. 189, pp. 344-352, 2009.

[263] S. Dou, “Review and prospect of layered lithium nickel manganese oxide as cathode materials for Li-ion batteries,” *J. Solid State Electr.,* vol. 17, pp. 911-926, 2013.

[264] S. Solchenbach, M. Wetjen, D. Pritzl, K.U. Schwenke and H.A. Gasteiger, “Lithium Oxalate as Capacity and Cycle-Life Enhancer in LNMO/Graphite and LNMO/SiG Full Cells Journal of The Electrochemical Society,” *J. Electrochem. Soc.,* vol. 165, pp. A512-A524, 2018.

[265] J. Zheng, J. Xiao, X. Yu, L. Kovarik, M. Gu, F. Omenya, X. Chen, X. Yang, J. Liu, G. Graff, M. Whittingham, and J. Zhang, “Enhanced Li ion transport in $LiNi_{0.5}Mn_{1.5}O_4$ through control of site disorder,” *Phys. Chem. Chem. Phys.,* vol. 14, pp. 13515-13521, 2012.

[266] Y. Xie, V. Srinivasan, H. Kaiya and K. Takahashi, “Particle-Scale Path-Dependent Behavior of $Li_xNi_{0.5}Mn_{1.5}O_4$ Electrode in Li-Ion Batteries: Part I. Experimental Study,” *J. Electrochem. Soc.,* vol. 166, pp. A2513-A2517, 2019.

[267] Y.J. Wei, L.Y. Yan, C.Z. Wang, X.G. Xu, F. Wu and G. Chen, “Effects of Ni Doping on $[MnO_6]$ Octahedron in $LiMn_2O_4$,” *J. Phys. Chem. B,* vol. 108, pp. 18547-18551, 2004.

[268] K. Raju, F.P. Nkosi, E. Viswanathan, M.K. Mathe, K. Damodaran and K.I. Ozoemena, “Microwave-enhanced electrochemical cycling performance of the $LiNi_{0.2}Mn_{1.8}O_4$ spinel cathode material at elevated temperature,” *Phys. Chem. Chem. Phys.,* vol. 18, pp. 13074-13083, 2016.

[269] J.S. Park, K.C. Roh, J.W. Lee, K. Song, Y.I. Kim and Y.M. Kang, “Structurally stabilized $LiNi_{0.5}Mn_{1.5}O_4$ with enhanced electrochemical properties through nitric acid treatment,” *J. Power Sources,* vol. 230, pp. 138-142, 2013.

[270] T. Okumura, M. Shikano and H. Kobayashi, “Contribution of oxygen partial density of state on lithium intercalation/de-intercalation process in $LixNi_{0.5}Mn_{1.5}O_4$ spinel oxides,” *J. Power Sources,* vol. 244, pp. 544-547, 2013.

[271] Z. Zhu, H. Yan, D. Zhang, W. Li and Q. Lu, “Preparation of 4.7 V cathode material $LiNi_{0.5}Mn_{1.5}O_4$ by an oxalic acid-pretreated solid-state method for lithium-ion secondary battery,” *J. Power Sources,* vol. 224, pp. 13-19, 2013.

[272] M.A. Kebede, N. Kunjuzwa, C.J. Jafta, M.K. Mathe and K.I. Ozoemena, “Solution-combustion synthesized nickel-substituted spinel cathode materials

($LiNi_xMn_{2-x}O_4$; $0 \leq x \leq 0.2$) for lithium ion battery: enhancing energy storage, capacity retention, and lithium ion transport," *Electrochim. Acta,* vol. 128, pp. 172-177, 2014.

[273] I. Tomeno, Y. Kasuya and Y. Tsunoda, "Charge and spin ordering in $LiMn_2O_4$," *Phys. Rev. B,* vol. 64, pp. 094422-1-094422-8, 2001.

APPENDIX A

Papers Presented at Local and International Conferences.

1. Malatji, K.T., Ngoepe, P.E. and Maphanga R.R. Computer Simulation Studies of Spinel $LiMn_2O_4$ and $LiNi_xMn_{2-x}O_4$ ($0 \leq x \leq 2$), SAIP Conference, July 2012, Pretoria, South Africa (Poster Presentation).
2. Malatji, K.T., Ngoepe, P.E. and Maphanga R.R. Faculty research day; 04-05 October 2012, Density Functional Theory Study of Spinel $LiMn_2O_4$ and Nickel Doped $LiMn_2O_4$ for Lithium-ion Batteries, University of Limpopo, South Africa (Oral presentation).
3. K.T Malatji, P.E Ngoepe, D Mkhonto and R.R Maphanga. *Ab initio* simulation study of spinel $LiMn_2O_4$ and nickel doped $LiMn_2O_4$ ASSAF: Young Scientist Conference; October 2012, Pretoria, South Africa (Poster Presentation).
4. Malatji, K.T., Ngoepe, P.E. and Maphanga R.R. Computational modelling studies of pure and Ni doped $LiMn_2O_4$ batteries, SAIP Conference, July 2013, Richards Bay Campus, University of Zululand, South Africa (Oral).
5. Malatji, K.T., Ngoepe, P.E. and Maphanga R.R. Faculty of Science and Agriculture: Faculty Research day; October 2013, University of Limpopo, South Africa (Oral presentation).
6. Malatji, K.T., Ngoepe, P.E. and Maphanga R.R. CHPC: Centre for High-Performance Computing. 2-6 December 2013, Cape Town International Convention Centre, South Africa (Oral).
7. Malatji, K.T., Ngoepe, P.E. and Maphanga R.R. Africa-MRS: the 7th International Conference of the Africa Materials Research Society. 8-13 December 2013, Addis Ababa United Nations (UN), Ethiopia (Oral).
8. R.S. Ledwaba, K.T. Malatji, M.G. Matshaba and P.E. Ngoepe, “Atomistic Simulation Studies of Spinel $LiMn_2O_4$”, South African Institute of Physics, 59th Annual Conference, 6-11 July 2014, University of Johannesburg (U.J), Johannesburg.

9. Malatji, K.T., Ngoepe, P.E. and Maphanga R.R. Phase Stability Study of Nickel Doped Spinel $LiMn_2O_4$ Using Cluster Expansion Method", South African Institute of Physics, 61st Annual Conference, 04-08 July 2016, University of Cape Town (UCT), Cape Town.
10. Malatji, K.T., Ngoepe, P.E. and Maphanga R.R. Structure and Phase Stability Study of Nickel Doped Spinel $LiMn_2O_4$ using Cluster Expansion Method", South African Institute of Physics, 62nd Annual Conference, 03-07 July 2017, Stellenbosch University, Cape Town.
11. Kemeridge. T Malatji, David Santos-Carballal, Umberto Terranova, Rapela. R Maphanga Phuti. E Ngoepe, Nora H. de Leeuw*. Controlling the lithium intercalation voltage in $LiMn_{2-2x}Ni_{2x}O_4$ spinel via tuning of the Ni concentration, CHPC: Centre for High-Performance Computing. 03-07 December 2017, Pretoria.
12. Kemeridge. T Malatji, David Santos-Carballal, Umberto Terranova, Rapela. R Maphanga Phuti. E Ngoepe, Nora H. de Leeuw*.Cation distribution and mixing thermodynamics in $LiMn_{1-x}Ni_xO_4$ spinel via tuning of the Ni concentration, 63rd SAIP ANNUAL CONFERENCE 25-29 June 2018, University Of Free State (Bloemfontein).
13. Malatji, K.T., Ngoepe, P.E. and Maphanga R.R. Computer Simulation and Phase Diagram Prediction of $Li(Mn_xNi_{1-x})_2O_4$, CHPC: Centre for High-Performance Computing. 02-06 December 2018, Century City Convention Centre, Cape Town.

Paper to be submitted to South African Journal of Chemistry (SAJC).

1. Controlling the lithium intercalation voltage in the $Li(Mn_xNi_{1-x})_2O_4$ spinel via tuning of the Ni concentration.

Paper to be submitted.

1. Theoretical investigation on vibrational and mechanical properties of a nickel doped $LiMn_{2-2x}Ni_{2x}0_4$ ($0 \leq x \leq 2$) spinel using Cluster Expansion Technique.